

# Effects of Magnetic Fields in Compact Stars

Dissertation  
zur Erlangung des Doktorgrades  
der Naturwissenschaften

vorgelegt beim Fachbereich Physik  
der Johann Wolfgang Goethe-Universität  
in Frankfurt am Main

von  
**Bruno Franzon**  
aus Tupi Paulista, Brasilien

Frankfurt am Main, Germany  
May 2017  
(D30)

vom Fachbereich Physik (13) der Johann Wolfgang Goethe-Universität als Dissertation angenommen.

Dekan: Prof. Dr. D. Owe Philipsen

Gutachter: Prof. Dr. S. Schramm

Gutachter: Prof. Dr. M. Bleicher

Datum der Disputation: 28.04.2017

# Abstract

Compact stars can be treated as the ultimate laboratories for testing theories of dense matter. They are not only extremely dense objects, but they are known to be associated with strong magnetic fields, fast rotation and, in certain cases, with very high temperatures. Here, we present several different approaches to model numerically the signatures and properties of these stars, namely:

- The effects of strong magnetic fields on hybrid stars by using a fully general relativistic approach. We solved the coupled Maxwell-Einstein equations in a self-consistent way, taking into consideration the anisotropy of the energy-momentum tensor due purely to the magnetic field, magnetic field effects on equation of state and the interaction between matter and the magnetic field (magnetization). We showed that the effects of the magnetization and the magnetic field on the equation of state for matter do not play an important role on global properties of neutron stars (only the pure magnetic field contribution does). In addition, the magnetic field breaks the spherical symmetry of stars, inducing major changes in the populated degrees of freedom inside these objects and, potentially, converting a hybrid star into a hadronic star over time.
- The effects of magnetic fields and rotation on the structure and composition of proto-neutron stars. We found that the magnetic field not only deforms these stars, but also significantly alters the number of trapped neutrinos in the stellar interior, together with the strangeness content and temperature in each evolution stage from a hot proto-neutron star to a cold neutron star.
- The influence of the quark-hadron phase transitions in neutron stars. In particular, previous calculations have shown that fast rotating neutron stars, when subjected to a quark-hadron phase transition in their interiors, could give rise to the backbending phenomenon characterized by a spin-up era. In this work, we obtained the interesting backbending phenomenon for fast spinning neutron stars. More importantly, we showed that a magnetic field, which is assumed to be axisymmetric and poloidal, can also be enhanced due to the phase transition from normal hadronic matter to quark matter on highly magnetized neutron stars. Therefore, in parallel to the spin-up era, classes of neutron stars endowed with strong magnetic fields may go through a 'magnetic-up era' in their lives.
- Finally, we were also able to calculate super-heavy white dwarfs in the presence of strong magnetic fields. White dwarfs are the progenitors of supernova Type Ia explosions and they are widely used as candles to show that the Universe is expanding and accelerating. However, observations of ultraluminous supernovae have suggested that the progenitor of such an explosion should be a white dwarf with mass above the well-known Chandrasekhar limit  $\sim 1.4 M_{\odot}$ . In corroboration with other works, but by using a fully general relativistic framework, we obtained also strongly magnetized white dwarfs with masses  $M \sim 2.0 M_{\odot}$ .



---

# Preface

This thesis is submitted to the Faculty of Physics of the Johann Wolfgang Goethe University for attaining the PhD degree of Natural Sciences. The research described herein was conducted under the supervision of Prof. Dr. Stephan Schramm at the Frankfurt Institute for Advanced Studies, between April 2013 and December 2016.

The results of this work have been presented in the following publications:

- Franzon, B.; Dexheimer, V.; S. Schramm. A self-consistent study of magnetic field effects on hybrid stars, *Mon.Not.Roy.Astron.Soc.* 456 (2015) no.3, 2937-2945.
- Franzon, B.; Schramm, S. Effects of magnetic fields on hybrid stars, *PoS(MPCS2015)018*.
- Franzon, B.; Gomes, Rosana; Schramm, Stefan. Effects of quark-hadron phase transition on highly magnetized neutron stars, *Mon.Not.Roy.Astron.Soc.* 463 (2016) 571-579.
- Franzon, B., V. Dexheimer and S. Schramm. Rotating proto-neutron stars under strong magnetic fields, *Phys.Rev.* D94 (2016) no.4, 044018.
- Franzon, B.; Schramm, S. Effects of strong magnetic fields and rotation on white dwarf structure, *Phys.Rev.* D92 (2015) 8, 083006.
- Franzon, B.; and Schramm, S. Accepted in *Mon.Not.Roy.Astron.Soc.*: AR Scorpii and possible gravitational radiation from pulsar white dwarfs, *arXiv:1609.00493*.

Furthermore, we refer to the following (recent) works in this thesis:

- submitted to *Physical Review Letter*: The magnetic field profile in strongly magnetized neutron stars, *arXiv:1612.05795*.  
Authors: Dexheimer, V.; Franzon, B.; Gomes, R.; R. L. S. Farias; S. S. Avancini; S. Schramm
- submitted to *Mon.Not.Roy.Astron.Soc.*: Crust effects and the cooling relaxation time in highly magnetized neutron stars, *arXiv:1612.04670*.  
Authors: Franzon, B.; Negreiros, R.; and Schramm, S.
- submitted to *Physical Review D*: Axisymmetric Magnetic Fields, Electron Capture and Pycnonuclear Reactions in Magnetized White Dwarfs, *arXiv:1609.05994*.  
Authors: Edson Otoniel, Franzon, B., Manuel Malheiro, Stefan Schramm, Fridolin Weber.

# Zusammenfassung

Alle Sterne unseres Universums sind im Laufe von mehreren Millionen Jahren einer Evolution unterworfen. Nachdem Sterne ihren Kernbrennstoff erschöpft haben, kollabiert ihr Kern in ihrer letzten Phase. Abhängig von der vor dem Kollabieren vorhandenen Sternmasse entsteht ein weißer Zwerg, ein Neutronenstern oder ein schwarzes Loch. Wie in Tabelle 1 zu erkennen, die die Beziehung zwischen Masse und Endstufe des Sterns zeigt, entstehen Neutronensterne, wenn Sterne mit anfänglichen Massen von etwa  $8-30 M_{\odot}$  bei Supernovae-Ereignissen kollabieren. Neutronensterne haben typischerweise Radien von 10 km und Massen, die zwischen ein und zwei Sonnenmassen liegen. Folglich existiert in diesen Sternen stark komprimierte ultradichte Kernmaterie und sie sind somit einzigartige Objekte für die Untersuchung fundamentaler Fragen in der Physik und der Astrophysik, wie z.B. von möglichen Phasenübergängen zu exotischer Materie und der Gravitationsphysik im starken Feldregime. Außerdem rotieren Neutronensterne sehr schnell. Viele dieser Objekte haben auch sehr starke Magnetfelder, die zur Emission von Strahlung führen, welche auf der Erde dann als Leuchtturmfeuer am Himmel erkannt werden kann. Diese Eigenschaften bieten durch die Möglichkeiten der Physik dichter Materie und den Fortschritten in der Beobachtungs-Astrophysik die einmalige Gelegenheit, das Verhalten von Materie und elektromagnetischen Feldern unter extremen Bedingungen zu testen und zu erforschen, was für terrestrische Experimente unmöglich ist.

Masses des Sterns [ $M_{\odot}$ ]	Endstadium
1-8	Weißer Zwerg
8-30	Neutronenstern
> 30	Schwarzes Loch

TABLE 1: Masse und Endstufe des Sterns.

Die vorliegende Arbeit beschäftigt sich mit der Wirkung starker Magnetfelder in den verschiedenen astrophysikalischen Systemen von Neutronensternen (NS), Proto-Neutronensternen (PNS) und weißen Zwergen (WD). Das Ziel der Arbeit war, realistische mikrophysikalische nukleare Zustandsgleichungen (EoS), die allgemeine Relativitätstheorie, Temperatur, magnetischen Felder und Rotation als Komponenten einzufügen, um die Genauigkeit der Neutronensternberechnung zu verbessern und so die möglichen Ergebnisse aus einer großen Menge an Berechnungen von physikalischen Bedingungen und Parametern zu erhalten.

Diese Arbeit beginnt mit einer Einführung, Kapitel 1, in der die allgemeinen Eigenschaften von Neutronensternen dargestellt werden. Zum Beispiel werden Beobachtungen in verschiedenen elektromagnetischen Spektren (Radio, visuell, infrarot, Röntgenstrahlen,  $\gamma$ -Strahlung) verwendet, um viele der intrinsischen Eigenschaften dieser Sterne abzuleiten. Die überwiegende Mehrheit der Neutronensterne wird als Pulsare beobachtet, am häufigsten in der Radiofrequenz, jedoch hat das Fermi-Gamma-Strahl-Weltraumteleskop in den letzten Jahren mehr als 100 Pulsare in Gammastrahlen beobachtet. Derzeit gibt es fast 2000 entdeckte Pulsare<sup>1</sup>. Jedoch lassen sich nur wenige Eigenschaften von Neutronensternen aus Pulsarbeobachtungen wie z.B. Massen, Rotationsgeschwindigkeiten, grobe Altersabschätzungen und magnetische Feldstärken ableiten. Von ihrer Geburt in einer Supernova-Explosion unterliegen NS extremen physikalischen Bedingungen nicht nur in Bezug auf Dichten, sondern auch bezüglich von Temperaturen, elektromagnetischen Feldern und Rotationsfrequenzen.

In Kapitel 1 wird die Tatsache erörtert, dass die Dichte innerhalb von Neutronensternen höhere Werte erreicht als die nukleare Sättigungsdichte. In der Tat wurden in den vergangenen Jahren

<sup>1</sup>Siehe <http://www.atnf.csiro.au/research/pulsar/psrcat> für Pulsar-Datenbank.

große Anstrengungen unternommen, um die noch offene Frage nach der Zustandsgleichung für ultradichte Kernmaterie zu untersuchen. Darüber hinaus wird in den folgenden Kapiteln 2 und 3 eine weitere wichtige Frage angesprochen: Die Auswirkungen des Magnetfeldes sowohl in der EoS als auch in der Struktur der Neutronensterne. In diesen Kapiteln ermöglichte die Kenntnis der mikroskopischen Theorie, die mit der Zustandsgleichung zusammenhängt, nicht nur die allgemeine Struktur des Sterns einschließlich seiner Verformung aufgrund des Magnetfeldes und aufgrund der Rotation zu studieren, sondern auch seine inneren Zusammensetzung einschließlich der möglichen Quark- und Hyperonphasen im stellaren Kern zu erforschen.

Bestimmte Klassen von Neutronensternen, die als Soft Gamma Repeater (SGR) und Anomalous X-ray Pulsars (AXPs) bekannt sind, haben Magnetfelder auf der Oberfläche in der Größenordnung von  $10^{15}$  G. Diese Objekte werden Magnetare genannt (Duncan and Thompson, 1992). Obwohl die internen Magnetfelder von Neutronensternen nicht direkt durch Beobachtungen erkannt werden können, prognostiziert das Virial Theorem, dass die internen Magnetfelder von hochmagnetischen Neutronensternen im stellaren Zentrum Werte bis zu  $10^{18}$  G erreichen können. Dieser Wert wird in der Newtonschen Mechanik berechnet, indem die in dem Stern gespeicherte stellare magnetische Energie,  $B^2/8\pi \times 4\pi/3R^3$ , und die Gravitationsbindungsenergie,  $3GM^2/5R$ , gleichgesetzt werden. Dies führt zu einer Magnetfeldstärke  $B \sim 1,4 \times 10^{18} (1.40 M_{\odot}/M)(R/10 \text{ km})^{-2}$  G.

Der Ursprung starker Magnetfelder in kompakten Sternen ist noch unklar. Eine verbreitete Hypothese bezieht die Fluss-Erhaltung des Vorläufer-Magnetfeldes ein. Allerdings ist diese Idee nicht für Magnetare geeignet, da ein typischer Neutronenstern mit  $1.40 M_{\odot}$  einen Radius erfordern würde der kleiner ist als sein Schwarzschild-Radius, um ein Flächenmagnetfeld in der Größenordnung von  $10^{15}$  G zu erzeugen. Eine andere Möglichkeit, die von Thompson (1993) vorgeschlagen wurde, beschreibt einen neugeborenen Neutronenstern, der Konvektion und Differentialrotation kombiniert, um einen Dynamo-Prozess zu erzeugen, der in der Lage ist, Felder zu generieren, die so groß wie  $10^{15}$  G auf der Oberfläche des Sterns sind. Die Erwartung ist, dass ein Teil der Rotationsenergie verwendet wird, um die Supernova zu einem schnellen magnetischen Bremsen zu bringen. Daraus schließt man, dass die Entstehung von Magnetaren von Supernovae begleitet wird, die eine Größenordnung energetischer sind als normale Supernovae. Jedoch zeigte sich, dass die Explosionsenergien der Supernova-Reste, die mit Magnetare assoziiert sind, nämlich Kes 73 (AXP 1E 1841-045), CTB109 (AXP 1E2259 + 586) und N49 (SGR 0526-66), nahe der typischen Supernova-Explosionsenergie sind. Als Ergebnis stellte sich heraus, dass Vink and Kuiper (2006) keinen Beweis fanden, dass Magnetare aus schnell rotierenden Proto-Neutronensternen gebildet werden. Deshalb stammen sie wahrscheinlich von stellaren Vorläufern mit hohen Magnetfeldkernen ab.

Was auch immer der Ursprung starker Magnetfelder sein mag, sie beeinflussen die Zustandsgleichung, wie beispielsweise aufgrund der Landau-Quantisierung der Energieniveaus der geladenen Teilchen und der Wirkung des anomalen magnetischen Momentes geladener und ungeladener Teilchen. Außerdem beeinflussen Magnetfelder die Struktur der Raum-Zeit, da Magnetfelder nun eine Quelle für das Gravitationsfeld durch den Maxwell-Energie-Momentum-Tensor sind. Zusätzlich beeinflussen sie die Struktur von Neutronensternen durch die Lorentzkraft, die mit den ein Magnetfeld erzeugenden makroskopischen Strömen verbunden ist. Der Einschluss des Magnetfeldes führt zu einer Modifikation des Energieimpuls-Tensors und durchbricht dadurch die sphärische Symmetrie des Sterns. Infolgedessen sind magnetisierte Sterne anisotrop und erfordern somit eine allgemeine Relativitätsbehandlung, die über die Lösung der Struktur der sphärisch symmetrischen Sterne durch die Tolman-Oppenheimer-Volkoff (TOV) Gleichungen (Tolman, 1939; Oppenheimer and Volkoff, 1939) hinausgeht. Dies geschieht in Kapitel 2.

Es ist seit langem bekannt, dass die Anwesenheit starker Magnetfelder die Landau-Quantisierung der Energieniveaus der geladenen Teilchen erzeugt. Darüber hinaus bewirken Landau-Quantisierungseffekte auf die EoS eine Anisotropie in den Energie-Impuls-Tensorkomponenten. Man würde also erwarten,

dass die EoS sowie Beobachtungsgrößen, wie die maximale Masse, durch starke Magnetfelder beeinträchtigt werden. Frühere Modelle hochmagnetisierter Neutronensterne, die Magnetfeldeffekte in der EoS enthielten, errechneten die entsprechenden Masse-Radius-Relation unter Verwendung isotroper TOV Gleichungen. Es ist jedoch zu beachten, dass bei starken Magnetfeldern, bei denen die Landau-Quantisierungseffekte beachtet werden sollen, die Abweichungen von der sphärischen Symmetrie signifikant sind.

In diesem Sinne wird im Kapitel 3, der Einschluss von Magnetfeldeffekten sowohl in der EoS als auch in der Struktur des Sterns durchgeführt. Die Berechnung der stellaren makroskopischen Struktur beinhaltet das Lösen der gekoppelten Einstein-Maxwell-Gleichungen unter Verwendung einer Metrik, die in der Lage ist, deformierte Objekte zu beschreiben, d.h. eine zweidimensionale Metrik, die sowohl radiale als auch polare Winkelkoordinaten berücksichtigt. Vereinfachte Lösungen für das Problem wurden von Mallick and Schramm (2014) vorgeschlagen, von denen eine Störung der Metrik durchgeführt wurde. Auf der anderen Seite wurde ein Formalismus mit vollständigen numerischen Lösungen von Bonazzola et al. (1993) entwickelt und in der LORENE C++ Bibliothek implementiert. Er berücksichtigt sowohl Drehung als auch Magnetfelder in der stellaren Strukturberechnung von Neutronensternen. Dieser Formalismus wurde zunächst auf eine Einparameter-Zustandsgleichung angewendet. Vor kurzem wurde eine selbstkonsistente Berechnung mit Magnetfeldern sowohl in der Zustandsgleichung als auch in der stellaren Struktur implementiert, um Quarksterne durch Chatterjee et al. (2015) und Hybridsterne von Franzon et al. (2016b) zu beschreiben.

Im Kapitel 3 nutzten wir die Lorene C++ library für die numerische Relativitätstheorie, um die Effekte starker Magnetfelder auf Hybridsterne mit Hilfe eines vollständigen Relativitätsansatzes zu untersuchen. Außerdem werden die gekoppelten Maxwell-Einstein Gleichungen unter Berücksichtigung der Anisotropie des Energieimpuls-Tensors (infolge des Magnetfeldes), der Magnetfeldeffekte auf die Zustandsgleichung und der Wechselwirkung zwischen Materie und dem Magnetfeld (Magnetisierung) gelöst. Nach unseren Ergebnissen wird die Neutronensternstruktur, wie z.B. ihre Masse-Radius-Relation, nicht drastisch durch die Einbeziehung des Magnetfeldes in der EoS und der Magnetisierung modifiziert. Genauer gesagt erhöht die Wirkung der Einbeziehung der Magnetfeldabhängigkeit oder der Magnetisierung die maximale Masse nicht, im Gegensatz zu dem, was in früheren Studien behauptet wurde (Paulucci et al., 2011; Rabhi et al., 2009; Dexheimer et al., 2013a). Andererseits bewirkt das Magnetfeld, dass die zentrale Dichte in diesen Objekten reduziert wird, was wesentliche Änderungen in der Teilchenzusammensetzung hervorruft und potentiell einen Hybridstern in einen hadronischen Stern umwandelt.

Das nächste Kapitel, Kapitel 4, behandelt stationäre Konfigurationen von stark magnetisierten Proto-Neutronensternen. PNS sind neugeborene Kompaktsterne unmittelbar nach dem Gravitationskollaps des Kerns massiver Sterne, die sich abkühlen und kontrahieren, um Neutronensterne zu werden. Die Entropie pro Baryon in PNS liegt in der Größenordnung von 1 oder 2 und macht aus ihnen daher sehr heiße Sterne, deren Temperatur  $T \sim 50$  MeV erreichen kann. Der Zustand in diesen Sternen ist so extrem, dass Neutrinos auf dynamischen Zeitskalen gefangen werden können. Die Zusammensetzung und die Struktur von PNS sind stark mit der Anzahl der gefangenen Neutrinos verbunden. Da das chemische Potential der Neutrinos im Laufe der Zeit im Absolutwert abnimmt, verändert dies das chemische Gleichgewicht und die Zusammensetzung des Sterns, was zu einem Einfluss auf die Struktur und Stabilität der Sterne führt. In diesem Zusammenhang hat das Magnetfeld auch einen großen Einfluss, nicht nur auf die Struktur der PNS, sondern auch auf ihre Teilchenpopulation.

Interessante Ergebnisse des Kapitels 4 sind die Veränderung der Zusammensetzung des Sterns aufgrund des Magnetfeldes, die Auflösung der sich im Stern befindenden Hyperonen, die Zunahme der Menge an Neutrinos und die Seltsamkeit am stellaren Kern, welche alle durch Magnetfelderfall induziert werden. Wie man sehen wird, nimmt mit abnehmendem Magnetfeld die Dichte innerhalb des Sterns zu, worauf eine Zunahme der Temperatur im stellaren Zentrum folgt. Insbesondere



nimmt unter der Annahme, dass das Magnetfeld über die Zeit abklingt, die Temperatur in der Äquatorialebene im inneren Kern zu, während sie in dem äußeren Kern abnimmt. Dies wird durch die Lorentzkraft verursacht, die ihre Richtung in der Äquatorebene umkehrt.

Abgesehen von Magnetfeldern, Rotations- und Temperatureffekten, kann auch eine Quark-Hadron-Phasenumwandlung mehrere interessante Phänomene verursachen und die Neutronensternstruktur stark beeinflussen. Dies wird im Kapitel 5 besprochen, wobei in schnell rotierenden isolierten Pulsaren ein Quarkdeconfinement eine große Auswirkung auf den sogenannten Bremsindex haben kann, der während der Spin-Down-Phase leicht messbar sein sollte. Die Umwandlung von hadronischer zu Quarkmaterie im Kern eines rotierenden Neutronensterns verändert sein Trägheitsmoment. Daher wird die Zeitspanne, über die die Umwandlung stattfindet, in den Spin-Down Charakteristiken der Pulsare angezeigt.

Der Wechsel von einer hadronischen zu einer Deconfinementphase im Zentrum von Neutronensternen durch einen Phasenübergang erster Ordnung führt zu einer drastischen Erweichung der Zustandsgleichung. Infolgedessen verringern Sterne mit festen Baryonmassen ihre Gravitationsmassen (und der zentrale Druck steigt) während der Evolutionssequenz. Wenn die Erweichung der EoS sehr ausgeprägt ist, führt dies zu einer plötzlichen Kontraktion des Neutronensterns bei einer bestimmten Umdrehungsgeschwindigkeit, die bei der Evolution von schnell rotierenden und isolierten Pulsaren durch die Spin-up-Ära, auch Backbending Phänomen genannt, beobachtet werden kann (Glendenning et al., 1997). In Kapitel 5 reproduzieren wir das Backbending Phänomen für schnell drehende Neutronensterne. Aber noch wichtiger ist, dass gezeigt werden kann, dass das Magnetfeld, das als axi-symmetrisch und poloidal angenommen wurde, auch durch den Phasenübergang von normaler hadronischer Materie zu Quark-Materie während der Evolution von einem hochmagnetisierten Neutronenstern zu einem nicht-magnetisierten erhöht wird. Daher können parallel zur Spin-up-Ära einige Klassen von Neutronensternen, die mit starken Magnetfeldern ausgestattet sind, eine 'Magnetic-up-Ära' in ihrem Leben durchlaufen.

Das nächste Kapitel, Kapitel 6, stellt ein weiteres Ergebnis dieser Forschung dar und zeigt, dass es möglich ist, super-schwere weiße Zwerge im Einfluss von starken Magnetfeldern zu berechnen. Dieses wichtige Problem ist interessant und aktuell, da solche Sterne die Chandrasekhar-Massengrenze überschreiten und zur Erforschung des superluminösen Typ-Ia-Supernova (SN Ia) beitragen können. Wenn sich die Masse des weißen Zwergs, der in einem binären System Materie einfängt, der begrenzenden Masse nähert, erfährt der Stern eine schnelle Kontraktion. Eine erhöhte Temperatur während dieses Kollaps kann eine unkontrollierte thermonukleare Reaktion auslösen, die zu einer Supernova-Explosion des Typs Ia führt. Die Standardbedingungen, die zur SN Ia führen, erlauben diesen Sternen, als Standardkerzen in der Kosmologie verwendet zu werden und haben zur Entdeckung der beschleunigten Expansion des Universums geführt. Jedoch wurden durch eine Reihe neuer Beobachtungen mehrere superluminöse SN Ia entdeckt, siehe z.B. (Taubenberger et al., 2011). Auf der Grundlage dieser Beobachtungen wurde vorgeschlagen, dass die Progenitormasse solcher Explosionen (SN 2006gz, SN 2007if, SN 2009dc, SN 2003fg) die Chandrasekhar-Massengrenze von  $M_{\text{Ch}} \sim 1.4 M_{\odot}$  deutlich übersteigt. Solch eine hohe Masse eines weißen Zwergs kann aus seiner schnellen Rotation oder einer vorübergehenden hohen Massenkongfiguration in der Fusion von zwei schweren weißen Zwergen gebildet werden (Moll et al., 2014). Darüber hinaus wurde auch vorgeschlagen, dass ein starkes Magnetfeld für die Stabilität der zusätzlichen Masse (Das and Mukhopadhyay, 2013) verantwortlich sein kann.

Im Kapitel 6 haben wir stationäre Gleichgewichte von weißen Zwergsternen, die ein starkes poloidales Magnetfeld enthielten, berechnet und wir stellten die Modifikation der Mass-Radius-Relation der weißen Zwerge dar, welche durch das Magnetfeld verursacht wurde. Wir fanden, dass eine maximale weiße Zwergmasse von etwa  $2.00 M_{\odot}$  unterstützt werden kann, wenn das innere Feld so stark ist

wie ungefähr  $10^{14}$  G. Diese Masse ist über 40 Prozent größer als die traditionelle Chandrasekhar-Grenze. Es soll erwähnt werden, dass die Möglichkeit von Super-Chandrasekhar stark magnetisierten WDs nicht aus aktuellen theoretischen Überlegungen vollständig ausgeschlossen oder bestätigt werden kann. Auch müssen noch wichtige Fragenstellungen bezüglich einer dynamischen Stabilität in einer Studie beantwortet werden, bevor feste Schlussfolgerungen über die Existenz solcher Sterne gezogen werden können.

Schließlich liefert das Magnetfeld einen anisotropen Druck, was zum Bruch der sphärischen Symmetrie der Sterne führt. In diesem Fall kann man das Quadrupolmoment der Massenverteilung berechnen. Mit dieser Größe präsentieren wir in Kapitel 5 und 6 eine Schätzung der Gravitationswelle, die von rotierenden und/oder magnetisierten Neutronensternen und weißen Zwergen emittiert wird. Im Kapitel 5 wird gezeigt, dass der Neutronenstern vor dem vollständigen Abfallen des Magnetfeldes eine Periode schnellerer Verringerung der Emission der Gravitationswellen aufgrund des Quark-Hadron-Phasenübergangs durchläuft. Im Kapitel 6, wird angesichts der neuen Beobachtung und Messung des rotierenden und hochmagnetisierten weißen Zwergs AR Scorpii (Marsh et al., 2016), dessen Masse im Bereich von  $0.81M_{\odot} < M_{\text{wd}} \leq 1.29M_{\odot}$  liegt, gezeigt, dass AR Scorpii, wie auch andere potentielle weiße Zwerge, nachweisbare Gravitationswellen mit Amplituden, die in der Bandbreite der nächsten diskutierten Generation von Weltraum-basierten GW-Detektoren liegen, erzeugen könnten.

Zusammenfassend war ein großer Fortschritt dieser Arbeit in Bezug auf Neutronensterne, die Lorentzkraft selbstkonsistent zu berechnen, indem die Gleichgewichtsgleichungen für Magnet- und Gravitationsfelder gelöst werden. Wir berücksichtigten die stellaren Verformungen durch Anisotropien, die durch Magnetfelder induziert wurden, und wir haben gezeigt, dass sowohl die Landau-Quantisierung als auch die Magnetisierung die Neutronensternstruktur nicht wesentlich verändern (Kapitel 3). Andererseits modifiziert der Einschluss von Magnetfeldern die Teilchenzusammensetzung von Neutronen- und Proto-Neutronensternen. Wie in Kapitel 3 und 4 besprochen, könnte dies das Abkühlverhalten des Sterns beeinträchtigen, da es stark von der Partikelzusammensetzung des Objekts abhängt, die wiederum die Neutrino-Emissionskanäle bestimmt. Der gleiche Formalismus und der mathematische Aufbau wurde im Kontext eines starken Quark-Hadron-Phasenübergangs im Kapitel 5 verwendet. In dem den weißen Zwerg behandelnden Kapitel 6 wurde die erste relativistische Lösung, die auf solche Systeme angewendet wurde, beschrieben. Dies ist darauf zurückzuführen, dass hochmagnetisierte Super-Chandrasekhar weiße Zwerge erst nach 2012 erforscht wurden. Das primäre Ziel dahinter war die Erklärung eigenartiger, stark leuchtender Typ-Ia-Supernovae. Dies wird uns zweifellos helfen, das wichtige Problem der besonderen superluminösen Ia-Supernovae zu verstehen und zu erhellen. Schließlich werden im Kapitel 7 die Ergebnisse dieser Arbeit zusammengefasst und diskutiert. Außerdem werden künftige Arbeitsideen vorgestellt, die hilfreich sein können, diese Berechnungen weiter zu verfeinern.

# Contents

<b>Abstract</b>	<b>iii</b>
<b>Zusammenfassung</b>	<b>vi</b>
<b>1 Introduction</b>	<b>1</b>
1.1 Charge neutrality and chemical equilibrium inside neutron stars	5
1.2 The stellar mass	6
1.3 Rotation	6
1.4 Magnetic fields	8
1.5 Description of this work	11
<b>2 Stationary, axisymmetric rotating and magnetized relativistic neutron stars</b>	<b>15</b>
2.1 Magnetized axysymmetric neutron stars	16
2.2 The Einstein-Maxwell Equations	19
2.3 General Relativity Virial Identities	21
2.3.1 GRV3	21
2.3.2 GRV2	22
2.4 Numerical procedure	22
2.5 Global Quantities	23
2.5.1 Total baryon number	23
2.5.2 Gravitational Mass	24
2.5.3 Angular momentum	25
2.5.4 Quadrupole moment	25
2.5.5 Circumferential radius	25
2.5.6 Magnetic dipole moment	26
<b>3 A self-consistent study of magnetic field effects on hybrid stars</b>	<b>27</b>
3.1 Magnetic field-dependent equation of state	27
3.2 Inclusion of gravity	29
3.3 Results	33
3.3.1 Global properties of magnetic neutron stars	34
3.3.2 Degrees of freedom in magnetic neutron stars	36
<b>4 Magnetic field effects in proto-neutron stars</b>	<b>41</b>
4.1 Stellar interior	41
4.2 General Relativistic Calculation	42
<b>5 Strong phase transition in magnetized neutron stars</b>	<b>51</b>
5.1 Motivation	51

5.2	Equation of state with quark-hadron phase transition . . . . .	52
5.3	Rotating neutron stars . . . . .	53
5.4	Magnetized neutron stars . . . . .	56
5.5	Gravitational wave emission from neutron stars . . . . .	59
<b>6</b>	<b>Effects of strong magnetic fields and rotation on white dwarf structure</b>	<b>61</b>
6.1	Introduction . . . . .	61
6.2	Mass-radius diagram for static highly magnetized white dwarfs . . . . .	62
6.3	Rotating magnetized white dwarfs . . . . .	65
6.4	Gravitational waves from white dwarfs . . . . .	67
<b>7</b>	<b>Summary</b>	<b>71</b>
7.1	Summary of Our Results . . . . .	71
7.2	Future Work . . . . .	74
<b>A</b>	<b>Electric current in Newtonian magnetized stars</b>	<b>77</b>
<b>B</b>	<b>A brief review of General Relativity</b>	<b>81</b>
B.1	General Relativity . . . . .	81
B.2	General Relativity . . . . .	83
B.2.1	Cristoffel symbols . . . . .	83
B.2.2	Einstein Equation . . . . .	84
B.3	Spherical solutions of Einstein Equations . . . . .	85
<b>C</b>	<b>Einstein equation in the 3+1 formalism</b>	<b>91</b>
C.1	3+1 decomposition of space time . . . . .	92
C.2	3+1 decomposition of Einstein equation . . . . .	94
C.2.1	Evolution and constraint equations . . . . .	95
C.3	Stationary, axisymmetric and circular spacetimes . . . . .	96
C.3.1	Quasi-isotropic and Maximum slice coordinates . . . . .	97
C.4	Einstein field equations in 3+1 formalism . . . . .	98
C.5	Application to astrophysical cases . . . . .	103
C.5.1	Perfect fluid without magnetic field . . . . .	103
C.5.2	Perfect fluid with magnetic field . . . . .	104
C.5.3	Maxwell equations . . . . .	104
	<b>Bibliography</b>	<b>107</b>
	<b>Acknowledgements</b>	<b>121</b>
	<b>Academic CV</b>	<b>123</b>

# List of Figures

1.1	Schematic view of a pulsar. The sphere in the middle represents the neutron star, the magnet curves are the magnetic field lines, the yellow cones represent the emission beams and the black line represents the axis on which the star rotates. . . . .	2
1.2	Optical and X-ray image of the Crab Nebula as measured by Chandra X-ray Observatory, showing synchrotron emission in the surrounding pulsar wind nebula, powered by injection of magnetic fields and particles from the central pulsar. . . . .	2
1.3	Possible internal composition . . . . .	3
1.4	Mass-radius diagram for neutron stars . . . . .	4
1.5	Measured neutron star masses . . . . .	7
1.6	Histogram of distribution of pulsar spin periods . . . . .	8
1.7	$P - \dot{P}$ diagram for radio pulsars . . . . .	9
1.8	. . . . .	13
3.1	EoS of the extended hadronic and quark SU(3) non-linear realization of the sigma model . . . . .	30
3.2	Relation between the gravitational mass and the central baryon number density for non-magnetized and magnetized models . . . . .	34
3.3	Mass-radius diagram for non-magnetized and magnetized models . . . . .	35
3.4	Microscopic and macroscopic star quantities . . . . .	36
3.5	Stellar particle population as a function of the baryon chemical potential. . . . .	37
3.6	Magnetic field surfaces (on the top panel), i.e $A_\phi$ iso-contours measured by the Eulerian observer $\mathcal{O}_0$ . . . . .	38
4.1	Equations of state for proto-neutron and neutron stars . . . . .	43
4.2	Strangeness density profile . . . . .	45
4.3	Baryon number density profile in the equatorial plane . . . . .	46
4.4	Electron neutrino density profile as a function of the equatorial and polar coordinate radii . . . . .	47
4.5	Temperature profile as a function of the equatorial and polar coordinate radii . . . . .	48
4.6	Same as in Fig. 4.5 but for one proto-neutron star with $s_B = 2$ and $Y_L = 0.4$ . . . . .	48
4.7	Particle population obtained for one proto-neutrons . . . . .	50
5.1	EoS for neutron star matter including a deconfinement phase transition . . . . .	53
5.2	Baryon mass versus equatorial radius for neutron stars at different fixed rotation frequencies . . . . .	54
5.3	Relation between the moment of inertia and the frequency for rotating neutron stars . . . . .	55
5.4	Braking index as a function of the frequency for rotating neutron stars . . . . .	56
5.5	Mass-radius diagram for magnetized models . . . . .	57
5.6	Relation between the moment of inertia and central magnetic field for magnetized neutron stars . . . . .	58

5.7	Same as in Fig. 5.6 but as a function of the surface magnetic field . . . . .	58
5.8	Gravitational wave amplitude as a function of the central magnetic field . . . . .	59
6.1	Isocontours of the magnetic field strength . . . . .	63
6.2	Isocontours of the baryon number density . . . . .	64
6.3	Behaviour of the different terms of the equation of motion . . . . .	64
6.4	Mass-radius diagram for magnetized white dwarfs . . . . .	65
6.5	Mass-radius diagram for static and rotating white dwarfs . . . . .	66
6.6	Keplerian frequency as function of the central baryon density for the sequence shown in Fig. 6.5 . . . . .	67
6.7	Keplerian frequency as function of the central magnetic field . . . . .	67
6.8	The spectra for LISA, DECIGO and BBO interferometers . . . . .	69
C.1	Foliation of the spacetime $\mathcal{M}$ by a family of hypersurfaces $\Sigma_t$ . . . . .	93
C.2	Spherical coordinates . . . . .	96

# List of Tables

1	Masse und Endstufe des Sterns. . . . .	vi
4.1	Relation between the current function $k_0$ , central baryon number density $n_B^c$ , central $B_c$ and surface magnetic fields $B_s$ , the gravitaional mass $M_g$ for a star at fixed baryon mass $M_B = 2.35 M_\odot$ . . . . .	44





# Chapter 1

## Introduction

Neutron stars (NS) are truly fascinating objects. They are formed in catastrophic astrophysical events such as supernova explosions. It is also in these events that other forms of compact objects, as white dwarfs (WD) or black holes (BH), can be created. In a few seconds, these explosions release the brightness of millions of suns. It is not surprising that such a phenomenon has been observed since ancient times. For example, the neutron star that formed in the Crab Nebula was observed in 1968 by [Hewish et al. \(1968\)](#). However, the creation of the Crab Nebula corresponds to a supernova recorded by Chinese astronomers in AD 1054. Also considered the densest stars known, neutron stars have about the same mass as the Sun (1 solar mass  $M_{\odot} = 1,989 \times 10^{30}$  kg), but distributed in a radius of about 10 km. As a result, these stars can harbor compressed ultra-dense nuclear matter in their interiors and provide unique sites for investigating fundamental questions in physics and astrophysics, including the influence of very fast spin rotation, strong magnetic fields, properties of nuclear force at high densities, possible phase transitions to exotic matter, and, of course, gravitational physics in the strong-field regime. Neutron stars are usually observed as pulsars, which are rotating magnetized neutron stars that produce periodic pulses of electromagnetic radiation, primarily at radio wavelengths. If these beams point towards Earth, the star becomes detectable as a pulsating source. Therefore, pulsars can be considered the lighthouses of the sky (Figs. [1.1](#) and [1.2](#)). These features, together with the cooperation between dense matter physics and progress in observational astrophysics, make these stars one of the most and sometimes the only suitable environment to study the behavior of matter and electromagnetic fields under extreme conditions.

Neutron stars are distinguished by their microscopic composition made up of nucleons, hyperons and even quarks. At high pressure, nuclear matter should undergo a phase transition to quark matter. As a result, hybrid stars (stars with quarks in their cores surrounded by an outer layer of nuclear matter) can also be formed. Neutron stars can be isolated sources or belong to binary systems where the companion is usually a lower density star. They have a typical density of  $\rho \sim 10^{14-15}$  g/cm<sup>3</sup> and are born with high temperatures of the order of  $T \sim 10^{11}$  K ( $T \sim 10$  MeV). During the evolution, temperatures drop to values of keV. At this point, these stars can be considered cold neutron stars, since the temperature is much smaller than the chemical potential of the particles in the stellar interior,  $T \ll \mu$ . As a consequence,  $T = 0$  is a good approximation while describing neutron stars. However, as we will see in [Chapter 4](#), this approximation is not valid for proto-neutron stars (PNS), in which the entropy per baryon is of the order of 1 or 2, making them, therefore, very hot stars with temperature up to 50 MeV in the stellar center.

One of the first investigations of the structure and the nature of dense stars was proposed by [Landau \(1932\)](#). The star density would be so high that the nuclei would merge. In addition, in this same

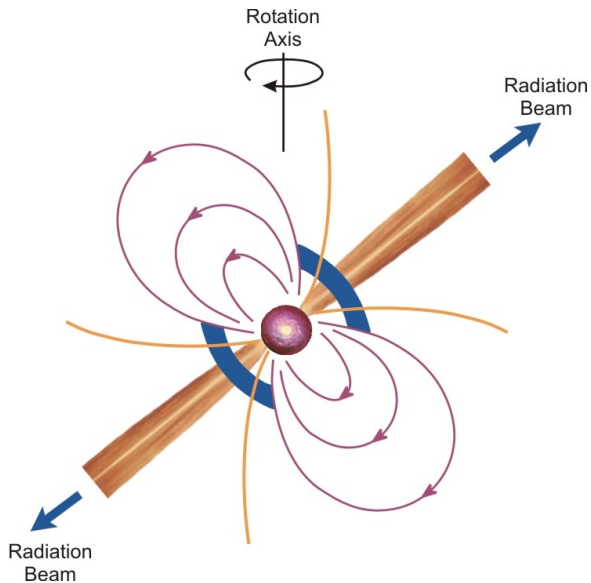


FIGURE 1.1: Schematic view of a pulsar. The sphere in the middle represents the neutron star, the magneta curves are the magnetic field lines, the yellow cones represent the emission beams and the black line represents the axis on which the star rotates.



FIGURE 1.2: Optical and X-ray image of the Crab Nebula as measured by Chandra X-ray Observatory, showing synchrotron emission in the surrounding pulsar wind nebula, powered by injection of magnetic fields and particles from the central pulsar.

work, it was proposed the existence of a mixed phase separating two distinguished phases, one that merged and formed a condensated stage and the other one composed of purely nuclei. After the discovery of the neutron by [Chadwick \(1932\)](#), it was suggested that neutron stars could be the end point of a supernova evolution ([Baade and Zwicky, 1934](#)). Although it is beyond the scope of this work to study supernovae events, we investigated properties of NS's and also WD's (Chapter 6), which are intrinsically related to such violent explosions. One example is the high angular velocity of pulsars. According to current observations, the fastest pulsar known, PSR J1748-2446ad, was detected by [Hessels et al. \(2006\)](#), and it has an incredibly rotation frequency of 716 Hz.

At present, it is commonly accepted that the huge range of densities inside NS's can be naturally divided into several regions, as shown in Fig. 1.3, where different theoretical predictions for neutron star matter are depicted. Typically, the neutron star structure can be divided into an atmosphere, an outer crust, an inner crust and a core. The outermost part is the atmosphere, which is a layer of plasma with a few millimeters, where most of the observed radiation is formed and emitted. With approximately 1 km in thickness, the crust region (inner+outer crust) of neutron stars has an equation of state (EoS) relatively well-known ([Chamel and Haensel, 2008](#); [Lattimer and Prakash, 2001](#)). The EoS describes the relation between the pressure and the energy density of the matter. The pressure can also depends on other parameters, as the proton fraction and the entropy per baryon, as we will see in Chapter 4. In general, the composition, the structure and the equation of state of the outer crust are determined by finding the ground state of cold ionic matter. In other words, this corresponds to minimizing the Gibbs energy per nucleon at a given pressure. In this case, one nucleus occupies one neutral unit Wigner-Seitz cell which, together with the nucleus and the electrons, contributes also to the total energy and pressure of the system.

The inner crust of neutron stars begins when neutrons start to drip out of the nuclei at densities of about  $\rho_{\text{drip}} \sim 4.3 \times 10^{11} \text{ g/cm}^3$ . From this value to the densities at the crust-core transition point, one has very neutron rich nuclei immersed in a gas of neutrons. In this case, the equation of state

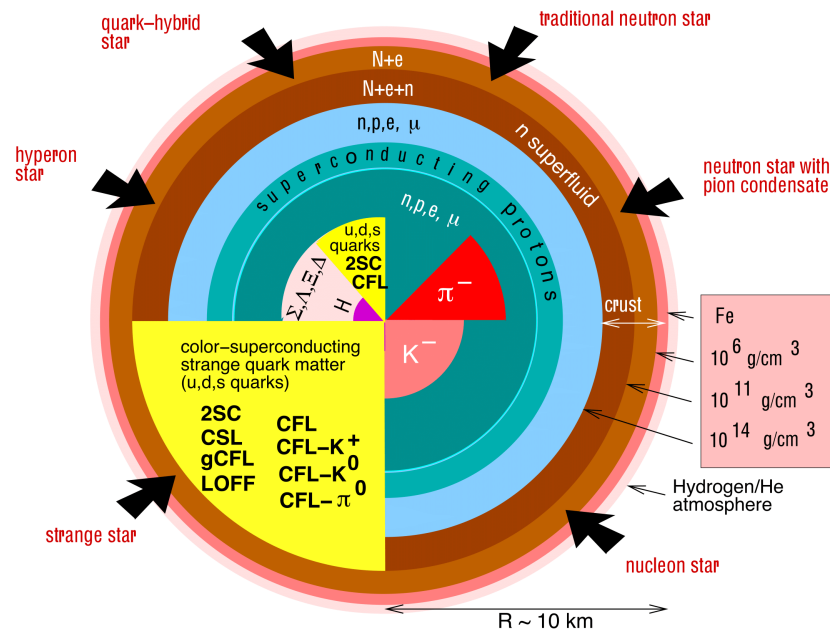


FIGURE 1.3: Possible internal composition of neutron stars. Illustration created by the astrophysicist Fridolin Weber (<http://www.physics.sdsu.edu/fweber>).

is usually obtained by many-body techniques such as Hartree-Fock, Thomas Fermi approximation, and the Compressible Liquid Drop Model.

The core is the region where the matter reaches densities significantly larger than the normal nuclear density  $\rho_0 \sim 2.4 \times 10^{14}$  g/cm<sup>3</sup>. For  $\rho > \rho_0$ , the EoS in the core is poorly understood. The higher the density, the higher the uncertainty in the EoS's, which are derived using different theories of dense matter and different methods of solution. Typically, the core is composed of electrons, protons and neutrons forming a relativistic fluid. It is also in the core that exotic degrees of freedom as hyperons (Glendenning, 1987; Vidaña, 2013; Gomes et al., 2015b), quark matter (Franzon et al., 2012; Weber, 1999a; Baldo, 2004; Alford et al., 2007) and superconducting phases might appear inside these objects (Baldo et al., 2003; Kaplan and Reddy, 2002; Lugones and Horvath, 2003). In this thesis, the stellar core of neutron stars are modeled in Chapter 3 by using a chiral SU(3) EoS containing nucleons, hyperons and quarks. In Chapter 4, the same model (without quarks) is employed to calculate the structure of hot PNS's. In Chapter 5, a different equation of state composed of two phases, one containing nucleons and one containing quarks was used to investigate the role played by a quark-hadron phase transition in neutron stars. Note that the results that we will show here depend quantitatively on the equation of state used to describe the stellar interior and different EoS's might result in stronger or weaker effects than those reported in this thesis. However, our focus is on the qualitative effects of magnetic fields and rotation on the global properties of stars and any other equation of state could be easily tested within this approach.

Fig. 1.4 shows the predictions for the stellar gravitational mass  $M$  (in units of solar mass) and its radius  $R$  (in km) for a variety of EoS models using both exotic (this includes hyperons, quarks, as well as meson condensates) and non-exotic cores (Demorest et al., 2010). The diagram in Fig. 1.4 is also referred in the literature to as mass-radius relation or mass-radius diagram. The sequence of stars, which are labeled by different EoS names, are obtained by solving the Tolman-Oppenheimer-Volkoff equations (TOV) for the structure of spherically symmetric stars in static gravitational equilibrium

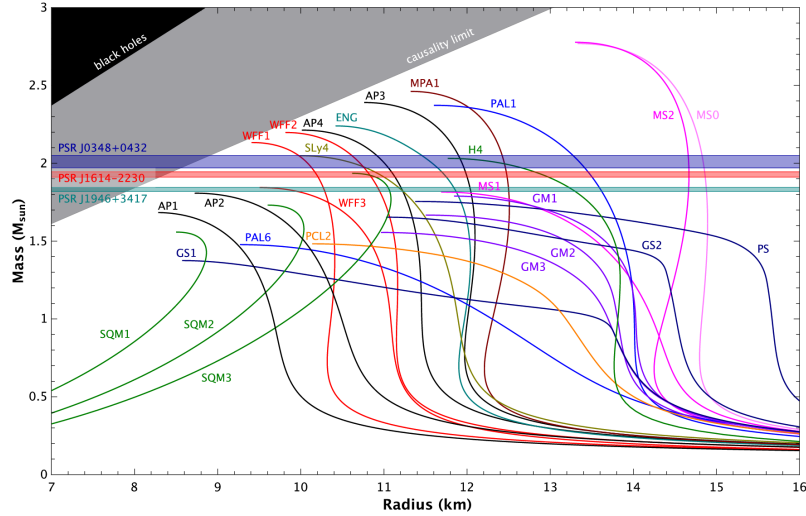


FIGURE 1.4: Mass-radius diagram for neutron stars assuming different equations of state. The horizontal bars correspond to the mass of the three most massive pulsars observed (Demorest et al., 2010), (Antoniadis et al., 2013) and (Antoniadis, 2014). Equations of state that predict maximum masses lower than the largest measured NS masses must be ruled out.

(Tolman, 1939; Oppenheimer and Volkoff, 1939). The TOV equations are given by:

$$\frac{dP}{dr} = -\frac{G\mathcal{E}(r)M(r)}{c^2r^2} \left[ 1 + \frac{P(r)}{\mathcal{E}(r)} \right] \left[ 1 + \frac{4\pi r^3 P(r)}{M(r)c^2} \right] \left[ 1 - \frac{2GM(r)}{c^2r} \right]^{-1}, \quad (1.1)$$

$$\frac{dM(r)}{dr} = 4\pi r^2 \mathcal{E}(r), \quad (1.2)$$

with  $G$  Newton's gravitational constant,  $P$  the pressure,  $\mathcal{E}$  the corresponding energy density,  $M(r)$  the total mass inside the sphere of radius  $r$  and  $c$  is the speed of light.

The Eqs. (1.1) and (1.2) show the balance between the gravitational force and the pressure that act on shell with thickness  $dr$  and mass  $dM(r)$ . To be able solve them, one needs to know the energy density in terms of the pressure. This relation is the equation of state,  $P = P(\mathcal{E})$ , for the matter making up the star. This is the reason behind so much effort to developing an appropriate equation of state for matter in neutron stars, which do need to satisfy the constraints obtained from the measurement of massive neutron stars by Demorest (Demorest et al., 2010) and Antoniadis (Antoniadis et al., 2013), with masses of  $(1.97 \pm 0.04) M_\odot$ , labeled by PSR J1614-2230, and  $(2.01 \pm 0.04) M_\odot$ , labeled by PSR J03487+0432, respectively. Although it is possible to model the stellar interior with different internal compositions, the detection of these high mass pulsars constrain many of the proposed EoS's and excludes the ones that do not explain high masses. In addition, the EoS must satisfy theoretical limits.

The top left regions in Fig. 1.4 are a set of fundamental constraints which are independent of the detailed physical properties of neutron matter. First, we have the Schwarzschild criterion ('black hole') in which spherical stars do not collapse to a black hole for  $R > 2GM/c^2$ . Second, the EoS is causal ('causality limit'), i.e., the sound velocity,  $c_s$ , does not exceed the speed of light  $c_s^2 := dP/d\mathcal{E} \leq c^2$ . This, together with the TOV equations, gives the constrain  $R > 2.9GM/c^2$ .

According to Eq. (1.1), the pressure inside stars decreases monotonically with the radius, since the pressure gradient is negative. As a consequence, the pressure is maximum at the stellar center and goes to zero at the surface. The TOV can be numerically integrated from the origin ( $r = 0$ ), with the initial conditions  $M(0) = 0$  and  $\mathcal{E}(0) = \mathcal{E}_c$  (energy density at stellar center), to the star's surface

where  $P(R)=0$ , with  $R$  being the stellar radius. From Eq. (1.2), there is a unique relation between  $\mathcal{E}_c$  and the mass of stars. Therefore, each equation of state in Fig. 1.4 provides a family of stars which are parametrized by  $\mathcal{E}_c$ , whose maximum value is reached at the maximum stellar mass. We shall have more to say on this matter in the next chapters, where we will build stellar sequences by changing the central enthalpy of stars and without making the assumption of spherical symmetry and zero angular velocities (i.e., a static spacetime).

From Fig. 1.4, the lowest maximum mass obtained is  $1.4 M_\odot$ , predicted by the model GS1 (Glendenning and Schaffner-Bielich, 1999). The other models predict masses above this value. According to strange quark matter (SQM) models (Prakash et al., 1995), the only one with quarks, the mass increases as the radius increases up to the maximum value of the mass. This is the case because quarks are incompressible and the stellar mass scales with the stellar volume, in other words,  $M \propto R^3$ . On the other hand, the greater the mass, the smaller the radius for nuclear matter EoS's.

In the present work, we have also considered the usual hypothesis of charge neutrality and beta equilibrium inside neutron stars. In the next section, we will briefly describe these features.

## 1.1 Charge neutrality and chemical equilibrium inside neutron stars

Neutron stars in equilibrium are electrically neutral. Let  $R$ ,  $M$  and  $Z_{\text{liq}}$  be the radius, the mass and the net charge of a neutron star. In addition, the star is composed of  $A$  baryons of mass  $m$ . Due to the gravitational binding energy, one expects  $M < mA$ . If we bring a proton of charge  $e$  and mass  $m$  from infinity to the stellar surface, the equilibrium configuration of the star is given by:

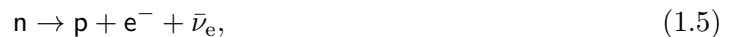
$$\frac{1}{4\pi\epsilon_0} \frac{Z_{\text{liq}}e^2}{R^2} = \frac{GMm}{R^2} < \frac{G(Am)m}{R^2}, \quad (1.3)$$

which gives us the net charge per nucleon in terms of fundamental constants, namely,

$$\begin{aligned} \frac{Z_{\text{liq}}}{A} &< \frac{4\pi\epsilon_0 Gm^2}{e^2}, \\ \frac{Z_{\text{liq}}}{A} &< 10^{-36}. \end{aligned} \quad (1.4)$$

As a result, the net charge per nucleon is practically zero inside neutron stars. We stress that this condition is global, not local. Thereby, there might exist regions in the star where the charge density is not zero.

Chemical reactions as



take place in the interior of the star up to the point when the amount of each constituent (in this case  $n$ ,  $p$ ,  $e^-$  and  $\bar{\nu}_e$ ) remain unchanged. At this point, the system has reached chemical equilibrium, also referred to as beta-equilibrium (in the case of Eq. (1.5)). In reality, one assumes stars populated by more complex degrees of freedom, as for example, the whole baryonic octet, quarks, electrons and muons, but charge neutrality and chemical equilibrium are necessary conditions to obtain the two most basic properties of a neutron star, i.e., its radius and its mass.

## 1.2 The stellar mass

The determination of neutron star masses is intriguing, both from the theoretical side and the observation one. Currently, only a few aspects of neutron stars can be inferred from pulsar observations, such as masses, spin rates, rough ages, and magnetic field strengths. The first estimate of the NS mass was carried out by [Oppenheimer and Volkoff \(1939\)](#), where a simple EoS of a relativistic neutron gas was employed. In this case, the mass for neutron stars was estimated to be  $0.7 M_{\odot}$ . On the other hand, based on the TOV equations and the causality principle, it was established that NS's with  $\sim 10$  km radius can not exceed  $\sim 3.0 M_{\odot}$  ([Rhoades Jr and Ruffini, 1974](#)).

The measurement of neutron star masses can only be done for neutron stars in binary systems. In fact, after the discovery of the first binary radio pulsar (Hulse and Taylor pulsar), it became clear that the measurement of relativistic orbital effects allow extremely precise mass estimates. In these systems, Keplerian parameters which are related to the pulsar and companion masses can be very precisely measured by pulse timing techniques ([Manchester and Taylor, 1977](#)).

[Fig. 1.5](#) depicts the measured neutron star masses, with an average mass of the order of  $1.34 M_{\odot}$  ([Lattimer, 2013](#)). This value can be used to make a simple estimate of the radius of a neutron star that rotates with a period of  $P \sim 1$  ms (see next section), assuming that a point at its equator is in equilibrium, i.e., the gravitational and centrifugal acceleration cancel each other. Based on this, the stellar radius is given by:

$$R = \left( \frac{GMP^2}{4\pi^2} \right)^{\frac{1}{3}}, \quad (1.6)$$

$$R \sim 15 \text{ km}, \quad (1.7)$$

with  $G$  being the Newton gravitational constant and  $M$  the mass of the star. With such a small radius, these stars are clearly very dense, and one can estimate the average density to be:

$$\rho \simeq \frac{3M}{4\pi R^3} \simeq 1.5 \times 10^{14} \text{ g/cm}^3, \quad (1.8)$$

while the nuclear matter density at saturation is  $\rho_0 \simeq 2.4 \times 10^{14} \text{ g/cm}^3$ . The pressure in the interior of one star decreases monotonically with the radius, as well the density, whose value can be, therefore, higher than the average value obtained in [Eq. \(1.8\)](#). In other words, the density at the stellar center easily can reach values higher than a couple of times  $\rho_0$ .

## 1.3 Rotation

Pulsars rotate extremely fast, which is related to their formation. As the star's core collapses, its rotation rate increases as a result of conservation of angular momentum, hence, neutron stars rotate up to several hundred times per second. In the case of millisecond pulsars, they are thought to achieve such high speeds because they are gravitationally bound in binary system with another star. During part of their life, matter flows from the companion star to the pulsar. Over time, the impact of the accreted matter spins up the pulsar's rotation.

It makes sense to separate pulsars into two groups: milliseconds and canonical ones. They differ by the magnetic field strength (see [Fig. 1.7](#)), age and rotation period. In [Fig. 1.6](#), we show the distribution of pulsars with respect to rotation period. One sees that their majority has periods  $\sim$

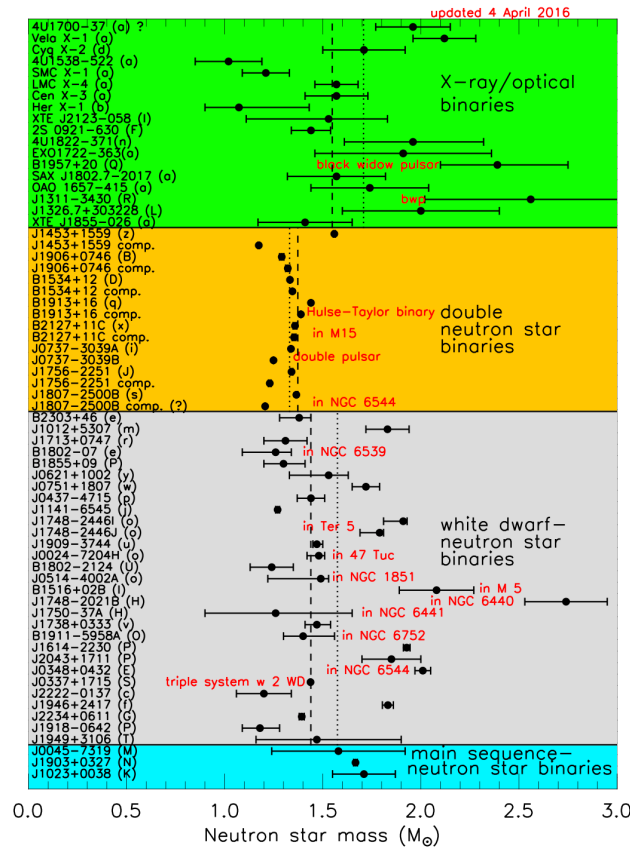


FIGURE 1.5: Measured neutron star masses. Picture taken from [Lattimer \(2013\)](#), updated in April 2016. Different colors represent different systems (NS's in a binary system with a main sequence, a white dwarf or another neutron star) where one can measure neutron star masses. Note that there are reported NS masses, as for example, the pulsar PSR B1957+20, that may reach  $2.40 \pm 0.12 M_{\odot}$  ([Van Kerkwijk et al., 2011](#)). However, in contrast to the considered most massive pulsars (PSR J1614-2230 and PSR J038+0432), the reliability of this value is questioned.

1 s ( $\log P \sim 0$ ). These are denominated canonical. The other group has rotation period up to  $P \sim 0.001$  s ( $\log P \sim -3$ ) and are, therefore, denominated millisecond pulsars.

It is important to remark that the first evidence of a pulsar was provided by the first observation of a rapidly pulsating radio source by [Hewish et al. \(1968\)](#), with a rotation period of  $P \sim 1.3$  s. Pulsars have periods extremely short and stable as, for example, the pulsar PSR 1937+214 with  $P = 0.00155780644887275$  s. These pulses are usually detected in radio frequency, that is why they are named, therefore, with the letters PRS (Pulsating Radio Source), followed by their right ascension and degree of declination.

Over time, many hypotheses were proposed to explain the origin of the first observed pulsating radio source e.g. models of pulsating white dwarfs, eclipsing and oscillating sources, but they were all ruled out. The correct explanation involved a rotating magnetized neutron star, whose rotation and magnetic axis are misaligned. This model was proposed independently by [Pacini \(1968\)](#) and [Gold \(1975\)](#). Thenceforth, the theory of pulsars developed fast and the discovery of the pulsar PSR B0531+21 ( $P \sim 30$  ms) in the Crab nebula ([Staelin and Reifenstein, 1968](#)) supported even more the idea of pulsars as rotating and magnetized neutron stars. Today, we understand that many astrophysical phenomena cannot be explained without neutron stars.

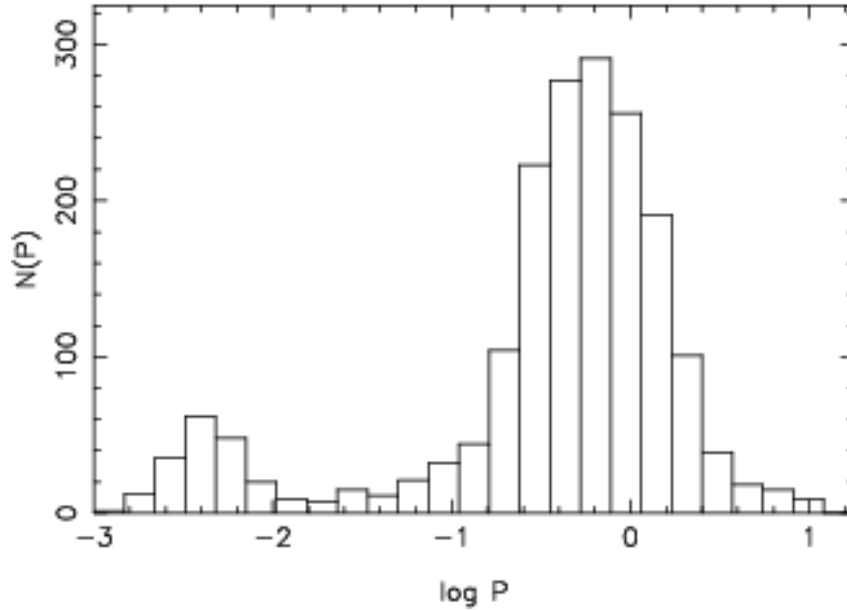


FIGURE 1.6: Histogram showing the distribution of pulsar spin periods, in seconds, of all known pulsars. Figure taken from [Konar \(2010\)](#).

We described above the basics properties of neutron stars. However, in order to comprehend their physical processes, it is crucial to understand other component: the magnetic field.

## 1.4 Magnetic fields

A useful tool to study the evolution of pulsars is the  $P - \dot{P}$  diagram as shown in Fig. 1.7, where  $P$  is the star period and  $\dot{P}$  is the (time) period derivative. Note that the pulsars are not uniformly distributed on Fig. 1.7, but in groups that have different evolution interpretations according to the region occupied on the diagram. Diagonal lines in  $P - \dot{P}$  diagram imply fundamentally different surface magnetic field strengths (in units of Gauss, G) and ages for each sub-group of the population.

Magnetic fields on stellar surfaces can be estimated from observations of star's period and period derivative. One considers a magnetic dipole which rotates and emits electromagnetic radiation. As a consequence, the star loses energy and spins down. In this case, if we assume a rotating magnetized sphere, the total energy loss of the star can be expressed in terms of the time derivative of the radiated energy as ([Shapiro and Teukolsky, 2008](#)):

$$\frac{dE}{dt} = -\frac{2}{3}R^6B\Omega^4 \sin^2 \alpha, \quad (1.9)$$

which, as in Classical Electrodynamics, represents the rate of energy emitted by a rotating magnetic dipole field. In Eq. (1.9),  $R$  is the radial coordinate of a surface point with the surface magnetic field strength  $B$ ,  $\Omega$  is the rotational frequency of the star, and  $\alpha$  is the angle of inclination between the magnetic field and the axis of rotation. Substituting the kinetic energy of a rotating body,

$$E = \frac{1}{2}I\Omega^2, \quad (1.10)$$



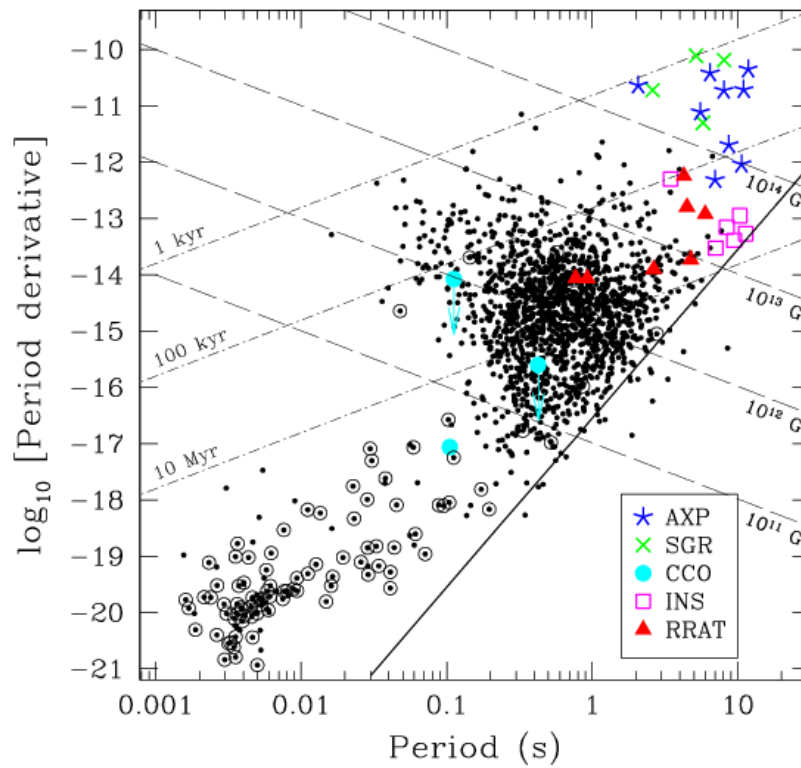


FIGURE 1.7:  $P - \dot{P}$  diagram for binary pulsar (black circles with dots in it), rotation powered pulsars (black dots), Anomalous X-ray Pulsars (blue stars), Soft Gamma Repeaters (green crosses), isolated neutron stars (magenta squares), central compact objects (blue dot) and rotating radio transient (red triangle). Contours of constant inferred surface magnetic field strength and pulsar age are drawn as diagonal dashed lines. See [Kaspi \(2010\)](#) for details.

with  $I$  being the moment of inertia of the star, the surface magnetic field strength (at the pole) in terms of  $P(= 2\pi/\Omega)$  and  $\dot{P}$  reads:

$$B = \sqrt{\frac{3I}{8\pi^2 R^6 \sin^2 \alpha} P \dot{P}}. \quad (1.11)$$

Note that the above expression is obtained under a few assumptions. First, the moment of inertia of the star is constant (in Chapter 5, we will show that the moment of inertia depends both on the rotation rate and on the magnetic field strength). Second, although the exact mechanism of the spin-down is a question of debate, the commonly accepted view is that it arises through emission of magnetic dipole radiation (Eq. 1.9), but other processes could also be considered, including the emission of gravitational radiation and relativistic particles (pulsar wind).

We can use Eq. (1.11) to estimate the surface magnetic field of stars. For example, the Crab pulsar has an observed period of  $P \sim 0.033$  s and a period derivative of  $\dot{P} \sim 4 \times 10^{-13}$  s/s, with an experimental mass of  $\sim 1.40 M_{\odot}$  and a radius of about 10 km. Taking  $\sin \alpha = 1$  (maximum value), which represents a perpendicular rotator, according to Eq. (1.11), the strength of the surface magnetic field at the pole is  $B \sim 4 \times 10^{12}$  G. Moreover, one defines a characteristic age of the star as  $\tau_c = P/2\dot{P}$ . For example, the isolated radio pulsars (black dots) in Fig. 1.7 are concentrated in the region with  $P = 0.2 - 2$  s and  $\dot{P}$  in the range  $10^{-16} - 10^{-13}$  s/s. Also, based on the dipole model, these stars have magnetic fields of the order  $10^{10} - 10^{13}$  G and a lifetime as a radio source

of a few  $10^7$  yr (it corresponds to the 10 Myr diagonal line in Fig. 1.7). A similar argument provides a magnetic field of  $10^{14} - 10^{15}$  G for Soft Gamma Repeaters (SGR) (green crosses in Fig. 1.7) and Anomalous X-ray Pulsars (AXPs) (blue stars in Fig. 1.7). To complete the star zoo, we have the population of binary pulsars plotted in black circles (with dots in it), which clearly indicate a connection to the rapidly spinning millisecond pulsars. Also plotted are the mysterious rotating radio transients (RRATs) and the compact central objects (CCOs). The dashed lines in Fig. 1.7 represent the surface magnetic field strength and the age of the star.

Soft Gamma Repeaters and Anomalous X-ray Pulsars (upper left corner in Fig. 1.7) are the relevant stars for this work. Although the internal magnetic fields of these stars cannot be directly constrained by observations, according to Virial theorem arguments, which give an upper estimate for the magnetic inside neutron stars, they can possess central magnetic fields as large as  $10^{18}$  G (Lai and Shapiro, 1991; Fushiki et al., 1989; Cardall et al., 2001). This value is obtained in Newtonian mechanics by equating the stellar magnetic energy stored within the star,  $B^2/8\pi \times 4\pi/3R^3$ , and the gravitational binding energy,  $3GM^2/5R$ . In doing so, the magnetic field strength satisfies  $B \sim 1.4 \times 10^{18} (1.40 M_{\odot}/M)(R/10 \text{ km})^{-2}$  G. It is important to note that the magnetic field contribution to the total mass density is  $\rho = B^2/8\pi c^2$ . For densities comparable to the nuclear saturation density,  $\rho_0 \sim 2.4 \times 10^{14} \text{ g/cm}^3$ , the corresponding magnetic field is  $B \sim 2 \times 10^{16}$  G. As a consequence, the field contribution can dominate the matter density in neutron stars. Therefore, the magnetic field cannot be neglected in the energy-momentum tensor of the system and must be included in the equations of equilibrium.

SGR and AXPs have typical rotation periods of the order of 10 s. Due to their 'slow' rotation - astrophysically speaking - they are powered by their huge magnetic energy reservoirs. These stars are usually referred to as magnetars (Duncan and Thompson, 1992; Thompson and Duncan, 1993, 1996; Paczynski, 1992; Melatos, 1999). According to the magnetar catalog<sup>1</sup> (Olausen and Kaspi, 2014), there is currently information available on 29 magnetars: 15 SGRs (11 confirmed, 4 candidates), and 14 AXPs (12 confirmed, 2 candidate). Moreover, estimates show that the magnetar population corresponds to about 10% of the NS population (Kouveliotou et al., 1998). Nevertheless, there is no mass measurement of magnetars. The problem is that one usually measures masses in binary systems, and all known magnetars are isolated, what makes their masses harder to be measured.

The origin of strong magnetic fields in compact stars is still unclear. One common hypothesis involves the flux conservation of the progenitor magnetic field (L., 1964). However, this idea is not suitable for magnetars since a canonical neutron star  $M \sim 1.4 M_{\odot}$  would require a radius less than its Schwarzschild radius in order to generate a surface magnetic field of the order of  $10^{15}$  G (Tatsumi, 2000). Another possibility suggested by Thompson and Duncan (1993) describes a newly born neutron star combining convection and differential rotation to generate a dynamo process which is able to generate fields as large as  $10^{15}$  G. Part of the rotation energy is then expected to power the supernova through rapid magnetic braking. One expects, therefore, that magnetar creation is accompanied by supernovae that are an order of magnitude more energetic than normal supernovae. However, Vink and Kuiper (2006) showed that the explosion energies of the supernova remnants associated with AXPs and SGRs, namely, Kes 73 (AXP 1E 1841045), CTB109 (AXP 1E2259+586) and N49 (SGR 052666), are close to the canonical supernova explosion energy. As a result, Vink and Kuiper (2006) did not find evidence that magnetars are formed from rapidly rotating proto-neutron stars, allowing for the possibility that they descend from stellar progenitors with high magnetic field cores.

<sup>1</sup><http://www.physics.mcgill.ca/pulsar/magnetar/main.html>

## 1.5 Description of this work

Whatever the origin of strong magnetic fields in compact stars (NS's and WD's) might be, we intend in this work to address some intriguing questions:

- what is largest magnetic field that compact stars can support?
- what is the effect of strong magnetic fields on the maximum mass of compact stars?
- how the internal degrees of freedom in neutron stars are affected by magnetic fields?

Magnetic fields affect locally the microphysics of the equation of state, as for example, due to the Landau quantization of the energy levels of charged particles and the effect of the anomalous magnetic moment of charged and uncharged particles. Globally, magnetic fields affect the structure of neutron stars through the Lorentz force associated with the macroscopic currents that generate the field. They also affect the structure of the spacetime, as magnetic fields become a source of the gravitational field through the Maxwell energy-momentum tensor, which is anisotropic. As a consequence, magnetized stars are also anisotropic and require a general-relativity treatment beyond the spherical solutions provided by the hydrostatic equilibrium equations of a non-rotating and non-magnetized neutron star as given by the Tolman-Oppenheimer-Volkoff equations. In addition, rotation or magnetic fields break the spherical symmetry of stars and such effects have to be included in a fully general relativistic formalism when describing such objects. This is addressed in Chapter 2, where a fully-consistent equilibria of magnetic stars in axial symmetry, with rotation, is described by using the 3+1 decomposition of spacetime in General Relativity.

We provide also in Chapter 2 a description of numerical methods used in our calculations. In order to solve the equilibrium configuration, it is assumed that the matter has infinite conductivity. This, in turn, implies that the magnetic flux is conserved and the magnetic field lines move with the fluid. This condition is also referred in the literature to as 'froze-in' magnetic fields, a common (and well justified) assumption in astrophysics.

In Chapter 3, a hybrid star model that includes the effect of the magnetic field on the equation of state, the interaction of the electromagnetic field with matter, the anisotropies in the energy-momentum tensor, as well as general relativistic aspects is investigated. This study was motivated by the fact that previous calculations with magnetic-field dependent EoS commonly solved the general relativistic equations of hydrostatic equilibrium with the assumption of spherical symmetry. In addition, the effect of the magnetic field gradient was introduced through an ad hoc magnetic field profile in order to obtain magnetized stellar models. However, as already pointed out by [Menezes and Alloy \(2016\)](#), ad hoc formulas for magnetic field profiles in neutron stars do not fulfill Maxwell's equations (more specifically, Gauss law) and, therefore, are not correct. As we will see in this work, neutron star models must be treated with more care in presence of anisotropies.

We proceed then to Chapter 4, where the influence of magnetic fields on composition and structure of proto-neutron stars is discussed. We are going to show in Chapter 3 that the magnetic field has a huge impact not only on the structure of NS's, but also on their particle population. Likewise, we will study in Chapter 4 the effects of strong magnetic fields on a hot and rapidly rotating proto-neutron star, since the magnetic field can effect the amount of trapped neutrinos and prevent or favour exotic phases with hyperons and quarks.

In Chapter 5, we discuss the effects of quark-hadron phase transition on the structure of neutron stars, considering rotation as well as strong magnetic fields. We employ an equation of state that describes massive hybrid stars composed of nucleons, leptons and quarks in the stellar interior. The

stellar models, as well as the modification of the mass-radius diagram, are investigated within the same general relativity approach as described in Chapter 2.

We investigate in Chapter 6 the influence of magnetic fields on the structure of white dwarfs. This is an important problem, since super-massive magnetized WD's, whose existence is partially supported by magnetic forces, could simplify the explanation of observed ultra-luminous explosions of supernovae Type Ia (SNe Ia). SNe Ia occur in binary systems, when a white dwarf accreting matter from a companion approaches the Chandrasekhar mass limit of  $1.40 M_{\odot}$  and becomes unstable. As a result, thermonuclear explosion develops and an immense amount of energy is suddenly released. A feature of these events is that SNe Ia have spectra and light curves (evolution of the supernova brightness with time) amazingly uniform, indicating a common origin and a common intrinsic luminosity. However, recent observations of several supernovae appear to be more luminous than expected. This would indicate that such explosions occur when the white dwarf has a mass well above the Chandrasekhar mass limit.

Finally, Chapter 7 summarizes the main findings and concludes this work. Moreover, we provide a set of appendices: Appendix A presents a description of the electric currents in magnetized Newtonian stars, Appendix B presents a brief introduction to General relativity and Appendix C contains the deduction of Einstein's equations within the 3+1 formalism in General Relativity.

Fig. 1.8 depicts the chapters and the main sections presented in this work. We show also the relation between them, together with their interdependencies. For example, if one is interested in the particle population inside magnetized neutron stars (section 3.3.2), which can be compared with the particle population in proto-neutron stars (section 4.2), then, as a prerequisite, the analysis of the mass-radius relationship for neutron stars is needed (section 3.3.1), which, in turn, requires the reading about the Einstein-Maxwell equations (section 2.2) and the global stellar quantities (section 2.5).

Parts of the presented texts and figures have been published already in the references listed in the *Preface*. Specifically, Chapter 3 is published in Franzon et al. (2015) and in the proceedings Franzon et al. (2016e), with a small fraction of section 3.3 submitted to PRL (Dexheimer et al., 2016). The entire Chapter 4 is published in Franzon et al. (2016a) and only adapted for this work. The Chapter 5 is published in Franzon et al. (2016c). The Chapter 6 is published in Franzon and Schramm (2015), with a little discussion in section 6.2 about the effects of the Lorentz force on the crust of neutron stars, as presented in Franzon et al. (2016d), submitted to MNRAS. Still in Chapter 6, section 6.3, we discuss effects of realistic equation of state in white dwarfs, which can be found in Otoniel et al. (2016), in refereeing process by PRD. We close then Chapter 6 and our results in section 6.4, by discussing the possibility of rotating and magnetized white dwarfs to be source of gravitational radiation Franzon and Schramm (2016).

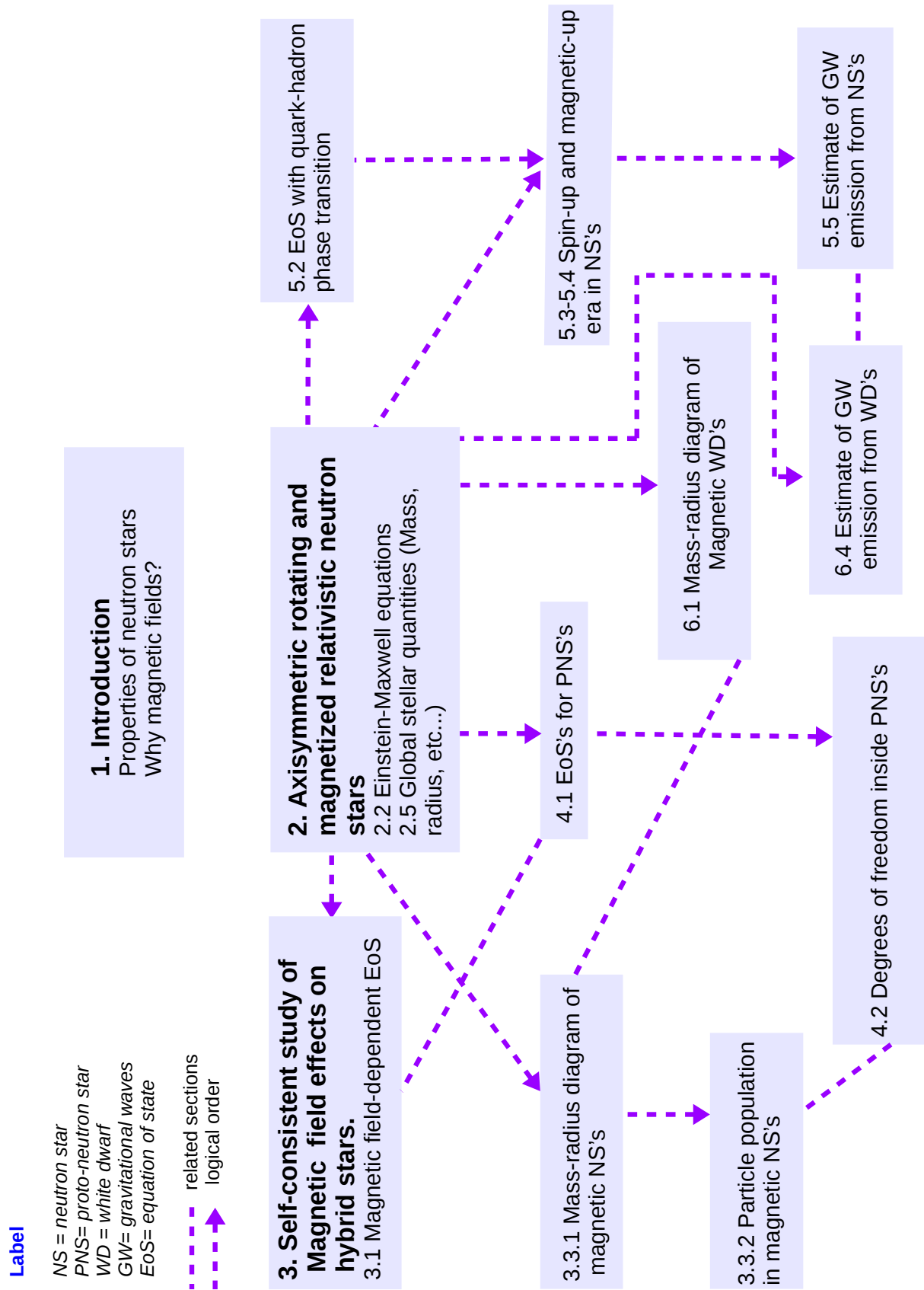


FIGURE 1.8: Organization of the thesis and interdependencies of chapters/sections.



## Chapter 2

# Stationary, axisymmetric rotating and magnetized relativistic neutron stars

*In this chapter, we will briefly present the Einstein field equations within the 3+1 formalism in General Relativity in order to obtain both rotating and magnetized axisymmetric neutron star configurations. The final system of Einstein equations can be found in Appendix C, as well as in different works quoted throughout this thesis.*

Albert Einstein's general theory of relativity (GR) is now more than one century old and has been a pillar for modern physics. Currently, there is no doubt it is a very successful theory, which explains not only the motion of the planets but it also describes the history and expansion of the universe, the physics of black holes and the bending of light from distant stars and galaxies. Moreover, neutron stars are so compact that general relativity is essential to describe their structures. Indeed, the existence of a maximum neutron star mass is a manifestation of general relativity.

The Einstein field equations describe the properties of the gravitational field around a given mass and can be written (see Appendix B) in a beautiful compact form as:

$$R_{\mu\nu} - \frac{1}{2}R g_{\mu\nu} = 8\pi T_{\mu\nu}, \quad (2.1)$$

with  $R_{\mu\nu}$  being the Ricci tensor,  $R$  is the Ricci scalar,  $g_{\mu\nu}$  is the metric tensor and  $T_{\mu\nu}$  the energy-momentum tensor of matter and electromagnetic fields. The indices  $\mu$  and  $\nu$  can range over the set 0,1,2,3. Throughout this chapter, we choose units such that  $G = c = 1$ .

In this section, we will summarize the numerical implementation for axisymmetric rotating and magnetized stars as developed by [Bonazzola et al. \(1993\)](#) and later on by [Bocquet et al. \(1995\)](#). The numerical code provides tools to solve partial differential equations by means of a multi-domain spectral method and the source code is publicly available on the homepage of C++ library LORENE, <http://www.lorene.obspm.fr>. The main codes used in this thesis are called *magstar.C* and *mag\_star\_eos.C* and are located in the directory *Lorene/Codes/Magstar* and *Lorene/Codes/Mag\_eos\_star* for isolated neutron stars. It is worth to mention that LORENE is a set of C++ classes to solve various problems in numerical relativity as, for example, simulations of binary neutron stars. Through the next sections, we will try to keep the original notation for the consistency with the original works.

## 2.1 Magnetized axisymmetric neutron stars

The equation (2.1) states an intrinsic relation between the geometry of spacetime (on the left-hand side) and the mass-energy content (on the right-hand side). Behind its economic form, Eq. (2.1) is highly non-linear. Due to the complexity of the field equations combined to the relativistic-hydrodynamics equations, analytic solutions are obtained only in special cases as, for example, when considering spherical symmetry.

As we will be dealing with macroscopic structure of neutron stars endowed with magnetic fields, the energy-momentum tensor of the system is given by:

$$T_{\mu\nu} = (\mathcal{E} + P) u_\mu u_\nu + P g_{\mu\nu} + \frac{1}{\mu_0} \left( F_{\mu\alpha} F_\nu^\alpha - \frac{g_{\mu\nu}}{4} F_{\alpha\beta} F^{\alpha\beta} \right), \quad (2.2)$$

where the first two terms in Eq. (2.2) are the perfect fluid contribution, with the matter energy density  $\mathcal{E}$ , the isotropic fluid pressure  $P$  and the 4-vector fluid velocity  $u_\mu$ . The third term represents the purely Maxwell energy momentum tensor, with  $F_{\alpha\beta}$  being the usual Faraday tensor defined in terms of the magnetic vector potential  $A_\alpha$  as  $F_{\alpha\beta} = \partial_\alpha A_\beta - \partial_\beta A_\alpha$ .

There are a few attempts to try to solve self-consistently the Einstein field equations coupled to the matter-field energy momentum tensor for magnetized stars. The presence of magnetic fields induces a Lorentz force, which breaks the spherical symmetry of the star. In this case, the stellar deformation needs to be taken into consideration when modelling highly magnetized objects. Recently, [Mallick and Schramm \(2014\)](#) attempted to compute the structure of neutron stars in strong magnetic fields by a Taylor expansion of the energy-momentum tensor and the metric around the spherically symmetric case. There are also global models of neutron stars in which the effect of magnetic fields on the structure of these stars have been included in a fully general relativistic formalism. In the case of poloidal magnetic fields, [Bocquet et al. \(1995\)](#) and [Cardall et al. \(2001\)](#) have shown that the star becomes oblate with respect to the symmetry axis, shrinking in the pole direction and expanding on the equatorial plane. This is an effect of the Lorentz force acting outward and against gravity. As we will see, this is the reason why magnetic stars can support more mass than their non-magnetic counterparts. Note that this deformation is also an effect of the assumption of a poloidal magnetic field, which makes the star more oblate. Calculations including toroidal magnetic field components have shown that magnetized stars become more prolate (more cigarette-like) with respect to the non-magnetized case ([Kiuchi and Kotake, 2008](#); [Friebe and Rezzolla, 2012a](#)).

We will now describe the assumptions, the basic equations and the numerical method used in this thesis in order to construct magnetized stellar models in the same way as in [Bonazzola et al. \(1993\)](#) and [Bocquet et al. \(1995\)](#). As a general reference, the review by [Gourgoulhon \(2012\)](#) is valuable. The choice of the coordinates in general relativity is crucial, not only to write the gravitational equations in an advantageous form, but also to make them easier to solve numerically. With this in mind, one makes use of symmetries and also of the properties of spacetime to rewrite Eq. (2.1). First, the spacetime is considered *stationary*. In practice, it means that the metric tensor components do not depend on the time or, in other words, it exists a Killing vector in the time direction. Note that a Killing vector implies the existence of a coordinate system where the metric tensor is independent of one of the coordinates. One then demands the space time to be *axisymmetric*, i.e., it should exist a Killing vector in the azimuth direction  $\phi$ . As a result, axially symmetry implies that the metric tensor does not depend on  $\phi$ . This condition is not restrictive in practice, since most of the astrophysics objects are axially symmetric. These two symmetries reduce considerably the number of equations in the final field equations. Finally, the spacetime should be *asymptotically flat* which is a natural condition since, at infinity, all GR equations must reduce to the special relativity limit



represented by the Minkowski metric tensor. Furthermore, this is important numerically, since the boundary conditions are well known at infinity (flat space time).

Now, let us summarize the general 3+1 formalism used in numerical General Relativity as already presented in some details in Appendix C. Einstein field equations can be split into dynamical equations and constraint equations for the metric tensor. The formalism consists in the foliation of the space time into hypersurfaces<sup>1</sup>  $\Sigma_t$ , labelled by the coordinate time  $t$  (Smarr and York Jr, 1978). In other words, the 3+1 decomposition simply separates the time and the 3-dimensional space by projecting vectors and tensors onto the hypersurface  $\Sigma_t$ , which has an induced 3-D metric  $\gamma_{ij}$ , and into the time direction, i.e., along the unit 4-vector  $n^\mu$  normal to  $\Sigma_t$ , whose components are  $n^\mu = \frac{1}{N}(1, 0, 0, N^\phi)$  and  $n_\mu = \frac{1}{N}(-1, 0, 0, 0)$ , such that  $n_\mu n^\mu = -1$ , with  $N$  and  $N^\phi$  being the lapse function and the shift vector (see below).

Assuming stationarity and axisymmetry, a general form of the metric tensor reads:

$$ds^2 = g_{\mu\nu} dx^\mu dx^\nu = -N^2 dt^2 + A^2(dr^2 + r^2 d\theta^2) + \lambda^2 r^2 \sin^2 \theta (d\phi - N^\phi dt)^2, \quad (2.3)$$

with  $N(r, \theta)$ ,  $A(r, \theta)$ ,  $\lambda(r, \theta)$  and  $N^\phi(r, \theta)$  function only of  $(r, \theta)$ . From Eq. (2.3), we immediately recognize the induced 3-D spatial metric as:

$$\gamma_{ij} = \text{diag}(A^2, r^2 A^2, \lambda^2 r^2 \sin^2 \theta), \quad (2.4)$$

with the square root of the determinant of the components  $\gamma_{ij}$  given by  $\sqrt{\gamma} = A^2 \lambda r^2 \sin^2 \theta$ . As we will see, this quantity will be important to calculate global properties, like the mass, of stars.

By the 3+1 decomposition of the energy momentum tensor in Eq. (2.2), the total energy  $E^T$  (perfect fluid + magnetic field) of a star endowed with magnetic fields as measured by an Eulerian observer  $\mathcal{O}_o$  (observer with four-velocity  $n^\mu$ ) is

$$E^T := T_{\mu\nu} n^\mu n^\nu = \Gamma^2 (\mathcal{E} + P) - P + \frac{1}{2\mu_0} (B^i B_i + E^i E_i), \quad (2.5)$$

with  $\Gamma := -n_\mu u^\mu$  being the Lorentz factor relating the Eulerian observer with the co-moving observer (observer with four-velocity  $u^\mu$ ). The total momentum density flux reads:

$$J^\phi := -T_{\mu\nu} n^\mu \gamma_i^\nu = (E^T + P) A^2 \lambda r \sin \theta U + \frac{1}{\mu_0} A^2 (B^r E^\theta - E^r B^\theta), \quad (2.6)$$

and the total stress  $S_{ij} := T_{\mu\nu} \gamma_i^\mu \gamma_j^\nu$  is given by:

$$S_r^r = P + \frac{1}{2\mu_0} (E^\theta E_\theta - E^r E_r + B^\theta B_\theta - B^r B_r) \quad (2.7)$$

$$S_\theta^\theta = p + \frac{1}{2\mu_0} (E^r E_r - E^\theta E_\theta + B^r B_r - B^\theta B_\theta) \quad (2.8)$$

$$S_\phi^\phi = P + (\mathcal{E} + P) U^2 + \frac{1}{2\mu_0} (E^i E_i + B^i B_i), \quad (2.9)$$

with  $U$  being the physical fluid velocity in the  $\phi$  direction, as measured by the Eulerian observer  $\mathcal{O}_0$ ,

$$U = \frac{\lambda r \sin \theta}{N} (\Omega - N^\phi), \quad (2.10)$$

<sup>1</sup> hypersurface is a generalization of the concept of hyperplane. Suppose an enveloping manifold  $M$  has  $n$  dimensions; then any submanifold of  $M$  of  $n-1$  dimensions is a hypersurface.

where  $\Omega$  is the rotation velocity of the star. The electric and the poloidal magnetic field components, as measured by  $\mathcal{O}_o$ , necessary to evaluate the quantities in Eqs. (2.5)-(2.9) are given by (Lichnerowicz et al., 1967):

$$E_\alpha := F_{\alpha\beta} n^\beta = (E_r, E_\theta, E_\phi) = \left( \frac{1}{N} \left[ \frac{\partial A_t}{\partial r} + N^\phi \frac{\partial A_\phi}{\partial r} \right], \frac{1}{N} \left[ \frac{\partial A_t}{\partial \theta} + N^\phi \frac{\partial A_\phi}{\partial \theta} \right], 0 \right), \quad (2.11)$$

$$B_\alpha := -\frac{1}{2} \epsilon_{\alpha\beta\gamma\sigma} F^{\gamma\sigma} n^\beta = (B_r, B_\theta, B_\phi) = \left( \frac{1}{\lambda r^2 \sin \theta} \frac{\partial A_\phi}{\partial \theta}, -\frac{1}{\lambda \sin \theta} \frac{\partial A_\phi}{\partial r}, 0 \right), \quad (2.12)$$

where  $\epsilon_{\alpha\beta\gamma\sigma}$  is the Levi-Civita tensor related to the metric  $g_{\mu\nu}$ . As we will see in the next section, the quantities  $A_\phi$  and  $A_\phi$  are derived from the Maxwell equations in curved spacetime. In this thesis, it is assumed that stars are endowed with poloidal magnetic fields ( $B_r$  and  $B_\theta$  are the only non-vanishing components). In this case, the magnetic vector potential  $A_\mu$  has the components  $A_\mu = (A_t, 0, 0, A_\phi)$  by construction. Note that Frieben and Rezzolla (2012a) constructed toroidal magnetic fields with the choice  $A_\mu = (0, A_r, A_\theta, 0)$ .

One important question about magnetic field in neutron stars is its decay due to dissipation. Hence, stationary models of neutron stars in magnetic fields require a separation of dynamical and dissipative timescales, encoded in an assumption of infinite conductivity, i.e., magnetic fields are 'frozen in' and carried with the fluid, which is a common assumption in astrophysics. This assumption is exceedingly well justified for neutron star matter, since the ohmic dissipation timescale is larger than the age of the universe. As a consequence, the electric current in the fluid would not suffer ohmic decay (Goldreich and Reisenegger, 1992). Therefore, we assume infinite conductivity inside the stars. In this case, the magnetic flux  $BR^2$  ( $R$  the stellar radius) is conserved and the electric field as measured by the co-moving observer is zero,  $E'_\alpha = F_{\alpha\beta} u^\beta = 0$ . As a result, we find the relation between the magnetic vector components:

$$A_t = -\Omega A_\phi. \quad (2.13)$$

The momentum-energy conservation equation

$$\nabla_\mu T^{\mu\nu} = 0, \quad (2.14)$$

gives an equation of stationary motion for the fluid endowed with magnetic fields,

$$\frac{1}{\mathcal{E} + \mathcal{P}} \frac{\partial \mathcal{P}}{\partial x^i} + \frac{\partial \ln N}{\partial x^i} - \frac{\ln \Gamma}{\partial x^i} + \frac{F^{\mu\nu} j_\nu}{\mathcal{E} + \mathcal{P}} = 0, \quad (2.15)$$

with the spatial coordinates  $x^i = (r, \theta)$ . The first term in Eq. (2.15) corresponds to the purely matter contribution, the second represents the gravitational potential, the third accounts for the centrifugal effects due to rotation, and the last one is the Lorentz force ( $F^{\mu\nu} j_\nu$ ) induced by the magnetic field, which, in our case, is generated by the four-electric current  $j_\nu$ . Since  $A_\mu = (A_t, 0, 0, A_\phi)$ , then  $j_\nu = (j_t, 0, 0, j_\phi)$ , which comes from the assumption of circularity condition. In other words, there are no meridional electric currents.

Eq. (2.15) is the relativistic version of the Euler equation in Eq. (A.1). In Appendix A, we took the curl of Eq. (A.1) to show that the Lorentz force in the equation of motion can be written as the divergence of a scalar function  $M$ . In the same way, we can write the Lorentz term in Eq. (2.15) as:

$$\begin{aligned} \frac{\partial M}{\partial x^i} &= \frac{F^{\mu\nu} j_\nu}{\mathcal{E} + \mathcal{P}} \\ &= \left( \frac{j^\phi - \Omega j^t}{\mathcal{E} + \mathcal{P}} \right) \frac{\partial A_\phi}{\partial x^i}. \end{aligned} \quad (2.16)$$

Rearranging the Eq. (2.16), the arbitrary function  $M$  can be chosen such that:

$$\frac{\partial M}{\partial A_\phi} = g(A_\phi) = \frac{j^\phi - \Omega j^t}{\mathcal{E} + P}. \quad (2.17)$$

In other words

$$M = M(A_\phi(r, \theta)) = \int_0^{A_\phi} g(u) du, \quad (2.18)$$

which is exactly the same expression as Eq. (A.22) for Newtonian stars endowed with magnetic fields. The function  $g(u)$  is called current function. The choice of the current function is a standard way to generate self-consistently a dipolar magnetic field throughout the star. Here, the magnetic star models are obtained by assuming a constant value  $g(u) = k_0$  for the dimensionless current function. From Eq. (2.17) the macroscopic electric current relates to  $k_0$  through the expression:

$$j^\phi = \Omega j^t + (\mathcal{E} + P) k_0. \quad (2.19)$$

For higher values of the current function, the electric current increases and, therefore, the magnetic field in the star increases proportionally. In Bocquet et al. (1995), other choices for  $g(u)$  different from a constant value were considered. These choices led to a electric current distribution slightly different from that corresponding to  $g(u) = k_0$ , being simply more concentrated in other regions of the star. As a result, the electromagnetic field had more or less the same structure as considering a constante current function. There are even more complicated current distributions that could, in principle, be used, but as shown by Bocquet et al. (1995), they do not allow for numerical convergence due to the highly non-linear character of Maxwell's equations (see in the next section).

Finally, the integral form of the equation of motion, Eq. (2.15), for a fluid in presence of magnetic fields reads:

$$H(r, \theta) + \ln N(r, \theta) - \ln \Gamma(r, \theta) + M(r, \theta) = \text{const}, \quad (2.20)$$

where  $H$  is the dimensionless log-enthalpy (also called pseudo-enthalpy or heat function) defined as:

$$H(P) = \int_0^P \frac{dP'}{\mathcal{E}(P') + P'}, \quad (2.21)$$

which can be cast in terms of the specific enthalpy  $h$ ,

$$h(P) = \frac{\mathcal{E}(P) + P}{m_b c^2 n_b}, \quad (2.22)$$

as

$$H(P) := \ln h(P) = \ln \left( \frac{\mu}{m_b c^2} \right), \quad (2.23)$$

with the mean baryon mass  $m_B = \text{Mass}(\text{Fe}^{56})/56 = 1.66 \times 10^{-27}$  kg (in the ground state at  $P=0$  and  $T=0$ ) and  $\mu$  the baryon chemical potential  $\mu = (\mathcal{E} + P)/n_b$ .

## 2.2 The Einstein-Maxwell Equations

The gravitational field is deduced from the integration of a coupled system of four elliptic partial differential equations for the four metric functions. In Appendix C, we show the deduction of these equations. For their original form, see Bonazzola et al. (1993). The final system of gravitational

equations for the four unknown metric potentials  $N$ ,  $A$ ,  $\lambda$  and  $N^\phi$  are:

$$\Delta_3 \nu = 4\pi A^2 (E^T + S_r^r + S_\theta^\theta + S_\phi^\phi) + \frac{\lambda^2 r^2 \sin^2 \theta}{2N^2} \partial N^\phi \partial N^\phi - \partial \nu \partial (\nu + \ln \lambda), \quad (2.24)$$

$$\Delta_2 [\ln A + \nu] = 8\pi A^2 S_\phi^\phi + \frac{3\lambda^2 r^2 \sin^2 \theta}{4N^2} \partial N^\phi \partial N^\phi - \partial \nu \partial \nu, \quad (2.25)$$

$$\Delta_2 [(N\lambda - 1)r \sin \theta] = 8\pi N A^2 \lambda r \sin \theta (S_r^r + S_\theta^\theta), \quad (2.26)$$

and

$$\left[ \Delta_3 - \frac{1}{r^2 \sin^2 \theta} \right] (N^\phi r \sin \theta) = -16\pi \frac{N A^2}{\lambda^2} \frac{J_\phi}{r \sin \theta} + r \sin \theta \partial N^\phi \partial (\nu - 3 \ln \lambda), \quad (2.27)$$

where the short notation was introduced:

$$\begin{aligned} \Delta_2 &= \frac{\partial^2}{\partial r^2} + \frac{1}{r} \frac{\partial}{\partial r} + \frac{1}{r^2} \frac{\partial^2}{\partial \theta^2} \\ \Delta_3 &= \frac{\partial^2}{\partial r^2} + \frac{2}{r} \frac{\partial}{\partial r} + \frac{1}{r^2} \frac{\partial^2}{\partial \theta^2} + \frac{1}{r^2 \tan \theta} \frac{\partial}{\partial \theta} \\ \nu &= \ln N \\ \partial_\alpha \partial_\beta &:= \frac{\partial_\alpha \partial_\beta}{\partial r \partial r} + \frac{1}{r^2} \frac{\partial_\alpha \partial_\beta}{\partial \theta \partial \theta}. \end{aligned}$$

The dynamical quantities of the perfect fluid were already defined in Eqs. (2.5)-(2.9). The system (2.24)-(2.27) forms a system of partial differential equations with boundary conditions provided by the asymptotic flatness, since the behavior of the metric potentials are known at infinity. In order words, the metric tensor tends towards the Minkowski metric. In this case, from the metric tensor in Eq. (2.3), one has  $N \rightarrow 1$ ,  $A \rightarrow 1$ ,  $\lambda \rightarrow 1$  and  $N^\phi \rightarrow 0$  at infinity. According to Bonazzola et al. (1993), the computation of the metric in the whole space outside the star provides a more precise numerical method than previous works, since the exact boundary conditions can be used. In addition, the existence of known boundary conditions at infinity is also useful to recognize the global quantities, like the mass and the angular momentum of the star. This will be addressed in the next section.

The components of the magnetic and electric fields in Eqs. (2.11) and (2.12) are determined by the Maxwell equations. The homogeneous Maxwell equation (Maxwell-Faraday),

$$\nabla_\alpha \left( \frac{1}{2} \epsilon^{\alpha\beta\gamma\sigma} F_{\gamma\sigma} \right) = 0, \quad (2.28)$$

which represents the Faraday's law of induction and Gauss's law for magnetism, is automatically fulfilled when taking the form  $F_{\alpha\beta} = \partial_\alpha A_\beta - \partial_\beta A_\alpha$  for the Faraday tensor. On the other hand, the Gauss's Law (Maxwell-Gauss) and Ampère's law (Maxwell-Ampère), which represent the inhomogeneous Maxwell's equations,

$$\nabla_\alpha F^{\alpha\beta} = \mu_0 j^\beta, \quad (2.29)$$

with  $j^\beta$  being the free electric current (to distinguish from the bound currents, as we will see in the next chapter), can be expressed in terms of the magnetic vector potential  $A_t$  and  $A_\phi$  as (Bonazzola et al., 1993; Cardall et al., 2001):

$$\Delta_3 A_t = \sigma_{A_t}, \quad (2.30)$$

and

$$\left[ \Delta_3 - \frac{1}{r^2 \sin^2 \theta} \right] \left( \frac{A_\phi}{r \sin \theta} \right) = \sigma_{A_\phi}, \quad (2.31)$$

with the sources given by:

$$\begin{aligned}
\sigma_{A_t} = & -\mu_0 A^2 (\mathbf{g}_{tt} \mathbf{j}^t + \mathbf{g}_{t\phi} \mathbf{j}^\phi) \\
& - \frac{\lambda^2}{N^2} N^\phi r^2 \sin^2 \theta \partial A_t \partial N^\phi \\
& - \left( 1 + \frac{\lambda^2}{N^2} r^2 \sin^2 \theta (N^\phi)^2 \right) \partial A_\phi \partial N^\phi \\
& - (\partial A_t + 2N^\phi \partial A_\phi) \partial (\ln \lambda - \nu) \\
& - 2 \frac{N^\phi}{r} \left( \frac{\partial A_\phi}{\partial r} + \frac{1}{r \tan \theta} \frac{\partial A_\phi}{\partial r} \right), \tag{2.32}
\end{aligned}$$

and

$$\begin{aligned}
\sigma_{A_\phi} = & -\mu_0 A^2 \lambda^2 (\mathbf{j}^\phi - N^\phi \mathbf{j}^t) r \sin \theta \\
& - \frac{\lambda^2}{N^2} r \sin \theta \partial N^\phi (\partial A_t + N^\phi \partial A_\phi) \\
& + \frac{1}{r} \partial A_\phi \partial (\ln \lambda - \nu). \tag{2.33}
\end{aligned}$$

In order to compute models of relativistic neutron stars endowed with poloidal magnetic fields in fully General Relativity, one needs 11 variables, where 3 are related to the fluid properties: the energy density  $\mathcal{E}$ , the pressure  $P$  and the enthalpy  $H$ . For the gravitational field, there are 4 metric potentials to be determined (Eqs. 2.24-2.27). Finally, 2 components of the electromagnetic potential (Eqs. 2.30-2.31) and 2 components of the electromagnetic current need also to be calculated. These quantities, together with the equation of state consist of a closed system of 11 equations. We have 6 Poisson equations, 4 of them for the metric variables  $A(r, \theta)$ ,  $\lambda(r, \theta)$ ,  $N(r, \theta)$  and  $N^\phi(r, \theta)$  and 2 for the components of the electromagnetic potential  $A_t(r, \theta)$  and  $A_\phi(r, \theta)$ , respectively. In addition, 1 equation is given by the relation between these quantities, see Eq. (2.13). The hydrodynamic equation of motion for a star endowed with magnetic field (Eq. 2.20), the expression for the log-enthalpy (Eq. 2.21) and the expression for the electric current (Eq. 2.19) close the system. Stationary and axisymmetric configurations are calculated once the EoS is specified, together with the rotation law, the central enthalpy and the current function  $k_0$ .

From the numerical point of view, the most important concern is the control of numerical errors during the calculation. In the next section, we will briefly describe a three-dimension relativistic generalization of the well-known virial theorem in Newtonian gravity, as formulated for any stationary and asymptotically flat spacetime by [Gourgoulhon and Bonazzola \(1994\)](#). This formulation (named GRV3) was obtained within the 3+1 formalism and it represents a useful consistency check of numerical solutions of the Einstein equations. In addition, a two-dimensional integral identity (named GRV2) was derived for a general asymptotically flat four-dimensional spacetime by [Bonazzola \(1973\)](#), and generalized and applied to stars in [Bonazzola and Gourgoulhon \(1994\)](#). Both GRV3 and GRV2 were used to check the accuracy of our solutions.

## 2.3 General Relativity Virial Identities

### 2.3.1 GRV3

The General Relativistic Virial Theorem GRV3 was derived by [Gourgoulhon and Bonazzola \(1994\)](#), taking the expression of the mass (see Eq. 2.42) as a starting point. The '3' in the name simply means

that the integral involving the identity is a 3-dimensional one. For a stationary and axisymmetric spacetime, GVR3 reads (Gourgoulhon, 2012):

$$\int_{\Sigma_t} \left[ 4\pi(S_r^r + S_\theta^\theta + S_\phi^\phi) - \frac{1}{A^2} \left( \partial\nu\partial\nu - \frac{1}{2A\lambda} \partial A \partial \lambda \right) + \frac{3\lambda^2 \sin^2 \theta}{8r^2 A^2 N^2} \partial N^\phi \partial N^\phi \right] A^2 \lambda r^2 \sin \theta dr d\theta d\phi$$

$$- \int_{\Sigma_t} \left\{ \frac{1}{2r} \left( \frac{1}{A^2} - \frac{1}{\lambda^2} \right) \left[ \frac{1}{A} \left( \frac{\partial A}{\partial r} + \frac{1}{r \tan \theta} \frac{\partial A}{\partial \theta} \right) - \frac{1}{2\lambda} \right] \right\} A^2 \lambda r^2 \sin \theta dr d\theta d\phi = 0. \quad (2.34)$$

The expression above reduces to the classical Virial Theorem for stationary configurations at the Newtonian limit (Gourgoulhon and Bonazzola, 1994).

### 2.3.2 GRV2

The second virial identity used in this work was obtained by Bonazzola (1973); Bonazzola and Gourgoulhon (1994) and it is called GRV2, since it involves a 2-dimensional integral. Contrary to GVR3, the derivation of GRV2 is much simpler once one considers Eq. (2.25) of the Einstein field equations.

The 2-dimensional flat Laplacian  $\Delta_2$  allows to write a generic solution of Eq. (2.25) in terms of its Green function,

$$\ln A(r, \theta) + \ln N(r, \theta) = \frac{\int_{\Sigma_t} \sigma r dr d\theta}{2\pi} + \mathcal{O}\left(\frac{1}{r}\right), \quad (2.35)$$

with  $\sigma$  being the source (right hand side term) in Eq. (2.25). However, one of the main properties of the spacetime considered here is its asymptotically flatness at  $r \rightarrow \infty$ . In this case, as we have already seen  $A \rightarrow 1$  and  $N \rightarrow 1$ . Therefore, the integral term in Eq. (2.35) is zero,

$$\int_{r=0}^{\infty} \int_{\theta=0}^{\pi} \left[ 8\pi A^2 S_\phi^\phi + \frac{3\lambda^2 r^2 \sin^2 \theta}{4N^2} \partial N^\phi \partial N^\phi - \partial\nu\partial\nu \right] r dr d\theta = 0. \quad (2.36)$$

This is the GRV2 identity that, together with GVR3, are used to check the consistency of our numerical solutions.

## 2.4 Numerical procedure

The treatment of tabulated EoS's within the code is extremely important, since simple interpolations can introduce numerical errors, which could result in thermodynamical inconsistency. In LORENE, the tabulated data are interpolated following the method described by Swesty (1996), to ensure thermodynamic consistency of the interpolated quantities. First, the enthalpy (Eq. 2.23) and the term  $dP/dH = (\mathcal{E} + P)$  (another form of Eq. (2.21)) are evaluated from the tabulated table. Then, the pressure  $P$  and  $dP/dH$  are interpolated from the data by means of Hermite polynomials. Finally, these values are used to evaluate the baryon number density and the energy density as:

$$n_B = (\mathcal{E} + P)e^{-H},$$

$$\mathcal{E} = dP/dH - P,$$

ensuring thermodynamic consistency of  $\mathcal{E}(H)$ ,  $P(H)$  and  $n_B(H)$ . In the next chapter, we will apply this formalism for a magnetic-field dependent EoS with  $\mathcal{E}(H, B)$ , where  $B$  is the magnetic field. By choosing the stellar central enthalpy  $H_c$ , the standard algorithm to numerically construct magnetized stellar models is:

- Step 1. One has to choose the constant current function  $k_0$  which will give the electric current distribution inside the star:

$$j^\phi - \Omega j^t = (\mathcal{E} + P)k_0; \quad (2.37)$$

- Step 2. At a given step in the iteration process,  $j^\phi$  is deduced from Eq. (2.37). In this equation,  $j^t$  cannot be freely chosen, but it is fixed by the Maxwell-Gauss (Eq. 2.30) equation in the stellar interior;
- Step 3. The component of the electric current  $j^\phi$  comes from the Maxwell-Gauss equation. With  $j^t$  and  $j^\phi$ , one solves the Maxwell-Ampère equation (Eq. 2.31);
- Step 4. Then, one solves the Maxwell-Gauss equation in the exterior only, where  $j^t = 0$ , with the following boundary conditions at the star's surface: the magnetic vector potential  $A_\phi$  must be continuous;
- Step 5. The next step consists in determining the matter distribution that agrees with the obtained electromagnetic field by making use of the equation of motion  $H + \ln N - \ln \Gamma + M = C_0$ , with the central enthalpy  $H$  as an input. The constant  $C_0$  can be evaluated at every point within the star. We choose to do it at the stellar center, since  $M(0, 0) = \Gamma(0, 0) = 0$  and then  $C_0 = H(0, 0) + \ln N(0, 0)$ ;
- Step 6. The last step consists in computing the electromagnetic stress-tensor adding them to the fluid ones and then solving the gravitational field equations.

Lorene code is based on multi-domain spectral methods. These methods provide, among other advantages, an unique tool for solving partial differential equations. The physical computational range into several domains. The boundary of each domain is chosen in order to coincide with a physical discontinuity e.g. the density jumps or the surface of the star, and to obtain the solution in each of those domains. In the case of stars, the last domain is compactified, with the radial coordinate  $u \rightarrow 1/r$ . In this way, the computational domain extend to spatial infinity. Details of mapping and spectral expansions in the general case of 3D compact object is described by [Bonazzola et al. \(1998\)](#).

## 2.5 Global Quantities

Let us now define several quantities that are essential when describing relativistic stars. The surface of the star is then defined by  $P = 0$ .

### 2.5.1 Total baryon number

As we will be dealing with isolated stars, the total number of baryons remains the same in the system. In other words, a four-baryon current  $J_b^\mu$  defined as:

$$J_b^\mu = n_b u^\mu, \quad (2.38)$$

where  $n_b$  is the baryon number and  $u^\mu$  the fluid four-velocity, obeys the conservation law:

$$\nabla_\mu J_b^\mu = 0, \quad (2.39)$$

that, by means of the Gauss-Ostrogradski theorem (Divergent theorem), can be written as:

$$\int_{\Sigma_t} J_b^\mu n_\mu dS, \quad (2.40)$$

with  $dS$  being the area of the 3-D hypersurface  $\Sigma_t$  defined as  $dS = \sqrt{\gamma} dr d\theta d\phi$ , with  $\sqrt{\gamma} = A^2 \lambda r^2 \sin \theta$ , and  $n_\mu$  is the four-velocity of the Eulerian observer  $\mathcal{O}_0$ . Therefore, making using of Eq. (2.38), the total number of baryons  $\mathcal{B}$  can be defined as:

$$\begin{aligned} \mathcal{B} &:= - \int_{\Sigma_t} n_b u^\mu n_\mu A^2 \lambda r^2 \sin \theta dr d\theta d\phi \\ &= \int_{\Sigma_t} \Gamma n_b A^2 \lambda r^2 \sin \theta dr d\theta d\phi, \end{aligned} \quad (2.41)$$

where we have used the fact that  $\Gamma = -u^\mu n_\mu$ . As a consequence, the stellar baryon mass is simply  $M_B = m_b \mathcal{B}$ , with  $m_b$  being the mean baryon mass.

### 2.5.2 Gravitational Mass

The concept of mass in general relativity is more complex than the concept of mass in special relativity. In fact, general relativity does not offer a single definition of the term mass, but offers several different definitions that are applicable under different circumstances. For example, the Komar mass can be defined in any stationary spacetime in terms of the metric and its Killing vector (Wald (2010), Eq. 11.2.10) as:

$$M := \int_{\Sigma_t} [2T_{\mu\nu} - Tg_{\mu\nu}] n^\mu \xi^\nu \sqrt{\gamma} dr d\theta d\phi, \quad (2.42)$$

with  $n_\mu$  being the future unit four-vector normal to  $\Sigma_t$ ,  $T$  the trace of  $T_{\mu\nu}$  with respect to  $g_{\mu\nu}$ , and  $\xi^\nu$  the time Killing vector given by  $\xi^\nu = N n^\nu + N^\nu$ , with the non-vanishing component of the shift vector  $N^\nu = N^\phi$ . By using  $T_{\mu\nu}$  as in Eq. (2.2), we obtain:

$$M = \int \left[ N(E^T + S_r^r + S_\theta^\theta + S_\phi^\phi) + 2N^\phi \lambda (E^T + P) U r \sin \theta \right] A^2 \lambda r^2 \sin \theta dr d\theta d\phi. \quad (2.43)$$

This common value, denoted here by  $M$ , is sometimes called gravitational mass, to distinguish it from the baryon mass,  $M_B = m_b \mathcal{B}$ . From the condition of asymptotic flatness,  $\nu = \ln N \rightarrow 0$ , the leading term of the solution for  $\nu$  in Eq. (2.24) is the gravitational potential  $\nu \sim -M/r$ , with  $M$  being the gravitational mass of the star as measured by an observer at infinity.



### 2.5.3 Angular momentum

The angular momentum is defined as:

$$\begin{aligned} J &:= - \int T_{\mu\nu} n^\mu e_\phi^\nu \sqrt{\gamma} dr d\theta d\phi \\ &= \int A^2 \lambda J_\phi r^2 \sin \theta dr d\theta d\phi, \end{aligned} \quad (2.44)$$

with  $e_\phi^\nu$  being the axisymmetry Killing vector. In this thesis, we often refer to the moment of inertia of the star, which is defined simply as  $I := J/\Omega$ .

### 2.5.4 Quadrupole moment

According to [Salgado et al. \(1994\)](#), the quadrupole momentum  $Q$  is identified as the leading term in the asymptotic behavior of the metric potential  $N(r, \theta)$ :

$$\ln N(r, \theta)_{r \rightarrow \infty} \sim -\frac{M}{r} + \frac{Q}{r^3} P_2(\cos \theta), \quad (2.45)$$

with  $P_2(\cos \theta)$  being the second order Legendre polynomial. According to [Bonazzola et al. \(1993\)](#) and [Salgado et al. \(1994\)](#), the quadrupole moment  $Q$  in Eq. (2.45) can be written as:

$$Q = -\frac{1}{4\pi} \int \sigma_{\ln N} P_2(\cos \theta) r^4 \sin \theta dr d\theta d\phi, \quad (2.46)$$

where  $\sigma_{\ln N}$  is the source term in Eq. (2.24) (see also Eq. (3.19) in [Bonazzola et al. \(1993\)](#)).

### 2.5.5 Circumferential radius

A coordinate-independent characterization of the stellar equator can be done by calculating the circumferential equatorial radius ( $\theta = \pi/2$ ):

$$R_{\text{circ}} := \frac{1}{2\pi} C, \quad (2.47)$$

with  $C$  the proper length of the circumference of the star in the equatorial plane given. In this case, one gets:

$$\begin{aligned} R_{\text{circ}} &= \frac{1}{2\pi} \int_0^{2\pi} \sqrt{\gamma_{\phi\phi}} d\phi \\ &= \frac{1}{2\pi} \int_0^{2\pi} B(r, \theta) r \sin \theta d\phi \\ &= r_{\text{eq}} B(r_{\text{eq}}, \pi/2), \end{aligned} \quad (2.48)$$

where  $r_{\text{eq}}$  is the equatorial coordinate radius.

### 2.5.6 Magnetic dipole moment

The magnetic dipole moment  $\mu$  is defined as the radial component (the orthonormal one) of the magnetic field of a magnetic dipole seen by an observer at infinity (Cardall et al., 2001):

$$\frac{2\mu\cos\theta}{r^3} = B_{(r)} \Big|_{r \rightarrow \infty}. \quad (2.49)$$

As we have already seen, the stationary and axi-symmetric stellar configurations are determined by the choice of the central enthalpy  $H_c$  and the current function  $k_0$ . As we will see in the next chapters, we can fix the current function  $k_0$  as the magnetic dipole moment varies. Note that, it is equivalent to fix or the current or the magnetic dipole moment, since a certain current function  $k_0$  corresponds to a single value of  $\mu$ , and vice-versa. Having said that, equilibrium star sequences can be also build at different fixed magnetic dipole moments,  $\mu$ . In the next Chapter, all stellar configurations are obtained at fixed  $\mu$ .

## Chapter 3

# A self-consistent study of magnetic field effects on hybrid stars

*In this chapter, we will study the effects of strong magnetic fields on hybrid stars in different ways. First, we investigate effects of the magnetization and a magnetic-field dependent equation of state on the global properties of stars. Secondly, we study the effects of magnetic fields on the populated degrees of freedom inside hybrid stars.*

### 3.1 Magnetic field-dependent equation of state

The effect of strong magnetic fields on the equation of state for compact stars were studied by many authors (Noronha and Shovkovy, 2007; Rabhi et al., 2008; Strickland et al., 2012; Sinha et al., 2013). Basically, charged particles become Landau quantized (Landau and Lifshitz, 1960) in the plane perpendicular to the magnetic field. For our numerical application, we will employ an extended hadronic and quark SU(3) non-linear realization of the sigma model that describes magnetized hybrid stars containing nucleons, hyperons and quarks (see Fig. 3.1). Let us now briefly summarize the main characteristics of this model.

We made use of the effective model that combines a SU(3)-flavor  $\sigma$  model with a Polyakov-loop-extended Nambu Jona-Lasinio (PNJL) type approach for deconfinement phase transition into quark degrees of freedom (Papazoglou et al., 1999; Dexheimer and Schramm, 2008, 2010) in a spirit similar to the PNJL model by Fukushima (2004). Moreover, this approach combines hadrons and quarks in a single equation of state. As a result, important features of the deconfinement phase transition, like the strength of the transition, the mixing of phases and also the accompanying chiral symmetry restoration can be studied.

In mean field approximation, the full Lagrangian reads:

$$\mathcal{L} = \mathcal{L}_{\text{Kin}} + \mathcal{L}_{\text{Int}} + \mathcal{L}_{\text{Self}} + \mathcal{L}_{\text{SB}} - U + \mathcal{L}_{\text{mag}}, \quad (3.1)$$

with  $\mathcal{L}_{\text{Kin}}$  being the kinetic energy term for hadrons, quarks, and leptons, and

$$\mathcal{L}_{\text{Int}} = - \sum_i \bar{\psi}_i [\gamma_0 (g_{i\omega}\omega + g_{i\phi}\phi + g_{i\rho}\tau_3\rho) + M_i^*] \psi_i, \quad (3.2)$$

a term that takes in account the interactions between baryons or quarks and vector and scalar mesons. Index  $i$  runs over the three lightest quark flavors (u, d, s), and the baryon octet.

The self interactions of scalar and vector mesons is represented by

$$\begin{aligned}
\mathcal{L}_{\text{Self}} = & \frac{1}{2}(m_\omega^2\omega^2 + m_\rho^2\rho^2 + m_\phi^2\phi^2) \\
& + g_4 \left( \omega^4 + \frac{\phi^4}{4} + 3\omega^2\phi^2 + \frac{4\omega^3\phi}{\sqrt{2}} + \frac{2\omega\phi^3}{\sqrt{2}} \right) \\
& - k_0(\sigma^2 + \zeta^2 + \delta^2) - k_1(\sigma^2 + \zeta^2 + \delta^2)^2 \\
& - k_2 \left( \frac{\sigma^4}{2} + \frac{\delta^4}{2} + 3\sigma^2\delta^2 + \zeta^4 \right) - k_3(\sigma^2 - \delta^2)\zeta \\
& - k_4 \ln \frac{(\sigma^2 - \delta^2)\zeta}{\sigma_0^2\zeta_0},
\end{aligned} \tag{3.3}$$

and

$$\mathcal{L}_{\text{SB}} = -m_\pi^2 f_\pi \sigma - \left( \sqrt{2} m_k^2 f_k - \frac{1}{\sqrt{2}} m_\pi^2 f_\pi \right) \zeta, \tag{3.4}$$

is an explicit chiral symmetry breaking term (responsible for producing the masses of the pseudo-scalar mesons), and

$$\begin{aligned}
U(\Phi) = & (a_0 T^4 + a_1 \mu^4 + a_2 T^2 \mu^2) \Phi^2 \\
& + a_3 T_0^4 \log(1 - 6\Phi^2 + 8\Phi^3 - 3\Phi^4),
\end{aligned} \tag{3.5}$$

it is a potential for the Polyakov  $\Phi$  field which is used as a order parameter for deconfinement.  $T$  is the temperature, which in our case  $T=0$ .

The later is important in order to reproduce a realistic structure for the QCD phase diagram over the whole range of chemical potentials and temperatures, including realistic thermodynamic behaviour at vanishing chemical potential as shown by [Dexheimer and Schramm \(2008\)](#). Finally, one has the magnetic field contribution,

$$\mathcal{L}_{\text{mag}} = - \sum_i \bar{\psi}_i (q_i e \gamma^\mu A_\mu + \frac{1}{2} \kappa \sigma^{\mu\nu} F_{\mu\nu}) \psi_i, \tag{3.6}$$

which represents the magnetic and anomalous magnetic moment interactions with the fermions.

In Eq. (3.6),  $q_i$  is the electric charge of each particle in multiples of the electron charge  $e$ ,  $A_\mu$  is the electromagnetic field,  $\kappa$  represents the tensorial coupling strength of baryons with the electromagnetic field tensor, and  $\sigma^{\mu\nu} = i[\gamma^\mu, \gamma^\nu]/2$ . The mesons included are the vector-isoscalars  $\omega$  and  $\phi$  (vector meson with hidden strangeness), the vector-isovector  $\rho$ , the scalar-isoscalars  $\sigma$  and  $\zeta$  (scalar meson with hidden strangeness) and the scalar-isovector  $\delta$ , with  $\tau_3$  being twice the isospin projection of each particle. The isovector mesons affect isospin-asymmetric matter and are, consequently, important for neutron star physics. The coupling constants of the model can be found in [Dexheimer and Schramm \(2008, 2010\)](#). The hadronic sector was fitted to reproduce the vacuum masses of the baryons and mesons, nuclear saturation properties, reasonable values for the hyperon potentials and the pion and kaon decay constants ( $f_\pi$  and  $f_k$ ). The quark sector was fitted to reproduce lattice QCD data at vanishing chemical potential and phase diagram information, such as the location of the critical end-point and a continuous first-order phase transition line that terminates on the zero temperature axis at around four times saturation density.

The effective masses of the baryons and quarks are generated by the scalar mesons except for a small explicit mass term  $M_0$  and the term containing  $\Phi$ :

$$M_B^* = g_{B\sigma}\sigma + g_{B\delta}\tau_3\delta + g_{B\zeta}\zeta + M_{0B} + g_{B\Phi}\Phi^2 \tag{3.7}$$

$$M_q^* = g_{q\sigma}\sigma + g_{q\delta}\tau_3\delta + g_{q\zeta}\zeta + M_{0q} + g_{q\Phi}(1 - \Phi). \quad (3.8)$$

With the increase of temperature and/or density, the  $\sigma$  field (non-strange chiral condensate) decreases in value, causing the effective masses of the particles to decrease towards chiral symmetry restoration. The field  $\Phi$  assumes non-zero values with the increase of temperature/density and, due to its presence in the baryons effective mass (Eq. 3.7), suppresses their presence. On the other hand, the presence of the  $\Phi$  field in the effective mass of the quarks, included with a negative sign (Eq. 3.8), ensures that they will not be present at low temperatures/densities. In this way, the interaction with the medium determines which are the degrees of freedom present in the system.

Charged Fermions endowed with magnetic fields (in the z-direction) have their total energy quantized into Landau levels  $\nu$  as (Landau and Lifshitz, 1960),

$$E_{i\nu s}^* = \sqrt{k_{z_i}^2 + \left( \sqrt{M_i^{*2} + 2\nu|q_i|B} - s_i\kappa_i B \right)^2}, \quad (3.9)$$

with  $k_i$  being the fermi momentum and  $s_i$  the spin of each fermion. The last term comes from the anomalous magnetic moment (AMM) of the particles that splits the energy levels with respect to the alignment/anti-alignment of the spin with the magnetic field. Note that, according to Eq. (3.9), uncharged particles also have their energy levels modified by the AMM  $\kappa_i$ . The AMM constants  $\kappa_i$  have values  $\kappa_p = 1.79$ ,  $\kappa_n = -1.91$ ,  $\kappa_\Lambda = -0.61$ ,  $\kappa_\Sigma^+ = 1.67$ ,  $\kappa_\Sigma^0 = 1.61$ ,  $\kappa_\Sigma^- = -0.38$ ,  $\kappa_\Xi^0 = -1.25$ ,  $\kappa_\Xi^- = 0.06$ . The sign of  $\kappa_i$  determines the preferred orientation of the spin with the magnetic field. For zero temperature, the sum over the Landau levels  $\nu$  runs up to a maximum value, beyond which the momentum of the particles in the z-direction would be imaginary

$$\nu_{\max} = \frac{E_{is}^{*2} + s_i\kappa_i B - M_i^{*2}}{2|q_i|B}. \quad (3.10)$$

We choose to include in our calculations the AMM effect for the hadrons only, since the coupling strength of the particles  $\kappa_i$  depends on the corresponding magnetic moment, that up to now is not fully understood for the quarks. Furthermore, it is stated in Weinberg (1990), that quarks in the constituent quark model have no anomalous magnetic moment, and in Ferrer et al. (2015), that the AMM of quarks from one-loop fermion self-energy is very small. For calculations including AMM effects for the quarks, see Chakrabarty (1996); Suh et al. (2001); Perez Martinez et al. (2005); Felipe et al. (2008). The AMM for the electrons is also not taken into account as its effect is negligibly small. Properties of the magnetized SU(3) non-linear realization of the sigma model were presented in Dexheimer et al. (2012a, 2013b) for an effective (ad hoc) variation of the magnetic field inside the star. In Fig. 3.1, we show the example of the chiral EoS for different asymptotic magnetic fields strengths.

## 3.2 Inclusion of gravity

In this section, we included magnetic fields effects in the EoS, something that was not taken into account by Bonazzola et al. (1993), Bocquet et al. (1995) and Cardall et al. (2001). Here, we follow the same general relativity formalism and setup as in Chatterjee et al. (2015); Ferrer et al. (2010). Let us now see how the magnetization term appears in the formalism. Starting from a microscopic Lagrangian, one can obtain the gauge-invariant fermion contribution to the energy-momentum tensor

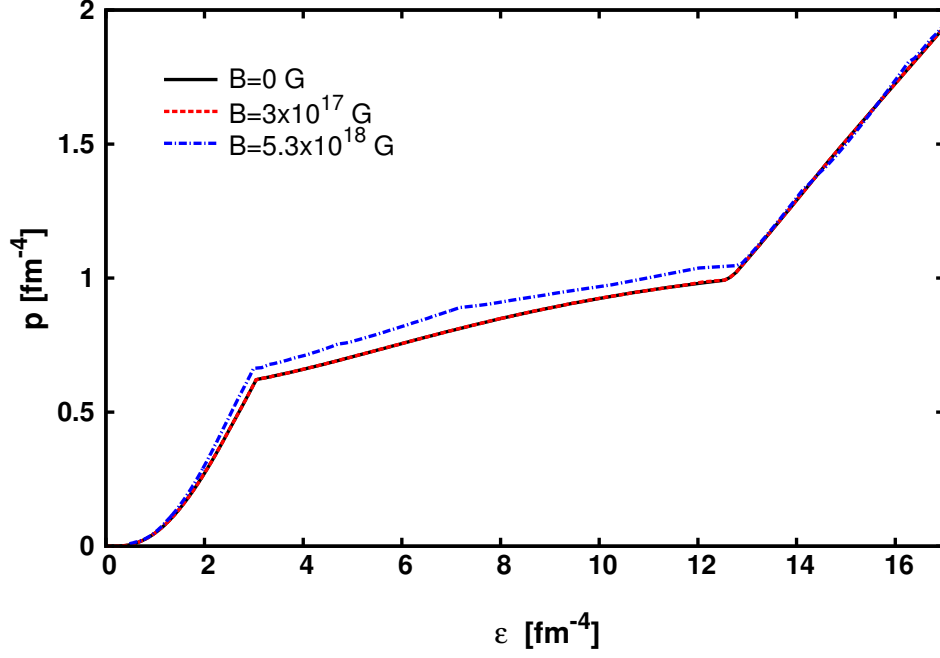


FIGURE 3.1: EoS of an extended hadronic and quark SU(3) non-linear realization of the sigma model that describes magnetized hybrid stars containing nucleons, hyperons and quarks for different asymptotic magnetic fields

(Ferrer et al., 2010; Chatterjee et al., 2015) as:

$$T_f^{\mu\nu} = \frac{1}{2}\bar{\psi}(\gamma^\mu\partial^\nu + \gamma^\nu\partial^\mu)\psi - \frac{1}{2}(j^\mu A^\nu + j^\nu A^\mu) - g^{\mu\nu}\mathcal{L}, \quad (3.11)$$

with  $j^\mu$  being the electromagnetic current defined as  $j_\mu = iq\bar{\psi}\gamma_\mu\psi$ ,  $A^\nu$  magnetic-vector potential and  $\mathcal{L}$  the Lagrangian density of the fermion system.

As we are interested in studying global properties of highly magnetized neutron stars, like the mass and the radius, it is necessary to take the thermodynamic average of the energy momentum tensor  $T_f^{\mu\nu}$ . In this case, as already shown by Chatterjee et al. (2015); Ferrer et al. (2010), the second term in Eq. (3.11) can be written as:

$$-\frac{1}{2}\langle j^\mu A^\nu + j^\nu A^\mu \rangle = \frac{1}{2}(F_\alpha^\mu M^{\alpha\nu} + F_\beta^\nu M^{\beta\mu}), \quad (3.12)$$

where the magnetization tensor is given by:

$$M^{\alpha\nu} = \epsilon^{\rho\sigma\alpha\nu}u_\rho m_\sigma, \quad (3.13)$$

with  $m_\sigma$  being the magnetization-four vector:

$$m_\sigma = -\frac{\partial\Omega_f}{\partial b^\sigma}, \quad (3.14)$$

with  $\Omega_f$  being the thermodynamic potential for the fermions and  $b^\sigma$  the magnetic field 4-vector. The electromagnetic field tensor can then be expressed as (Gourgoulhon, 2012):

$$F^{\alpha\nu} = \epsilon^{\rho\sigma\alpha\nu}u_\rho b_\sigma, \quad (3.15)$$

with the Levi-Civita tensor  $\epsilon$  associated here with the Minkowski metric.

Defining the scalar quantity:

$$\mathcal{M} := \mu_0 \frac{m_\sigma}{b_\sigma}, \quad (3.16)$$

the total energy momentum tensor (fluid + magnetization contribution + pure magnetic field) reads:

$$\begin{aligned} T^{\mu\nu} = & (\mathcal{E} + P)u^\mu u^\nu + pg^{\mu\nu} \\ & + \frac{\mathcal{M}}{B} [b^\mu b^\nu - (b \cdot b)(u^\mu u^\nu + g^{\mu\nu})] \\ & + \frac{1}{\mu_0} \left( -b^\mu b^\nu + (b \cdot b)u^\mu u^\nu + \frac{1}{2}g^{\mu\nu}(b \cdot b) \right). \end{aligned} \quad (3.17)$$

In Eq. (3.17) the first two terms on the right hand side can be identified as the pure (perfect fluid) fermionic contribution, followed by the magnetization term (the new term in comparison with Eq. 2.2) and the third term is the pure electromagnetic contribution to the energy-momentum tensor.  $B$  here is the length of the magnetic field 4-vector. As we already have seen, the magnetization  $\mathcal{M}$  represents the interaction of the electromagnetic field with matter and it is given by the coupling between the electric current  $j_\mu$  and the magnetic vector potential  $A_\nu$  (Eq. 3.12).

The magnetic field in the fluid rest frame is  $b^\mu = \text{diag}(0, 0, 0, B)$ , where  $B$  is defined to point into the z-direction. In the rest frame of the fluid (using  $u^\mu = \text{diag}(1, 0, 0, 0)$  and  $g^{\mu\nu} = \text{diag}(-1, 1, 1, 1)$ ), the matter term (perfect fluid + magnetization) in Eq. (3.17) reads:

$$T_{m0}^0 = \mathcal{E}(B), \quad (3.18)$$

$$T_{m1}^1 = P(\mathcal{E}, B) - \mathcal{M}B, \quad (3.19)$$

$$T_{m2}^2 = P(\mathcal{E}, B) - \mathcal{M}B, \quad (3.20)$$

$$T_{m3}^3 = P(\mathcal{E}, B), \quad (3.21)$$

where the components  $T_{m1}^1$  and  $T_{m2}^2$  are usually referred to as perpendicular or transversal pressure (with respect to  $B$ ) and  $T_{m3}^3$  as parallel or longitudinal pressure, respectively. It is important to note that both the pressure and the energy density depend now on the magnetic field and, therefore, the EoS has the form  $P(\mathcal{E}, B)$ . The third term in Eq. (3.17) corresponds to the usual pure magnetic field contribution. It can be written as:

$$T_{B0}^0 = \frac{B^2}{2\mu_0}, \quad (3.22)$$

$$T_{B1}^1 = \frac{B^2}{2\mu_0}, \quad (3.23)$$

$$T_{B2}^2 = \frac{B^2}{2\mu_0}, \quad (3.24)$$

$$T_{B3}^3 = -\frac{B^2}{2\mu_0}. \quad (3.25)$$

In this way, the total contribution to the energy momentum tensor is simply given by  $T_0^0 = T_{m0}^0 + T_{B0}^0$  and  $T_i^i = T_{mi}^i + T_{Bi}^i$ , with  $i=1,2,3$ . Therefore, in the rest frame of the fluid, the energy momentum tensor when considering a magnetic field depend EoS and the magnetization term  $\mathcal{M}$  is:

$$T^\mu_{\mu} = \begin{bmatrix} \mathcal{E} + \frac{B^2}{2\mu_0} & 0 & 0 & 0 \\ 0 & P - \mathcal{M}B + \frac{B^2}{2\mu_0} & 0 & 0 \\ 0 & 0 & P - \mathcal{M}B + \frac{B^2}{2\mu_0} & 0 \\ 0 & 0 & 0 & P - \frac{B^2}{2\mu_0} \end{bmatrix}$$

Here, let us mention two important points. First, the magnetization term reduces the total pressure of the system. As a result, we will see that the total mass of the star decreases with the inclusion of  $\mathcal{M}$ . Second, the pressure parallel to the magnetic field ( $T^3_3$ ) decreases with the magnetic field, while the components perpendicular to  $B$  increases ( $T^1_1$  and  $T^2_2$ ). As a consequence, magnetic fields induce different pressures in different directions in the star, causing the stars to be deformed with respect to the symmetry axis.

In the same way as done in Eqs. (2.5-2.9), let us now use Eq. (3.17) in order to obtain the components of the energy momentum tensor (to appear in the source terms of the field equations) in the 3+1 formalism with the inclusion of the magnetization term  $\mathcal{M}$ . The corresponding contribution of the magnetization (mag) to the energy density is:

$$E^{(\text{mag})} = \frac{1}{\mu_0} \left[ \frac{\mathcal{M}}{B} \left( E^\theta E_\theta + E^r E_r \right) \right], \quad (3.26)$$

which needs to be added to Eq. (2.5) in order to have the total energy of the system like  $E^T \rightarrow E^T + E^{(\text{mag})}$ . The momentum density flux can be written as:

$$J_\phi^{(\text{mag})} = \frac{1}{\mu_0} \left[ \frac{\mathcal{M}}{B} \left( B^\theta B_\theta + B^r B_r \right) \right], \quad (3.27)$$

which is added to Eq. (2.6) to give the total momentum density flux of the system  $J_\phi \rightarrow J_\phi + J_\phi^{(\text{mag})}$ . Finally,  $\mathcal{M}$  contributes to the 3-tensor stress components as:

$$S_r^{(\text{mag})r} = \frac{2\mathcal{M}}{B} \frac{B^\theta B_\theta}{\Gamma^2}, \quad (3.28)$$

$$S_\theta^{(\text{mag})\theta} = \frac{2\mathcal{M}}{B} \frac{B^r B_r}{\Gamma^2}, \quad (3.29)$$

$$S_\phi^{(\text{mag})\phi} = \frac{2\mathcal{M}}{B} \left( \frac{1}{\Gamma^2} + U^2 \right) \left( B^\theta B_\theta + B^r B_r \right), \quad (3.30)$$

where, again, these components are added to the fluid and purely field ones in Eqs. (2.7-2.9) to obtain the total stress of the system.

The Maxwell equations are also modified with the inclusion of  $\mathcal{M}$ . In this case, the inhomogeneous Maxwell equation (Gauss-Ampère) in presence of external magnetic field reads:

$$\nabla_\alpha F^{\alpha\beta} = \mu_0 j^\beta + \mu_0 \nabla_\alpha M^{\alpha\beta}. \quad (3.31)$$

With the definitions of Eq. (3.13), Eq. (3.15) and Eq. (3.16), the last term can be written as:

$$\mu_0 \nabla_\alpha M^{\alpha\beta} = \mathcal{M} \nabla_\alpha F^{\alpha\beta} + F^{\alpha\beta} \nabla_\alpha \mathcal{M}, \quad (3.32)$$



therefore, the Eq. (3.31) becomes:

$$\nabla_\alpha F^{\alpha\beta} = \frac{1}{1-\mathcal{M}} \left[ \mu_0 j^\beta + F^{\alpha\beta} \nabla_\alpha \mathcal{M} \right], \quad (3.33)$$

which can be expressed in terms of the magnetic vector potential  $A_\phi$  in the same way as in Eq. (2.30) and (2.31). However, the source terms with the inclusion of  $\mathcal{M}$  become:

$$\begin{aligned} \sigma_{A_t} = & \frac{1}{\mathcal{M}-1} \left[ \mu_0 A^2 (\mathbf{g}_{tt} \mathbf{j}^t + \mathbf{g}_{t\phi} \mathbf{j}^\phi) + \partial A_t \partial \mathcal{M} \right] \\ & - \frac{\lambda^2}{N^2} N^\phi r^2 \sin^2 \theta \partial A_t \partial N^\phi \\ & - \left( 1 + \frac{\lambda^2}{N^2} r^2 \sin^2 \theta (N^\phi)^2 \right) \partial A_\phi \partial N^\phi \\ & - (\partial A_t + 2N^\phi \partial A_\phi) \partial (\ln \lambda - \nu) \\ & - 2 \frac{N^\phi}{r} \left( \frac{\partial A_\phi}{\partial r} + \frac{1}{r \tan \theta} \frac{\partial A_\phi}{\partial r} \right), \end{aligned} \quad (3.34)$$

and

$$\begin{aligned} \sigma_{A_\phi} = & \frac{1}{\mathcal{M}-1} \left[ \mu_0 A^2 \lambda^2 (\mathbf{j}^\phi - N^\phi \mathbf{j}^t) r \sin \theta + \frac{1}{r \sin \theta} \partial A_\phi \partial \mathcal{M} \right] \\ & - \frac{\lambda^2}{N^2} r \sin \theta \partial N^\phi (\partial A_t + N^\phi \partial A_\phi) \\ & + \frac{1}{r} \partial A_\phi \partial (\ln \lambda - \nu), \end{aligned} \quad (3.35)$$

which is easily reduced to Eq. (2.32) and Eq. (2.33) for  $\mathcal{M} = 0$ .

In the next section, we will use this fully general-relativity approach to study the effects of strong magnetic fields on hybrid stars by solving the Maxwell equations (Eqs. 2.30-2.31 with the new sources as given above) coupled to Einstein equations (Eqs. 2.24-2.27, together with the contribution due to the magnetization as given by Eqs. 3.26-3.30) in a self-consistent way taking into consideration the anisotropy of the energy-momentum tensor due to the magnetic field, magnetic field effects on equation of state and the interaction between matter and the magnetic field (magnetization). The equation of state for charge neutral chemically-equilibrated matter was calculated at zero temperature and over a wide interval of densities and magnetic fields with very small steps (around 100 different values of magnetic field ranging from  $10^{15}$  G to  $1 \times 10^{19}$  G). This 2-dimensional table was included in the Lorene C++ class library for numerical relativity (Bonazzola et al., 1993; Bocquet et al., 1995) in order for the code to find the correct magnetic field for each density in each direction of the star and, then, find the corresponding values for the system's thermodynamical properties.

### 3.3 Results

The equilibrium configurations are determined by the central enthalpy  $H_c$  and the choice of the magnetic dipole moment  $\mu$ . We could have, instead, chosen a fixed current function  $k_0$  and allow the magnetic dipole moment to vary. We chose the former in order to have a better control of the parameter space. In order to compare the effects of including or not magnetic field into the equation of state, we perform calculations considering sequences of constant magnetic moment  $\mu$  and increasing the central enthalpy (that can be translated into the baryon number density  $n_B^c$ ).

### 3.3.1 Global properties of magnetic neutron stars

Figure 3.2 displays the gravitational mass (in units of solar mass) as a function of the baryon number density (in units of  $\text{fm}^{-3}$ ) for a sequence of stars at different fixed magnetic dipole moments  $\mu$ . We show i) the case when the magnetic field is included only in the structure of the star (no EoS(B), no mag); ii) the effect of the magnetic field into the equation of state, but without the magnetization term (EoS(B), no mag) and iii) the effect of the magnetic field into the equation of state plus the magnetization term (EoS(B), mag) on the neutron stars structure. We also show the non-magnetized case denominated TOV.

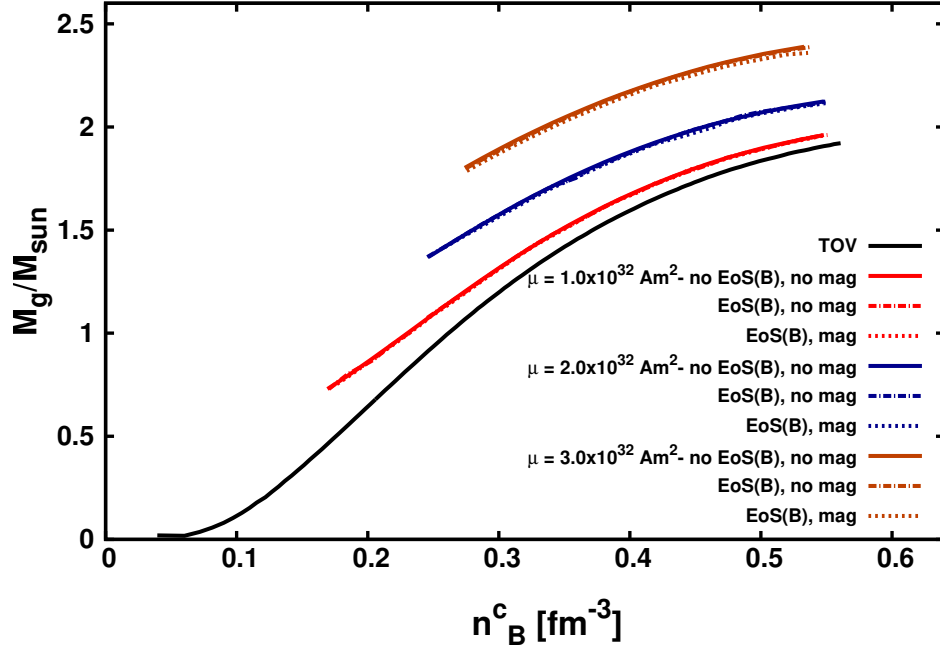


FIGURE 3.2: Relation between the gravitational mass and the central baryon number density for non-magnetized and magnetized models. In the last case, we also included the effects of the magnetic field into the equation of state (EoS(B)) and the magnetization term (mag).

According to Figure 3.2, a magnetic-field dependent equation of state does not affect considerably the mass of highly magnetized neutron stars through the effect on the equation of state for given magnetic fields when comparing stars with the same baryon number density. For example, the curves EoS(B) - mag and EoS(B) - no mag, almost overlap in all cases. In addition, when the magnetization term  $\mathcal{M}$  is considered, we see a difference in the curve for  $\mu = 3.0 \times 10^{32} \text{ Am}^2$ . This is due to the fact that the magnetization reduces the total pressure through, for example, the energy-momentum component  $T_{m1}^1 = P(\mathcal{E}, B) - \mathcal{M}B$ . As a consequence, the effect of the magnetization is to decrease the stellar masses.

From this point on, for consistency, we make use of the magnetic field dependence in the EoS and the inclusion of the magnetization term in all the results that will be shown. For example, the mass-radius diagram for highly magnetized neutron stars determined by a constant magnetic dipole moment  $\mu$  is presented in Figure 3.3. In this figure, we also show calculations for evolutionary sequences at fixed star baryonic mass of  $M_B = 2.20 M_\odot$  (gray line). We choose to fix the baryon mass instead the usual gravitational mass since this is the fixed quantity during the evolution of isolated neutron stars. In addition, we have chosen a fixed baryon mass of  $2.20 M_\odot$  because its evolution line ends almost at the maximum mass for the non-magnetized and spherical configuration. In this case, the

full purple circles represent a possible evolution from a highly magnetized neutron star (a younger star) to a non-magnetized and spherical one (an older star).

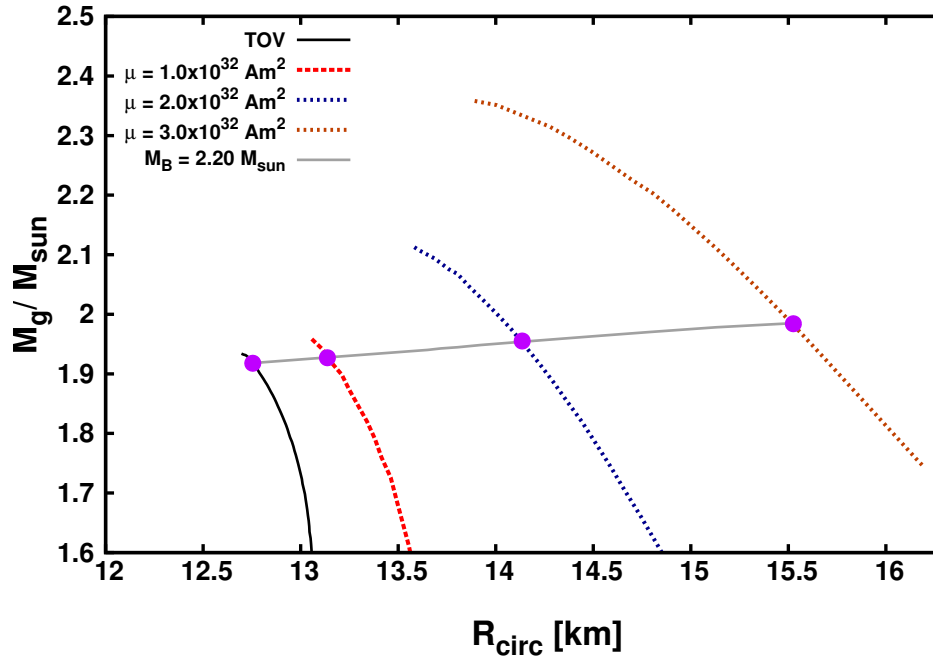


FIGURE 3.3: Mass-radius diagram for non-magnetized and magnetized models. The calculation was done for different fixed magnetic moments  $\mu$ . The higher the magnetic moment, the higher the magnetic field strengths throughout the star. Effects of the magnetic field into the equation of state and the magnetization are also included. The gray line shows an equilibrium sequence for a fixed baryon mass of  $2.2 M_{\odot}$ . The absolute values of GRV2 and GRV3 for the spherical star at  $M_B = 2.2 M_{\odot}$  are  $8.68 \times 10^{-6}$  and  $3.87 \times 10^{-6}$ , while with magnetic fields the typical values are  $\sim 10^{-4}$  for both GVR2 and GVR3.

Looking at different magnetic dipole moment lines in Fig. 3.2 and Fig. 3.3, i.e.,  $\mu = 1.0 \times 10^{32} \text{ Am}^2$ ,  $2.0 \times 10^{32} \text{ Am}^2$  and  $\mu = 3.0 \times 10^{32} \text{ Am}^2$ , one sees that increasing  $\mu$  (and therefore the magnetic field strengths throughout the star) affects the structure of the neutron star in many ways. First, the maximum mass increases. This is an effect of the Lorentz force acting outward and against gravity. For this reason, the star can support more mass. Second, the circular equatorial radius of the sequence increases and the star becomes much more deformed with respect to the symmetry axis. This deformation is also an effect of the assumption of a poloidal magnetic field, which makes the star more oblate. Calculations including toroidal magnetic field components have shown that magnetized stars become more prolate with respect to the non-magnetized case (Pili et al., 2014a; Frieben and Rezzolla, 2012b; Mastrano et al., 2015).

Now, we make use of the star with fixed stellar baryon  $M_B = 2.20 M_{\odot}$  in Fig. 3.3 to present microscopic and macroscopic properties as a function of the central magnetic field. First, as shown in Fig. 3.4, the central baryon number density decreases with the central magnetic field and it has the maximum value only in the static case. In the other cases, the central baryon number density reduces at the stellar center. This is due to the Lorentz force, which is related to the macroscopic currents that create the magnetic field, acting on the matter which has been pushed off-center. This is analogous to the number density reduction in the rotating star case. As we will see, this has a huge impact on the particle population of these objects. Second, the gravitational mass also increases induced by magnetic fields. This is because the gravitational mass as given by Eq. (2.43) is proportional to the sources of Einstein equations, i.e energy density, pressure, etc., which includes now the magnetic field contribution. Third, the magnetic dipole moment  $\mu$  increases with the central

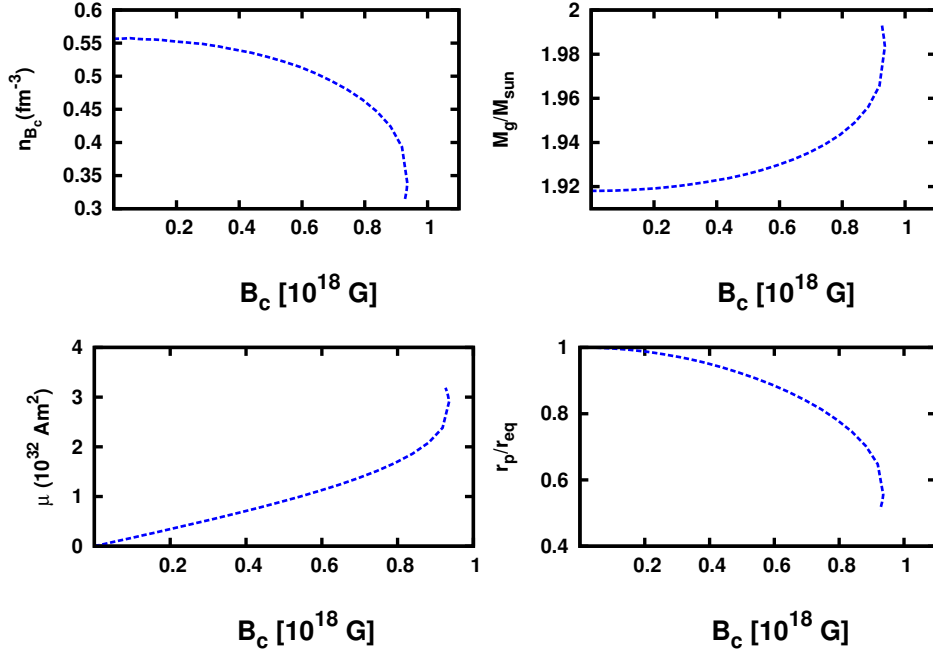


FIGURE 3.4: Microscopic and macroscopic star quantities, i.e central baryon number, gravitational mass, dipole magnetic moment and ratio between polar and equatorial coordinate radii, as a function of the central magnetic field. These curves represent an equilibrium sequence at fixed baryon mass  $M_B = 2.20 M_\odot$  for different magnetic field intensities. See the line for  $M_B = 2.20 M_\odot$  in Fig. 3.3).

magnetic field, as expected. Fourth, the ratio between the polar and the equatorial radii increases as the magnetic field increases and, therefore, the star becomes more deformed (oblate). For all quantities in Figure 3.4, the curves have a qualitative change in behaviour for a magnetic field strength of  $0.9 - 1.0 \times 10^{18}$  G. At this point, the magnetic force has pushed the matter off-center and a topological change to a doughnut-shaped density distribution (no matter at the stellar center) within the stellar interior can take place (Cardall et al., 2001). However, our current numerical tools do not enable us to handle toroidal configuration, which gives a limit for the magnetic field strength that we can obtain within this approach. As a consequence, the baryon number density, for example, will never reach zero at the center of the star. Still, the value of the magnetic field shown in Figure 3.4 represents the limit in terms of magnetic field strength for a star at fixed baryon mass of  $M_B = 2.20 M_\odot$ .

Note that in Figure 3.4, the ratio between the polar and the equatorial radii can reach 50% for a magnetic field strength of  $\sim 10^{18}$  G at the center. Therefore, one sees that the deviations from spherical symmetry are quite significant and need to be taken into consideration while modelling these highly magnetized objects and a simple TOV solution can not be applied.

### 3.3.2 Degrees of freedom in magnetic neutron stars

The changes in the global properties of stars due to the inclusion of the magnetic field into the gravitational equations are remarkable and, in order to study how the microphysics is modified with the magnetic field, we present in Figure 3.5 the particle population ( $Y_i = \rho_i/\rho_b$ , with  $\rho_i$  being the density of each particle and  $\rho_b$  the baryon density) as a function of the baryon chemical potential  $\mu_B$  for different values of the magnetic dipole moment  $\mu$  for a fixed baryon mass  $M_B = 2.20 M_\odot$ . The kinks in the population plot that can be observed for values equal to or greater than  $\mu =$

$2.0 \times 10^{32} \text{ Am}^2$  are due to the Landau quantization. See Fig. 3.4 for the magnetic field values that correspond to magnetic dipole moments shown in Figure 3.5.

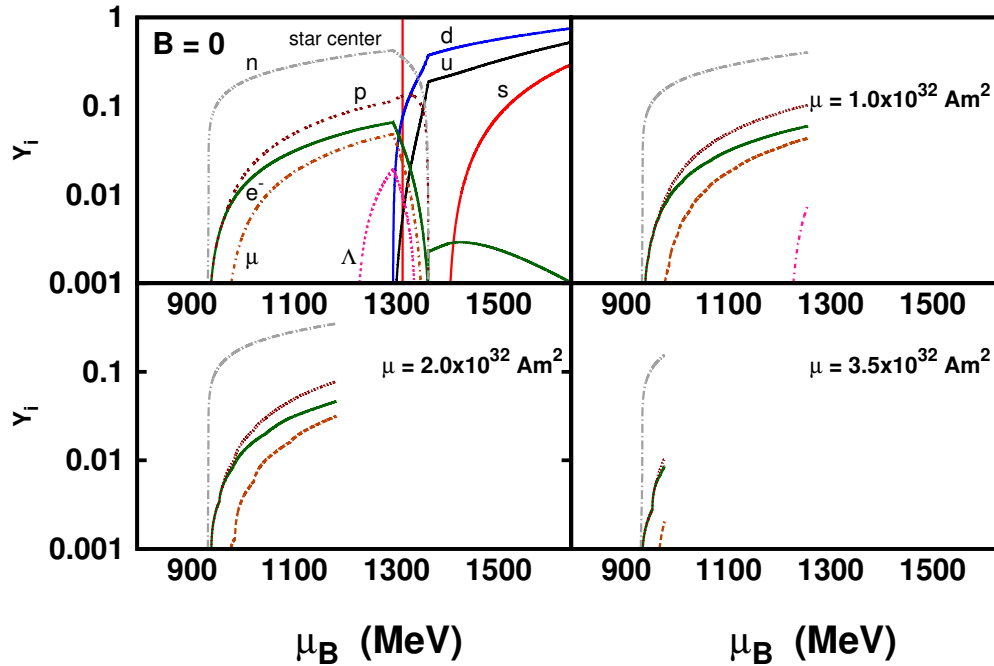


FIGURE 3.5: Stellar particle population as a function of the baryon chemical potential. All figures represent an equilibrium sequence at fixed baryon mass  $M_B = 2.20 M_\odot$ . As one increases the magnetic field, the particle population changes inside the star. These stars are represented in Fig. 3.3 by the full purple circles. For the non-magnetized case ( $B=0$ ), the vertical red curve represents the chemical potential reached at the center of the star, namely, 1320 MeV.

For the spherical non-magnetized case, the TOV solution was obtained for a hybrid star (with mixed phase) composed by the baryon octet, electrons, muons and  $u$ ,  $d$  quarks (no  $s$  quark). In Figure 3.5, the red vertical line represents the baryon chemical potential reached at the center of the maximum mass star in the non-magnetized case. With the inclusion of the magnetic field through the dipole magnetic moment of  $\mu = 1.0 \times 10^{32} \text{ Am}^2$ , the central baryon chemical potential is reduced due to the Lorentz force. The new central value for  $\mu_B$  is below the threshold for the creation of quarks, which are, therefore, suppressed. An even larger effect can be seen in the star for higher values of the magnetic dipole moments  $\mu = 2.0 \times 10^{32} \text{ Am}^2$ ,  $\mu = 3.5 \times 10^{32} \text{ Am}^2$ , when even the hyperons are suppressed. As a result, the properties of these objects such as neutrino emission and consequently the star cooling, are strongly affected by the magnetic field strength in their interior as already pointed out by [Dexheimer et al. \(2012a\)](#) for a spherical solution.

From Figure 3.5 it is evident that a quark and mixed phase are suppressed if a strong magnetic field is present in the interior of neutron stars. Therefore, according to our models, we do not expect to find exotic or quark matter in highly magnetized neutron stars, only protons, neutrons and leptons.

Figure 3.6 shows the magnetic field profile and the enthalpy iso-contours for a star with the maximum mass for a magnetic dipole moment of  $\mu = 3.5 \times 10^{32} \text{ Am}^2$ . This value roughly corresponds to the solution with maximum field configuration achieved with the code. In this case, other configurations different from Fig. 3.4, as depicted in Figure 3.6, can reach magnetic field values higher than  $1.0 \times 10^{18} \text{ G}$ .

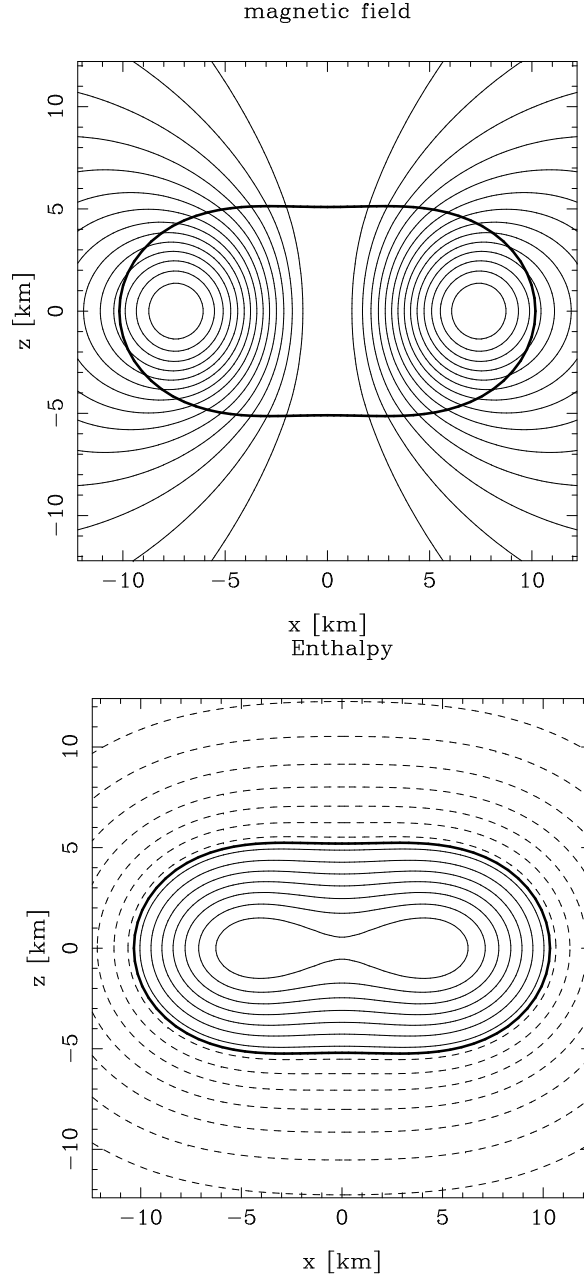


FIGURE 3.6: Magnetic field surfaces (on the top panel), i.e.  $A_\phi$  iso-contours measured by the Eulerian observer  $\mathcal{O}_0$  for the EoS described in the previous sections. This star is near the maximum equilibrium configuration achieved by the code and the maximum mass for the value  $\mu = 3.5 \times 10^{32} \text{ Am}^2$ , as shown in Figure 3.3. In the bottom panel, the corresponding enthalpy profile is shown, which corresponds to a central enthalpy of  $H_c = 0.26 c^2$  ( $n = 0.463 \text{ fm}^{-3}$ ). The gravitational mass obtained for the star is  $2.46 M_\odot$  and the polar and the central magnetic fields are  $8.59 \times 10^{17} \text{ G}$  and  $1.62 \times 10^{18} \text{ G}$ , respectively. The ratio between the magnetic pressure and the matter pressure in the center for this star is 0.793.

It is instructive to discuss the poloidal magnetic field geometry considered here to describe magnetized neutron stars. It was already outlined in Chapter 1 that the poloidal field geometry is intuitive, but it is not the most general case. Unlike the external field geometry, the internal magnetic field configuration cannot be constrained by direct observations. In addition, it has been suggested that differential rotation in newborn neutron stars could create a strong toroidal magnetic component. The effect of purely toroidal fields on the structure of neutron stars were studied in (Kiuchi et al.,

2009; Friebe and Rezzolla, 2012a). Numerical simulations of purely poloidal or purely toroidal geometries have found them to be unstable (Braithwaite, 2006; Lander and Jones, 2012). Among mixed-field configurations, the twisted-torus geometry was found to be the most promising candidate for a stable magnetic field configuration (Yoshida et al., 2006; Glampedakis et al., 2012; Ciolfi et al., 2009; Pili et al., 2014b). All these models consider a poloidal-dominated geometry, with toroidal-to-poloidal energy ratio restricted to less than 10%. Recently, Ciolfi and Rezzolla (2013) succeeded in producing toroidal dominated twisted-torus configurations, but their stability in nonlinear simulations needs still to be established. It has been found that while purely poloidal magnetic fields deform a neutron star shape and matter distribution to an oblate shape (equatorial radius larger than polar radius), purely toroidal fields deform them to a prolate shape. Thus, for magnetized stars with a purely toroidal geometry, different combinations of the surface deformation are possible depending on the relative strength of the field. As a consequence, the matter distribution of the star can vary with the magnetic field geometry in a very complicated way. But, this is beyond the scope of this work and we leave the general case for future study.

Finally, based on the results presented in this chapter, we recently reported a realistic calculation of the magnetic field profile for the microscopic description of matter inside strongly magnetized neutron stars (Dexheimer et al., 2016). Unlike previous estimates, which are widely used in the literature, we found that magnetic fields increase relatively slowly with increasing baryon chemical potential (or baryon density) of magnetized matter. More precisely, the increase is polynomial instead of exponential, as previously assumed. Through the analysis of several different realistic models for the microscopic description of matter in the star (including hadronic, hybrid and quark models) combined with general relativistic solutions endowed with a poloidal magnetic field obtained by solving Einstein-Maxwell's field equations in a self-consistent way, we generated a phenomenological fit for the magnetic field profile to be used as input in microscopic calculations.





## Chapter 4

# Magnetic field effects in proto-neutron stars

*This chapter contains the results of numerical calculations of magnetized and rotating proto-neutron stars (PNS) within the framework of General Relativity. We applied a hadronic chiral  $SU(3)$  model (already described in Chapter 3 for cold and magnetized neutron stars) to proto-neutron stars with trapped neutrinos and at fixed entropy per baryon. In the case of PNS's, as the neutrino chemical potential decreases in value over time, this alters the chemical equilibrium and the composition inside stars, leading to a change in the structure and in the particle population of these objects. We will see how the magnetic field alters the number of trapped neutrinos in the stellar interior, together with strangeness content and temperature in each evolution stage.*

### 4.1 Stellar interior

When a supernova explodes, it leaves a hot, lepton-rich and rapidly rotating remnant: a proto-neutron star. [Burrows and Lattimer \(1986a\)](#) and [Pons et al. \(1999\)](#) showed that in a time scale of 10-20 seconds, PNS's cool significantly and lose their high lepton content mainly through electron neutrino ( $\nu$ ) emission. As we will see, PNS's are very hot stars with temperature up to 50 MeV in the center. The environment in these stars is so extreme, that neutrinos can be trapped on dynamical time scales and develop a finite chemical potential ([Prakash et al., 1997](#)). In addition, it has been shown that rotation can play an important role in the description of these objects ([Goussard et al., 1997, 1998](#)).

Although the initial evolution of PNS's from hot,  $\nu$ -trapped and lepton-rich to cold and  $\nu$ -free NS's is far from equilibrium and characterized by strong instabilities, just a few seconds after the bounce, they can be approximately considered as a sequence of equilibrium configurations. This is the so-called Kelvin-Helmholtz phase ([Pons et al., 1999](#); [Fischer et al., 2010](#)). During this process, the structure of the PNS can be divided into a core region, that we will study in this chapter, and an envelope with entropy per baryon much higher than in the core. In the core, the entropy per baryon can reach values of  $s_B \simeq 1, 2$ . A fixed entropy per baryon allows to model a temperature increase towards the center of the star. These properties make PNS's quite different objects from the ordinary cold neutron stars as we saw in Chapter 3. It is worth to mention that the explosion of core-collapse supernovae is a still poorly understood mechanism. However, as NS's are born from PNS's, one expects that some features currently presented in neutron stars as, for example, magnetic fields and rotation rates, are related to their progenitors.

We saw in Chapter 1 and Chapter 3 that certain classes of neutron stars possess very strong magnetic fields on their surfaces on the order of  $10^{12-15}$  G (Shapiro and Teukolsky, 2008; L., 1964), but the origin of such high magnetic fields are still under debate. Many authors (Akiyama et al., 2003; Obergaulinger et al., 2009; Sawai et al., 2013; Sawai and Yamada, 2016; Cerdá-Durán et al., 2008; Mösta et al., 2015) showed that magnetorotational instabilities (MRI) in proto-neutron stars can amplify small seed magnetic fields over very short time scales. However, the limit of this amplification is still unknown. Recently, Rembiasz et al. (2016) showed that the amplification factor seems to be small and, therefore, the magnetic field cannot be amplified through MRI channel modes. In addition, Rembiasz et al. (2016) suggested that another physical process, a MRI-driven turbulent dynamo, could further amplify small seed magnetic fields in PNS's.

Our study here focus mainly on the effects of magnetic fields in PNS's, not on the origin of the field itself. With this in mind, we will investigate the response of the structure of PNS's, as well the number of trapped neutrinos and particle composition to a given magnetic field in the stellar interior. Pons et al. (2001b) addressed the importance of quarks in the evolution process of PNS's. The appearance of quarks softens the equation of state and may lead to less massive and smaller stars (Lattimer and Prakash, 2001). In addition, quarks would alter the neutrino emissivities and, therefore, influence other properties like the surface temperature in PNS's and NS's. In a future work, we hope also to investigate the role played by phase transitions from quark to hadronic matter inside the stars, but here, we neglect possible effects of a quark phase. This is a good approximation since we have shown in Chapter 3 that quarks are suppressed by strong magnetic fields. However, in the hadronic version of the model as described in Chapter 3, hyperons are included as the "exotic matter" component that can, potentially, soften the equation of state. Note that there is no reason to ignore the appearance of hyperons, as they should appear at about two times saturation density, and their presence might produce distinct neutrinos signals that can be detected in the next generation neutrino detectors (Diwan and Jung, 2000).

In order to simulate proto-neutron star conditions, trapped neutrinos are included by fixing the lepton fraction  $Y_L = \sum_i Q_i n_i / n_B$ , with the lepton number  $Q_i$  being non-zero only for leptons (Burrows and Lattimer, 1986b; Keil and Janka, 1995; Gudmundsson and Buchler, 1980). The entropy per baryon  $s_B = S/A = s/n_B$  is also fixed in the core of the star (Burrows and Lattimer, 1986b; Pons et al., 2001b, 1999; Stein and Wheeler, 2006). For the first approximate stage of a PNS evolution, we choose  $s_B = 2$ ,  $Y_L = 0.4$ . For the second stage, the star has cool down through neutrino emission and has reached beta  $\beta$ -equilibrium. This state is represented by  $s_B = 1$ . The last and final stage, a cold NS in beta equilibrium, is simply represent by  $T = 0$ .

The temperature is not expected to be constant in the interior of compact stars. Sophisticated approaches have realistic profiles for temperature (Reddy et al., 1998b; Pons et al., 2001a), but, in this thesis, we do not attempt to make use of them since the aim is only to investigate magnetic field effects on different approximate stages of the star evolution. For this reason, as an approximation, we are going to consider different values of fixed entropy per baryon throughout the star. In Fig. 4.1, it is shown the three equations of state used to describe both a cold neutron star ( $T=0$  and  $\beta$ -equilibrium) and two different approximate stages of evolution of PNS's ( $s_B = 1$ ,  $\beta$ -equilibrium and  $s_B = 2$ ,  $Y_L = 0.4$ ).

## 4.2 General Relativistic Calculation

In order to model stationary and axi-symmetric neutron and proto-neutron stars in presence of strong poloidal magnetic fields, we solve the coupled Einstein-Maxwell field equations by using the equations of state shown in Fig. 4.1. As it was already shown by Goussard et al. (1997), the equation of motion

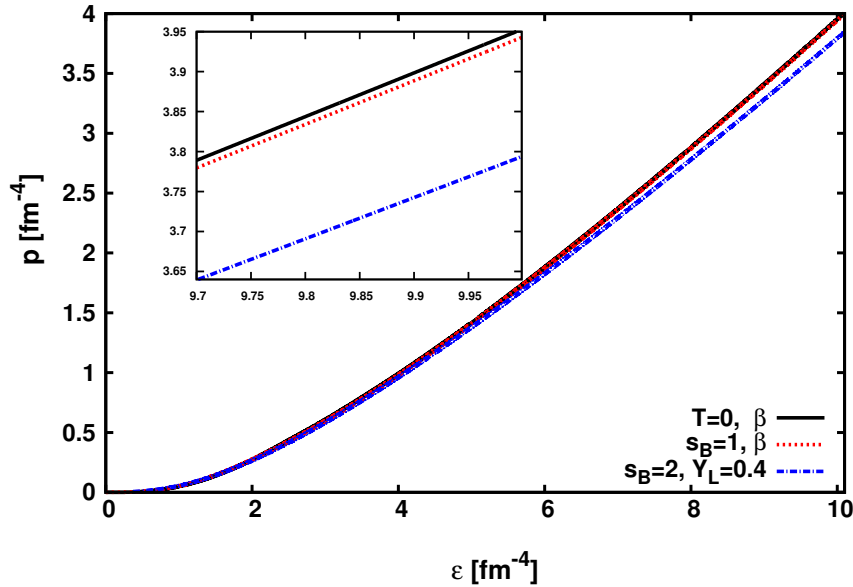


FIGURE 4.1: Equations of state for proto-neutron and neutron stars. Note that the  $T = 0$  and  $s_B = 1$  in  $\beta$ -equilibrium lines almost overlap.

Eq. (2.15) remains the same when describing proto-neutron stars at fixed entropies per baryon  $s_B$ . In this case, there is no entropy gradient throughout the star, i.e.,  $\partial_i s_B = 0$ , where  $i$  stands for the spatial coordinates  $(r, \theta)$ . Consequently, the additional term  $Te^{-H}\partial_i s_B$  present in the equation of motion (Eq.4 in Goussard et al. (1997)) for hot stars disappears and the standard numerical procedure (as described in Chapter 2) can be used both for cold and hot stars. Finally, let us note that the special case with  $T = \text{const}$  is not realistic, since one expects higher temperatures at higher densities in stars.

As we are interested in studying how the internal properties of isolated proto-neutron stars change over time, we have fixed the stellar baryonic mass to  $M_B = 2.35 M_\odot$ . This value represents a star whose gravitational mass is close to the maximum mass allowed by TOV solutions of neutron and proto-neutron stars described within the EoS's in Fig. 4.1. At a fixed baryon mass, we can then compare how strangeness (through the presence of hyperons) and neutrinos are distributed inside the star along its temporal evolution.

The magnetic equilibrium configurations are determined by the choice of the current function  $k_0$ . In table 4.1, we show the corresponding central baryon number density and the central magnetic field reached in stars for a given  $k_0$ . Increasing the value of  $k_0$  arbitrarily, we will find a point where the magnetic force will push the matter off-center so strongly that a topological change to a toroidal configuration takes place (Cardall et al., 2001). As our current numerical tools do not enable us to solve such equilibrium configurations (our input is the stellar central enthalpy is finite and cannot be zero, as it would be the case for toroidal shape solutions), there is a limit for the magnetic field strength that one can obtain within this approach. We obtain a maximum current function close to  $k_0 = 39000$ , which corresponds to a central magnetic field  $\sim 10^{18}$  G in all three approximate stages of star evolution.

Throughout this chapter, we make use of equations of state that contain hyperon degrees of freedom. Hyperons contain one or more strange quarks as their internal constituents. This enables us to study how strangeness is distributed inside stars. For example, in Fig. 4.2, we depict the strangeness density,  $n_s$ , which is defined as the sum over the amount of strangeness of each baryon species multiplied by

TABLE 4.1: Relation between the current function  $k_0$ , central baryon number density  $n_B^c$ , central  $B_c$  and surface magnetic field  $B_s$ , and gravitational mass  $M_g$  for a star at fixed baryon mass  $M_B = 2.35 M_\odot$ . We considered three different approximate evolution states from a hot proto-neutron star to a cold neutron star. We have also added the absolute values of the GRV2 and GRV3 (numerical errors) for all solutions.

EOs	$k_0$	$n_B^c(\text{fm}^{-3})$	$B_c(10^{18}\text{G})$	$B_s(10^{18}\text{G})$	$M_g(M_\odot)$	GRV2	GRV3
T=0	0	0.694	0	0	2.03	$3.88 \times 10^{-6}$	$5.24 \times 10^{-6}$
	35000	0.509	1.01	0.36	2.07	$9.63 \times 10^{-6}$	$9.78 \times 10^{-6}$
	39000	0.424	1.07	0.46	2.09	$1.01 \times 10^{-5}$	$1.23 \times 10^{-5}$
$s_B = 1$ $\beta$	0	0.721	0	0	2.04	$6.81 \times 10^{-4}$	$9.03 \times 10^{-4}$
	35000	0.514	1.02	0.34	2.08	$8.54 \times 10^{-4}$	$9.68 \times 10^{-4}$
	39000	0.402	1.06	0.45	2.11	$9.01 \times 10^{-4}$	$9.82 \times 10^{-4}$
$s_B = 2$ $Y_L = 0.4$	0	0.790	0	0	2.01	$4.80 \times 10^{-4}$	$1.30 \times 10^{-4}$
	35000	0.575	1.04	0.37	2.04	$4.73 \times 10^{-4}$	$1.42 \times 10^{-4}$
	39000	0.474	1.10	0.47	2.06	$5.01 \times 10^{-4}$	$1.57 \times 10^{-4}$

its number density, as a function of the stellar coordinate radius  $r$  for several  $k_0$  values. The panel on the top corresponds to a cold neutron star, T=0 in  $\beta$ -equilibrium. In the middle and in the bottom panels in Fig. 4.2, we depict the strangeness density profile as a function of the coordinate radius for proto-neutron star matter in two situations: hot with  $s_B = 1$  and in  $\beta$ -equilibrium and at very high entropy per baryon  $s_B = 2$  with trapped neutrinos  $Y_L = 0.4$ , always assuming a fixed star baryon mass  $M_B = 2.35 M_\odot$ . In this figure, the vertical lines represent the stellar surface (coordinate radius) for non-magnetized stars. We have chosen to show all quantities as function of the coordinate radius, since there is no appropriate definition for the circular coordinate radius in the polar direction.

Hyperons are supposed to appear inside cold, beta-equilibrated, neutrino-free stellar matter at a density of about 2 times nuclear saturation density. According to the upper panel in Fig. 4.2, the magnetic field changes significantly the amount of strange matter in neutron stars. In particular, strangeness disappears completely for a central magnetic field strength of  $\sim 10^{18}$  G (see table 4.1). The Lorentz force acts outwards and reduces the stellar central baryon density, so that its value is below the threshold for the creation of hyperons, which are, therefore, suppressed inside the star.

In Fig. 4.2, we show the strangeness density profile in equatorial ( $\theta = \pi/2$ ) and polar directions ( $\theta = 0$ ). For spherical stars, the amount of strangeness is the same in all directions. However, since the magnetic field breaks the spherical symmetry, magnetized stars will be deformed with respect to the symmetry axis. In this case, they will become oblate objects with polar radius ( $\theta = 0$ ) smaller and equatorial radius ( $\theta = \pi/2$ ) which will be larger than in the case without magnetic fields. As a result, strangeness will be asymmetrically distributed throughout the star. For higher values of the magnetic field, the strangeness density can be considered almost constant for a large range of radii, see e.g. the middle panel in Fig. 4.2 for a central field of  $\sim 10^{18}$  G ( $k_0 = 39000$ ) and  $\theta = \pi/2$ . Note that the corresponding surface magnetic field obtained for the models in Fig. 4.2 are higher than the observed ones in the surface of neutron stars. Nevertheless, according to the Virial theorem the magnetic field reached at the center (where strangeness will appear) of neutron stars is expected to be so high as the magnetic field values found here.

The study of strangeness distribution inside NS or PNS are motivated also by the change of the neutron star cooling rates in presence of hyperons (Prakash et al., 1992; Pethick, 1992; Chatterjee and Vidaa, 2016). Since the strangeness is directly related to the amount of hyperons and the

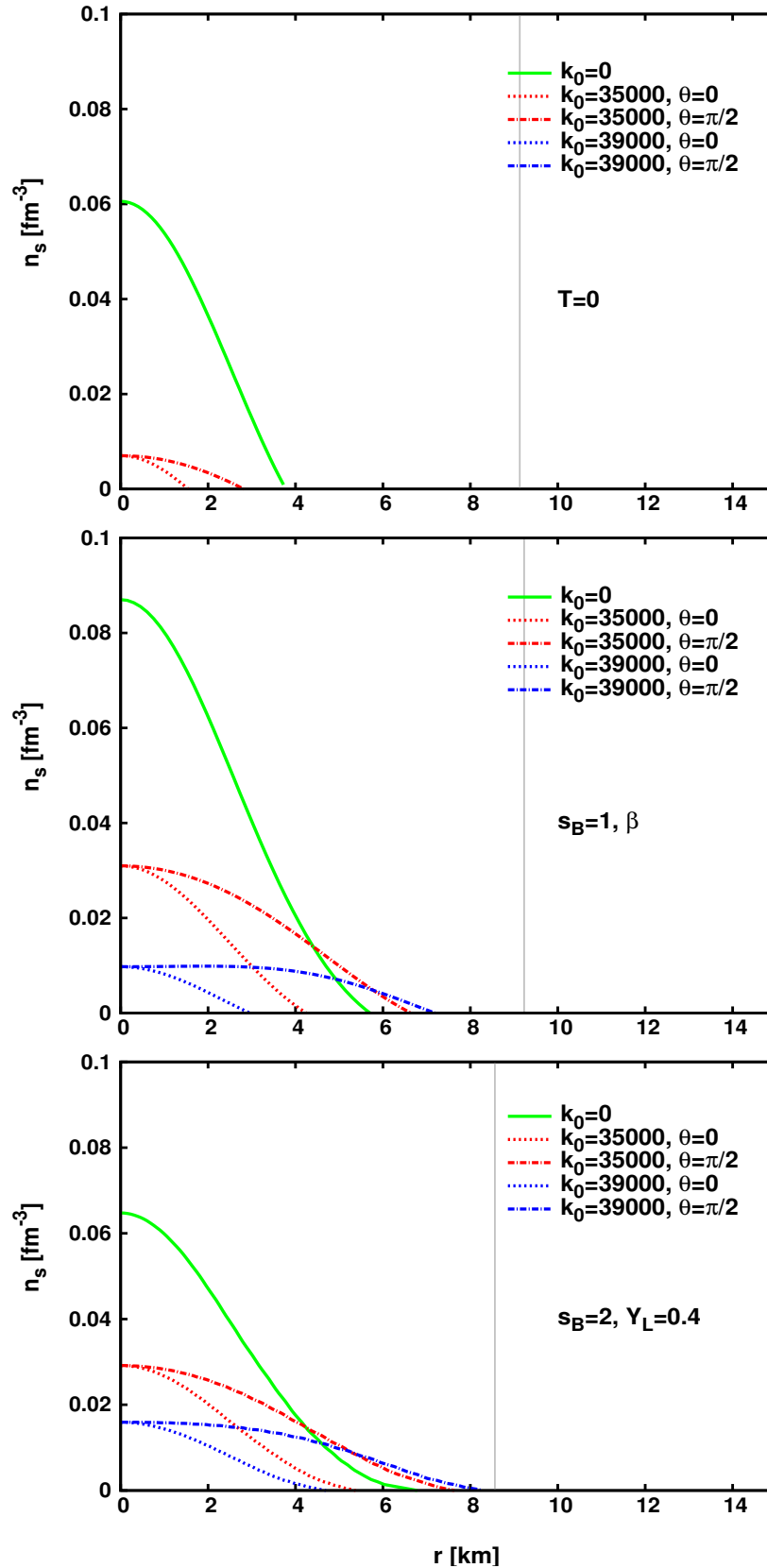


FIGURE 4.2: Strangeness density profile on equatorial ( $\theta = \pi/2$ ) and polar coordinate radii ( $\theta = 0$ ) for one neutron star,  $T=0$  in  $\beta$ -equilibrium, one PNS with fixed entropy per baryon  $s_B = 1$  in  $\beta$ -equilibrium and one PNS star with  $s_B = 2$  and fixed lepton fraction  $Y_L = 0.4$ . All stars have the same fixed baryon mass  $M_B = 2.35 M_\odot$  (see Table 4.1 for the corresponding gravitational masses). Different  $k_0$ 's correspond to different current functions and characterize different magnetic field strength profiles. For the largest  $k_0$  values, the cold star has no strangeness.

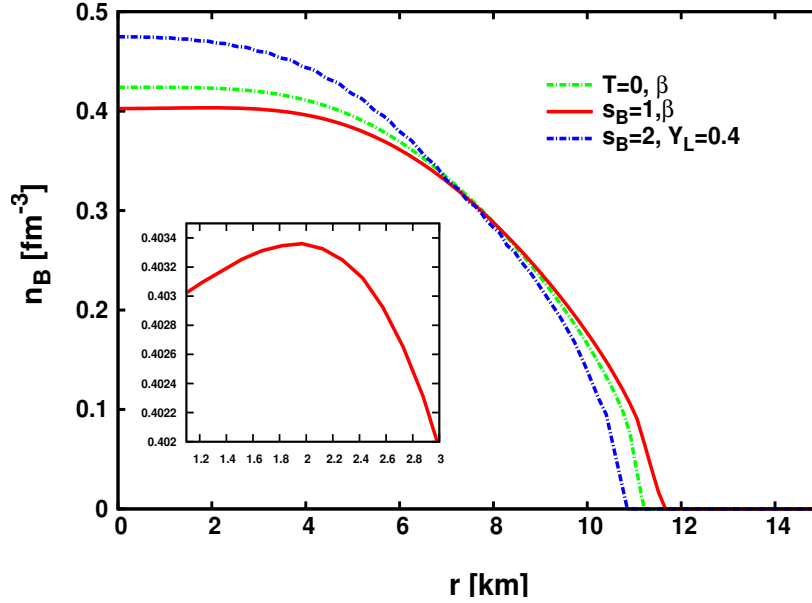


FIGURE 4.3: Baryon number density profile in the equatorial plane ( $\theta = \pi/2$ ) for the most magnetized stars studied at fixed baryon mass of  $M_B = 2.35 M_\odot$  (see Table 4.1 for more details), assuming 3 different approximate stages of evolution:  $T=0$  and  $\beta$ -equilibrium;  $s_B = 1$  and  $\beta$ -equilibrium and  $s_B = 2$  with  $Y_L = 0.4$ . In all cases, the current function is  $k_0 = 39000$ .

corresponding channels for neutrino emission, it will affect the cooling behaviour of the star due to the magnetically induced deformation of the star.

As stated by Cardall et al. (2001); Franzon and Schramm (2015), the Lorentz force can reverse its direction in the equatorial plane in magnetized stars. The Lorentz force is obtained from the derivative of the magnetic potential  $M(r, \theta)$ , which has a minimum at some radius inside the star (see Fig. 6.3 in Chapter 6). This means that the Lorentz force will change its sign and, therefore, act differently in different parts of the star. In addition, if we suppose that the magnetic field decays over time during the magnetic field evolution in proto-neutron stars, we see from Fig. 4.2 that for  $s_B = 1$  and  $\beta$ -equilibrium and  $s_B = 2$  with  $Y_L = 0.4$  that the amount of strangeness becomes higher in the inner core of the star, but it is reduced in the outer layers (crossing lines) for a decreasing  $k_0$ . This behaviour is not seen for cold neutron stars, where the strangeness increases in all directions as the magnetic field decays (see upper plot Fig. 4.2).

Note that for the most magnetized stars studied here (see larger  $k_0$  in table 4.1), the maximum density can be reached away from the stellar center. To illustrate this, in Fig. 4.3 we show the baryon number density profile in the equatorial plane for a star with  $M_B = 2.35 M_\odot$  assuming the 3 different approximate evolution states: 1)  $T=0$  and  $\beta$ -equilibrium; 2)  $s_B = 1$  and  $\beta$ -equilibrium and 3)  $s_B = 2$  with  $Y_L = 0.4$ . In the second case, the maximum baryon number density is not at the stellar center. The other cases do not present this behaviour. This is because stars with lower densities in the inner core become easily more deformed due magnetic fields. As one can see from Fig. 4.3, the maximum baryon number density is shifted away from the center (for the second case), however, this tiny effect is not enough to change the particle population inside stars. Nevertheless, a more comprehensive study of the subject would be very desirable by using the formalism from Cardall et al. (2001).

Neutrinos are mainly produced by electron capture as the progenitor star collapses. However, most of them are temporarily prevented from escaping because their mean free paths are considerably smaller than the radius of the star. This is the well-known trapped-neutrino era, where the entropy

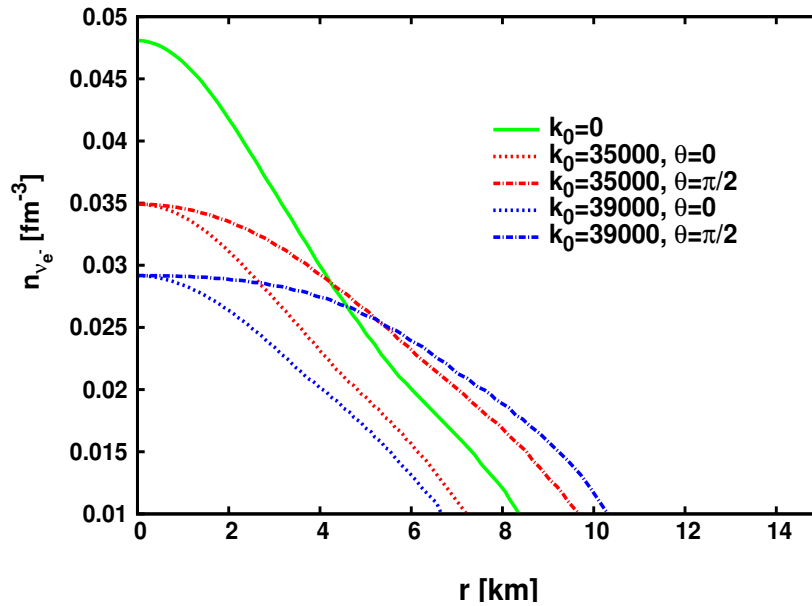


FIGURE 4.4: Electron neutrino density profile as a function of the equatorial and polar coordinate radii for one proto-neutron star with  $M_B = 2.35 M_\odot$  (see Table 4.1 for the corresponding gravitational masses) assuming  $s_B = 2$  and  $Y_L = 0.4$ .

per baryon is about 1-2 through most of the star and the total number of leptons per baryon has a typical value of  $Y_L \simeq 0.4$ . It is worth to mention that the amount of neutrinos, on the other hand, depends on the EOS used (Tan et al., 2016).

In Fig. 4.4, we show the electron neutrino number density profile as a function of the coordinate radius for a star at fixed baryon mass of  $M_B = 2.35 M_\odot$ . This same star is depicted in the bottom plot in Fig. 4.2. The magnetic field reduces the amount of neutrinos present at the center of the star. For example, for the free magnetic field solution, the maximum electron neutrino density is  $\sim 0.048 \text{ fm}^{-3}$  at the center of the star. In the maximally magnetized case, this value is reduced to  $\sim 0.030 \text{ fm}^{-3}$ . Note that according to Fig. 4.4, the amount of trapped neutrinos decreases as the magnetic field significantly drops for coordinate radii  $\gtrsim 5 \text{ km}$  (in the equatorial plane,  $\theta = \pi/2$ ). However, the opposite effect is seen for radii  $\lesssim 5 \text{ km}$ . In addition, since the stars are deformed due to the magnetic field, the neutrino flux leaving the PNS's will be asymmetric, having different values in the polar and equatorial directions. These differences may have an observable impact on the neutrino flux from magnetized PNS's.

In Figs. 4.5 and 4.6, we show the temperature throughout a PNS for two approximate stages that reproduce temporal evolution stages. In Fig. 4.6, the expected initial star (just after the bounce) is lepton rich and extremely hot. For a non-magnetized and spherical star, the temperature at the center reaches values close to 50 MeV. On the other hand, when the strong magnetic field is included, the central temperature reaches values below 40 MeV. This same effect is observed (with lower values) for a hot and  $\beta$ -equilibrated PNS model. In Fig. 4.5, the difference in the central temperature between the non-magnetized and the highest magnetized solution is of the order of 2 MeV, much less than in the neutrino  $\nu$  trapped era. This is related to the stiffness of the equation of state. According to our model, the equation of state describing the first approximate stage of evolution is softer than in the other stages.

According to Prakash et al. (2001); Reddy et al. (1998a); Pons et al. (2001a); Prakash et al. (2001), larger lepton fraction  $Y_L$  disfavours hyperonic degree of freedom in the stellar interior. As a result,

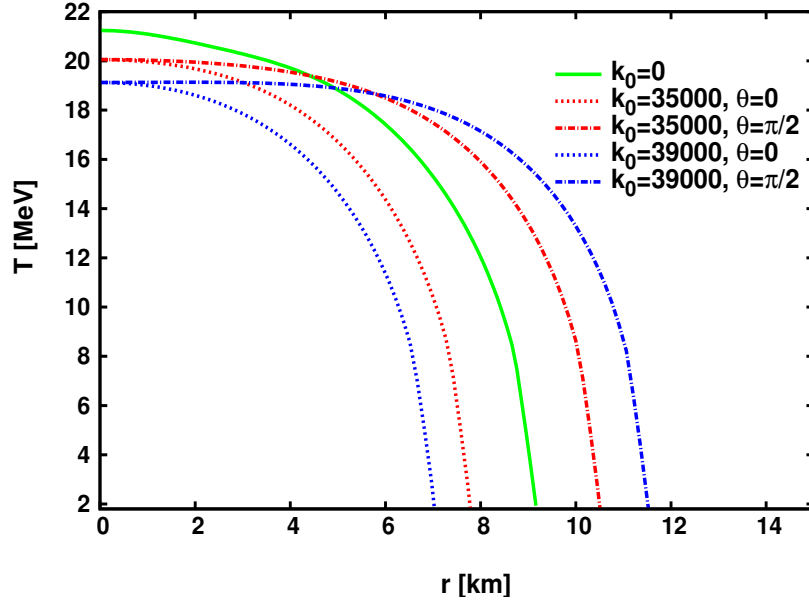


FIGURE 4.5: Temperature profile as a function of the equatorial and polar coordinate radii for one proto-neutron star with  $M_B = 2.35 M_\odot$  (see Table 4.1 for the corresponding gravitational masses) assuming  $s_B = 1$  and  $\beta$ -equilibrium.

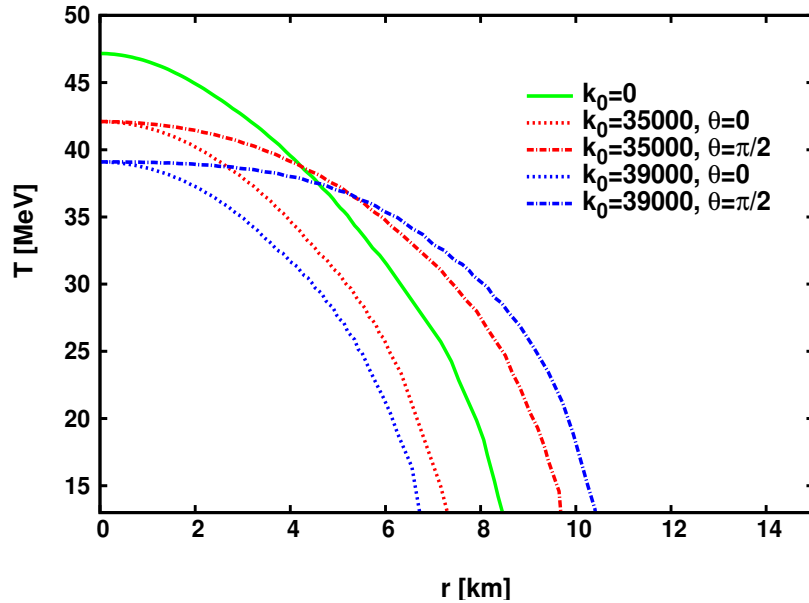


FIGURE 4.6: Same as in Fig. 4.5 but for one proto-neutron star with  $s_B = 2$  and  $Y_L = 0.4$  (see Table 4.1 for the corresponding gravitational masses).

the respective EOS's becomes stiffer. This can be seen in [Prakash et al. \(2001\)](#), where a lot of hyperons were present in a  $\beta$ -equilibrated matter. In our approach, the couplings do not favor a large amount of hyperons in  $\beta$ -equilibrated matter. In this case, the main effect of fixing  $Y_L$  is to make the star more isospin symmetric and, as a consequence of a softer EOS, less massive.

For a PNS with  $s_B = 2$  and  $Y_L = 0.4$ , the surface temperature of the core is  $\sim 13$  MeV while for  $s_B = 1$  and  $\beta$ -equilibrium it is  $\sim 2$  MeV. However, in both cases, with the decay of the magnetic field, the temperature increases in the inner layers of the star and decreases in the outer layers. Note



that the same effect was observed for the strangeness density and neutrino distribution inside the star.

The presence of strong magnetic fields affects the star surface thermal distribution (Aguilera et al., 2008). The knowledge of the correct temperature distribution in PNS's and NS's is crucial for modelling the cooling of these stars. Thus, models that include the presence of high magnetic fields should be reconsidered, not only to investigate the effects of the anisotropy of the energy-momentum tensor due to the magnetic field, but also to include the asymmetric temperature distribution in these objects.

To close this chapter, we will investigate the contribution of rotation to the breaking of the spherical symmetry. In the cases studied here, we have seen that the magnetic field does not only affect the macroscopic structure of stars, but also it impacts their microscopic composition. Such a study is extremely important if one wants to understand the thermal evolution of stellar systems where spherical symmetry is broken.

Although PNS's are probably strongly differentially<sup>1</sup> rotating (Baumgarte et al., 1999; Morrison et al., 2004; Ansorg et al., 2009), we model uniformly rotating stars in order to estimate the effect of rotation on strongly magnetized stellar models within a fully general relativity calculation. The effect of the centrifugal force due to rotation in neutron stars was considered already by many authors (Cook et al., 1994; Nozawa et al., 1998; Salgado et al., 1994; Negreiros et al., 2010; Komatsu et al., 1989; Weber et al., 1991). However, only few works presented self-consistent calculations taking into account both magnetic field and rotation effects on the neutron star structure (Bocquet et al., 1995; Pili et al., 2014b; Frieben and Rezzolla, 2012a). Here, we contribute to this discussion by including the temperature effects on a rotating and magnetized lepton rich PNS described by the EoS with  $s_B = 2$  and trapped neutrinos  $Y_L = 0.4$ .

In the same spirit as we already showed in Fig. 3.5 in Chapter 3, in Fig. 4.7 we depict the internal composition of proto-neutron stars in 3 scenarios: A) a non-rotating and non-magnetized proto-neutron star at fixed baryon mass of  $M_B = 2.35 M_\odot$ ; B) the same star as in A), but rotating at a frequency of 900 Hz. This frequency is used since the star becomes strongly deformed and it allows us to better study the effects of rotation on the microscopic properties of proto-neutron stars. The results of this analysis can be generalized to other frequencies. Finally, we include the magnetic field in the solution B). In this case, one obtains a rotating and magnetized proto-neutron star model denoted by C) for the maximum value of the magnetic field achieved with the code. In this star, the maximum central magnetic field is  $3.76 \times 10^{17}$  G. Note that this maximum magnetic field lies below the value obtained for non-rotating proto-neutron stars  $\sim 10^{18}$  G for the same baryon mass. In Fig. 4.7, the particles on the left hand side of the dashed black lines A), B) and C) represent the populated degrees of freedom inside the corresponding PNS's.

The centrifugal force due to rotation pushes the matter outwards. As a consequence, the star expands in the equatorial direction and decreases the central number density. For example, in the case A) the baryon density at the center is  $0.790 \text{ fm}^{-3}$ . But if this star rotates at 900 Hz (case B), one obtains a central density of  $0.541 \text{ fm}^{-3}$ . And, finally, the corresponding rotating and magnetized star C) yields a central baryon number density of  $0.497 \text{ fm}^{-3}$ . For stronger magnetic fields such an effect is further increased. From Fig. 4.7, we see that the amount of electron neutrinos is not reduced in rotating PNS's. On the other hand, exotic particles are almost suppressed inside these objects. They might vanish completely in stars rotating faster than the case considered here. Moreover, the magnetic field (in case C) further reduces the central number density and, therefore, further modifies the internal degrees of freedoms.

<sup>1</sup>Differential rotation is seen when different parts of a rotating object move with different angular velocities at different latitudes and/or depths of the body and/or in time. This indicates that the object is not solid.

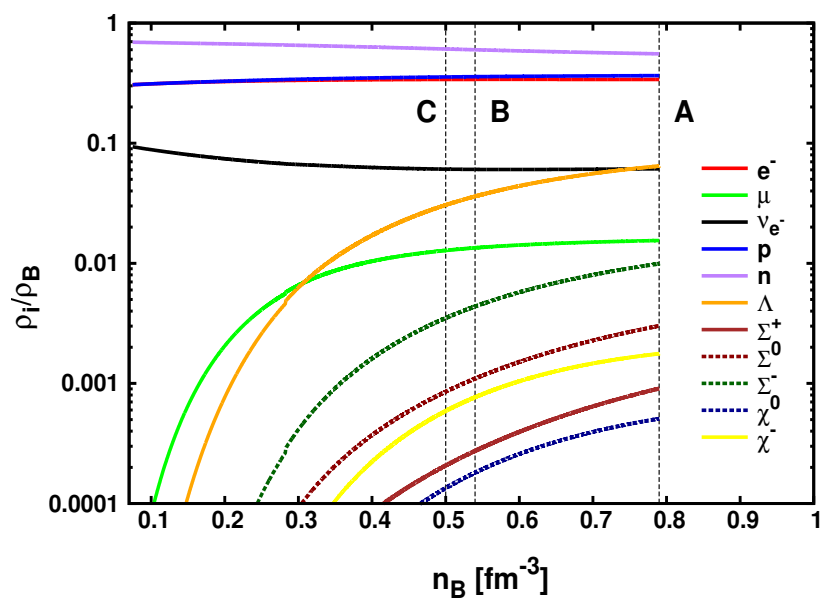


FIGURE 4.7: Particle population obtained for one proto-neutron star in 3 different cases: A) non-rotating and non-magnetized; B) rotating at a frequency of 900 Hz and non-magnetized (the corresponding gravitational mass is  $M_g = 2.04 M_\odot$ ) and C) rotating and magnetized (the corresponding gravitational mass is  $M_g = 2.05 M_\odot$ ). In all cases, the baryonic mass is fixed at  $M_B = 2.35 M_\odot$  assuming  $s_B = 2$  and  $Y_L = 0.4$ .

## Chapter 5

# Strong phase transition in magnetized neutron stars

*In this chapter, we study the effects of a strong quark-hadron phase transition in magnetized neutron stars. Previous calculations have shown that fast rotating neutron stars, when subjected to a quark-hadron phase transition in their interiors, could give rise to the backbending phenomenon characterized by a spin-up era. First, we reproduce the results as already obtained by many authors in the case of fast spinning neutron stars (Zdunik et al., 2006; Chubarian et al., 2000; Cheng et al., 2002; Heiselberg and Hjorth-Jensen, 1998; Zdunik et al., 2004; Glendenning et al., 1997). Then, we include magnetic field effects into the problem and study the consequences.*

### 5.1 Motivation

Glendenning et al. (1997) proposed a method for finding the dependence of a specific EoS on the behavior of neutron stars observables, such as the spin frequency and the frequency derivative. They showed that phase transitions inside neutron stars can be accessed through the backbending phenomenon, where stars spin up over time as a consequence of a phase change in their cores. However, the exact mechanism responsible for the spin-down of stars is still unclear. The most accepted idea is that these stars spin down because of magnetic torques, losing energy through magnetic dipole radiation (MDR). In this way, rotating magnetized stars behave as oblique rotators (Pacini, 1967, 1968; Gold, 1975). In addition to the dipole radiation, processes such as emission of gravitational radiation and pulsar wind can also contribute to the braking index of neutron stars (Ostriker and Gunn, 1969; Ferrari and Ruffini, 1969; Blandford and Romani, 1988; Manchester et al., 1985). In all cases, the star energy loss can be described by a power law:

$$\frac{dE}{dt} = -C\Omega^{n+1}, \quad (5.1)$$

with  $C$  being a term that accounts for the pulsar structure,  $E$  the kinetic energy,  $\Omega$  the pulsar angular velocity and  $n$  the braking index (see Eq. 5.3). In this way, this equation describes the dependence of the braking torque on the rotation frequency.

According to the MDR theory, a rigid star with a constant dipole magnetic field and a constant moment of inertia has the canonical braking index of  $n = 3$  (see Eq. 5.5). However, in the presence of rotation, the moment of inertia is not constant in time and, therefore, one has to consider the

dependence  $I(\Omega)$ . In this case, the star responds to changes due to the centrifugal force becoming oblate. This effect reduces the value of the braking index from the standard oblique rotator model to a value of  $n < 3$  (Hamil et al., 2015). Furthermore, the microphysics impacts strongly the braking index, which can have values in the range of  $-\infty < n < \infty$  in presence of a first-order phase transition (Glendenning et al., 1997; Chubarian et al., 2000).

In case of a phase transition, its duration epoch is governed by a slower loss of the star angular momentum due to radiation. This can be seen in the behaviour of the  $I(\Omega)$  curves in the next sections. In addition, the phase change in the stellar interior can introduce not only a spin-up era, but also an increase in the magnetic field throughout the star.

## 5.2 Equation of state with quark-hadron phase transition

The transition from confined to deconfined matter inside neutron stars has been extensively studied over the last years and, in many cases, also applied to study properties of hybrid stars (Bombaci et al., 2007, 2009; Yasutake et al., 2011; Dexheimer et al., 2012b; Lenzi and Lugones, 2012; Ayvazyan et al., 2013; Brillante and Mishustin, 2014; Alvarez-Castillo and Blaschke, 2015; Dexheimer et al., 2015; Franzon et al., 2015; de Carvalho et al., 2015). Despite this progress, at the present moment, there are still substantial uncertainties in the equation of state regarding the description of the stellar matter at supra-nuclear densities.

In this chapter, we make use of an equation of state with quark-hadron phase transition to describe the stellar interior. The hadronic phase, composed of nucleons (together with leptons), is described in the framework of a relativistic mean-field theory and takes into account many-body forces contributions in the baryon couplings. For the quark phase, the MIT bag model with vector interaction was used. In addition, we describe here the deconfinement phase transition by using the usual Maxwell construction (not Gibbs, like in the model presented in Chapter 3) in order to reproduce a sharp phase transition, since we are interested in maximum effects due to the phase transition. The equation of state is depicted in Fig. 5.1 and it is described in details by Gomes et al. (2015a).

Both hadronic (H) and quark (Q) phases are charge neutral and the conditions of chemical equilibrium determine the position or the transition density. This transition is described by a regime of constant pressure, which leads to a discontinuity in the energy density and in the baryon number density,

$$P_H = P_Q \quad \text{and} \quad \mu_n^H = \mu_n^Q, \quad (5.2)$$

which is known as the Maxwell criteria. For the parametrizations used in this work, the phase transition occurs at  $\mu_B = 1101.30$  MeV, which corresponds to a transition pressure of  $P_0 = 0.16$  fm<sup>-4</sup> and an energy gap of  $\Delta\varepsilon = 0.52$  fm<sup>-4</sup>.

The issue of whether the phase transition takes place in a Maxwell or a Gibbs scenario (energy density changes in the phase transition) depends on the surface tension between the two phases. The comparison of both scenarios in the investigation of hybrid stars has been studied in several works, see e.g. Bhattacharyya et al. (2010); Hempel et al. (2009); Yasutake and Kashiwa (2009); Yasutake et al. (2011); Alaverdyan et al. (2010). Furthermore, the threshold values of the surface tension necessary to describe each type of transition scenario have been calculated by Lugones et al. (2013) and Garcia and Pinto (2013). However, such estimations are highly model dependent, and the issue of possible phase transition scenarios remains an open question. Finally, we could have used other equations of state with quark-hadron phase transition, and it could be that other EoS's show stronger quantitatively effects. However, we do not expect that the results will change qualitatively by the use of other equations of state.

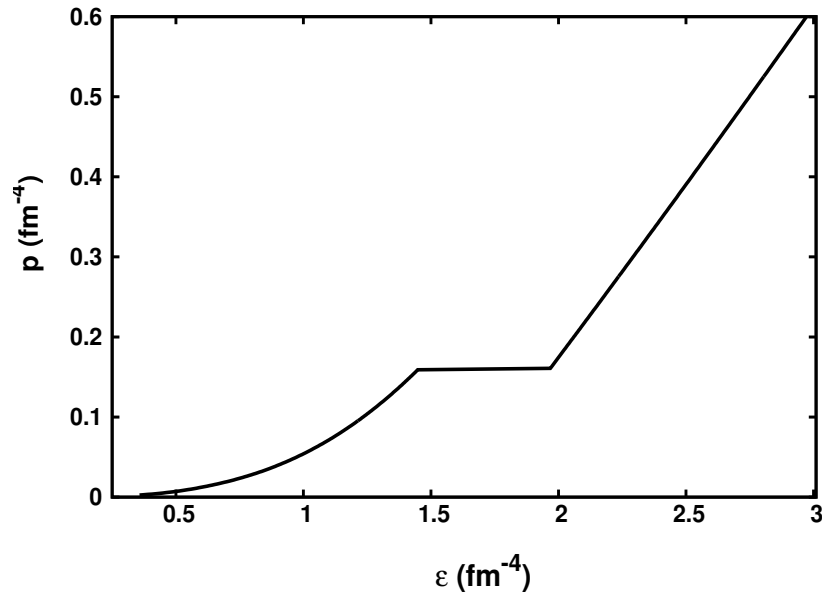


FIGURE 5.1: EOS for neutron star matter including a deconfinement phase transition for the parametrization  $\zeta = 0.040$  of the MBF formalism. The bag constant is  $B = 160 \text{ MeV}^4$  and the vector coupling  $(g_V/m_V)^2 = 2.2 \text{ fm}^2$ .

### 5.3 Rotating neutron stars

Aside from magnetic fields, rotation is a crucial observable in stellar astrophysics. Rapidly rotating general relativistic stars were already described by Komatsu et al. (1989); Cook et al. (1992); Stergioulas and Friedman (1994). In this section, we calculate stationary equilibrium configurations of uniformly rotating cold neutron stars within the general relativity framework as already discussed in the previous chapters.

We assume that the internal composition of rotating neutron stars is described by the equation of state as depicted in Fig. 5.1. The dependence of the internal structure of the NS with rotation is crucial, since the centrifugal force due to the rotation will help to stabilize the star against collapse and the star will be deformed, i.e., compressed in the polar direction and enlarged in the equatorial direction. With this in mind, different rotation frequencies produce different relations between the mass and the radius for rapidly rotating stars as shown by Friedman and Ipser (1992); Spyrou and Stergioulas (2002); Zdunik et al. (2008); Haensel et al. (2009); Zdunik et al. (2004).

Effects of rotation on the backbending phenomenon in neutron stars were considered before by Zdunik et al. (2006); Chubarian et al. (2000); Cheng et al. (2002); Heiselberg and Hjorth-Jensen (1998). As the stars spin down due to the loss of angular momentum, the central density increases and a phase transition to pure quark matter might occur (Cheng et al., 2002; Glendenning et al., 1997). In order to investigate if the equation of state in Fig. 5.1 produces similar mass-radius diagrams as in Zdunik et al. (2006), we show in Fig. 5.2 the baryonic mass as a function of the circular equatorial radius for neutron stars with frequencies ranging from 0 to 1200 Hz. Similar mass-radius diagrams  $M_B(R_{\text{eq}})$  were also obtained by Zdunik et al. (2004). In their case, it was shown that equations of state with hyperon degrees of freedom can also produce the backbending phenomenon. Here, we have neglected additional exotic phases with hyperons in order to investigate exclusively the effects of a quark-hadron phase transition.

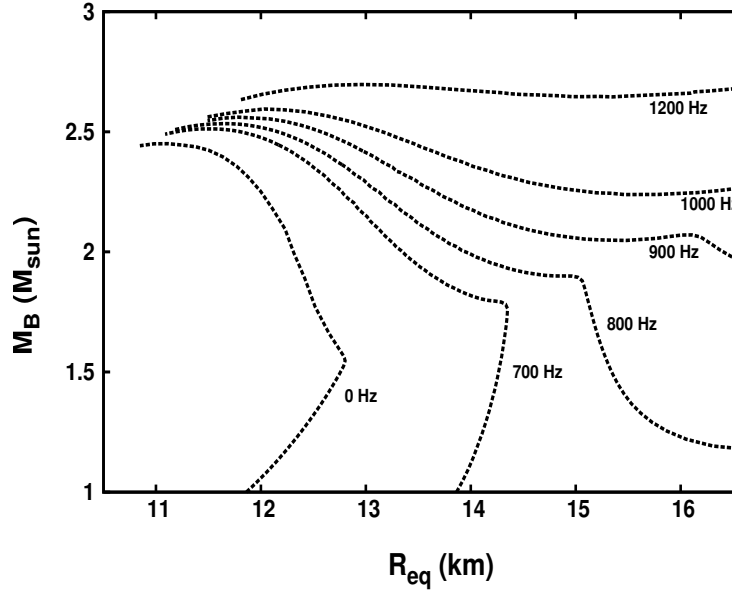


FIGURE 5.2: Baryon mass versus equatorial radius for neutron stars at different fixed rotation frequencies. These configurations were calculated using the EoS presented in Fig. 5.1.

According to Fig. 5.2, the mass-radius curves present inflexion points (with a minimum in the baryon mass  $M_B$ ) for frequencies between  $\sim 900$  Hz and  $\sim 1200$  Hz. This defines a region (at fixed baryon masses) where the backbending phenomenon may appear in the stars. Conclusions along this line were already studied by [Zdunik et al. \(2006\)](#). The diagram in Fig. 5.2 shows that, as the frequency increases, both the baryon mass and the radius of the stars increase, which is a direct effect of the centrifugal forces due to rotation. We choose to show in Fig. 5.2 the baryon mass instead the usual gravitational mass since this is the fixed quantity during the evolution of isolated neutron stars, as it was already discussed in the context of PNS evolution in Chapter 4.

In Fig. 5.3, we present the moment of inertia as a function of the rotational frequency  $f$  for two different stars at fixed baryon masses of  $M_B = 1.90 M_\odot$  and  $M_B = 2.15 M_\odot$ . Both the moment of inertia  $I$  and the angular velocity  $\Omega$  are decreasing functions of time. According to the Figure 5.3, for the star with  $M_B = 1.90 M_\odot$ , there is a reduction in the spin-down rate when this star undergoes a phase transition. This effect is more pronounced in the case of  $M_B = 2.15 M_\odot$ , in which the quark-hadron phase transition induces a spin-up era in the star's evolution. During this time, the star will lose energy due to dipole radiation but, still, it will spin faster. This same effect was already reported by [Glendenning et al. \(1997\)](#) and [Weber et al. \(1997\)](#).

The braking index  $n$  is defined through the relation ([Gao et al., 2015](#)):

$$n = \frac{\Omega \ddot{\Omega}}{\dot{\Omega}^2}, \quad (5.3)$$

in other words, the braking index of a star can be obtained directly from the frequency  $\Omega$  of the pulsar and its time derivatives,  $\dot{\Omega}$  and  $\ddot{\Omega}$ . The rotating energy loss (Eq. 5.1) due to the emission of radiation can be represented by the equation:

$$\frac{dE}{dt} = \frac{d}{dt} \left( \frac{1}{2} I \Omega^2 \right) = -C \Omega^{n+1}. \quad (5.4)$$

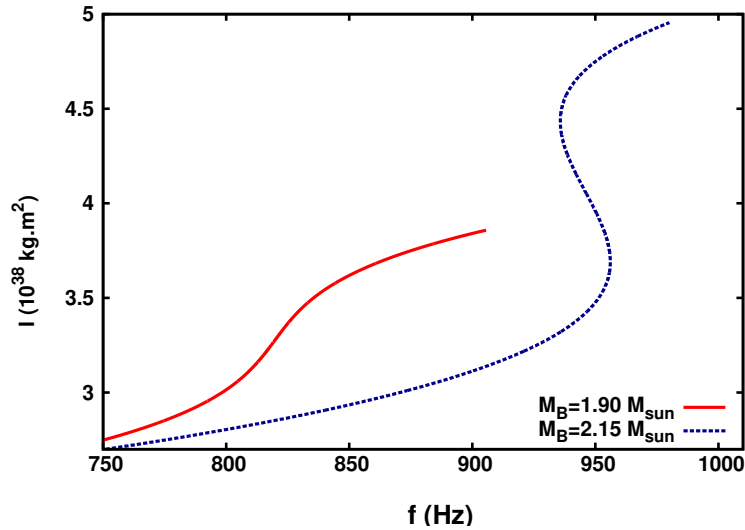


FIGURE 5.3: Relation between the moment of inertia and the frequency for rotating neutron stars at different fixed baryon masses,  $1.90 M_{\odot}$  and  $2.15 M_{\odot}$ .

From equation Eq. (5.4), one can rewrite Eq. (5.3) in the form:

$$n(\Omega) = 3 - \frac{3I'\Omega + I''\Omega^2}{2I + I'\Omega}, \quad (5.5)$$

with  $I'$  and  $I''$  being the first and the second derivatives of the angular momentum with respect to the angular velocity  $\Omega$ ,  $\frac{dI}{d\Omega}$  and  $\frac{d^2I}{d\Omega^2}$ , respectively. As a result, the braking index is now written in a frequency-dependent manner,  $n(\Omega)$ .

If one ignores the changes in the moment of inertia during the spin-down evolution, it can be seen from Eq. (5.5) that a purely dipole radiation yields a braking index of 3. However, few measurements of braking indices of isolated neutron stars are available in the literature (Gao et al., 2015; Hamil et al., 2015), and in all cases, one has  $n < 3$ . In order to determine accurately the braking index  $n$ , high precision measurements of the angular velocity  $\Omega$  and their corresponding time derivatives  $\dot{\Omega}$  - which show how stars are slowing down - are necessary. For this reason, braking index observations are much easier for young pulsars, not only because they spin very fast, but also because the braking is not affected by low timing noise or glitches (sudden increase in the rotational frequency of a rotation-powered pulsar). In addition, for older pulsars, the measurements of  $\dot{\Omega}$  and  $\ddot{\Omega}$  might require many years and yield very small values.

In order to evaluate the braking index in presence of a quark-hadron phase transition, we make use of the rotating configurations already shown in Fig. 5.3. The results are depicted in Fig. 5.4. In this case, the braking index does not deviate from 3 for slow rotation. However, as the frequency increases, it can reach values far from 3. In addition, when the phase transition is reached in the core of the star, there is an anomalous behaviour in the braking index curve  $n(\Omega)$ , whose extreme case is seen for the higher mass case  $M_B = 2.15 M_{\odot}$ , where the braking index reaches values from  $-\infty$  to  $+\infty$ .

From this point on, we will focus on the effects of a quark-hadron phase transition on highly magnetized neutron stars. Bear in mind that, in contrast to rotation-powered pulsars, the strongly magnetized neutron stars rotate slowly ( $P \sim 10$  s, as we showed in the  $P - \dot{P}$  diagram in Chapter 1) and, therefore, are powered by their magnetic fields.

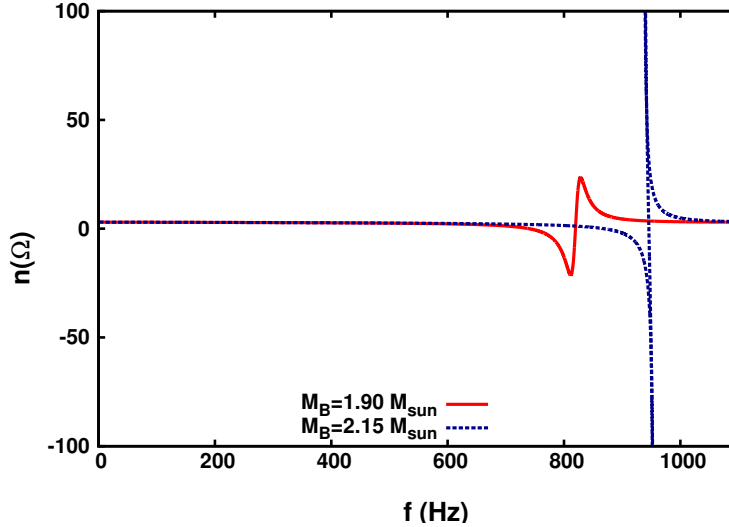


FIGURE 5.4: Braking index as a function of the frequency for rotating neutron stars. The curves correspond to the same stars as shown in Fig. 5.3.

## 5.4 Magnetized neutron stars

In this section, we will discuss the effects of strong magnetic fields on the global properties of neutron stars, which are subjected to a sharp quark-hadron phase transition in their interior. Stationary and axi-symmetric stellar models are constructed with the same numerical procedure and mathematical set-up as in Chapter 2.

In Chapter 2, we saw that the magnetic field is generated by the azimuthal component the electromagnetic current 4-vector  $j^\mu$ :

$$j^\phi = \Omega j^t + (\mathcal{E} + P)k_0, \quad (5.6)$$

with  $j^t$  being the time component of the electric current,  $\Omega$  the stellar angular velocity,  $\mathcal{E}$  the energy density and  $P$  the isotropic contribution to the pressure. The magnetic stellar models are obtained by assuming a constant current functions  $k_0$  and a constant magnetic dipole moment  $\mu$ . Although other choices for  $k_0$  do not alter the conclusions qualitatively, we stress that a more comprehensive study of the field changes and the corresponding variation of current distributions would be very desirable. Such an analysis, however, requires much more insight into the microscopics of the currents in the different hadronic and quark phases and is beyond the scope of this chapter, where just an initial discussion of possible observable effects of field decay in highly magnetized stars is addressed.

We show in Fig. 5.5 the mass-radius diagram for stars at different fixed magnetic dipole moments  $\mu$  and different current functions  $k_0$ . From Fig. 5.5, the masses and the radii increase by increasing the magnetic dipole moment that reaches  $\mu = 3 \times 10^{32} \text{ Am}^2$  and the current function that reaches  $k_0 = 40000$ . A star with  $M_B = 2.15 M_\odot$  would be represented by a horizontal line in Fig. 5.5, in such a way that it does not reach the largest value of  $\mu$ , in other words, it corresponds to a set of evolutionary sequences with smaller magnetic dipole moments.

The existence of the backbending phenomenon in fast rotating neutron stars is determined by the combination of three quantities: the baryon mass  $M_B$ , the total angular momentum  $J$  and the rotational frequency  $f$ . Minimum values of  $M_B$  at fixed  $f$  with a monotonic behaviour of  $M_B$  versus  $J$  leads to the backbending phenomenon (Zdunik et al., 2006, 2004). In parallel to this, we conclude that the backbending in highly magnetized neutron stars depends also on three quantities: the baryon



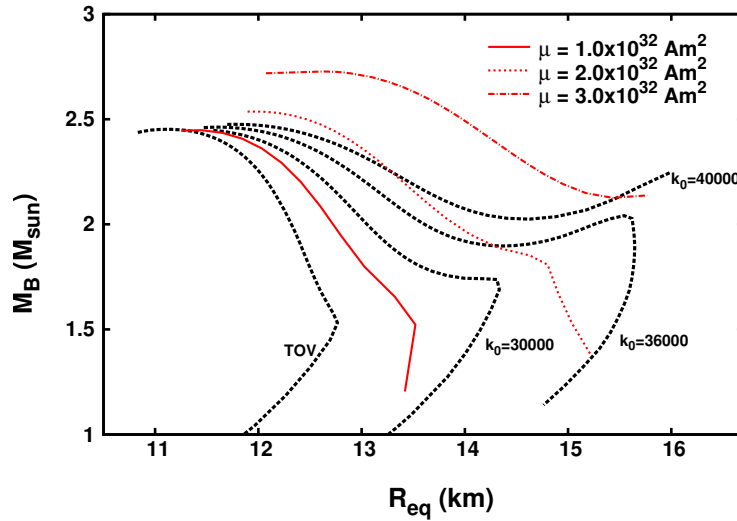


FIGURE 5.5: Mass-radius diagram for magnetized models. The calculations were done for different fixed current functions  $k_0$  and different fixed magnetic dipole moments  $\mu$ .

mass  $M_B$ , the magnetic dipole moment  $\mu$  and the current function  $k_0$ . In this case, the magnetic dipole loss leads to a quark-hadron phase transition inside the stars, followed by an increase in the electric current (and, therefore, the magnetic field) through Eq. (5.6), which it is related to the change of the type of matter in the star with a different equation of state. In contrast, rotating stars at fixed baryon masses have their frequency increased by angular momentum loss during the backbending epoch.

As we already discussed for the case of rotation (but without magnetic field in Fig. 5.3), the moment of inertia changes drastically from a constant value in the case of a more realistic treatment. In addition, a slower reduction of the moment of inertia, which is followed by a spin-up of the star, is observed when the equation of state that describes the matter inside these objects includes a strong quark-hadron phase transition. We show the effect of magnetic fields on the moment of inertia  $I$  for highly magnetized stars in Fig. 5.6 and Fig. 5.7. We present  $I$  as a function of the central and surface star magnetic fields,  $B_c$  and  $B_s$ , respectively. These calculations are done for stars with the same fixed baryon masses as the ones presented in Fig. 5.3.

From Fig. 5.6, one can see that the higher the central magnetic field, the higher the moment of inertia of the stars. This effect is due to the Lorentz force which allow stars to support more mass. In addition, the circular equatorial radius of the sequence increases, as can be seen in the mass-radius diagram in Fig. 5.5 for higher current functions or magnetic dipole moments. According to Fig. 5.6, the maximum central magnetic field reached in stars depends strongly on the stellar mass. For example, a star with  $M_B = 1.90 M_\odot$  has a maximum central magnetic field of  $\sim 7.0 \times 10^{17}$  G, whereas the star with  $M_B = 2.15 M_\odot$  can have a central magnetic field up to  $1.0 \times 10^{18}$  G.

By assuming that the magnetic field decays over time, and fixing the baryon mass, each curve depicted in Fig. 5.6 represents the time evolution of the stellar magnetic field and moment of inertia of a different star. In other words, younger stars decrease in size and as the magnetic field decays, the central density increases. During this time, these stars might change from a hadronic to a quark phase in the core. In particular, the increase of the central magnetic field as shown in Fig. 5.6 may represent a signature of a phase transition inside these objects. However, internal magnetic fields cannot be directly constrained by observation. For this reason, we present in Fig. 5.7 the same star

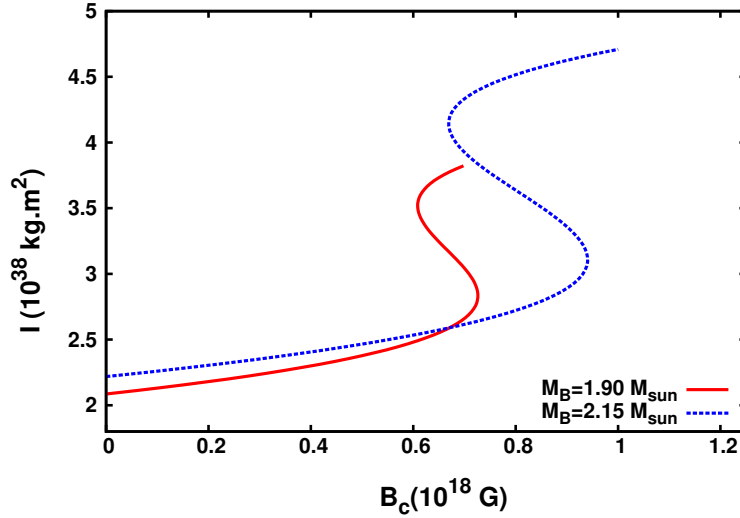


FIGURE 5.6: Relation between the moment of inertia and central magnetic field for magnetized neutron stars with different fixed baryon masses,  $1.90 M_{\odot}$  and  $2.15 M_{\odot}$ , respectively.

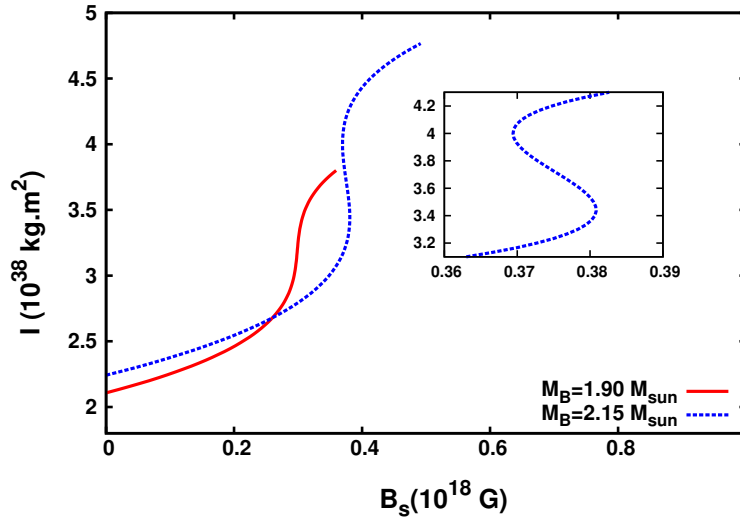


FIGURE 5.7: Same as in Fig. 5.6 but as a function of the surface magnetic field.

configurations as shown in Fig. 5.6, but as a function of the (polar) surface magnetic field, which can potentially be observed.

Looking at the star with fixed baryon mass of  $1.90 M_{\odot}$  in Fig. 5.7, one sees that the moment of inertia, which decreases in time, has a slower reduction when the star passes through the phase transition. However, for the star with baryon mass of  $2.15 M_{\odot}$ , the surface magnetic field in fact increases due to the phase transition. In this case, the moment of inertia as a function of  $B_s$  exhibits a small “magnetic-up era”, whereas this same effect is much more evident when the central magnetic field  $B_c$  is considered.

According to Fig. 5.6, during the “magnetic-up era”, a  $M_B = 2.15 M_{\odot}$  star has increased the value of its central magnetic field by an amount of  $0.23 \times 10^{18}$  G, while the surface magnetic field varies from  $0.37 \times 10^{18}$  G to  $0.38 \times 10^{18}$  G (see Fig. 5.7). For a star with  $M_B = 1.90 M_{\odot}$ , the central magnetic

field increases by an amount of  $0.1 \times 10^{18}$  G, while the surface magnetic field always decreases. Such effects might be associated with giant flares presented in magnetars (Mallick and Sahu, 2014).

## 5.5 Gravitational wave emission from neutron stars

We will use now the model described in the previous sections to make a simple estimate of the gravitational wave (GW) strength in highly magnetized neutron stars. The deformation of magnetized neutron stars can be quantified by their quadrupole moment  $Q$  with respect to the rotational axis. According to Bonazzola and Gourgoulhon (1996), the gravitational wave amplitude  $h_0$  emitted by a perpendicular rotator is given by:

$$h_0 = \frac{6G}{c^4} \frac{\Omega^2}{D} Q, \quad (5.7)$$

with  $G$  being the gravitational constant,  $c$  the speed of light,  $D$  the distance of the star and  $\Omega$  its rotational velocity.

Assuming that a star with  $M_B = 2.15 M_\odot$  rotates at a frequency of  $f = \Omega/2\pi = 1$  Hz at a distance  $D = 10$  kpc (typical distance of observed magnetars), we show in Fig. 5.8 the GW emission amplitude for different central magnetic fields. As already depicted in the relation between the moment of inertia  $I$  and the magnetic field (see Fig. 5.6), one sees that the GW amplitude  $h_0$  can change significantly as the magnetic field decays over time showing a backbending behaviour as the star undergoes a quark-hadron phase transition. According to Fig. 5.8, the star may have a period of faster reduction in the gravitation waves emission before the magnetic field reduces to lower values.

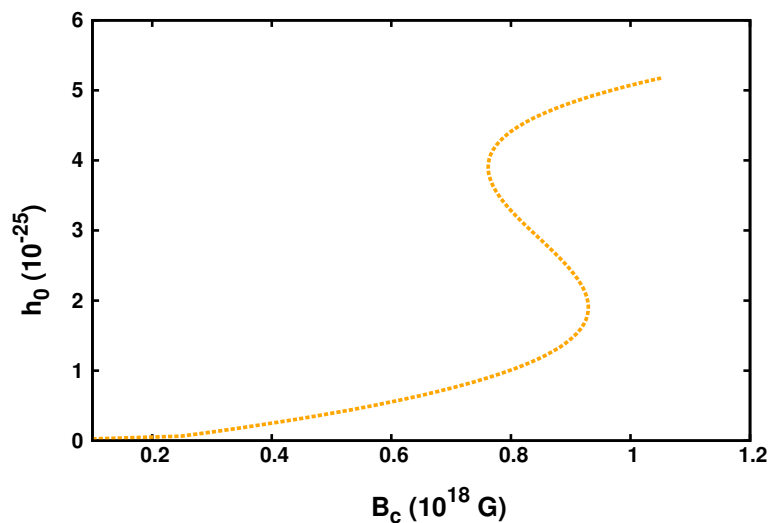


FIGURE 5.8: Gravitational wave amplitude as a function of the central magnetic field for a star with  $M_B = 2.15 M_\odot$ .

In the models considered here, the rotation and magnetic axes are aligned. In this case, even stars strongly deformed do not emit gravitational radiation. However, an estimate of the strength of gravitational wave emission can be deduced if we assume that the magnetic axis and the rotation axis are not aligned, as it seems to be the case, for example, in observed pulsars. This is a good approximation as long as rotational and magnetic field effects do not start to compete in deforming the star. For strong magnetic fields and as long as the rotation frequency is small, this assumption should hold true.



## Chapter 6

# Effects of strong magnetic fields and rotation on white dwarf structure

*In this final chapter, as a spin-off of our studies, we compute models for white dwarfs in the presence of strong magnetic fields and rotation. We obtain models of super-Chandrasekhar magnetized white dwarfs assuming white dwarfs composed of Carbon atoms in an electron background. These models possibly contribute to super-luminous supernova Type Ia, showing that magnetic white dwarfs might be the progenitors of such peculiar events. Finally, we show also the possibility of white dwarfs to be source of gravitational radiation.*

### 6.1 Introduction

It is generally accepted that stars born with masses below around 10 solar masses end up their evolutions as white dwarfs (Weber, 1999b; Shapiro and Teukolsky, 2008; Glendenning, 2012). With a typical composition mostly made of carbon, oxygen, or helium, white dwarfs possess central densities up to  $\sim 10^{11}$  g/cm<sup>3</sup> with a mass comparable to that of the Sun, which is distributed in a volume comparable to that of the Earth. Together with neutron stars and black holes, they are endpoints of stellar evolution and play a key role in astrophysics.

However, the existence of white dwarfs was one of the major puzzles in astrophysics until Fowler (1926), based on the quantum-statistical theory developed by Fermi (1926) and Dirac (1926), showed that white dwarfs are supported by the pressure of a degenerate electron gas. In addition, Chandrasekhar (1931) found that there is a limit in the stellar mass, beyond which degenerate white dwarfs are unstable. This critical mass is the so-called *Chandrasekhar limit* and is about  $1.4 M_{\odot}$ .

White dwarfs can be very hot (Althaus et al., 2009), fast rotating (Arutyunyan et al., 1971; Boshkayev et al., 2013) and strongly magnetized (Coelho et al., 2014a; Lobato et al., 2016). Their observed surface magnetic fields can be so strong as  $10^9$  G (Terada et al., 2008; Reimers et al., 1996; Schmidt and Smith, 1995; Kemp et al., 1970; Putney, 1995; Angel, 1978). As in the neutron star case, an estimate for the internal magnetic field in WD's follows from the Virial theory by equating the magnetic field energy with the gravitational binding energy, which leads to an upper limit for the magnetic fields inside WD's of  $\sim 10^{13}$  G. On the other hand, analytic and numeric calculations, both in Newtonian theory as well as in General Relativity theory, showed that WD's may have internal magnetic fields as large as  $10^{12-16}$  G (Angel, 1978; Shapiro and Teukolsky, 2008; Bera and Bhattacharya, 2014; Franzon and Schramm, 2015).

As the mass of an accreting white dwarf in a binary system approaches the limiting mass, the star undergoes a rapid contraction. Elevated temperature during this collapse can trigger a runaway thermonuclear reaction resulting in a supernova Type Ia (SNIa) explosion. The standard conditions that lead to the SNIa allow them to be used as standard candles in cosmology, and has led to the discovery of the accelerating expansion of the Universe (Riess et al., 1998). However, based on recent observations of several superluminous supernovae Type Ia (Scalzo et al., 2010; Howell et al., 2006; Hicken et al., 2007; Yamanaka et al., 2009; Taubenberger et al., 2011), it has been suggested that the progenitor mass of such explosions (SN 2006gz, SN 2007if, SN 2009dc, SN 2003fg) significantly exceeds the Chandrasekhar mass limit.

Previous studies showed that magnetic white dwarfs can have their masses increased up to  $2.58 M_{\odot}$  for a magnetic field strength of  $10^{18}$  G at the center of the star (Das and Mukhopadhyay, 2013). Nonetheless, such approach violates not only macro physics aspects, as for example, the breaking of spherical symmetry due to the magnetic field, but also microphysics considerations, which are relevant for a self-consistent calculation of the structure of these objects (Coelho et al., 2014b). In addition, a self-consistent newtonian structure calculation of strongly magnetized white dwarfs showed that these stars exceed the traditional Chandrasekhar mass limit significantly ( $M \sim 1.9 M_{\odot}$ ) for a maximum field strength of the order of  $10^{14}$  G (Bera and Bhattacharya, 2014).

In this chapter, we model static and rotating magnetized white dwarfs in a self-consistent way by solving Einstein-Maxwell equations with the same approach as in the previous chapters. The presence of such a strong magnetic field can locally affect the microphysics of the stellar matter, as for example, due to Landau quantization. However, Bera and Bhattacharya (2014) showed that Landau quantization does not affect the global properties of white dwarfs. Globally, the magnetic field can affect the structure of WD's, since it contributes to the Lorenz force, which acts against gravity. In addition, it contributes also to the structure of spacetime, since the magnetic field is now a source for the gravitational field through the Maxwell energy-momentum tensor. In the following, as we are interested in global effects that magnetic fields and rotation can induce in WD's, we simplify the discussion assuming white dwarfs that are predominately composed by  $^{12}\text{C}$  ( $A/Z = 2$ ) in a electron background.

## 6.2 Mass-radius diagram for static highly magnetized white dwarfs

In this section, we present the mass-radius diagram for static magnetized white dwarfs. The relation between mass and radius of non-magnetized white dwarfs was first determined by Chandrasekhar (Chandrasekhar, 1939). Recently, studies of modified mass-radius relations of magnetic white dwarfs were proposed, for example by Das and Mukhopadhyay (2012), Suh and Mathews (2000) and Bera and Bhattacharya (2014). As we also found in this work, these authors show that the mass of white dwarfs increases in the presence of magnetic fields.

In Fig. 6.1, we show the isocontours in the  $(x, z)$  plane of the poloidal magnetic field lines for a static star with central enthalpy of  $H_c = 0.0063 c^2$ . As we will see in Fig. 6.4, this value of the enthalpy results in the maximum gravitational mass of relativistic, static and magnetized white dwarfs achieved within the code, namely,  $2.09 M_{\odot}$ , which corresponds to a central mass density of  $2.79 \times 10^{10}$  g/cm<sup>3</sup>. It is known that at sufficiently high densities, reactions as inverse  $\beta$ -decay or nuclear fusion can take place in the interior of white dwarfs (Chamel et al., 2013; Coelho et al., 2014b). The issue has been addressed in a recent work by collaborators and I in Otoniel et al. (2016).

In Fig. 6.2, we show the mass density distribution for the same star as in Fig. 6.1. As expected, the mass density is not spherically distributed and the maximum mass density is not at the center

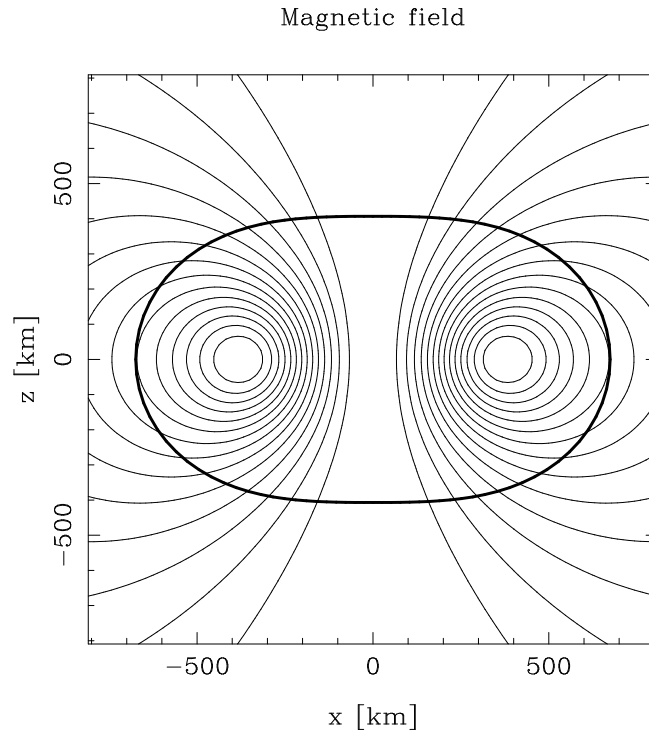


FIGURE 6.1: Isocontours of the magnetic field strength in the  $(x, z)$  plane, with a gravitational mass of  $2.09 M_{\odot}$  and a magnetic dipole moment of  $1.30 \times 10^{34} \text{ Am}^2$ . The ratio between the magnetic pressure and the matter pressure at the center of the star is about 1, and the magnetic field at center reaches  $1.03 \times 10^{15} \text{ G}$ .

of the star. In this case, the central magnetic field reaches a value of  $1.03 \times 10^{15} \text{ G}$ , whereas the surface magnetic field was found to be  $2.02 \times 10^{14} \text{ G}$ . The figure illustrates that the Lorentz force exerted by the magnetic field breaks the spherical symmetry of white dwarfs considerably and acts as a centrifugal force that pushes the matter off-center. For a better understanding of this aspect, we make use the equation of motion (Chapter 2, Eq. 2.15) for the static case,  $\Gamma = 0$ ,

$$H(r, \theta) + \nu(r, \theta) + M(r, \theta) = C, \quad (6.1)$$

and plot these quantities in the equatorial plane as shown in Fig. 6.3. The constant  $C$  can be calculated at every point in the star. We have chosen the center, since the central value of the magnetic potential  $M(r, \theta)$  is zero and the central enthalpy  $H_c$  is our input to construct solutions. The Lorentz force is the derivative of the magnetic potential  $M(r, \theta)$  in the equation Eq. (6.1) and reaches its maximum value off-center ( $r_{\text{eq}} \sim 350 \text{ km}$ , see Fig. 6.3). As already discussed by Cardall et al. (2001), the direction of the magnetic forces in the equatorial plane depends on the current distribution inside the star. In addition, the magnetic field changes its direction in the equatorial plane and, therefore, the Lorentz force reverses the direction inside the star. In our case, this can be seen from the qualitative change in behaviour of the function  $M(r, \theta)$  around  $r_{\text{eq}} \sim 350 \text{ km}$  (Fig. 6.3). It is worth to mention that we have studied also the effects of the Lorentz force due to high magnetic fields on the geometry of the neutron-star crust in Franzon et al. (2016d), showing that the thickness of the crust can change (either increase or decrease), depending on the polar angle under the influence of the Lorentz force.

Fig. 6.4 depicts the relation between the mass and the circular equatorial radius for magnetized white dwarfs. The magnetic field is included in the calculation through the current function  $k_0$ . The higher  $k_0$ , the higher the magnetic field strength. The stellar sequence (different curves labeled by different  $k_0$ 's) is obtained by changing the central enthalpy of the star (or the central density). The value

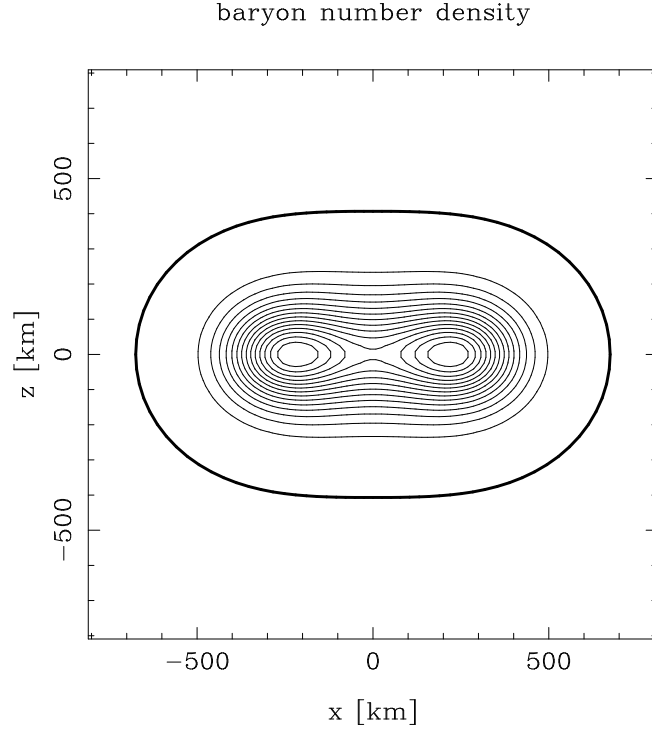


FIGURE 6.2: Isocontours of the baryon number density in the  $(x, z)$  plane for the same star as shown in Fig. 6.1. The central baryon density for this star is  $1.679 \times 10^{-5} \text{ fm}^{-3}$  ( $2.79 \times 10^{10} \text{ g/cm}^3$ ).

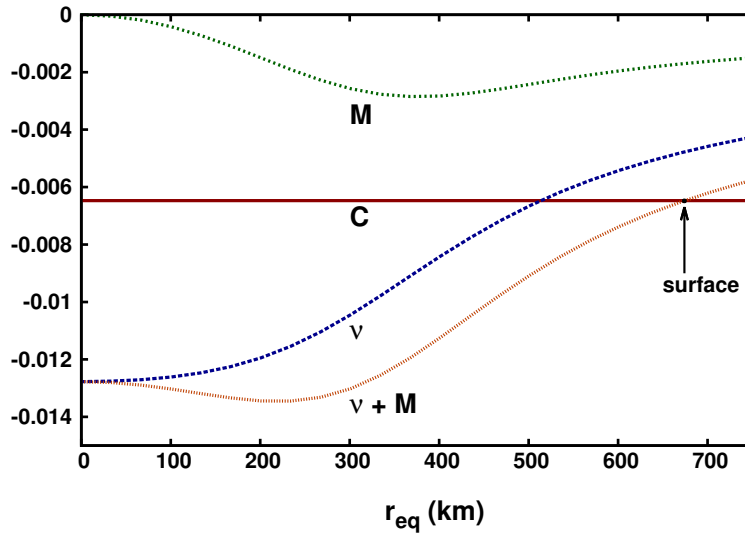


FIGURE 6.3: Behaviour of the different terms of the equation of motion as a function of the equatorial coordinate radius for the same star as shown in Fig. 6.1.

$k_0 = 800$  roughly corresponds to the solution with maximum field configuration achieved within the code. For low magnetic fields, the sequences follow the mass-radius relation as for non-magnetic WD's, ultimately reaching the Chandrasekhar mass limit. As the magnetic field strength is increased, the deviation from the non-magnetic curve increases, resulting in configurations with masses well above the Chandrasekhar limit of  $1.4 M_\odot$ . In this calculation, we found a maximum mass for a relativistic white dwarf of  $2.09 M_\odot$  for a magnetic field strength at the stellar center of  $B \sim 10^{14} \text{ G}$  (end of the yellow line in Fig. 6.4). Fig. 6.4 clearly demonstrates that WD masses larger than the standard Chandrasekhar limit for the non-magnetic case can be supported by strong magnetic fields.



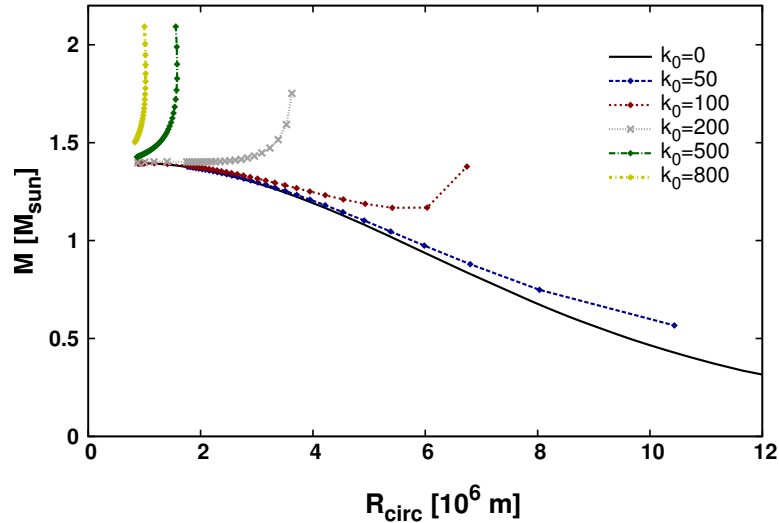


FIGURE 6.4: Mass-radius diagram for magnetized white dwarfs. Different curves represent different values of the current function  $k_0$ . We also compare the maximum white dwarf mass obtained in the Newtonian case (in black) and in the relativistic one (in red) for the maximum electric current value for which numerical convergence is achieved. This diagram is quite similar to the MR diagram calculated in [Bera and Bhattacharya \(2014\)](#). However, those authors have evaluated only Newtonian white dwarfs. All curves in this figure were calculated for a ratio between the magnetic and matter pressure less than or quite close to 1 at the center of the star.

Recently, during the writing process of this thesis, collaborators and I improved the work presented above, taking into account possible instabilities due to electron capture and nuclear fusion reactions in the cores of white dwarfs ([Otoniel et al., 2016](#)). The stellar interior was composed of a regular crystal lattice made of carbon ions immersed in a degenerate relativistic electron gas. We found that magnetized white dwarfs violate the standard Chandrasekhar mass limit significantly, even when electron capture and pycnonuclear instabilities are present in the stellar interior. In addition, the maximum magnetic field found is an order of magnitude smaller than in [Franzon and Schramm \(2015\)](#). This is because we modeled the stellar interior with a much more realistic equation of state than just a simple electron gas, and we considered the density threshold for nuclear fusion reactions, which restricts the central density of white dwarfs in  $\sim 9.25 \times 10^9 \text{ g/cm}^3$ , limiting the stellar masses and, therefore, their radii, which for very massive and magnetized white dwarfs cannot be smaller than  $\sim 1100 \text{ km}$ .

### 6.3 Rotating magnetized white dwarfs

White dwarfs can also spin very fast. Typically, white dwarfs can rotate with periods of days or even years. On the other hand, according to [Mereghetti et al. \(2009\)](#), one of the fastest observed WD possesses a spin period of 13.2s, a value similar to the ones observed in Soft Gamma Repeaters and Anomalous X-ray pulsars, known as magnetars ([Duncan and Thompson, 1992](#); [Thompson and Duncan, 1993](#)). A relation between white dwarfs and magnetars was addressed by [Malheiro and Coelho \(2015\)](#), where the authors speculated that SGRs and AXPs with low magnetic fields on the surface might be rotating magnetized white dwarfs.

Rigidly rotating non-magnetized white dwarfs were already studied long time ago in the Newtonian framework ([Krishan and Kushwaha, 1963](#); [Anand, 1965](#); [James, 1964](#); [Roxburgh and Durney, 1966](#); [Monaghan, 1966](#); [Geroyannis and Hadjopoulos, 1989](#)). In addition, the structure of rapidly rotating

white dwarfs was performed in general relativity by [Arutyunyan et al. \(1971\)](#), and more recently by [Boshkayev et al. \(2013\)](#), where the authors used Hartle's formalism ([Hartle, 1967](#)) to solve the approximate Einstein equations. It is obvious that all rotating stars have to satisfy the mass-shedding, or Keplerian limit, as a condition of stability. This limit is reached when the centrifugal force due to rotation does not balance gravity anymore and the star starts to lose particles from the equator, defining an upper limit to the angular velocity of uniformly rotating stars.

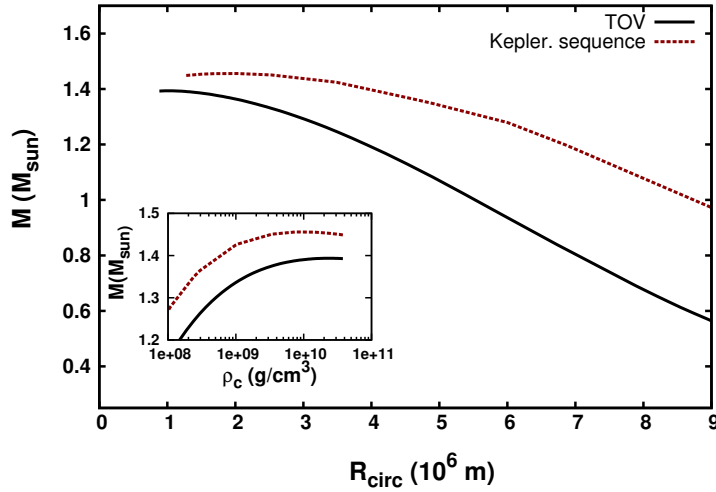


FIGURE 6.5: Mass-radius diagram for static and rotating white dwarfs. The TOV solution is shown in black, and the red (dotted) curve indicates the Keplerian sequence for rotating WD's. In the bottom left-hand corner the gravitational mass as a function of the central density for the same sequence of stars is shown.

In Fig. 6.5, we depict the Tolman-Oppenheimer-Volkoff solution for the structure of a spherically symmetric white dwarf, together with the mass-shedding frequency limit solutions. In the first place, by comparison of Fig. 6.4 and Fig. 6.5, one sees that magnetic fields are more efficient than rotation in increasing the maximum mass of white dwarfs. The maximum mass obtained for a relativistic and magnetic white dwarf is  $2.09 M_{\odot}$ , whereas the maximum mass achieved by rotation is  $\sim 1.45 M_{\odot}$ .

The relation between the Keplerian frequency ( $f_K$ ) and the central density of the star is displayed in Fig. 6.6. With higher angular velocity, the centrifugal forces increase, pushing the matter outward, therefore acting against gravity. As a result, the stars are allowed to have more mass, increasing the central density. This is possible, because the centrifugal forces due to rotation ( $f_c \propto r\Omega^2$ ) have much more effect on the outer layers of the star. On the other hand, for non-rotating magnetized stars, the Lorentz force acts mainly in the inner layers of the star, reducing, and not increasing, the central densities in these objects as shown by [Franzon et al. \(2015\)](#).

Henceforth we investigate the role played by the magnetic field in uniformly rotating white dwarfs. For a star with central enthalpy of  $H_c = 0.005 c^2$ , whose mass is close to the maximum mass in the static case, we present results for a white dwarf which is A) rotating with its Keplerian frequency and non-magnetized and B) rotating (with its Keplerian frequency) and magnetized. For the case A), the star rotates with its Keplerian frequency of 0.99 Hz. In addition, in order to compute stellar solutions for the case B), we turn on the magnetic field until the limit of numerical convergence is reached. We perform a calculation for different current functions  $k_0$ , from zero (case A) to the maximum value of the magnetic field (case B). As a result, the Keplerian frequency increases with the magnetic field as shown in Fig. 6.7. In this way, equilibrium configurations are obtained for higher centrifugal forces and, therefore, if the star can rotate faster, in consequence it can also support higher masses. According to Fig. 6.6, non-magnetized white dwarfs can reach a maximum Keplerian frequency of 1.52 Hz. However, in the magnetic case (Fig. 6.7), the maximum Keplerian frequency

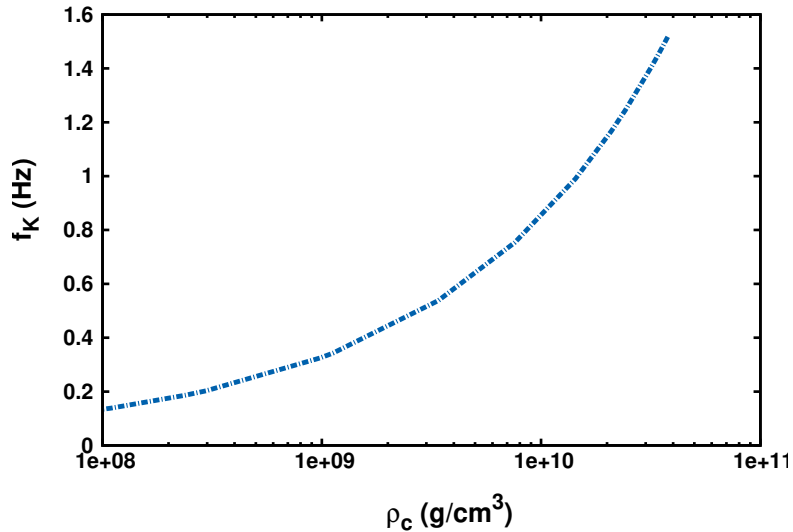


FIGURE 6.6: Keplerian frequency as function of the central baryon density for the sequence as shown in Fig. 6.5. The maximum frequency reached by a non-magnetized and uniformly rotating white dwarf is 1.52 Hz.

is reduced to 1.13 Hz, which corresponds to a white dwarf with gravitational mass of  $\sim 1.57 M_\odot$  and a central magnetic field of  $1.87 \times 10^{14}$  G.

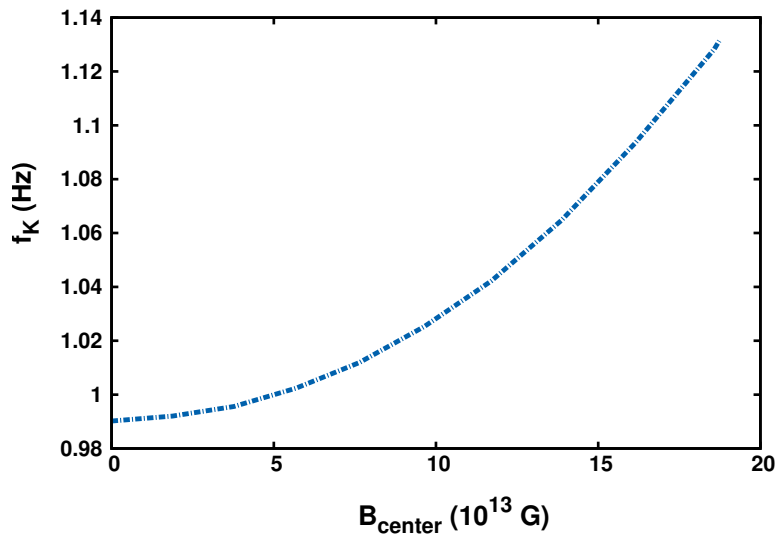


FIGURE 6.7: Keplerian frequency as function of the central magnetic field for a white dwarf at fixed central enthalpy of  $H_c = 0.005 c^2$ .

## 6.4 Gravitational waves from white dwarfs

The main motivation of this section is provided by the recent binary system discovered by [Marsh et al. \(2016\)](#). This system is composed of a main sequence star and a fast spinning and magnetized white dwarf with a mass that lies in the range  $0.81M_\odot < M_{\text{wd}} \leq 1.29M_\odot$ . The pulsating white dwarf is called AR Scorpii, AR Sco for short. In the case of AR Sco, this was the first radio pulsations detected in any white dwarf system. In addition, due to its high magnetic field combined with rotation, such

type of WD's are called 'white dwarf pulsar'. AR Sco rotates at a frequency of  $f = 8.538$  mHz in a distance of  $d \sim 116$  pc ( $1\text{pc} = 3.08 \times 10^{13}$  km) from Earth. In view of this new recent observation and measurement, we make an estimate of the GW strength  $h_0$  (as already shown in Eq. 5.7) emitted by rotating and magnetized white dwarfs.

The Lorentz force induced by magnetic fields change the structure of white dwarfs, which, in the case of poloidal fields, become oblate objects. This is the same effect as the one produced by rotation. In both cases, the star deformation with respect to the magnetic and/or rotation axis can be quantified by the stellar quadrupole moment.

As predicted by Einstein (1916), gravitational waves are generated by objects that have quadrupole moment varying in time, such as colliding black holes, collapse of stellar cores, coalescing neutron stars, white dwarf stars, etc. Such systems disrupt the space-time producing GW that radiate from the source and travel at the speed of light through the Universe, carrying information about their sources, as well as the nature of gravity itself.

Currently, the main ground-based gravitational waves interferometer operating is the twin Laser Interferometer Gravitational-wave Observatory (LIGO) which sensitivity is designed to detect GW amplitude of one part in  $10^{21}$  within the frequency bandwidth in the range 30 - 7000 Hz. In the next years, a second generation of detectors, as for example, advanced-LIGO and advanced-Virgo, will be operating. Furthermore, the space-based gravitational waves detector Laser Interferometer Space Antenna (LISA) (Danzmann et al., 1996) has been planning to be launched. LISA operates a space-based gravitational waves detector sensitive at frequencies between 0.03 mHz and 0.1 Hz.

The Deci-Hertz Interferometer Gravitational Wave Observatory (DECIGO) (Seto et al., 2001) is a plan of a future Japanese space mission for observing GW's in frequency bandwidth similar to LISA, however, at lower gravitational waves amplitudes. This fact, as we are going to see, makes DECIGO suitable to detect gravitational waves from fast rotating and/or magnetized white dwarfs. Meanwhile, another space-based interferometer has been proposed as a successor to LISA, the Big Bang Observer (BBO) (Phinney et al., 2003), with both frequency bandwidth and gravitational waves amplitudes similar to the ones of DECIGO.

In Fig. 6.8, we depict the frequency bandwidth of different space-borne gravitational wave interferometers, the Laser Interferometer Space Antenna (LISA), BBO and DECIGO. In this figure, we show also the estimate of gravitational wave amplitude for stars at different fixed baryon masses. First, a white dwarf with  $M_B = 1.29 M_\odot$ , rotating at 8.538 mHz, is represented by the letter (d), having  $h_0$  lower than the ones expected to be detected by BBO and DECIGO. This star, however, has its gravitational wave amplitude raised with the inclusion of magnetic fields, case (c), and can be, potentially, detected by BBO. This behavior is similar to the case of a white dwarf with  $M_B = 0.81 M_\odot$  (red line), which lies in the amplitude range of both BBO and DECIGO when magnetized, case (a), not being, however, a potential candidate when purely rotating, case (b).

In order to investigate if purely rotating white dwarfs are able to produce detectable GW, we included in Fig. 6.8 calculations for magnetized and rotating white dwarf models at fixed baryon mass of  $M_B = 0.50 M_\odot$ . This star rotates at different rotation frequencies of  $f = 10^{-5}$  Hz (yellow line),  $10^{-3}$  Hz (blue line) and  $10^{-2}$  Hz (green line), respectively. We fix then  $f$  and we include the magnetic field. As can be seen from Fig. 6.8, the white dwarf  $M_B = 0.50 M_\odot$  rotating at  $f = 10^{-2}$  Hz and without magnetic fields (begin of the green line), is in the range of detectability of the BBO detector. In addition, if this star is magnetized, this would lead to a maximum GW amplitude in the range of detectability of both BBO and DECIGO interferometers (also close to LISA line). The results of this analysis can be generalized to other frequencies or masses. However, as the frequency increases, the star approaches to the mass-shedding (Kepler) limit, which for the white dwarf  $M_B = 0.50 M_\odot$  is  $f \sim 0.02$  Hz.

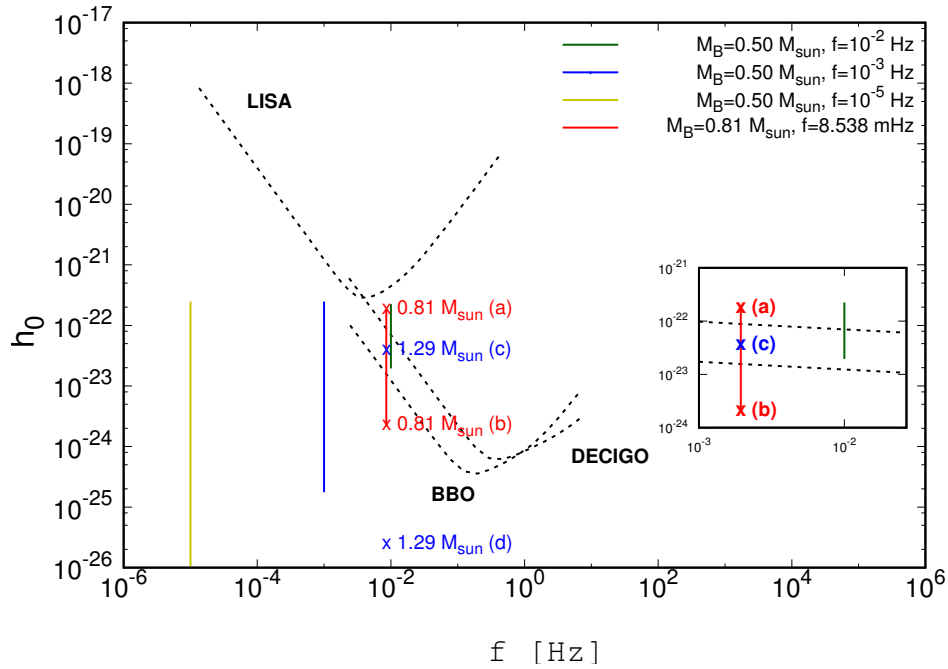


FIGURE 6.8: The dashed black curves represent the spectra for LISA, DECIGO and BBO interferometers. The vertical yellow, blue and green lines are rotating and magnetized white dwarfs at a fixed baryon mass of  $M_B = 0.50 M_\odot$ , while the red line represents AR Scorpii (with and without magnetic fields) at a frequency of 8.538 mHz. The models (a), (b), (c) and (d) are estimates of gravitational wave amplitudes by using the supposed masses and the rotation frequency of the pulsar white dwarf AR Scorpii.

In addition, for the star  $M_B = 0.50 M_\odot$  the magnetic field that corresponds to the minimum GW amplitude that lies on the DECIGO predictability curve is  $\sim 10^{10}$  G. More importantly, this value is just one order of magnitude higher than surface magnetic fields already observed in white dwarfs. Therefore, this makes magnetized white dwarfs good candidates of future GW observation and detection by the new generation of GW interferometers.

Note that white dwarfs with lower masses have gravitational wave amplitude of about three order of magnitude higher than (non rotating) highly magnetized neutron stars, as presented in the Chapter 5. This is related to the scale of the quadrupole moment, which is of the order of  $Q \sim 10^{42}$  kg.m<sup>2</sup> in magnetic white dwarfs, while this value reduces to  $\sim 10^{38}$  kg.m<sup>2</sup> for neutron stars. In addition, the WD's considered here are much closer to Earth than a typical neutron star, contributing to make them good sources for gravitational wave emission and detection.



# Chapter 7

## Summary

This thesis reflected our interest in understanding the effects of strong magnetic fields in different astrophysical systems: neutron stars, proto-neutron stars and white dwarfs. For this purpose, we incorporated realistic microphysical nuclear equations of state, general relativity, temperature, magnetic fields and rotation in order to increase the realism of compact star calculations and, thus, explore the possible outcomes from a large set of physical conditions and parameters.

### 7.1 Summary of Our Results

In Chapter 1 (Introduction), general properties of neutron stars were presented. Among them, the fact that the vast majority of neutron stars are observed as pulsars, most of them in radio frequency. We also discussed the fact that magnetars are neutron stars in which strong magnetic fields are the main source of energy. Moreover, their spin periods (2-12 s) and spin-down rates ( $10^{-13} - 10^{-10} \text{ ss}^{-1}$ ) indicate external dipole fields on the stellar surface of up to  $10^{15}$  G. In addition, the virial theorem allows to estimate a maximum limit to the magnetic field (irrespective of the configuration) in the interior of these stars. Most estimates point towards a maximal theoretical value of about  $10^{18}$  G in the stellar center, indicating that the maximum values considered within this work are still realistic. Therefore, magnetars are stars powered by their magnetic energy reservoir. However, the exact mechanism responsible for the origin of such strong fields in compact stars is still unclear, although hypotheses involving magnetic flux conservation and dynamo process are the most accepted ones.

Independently of the origin of such strong magnetic fields, they affect locally the microphysics of the equation of state and globally the structure of neutron stars, since magnetic fields induce different pressures in different directions in the star, causing them to be deformed with respect to their symmetry axis. It has been also shown that the presence of strong magnetic fields generates Landau quantization on the energy levels of charged particles. Moreover, magnetic field effects on the EoS gives rise to an anisotropy in the energy-momentum tensor components and, thus, one would expect that observational quantities, such as stellar maximum mass, to be affected by strong magnetic fields through effects in the EoS.

In Chapter 3, we made use of the Lorene C++ library for numerical relativity (presented in Chapter 2) to study self-consistently the effects of strong magnetic fields on hybrid stars by the use of a fully general-relativity approach. We solved numerically the coupled Maxwell-Einstein equations by means of a pseudo-spectral method, taking into consideration the anisotropy of the energy-momentum tensor due to the magnetic field, magnetic field effects on the equation of state, the interaction

between matter and the magnetic field (magnetization), and the anomalous magnetic moment of the hadrons. Previous models of highly magnetized neutron stars, which included magnetic field effects on the EoS, computed the corresponding mass-radius relations using (incorrectly) isotropic TOV equations. However, as we showed, EoS corrections are small when compared with the corrections due to the anisotropy from the pure magnetic field contribution. More specifically, the effect of inclusion of a magnetic-field dependent equation of state or the magnetization does not increase the maximum mass significantly in contrast to what has been claimed by previous studies (Paulucci et al., 2011; Rabhi et al., 2009; Dexheimer et al., 2013a). In addition, we found that the maximum magnetic field reached at the center of neutron stars is of the order of  $1.6 \times 10^{18}$  G. Furthermore, the Lorentz force induced by the field acts against gravity and pushes the matter outwards, reducing the central density in these objects. In this case, assuming that the magnetic field decays over time, stars would not only become less massive and smaller, but also go through phase transitions to more exotic phases with hyperons and quarks in their interior. Thereby, these features potentially modify the cooling behaviour of magnetized stars. This topic will be studied in detail in forthcoming studies.

In the next chapter, Chapter 4, we treated stationary configurations of strongly magnetized proto-neutron stars. We saw that the same general relativity formalism presented in Chapter 2 can be used for both cold and hot stars when the equation of state for proto-neutron stars is given at fixed entropies per baryon. Moreover, the composition and the structure of PNS's are strongly related to the number of trapped neutrinos. As the neutrino chemical potential decreases, this alters the chemical equilibrium and the composition inside the star, leading to an impact on the stellar structure. In this context, we showed that the magnetic field has also a very large impact not only on the structure of PNS's, but also on their particle population.

More specifically, there is a change in the composition of stars due to the magnetic field, pushing hyperons out, and decreasing the amount of neutrinos and the strangeness at the stellar center. Furthermore, as the magnetic field decreases over time, the density inside stars increases, which is followed by an increase in temperature. Especially important (giving that the magnetic field reduces during the life of stars), is the fact that the temperature in the equatorial plane increases in the inner core, while it decreases in the outer core. This fact is related to the Lorentz force, which reverses its direction in the equatorial plane, acting, therefore, differently throughout the star.

Still in Chapter 4, we studied the properties of PNS's subjected to fast rotation. The results indicate that the electron neutrino distribution of rotating proto-neutron stars does not differ much from their non-rotating counterpart. This is due to the fact that the centrifugal forces ( $f_c \propto r\Omega^2$ ) act mainly on the outer layers of the star. We also included magnetic fields in the rotating PNS model. As expected, the reduction in the central densities is even more pronounced and magnetic fields suppress exotic phases in rotating PNS even further, as in the case of cold neutron stars. A combination of both magnetic field and rotation effects can impact, for example, the nucleosynthesis in the winds of PNS's (Vlasov et al., 2014).

In addition, the scenario of transformation of a proto-neutron star into a neutron star could be influenced by a quark-hadron phase transition, since at higher temperatures the transition happens at lower densities. Such stars would be composed of hot quark and hadronic matter at different leptons fractions and fixed entropies. In the future, it would be interesting to couple the results showed in Chapter 4 to a hybrid star scenario with a quark-hadron phase transition in the star core.

Aside from magnetic fields, rotation and temperature effects, a quark-hadron phase transition can also be related to several interesting phenomena. This was discussed in Chapter 5, where fast rotating isolated pulsars provided an observable of quark deconfinement called braking index, a quantity that can be measurable during the star spin-down epoch. The conversion of nuclear matter to quark matter in the core of a rotating neutron star alters its moment of inertia. Hence, the epoch over which conversion takes place is signaled in the spin-down characteristics of pulsars.



We showed that the change from a confined to a deconfinement quark phase at the center of neutron stars leads to a drastic softening of the equation of state. As a result, stars at fixed baryon masses decrease their gravitational masses (although their central pressure increase) during their evolutionary sequence. When the softening of the EoS is very pronounced, this leads to a sudden contraction of the neutron star at a critical angular velocity, which can be observed during the evolution of fast rotating and isolated pulsars through the spin-up era, also known as backbending phenomenon (Glendenning et al., 1997). We reproduced the backbending phenomenon for fast spinning neutron stars. But, more importantly, we showed that the magnetic field, assumed here to be axi-symmetric and poloidal, can also be enhanced due to the phase transition from normal hadronic matter to quark matter during the evolution from a highly magnetized neutron star to a non-magnetized one. Therefore, in the same way that isolated pulsars have their frequencies increased in presence of a quark-hadron phase transition, the magnetic field can be amplified in highly magnetized hybrid neutron stars. As a result, stars endowed with strong magnetic fields may go through a “magnetic-up era” in their lives.

In Chapter 5, we calculated the mass-radius relationship,  $M_B(R_{\text{eq}})$ , for both rotating and magnetized neutron stars. We concluded that the mass-radius diagram and the shape of stars change significantly with the consistent inclusion of magnetic fields. The excess mass of the star is related to the Lorentz force, which increases with the magnetic field and, therefore, helps the star to support more mass than in the non-magnetized case. At the same time, the equatorial radii of these stars increase, becoming much larger than their non-magnetized counterpart.

In addition to the already known backbending phenomenon for fast spinning pulsars, which depends on a specific relation between the baryon mass  $M_B$ , the angular momentum  $J$  and the rotation frequency  $f$  of the star, we saw that the mass-radius diagram for highly magnetized neutron stars presents inflexions in the diagram  $M_B(R_{\text{eq}})$  versus the current function  $k_0$ , with a monotonic behaviour at fixed magnetic dipole moment  $\mu$ . This is a similar condition that generates the backbending in rotating pulsars. Based on this, we found that the backbending phenomena depends on the triple values  $(M_B, \mu, k_0)$  for neutron stars endowed with strong magnetic fields. This set of quantities has, therefore, its rotating counterpart given by  $(M_B, J, f)$ .

The next chapter, Chapter 6, presented a spin-off of our research, where we were able to calculate super-heavy white dwarfs in the presence of strong fields. This is an interesting and timely important problem, since such stars can exceed the Chandrasekhar mass limit and contribute to superluminous Type Ia supernovae. With this in mind, static equilibria of stationary and axisymmetric white dwarf stars endowed with strong poloidal magnetic fields were carried out. Moreover, we presented a modification on the white dwarf mass-radius relation generated by the magnetic field. We found that a maximum white dwarf mass of about  $2.00 M_\odot$  may be supported if the interior field is as strong as approximately  $10^{14}$  G. This mass is over 40 percent larger than the traditional Chandrasekhar limit.

The structure of relativistic, axisymmetric and uniformly rotating magnetized white dwarfs were also investigated self-consistently and all effects of electromagnetic field on the star equilibrium were taken into account. In this context, we have also shown the increasing of the Keplerian frequency with the magnetic field. The higher the magnetic field, the higher the Lorentz force, which, in turn, helps the star to support more mass than in the non-magnetized case. As a result, if these stars are more massive, they can rotate faster.

As we showed throughout this work, stellar magnetic fields supply anisotropic pressure, leading to the braking of spherical symmetry in stars. In this case, one can also compute the quadrupole moment of the mass distribution. With this quantity in hand, we presented in Chapter 5 and 6 an estimate of the gravitational wave strength emitted by magnetized neutron stars and white dwarfs. In Chapter 5, before the magnetic field decays completely, the neutron star presented a period of faster reduction in the gravitational waves emission due to the quark-hadron phase transition. In Chapter 6, in view of

the new recent observation and measurement of the rotating and highly-magnetized white dwarf AR Scorpii, we showed this star, as well as other white dwarfs, might generate detectable gravitational waves with amplitudes that lie in the bandwidth of the next discussed generation of space-based gravitational waves detectors.

Finally, due to the lack of Earth-based experiments involving matter and electromagnetic fields at extreme conditions, astrophysical observations of compact objects can provide a unique chance of understanding the underlying physics. In addition, the solutions presented in this work are fully relativistic and self-consistent, since all the effects related to the magnetic field on the equilibrium of stars were taken into account. Note that our results might depend on the equation of state used to describe stellar interiors and different EoS's might result in stronger or weaker effects than those reported in this thesis. Nevertheless, we believe that the general conclusions obtained within our consistent models will remain the same. In addition, although we have assumed a purely poloidal magnetic field in this work, which is not the most general one, one can have a fair idea of the maximum magnetic field strength that can be reached inside these stars. Furthermore, we have shown using full general relativity, that strong magnetic fields severely impact both the microphysics and the global structure of compact objects.

## 7.2 Future Work

Finally, we present several issues to be explored in the future.

1. The phase transition from hadronic to quark matter impacts the structure of NS's. In this case, one can study the effects of quark-hadron phase transition and hyperonic matter on the evolution of binary neutron stars systems. The stars will spiral in toward each other and will release gravitational radiation which may be observable with ground-based detectors. The use of numerical-relativity simulations of binaries with distinct nuclear equations of state with hyperons degree of freedom and quark-hadron phase transition to describe the neutron stars interior could be used to study the impact of the nuclear equation of state on the last orbits of binary neutron stars and possible signature of these exotic phases through the postmerger GW's emission. As a first kick-off, we have been using LORENE C++ library to perform calculations of the final phase of inspiral of a binary system consisting of two neutron stars. This calculation will be used to study the effects of different microphysics on the gravitational wave frequency at the innermost stable circular orbit (ISCO), which marks the end of the inspiral phase. More importantly, such a calculation and the models presented in this work will serve in the future as the initial data conditions for simulations of realistic EoS hydrodynamical mergers.

2. An extension of our work is the study of global properties of magnetized neutron stars endowed with both poloidal and toroidal magnetic field components. In order to achieve this goal, we will implement the publicly available numerical code XNS<sup>1</sup> and include realistic EoS tables into the code. The XNS code solves axisymmetric equilibrium configuration of neutron star in General Relativity (Bucciantini and Del Zanna, 2011; Pili et al., 2014b). XNS allows to include and model rotating stars endowed with magnetic fields either purely toroidal, purely poloidal or in the mixed twisted torus configuration.

3. Moreover, the matter in the inner crust of neutron stars is made of nuclei embedded in a neutron gas along with the uniform electron gas. Further, the matter is in beta-equilibrium and maintains charge neutrality. The outer crust contains nuclei arranged in a body-centered cubic lattice immersed in a gas of free electrons. In these cases, the magnetic field may impact the composition and the

<sup>1</sup><http://www.arcetri.astro.it/science/ahead/XNS/>

---

equation of state of crustal matter. Consequently, one can investigate the change in the nuclei composition induced by magnetic fields in the inner and outer crust of neutron stars in order to build self-consistent magnetized stellar models, not only for the core, but also for the crust region.



## Appendix A

# Electric current in Newtonian magnetized stars

The Euler equation in presence of magnetic fields can be written as:

$$\frac{1}{\rho} \vec{\nabla} p + \vec{\nabla} \phi - \vec{\nabla} \phi_r + \frac{\vec{F}}{\rho} = 0, \quad (\text{A.1})$$

with  $\vec{F}$  being the Lorentz force  $\vec{F} = \vec{j} \times \vec{B}$ . Taking the curl of Eq. (A.1), we have:

$$\vec{\nabla} \times \left( \frac{\vec{F}}{\rho} \right) = 0, \quad (\text{A.2})$$

since the curl of a gradient is zero, Eq. (A.3) can be expressed in terms of a scalar function  $M$  (to be determined):

$$\vec{\nabla} M = \frac{\vec{F}}{\rho}. \quad (\text{A.3})$$

Note that:

$$\vec{\nabla} M \cdot \vec{B} = \frac{\vec{F} \cdot \vec{B}}{\rho} = \frac{(\vec{j} \times \vec{B}) \cdot \vec{B}}{\rho} = 0, \quad (\text{A.4})$$

in other words,  $M$  is constant along the magnetic field lines  $B$ . The magnetic field  $B$  satisfies also the Maxwell equation:

$$\vec{\nabla} \cdot \vec{B} = 0. \quad (\text{A.5})$$

In this case,  $B$  can be written in terms of a stream function, so that  $\vec{B} = \vec{\nabla} \times \vec{u}$ . In spherical coordinates  $(r, \theta, \phi)$ , the components of the axisymmetric magnetic fields (no dependence on  $\phi$ ) are:

$$B_r = \frac{1}{r^2 \sin \theta} \frac{\partial u}{\partial \theta}, \quad (\text{A.6})$$

$$B_\theta = -\frac{1}{r \sin \theta} \frac{\partial u}{\partial r}, \quad (\text{A.7})$$

and, therefore, the total magnetic field is:

$$\vec{B} = \frac{1}{r^2 \sin \theta} \frac{\partial u}{\partial \theta} \hat{r} - \frac{1}{r \sin \theta} \frac{\partial u}{\partial r} \hat{\theta} + B_\phi \hat{\phi}. \quad (\text{A.8})$$

Now, using the definitions of  $B_r$  and  $B_\theta$ , it is possible to show that  $\vec{\nabla} u \cdot \vec{B} = 0$ . By comparing this with Eq. (A.4), the function  $M$  has the same property as  $u$ . As a consequence, one has  $M = M(u)$ . And, according to the Ampère-Maxwell equation, the electric current is given by:

$$\begin{aligned} 4\pi \vec{j} &= \vec{\nabla} \times \vec{B} \\ &= \frac{1}{r \sin \theta} \frac{\partial}{\partial \theta} (B_\phi \sin \theta) \hat{r} - \frac{1}{r} \frac{\partial}{\partial r} (r B_\phi) \hat{\theta} \\ &\quad + \frac{1}{r} \left[ \frac{\partial}{\partial r} (r B_\phi) - \frac{\partial}{\partial \theta} B_r \right] \hat{\phi} \end{aligned} \quad (\text{A.9})$$

$$= 4\pi (\vec{j}_{pol} + \vec{j}_{tor} \hat{\phi}), \quad (\text{A.10})$$

where the poloidal component  $\vec{j}_{pol}$  rewritten as:

$$\vec{j}_{pol} = \frac{1}{4\pi r \sin \theta} \vec{\nabla} (r B_\phi \sin \theta) \times \hat{\phi}, \quad (\text{A.11})$$

Note that in Eq. (A.11) the electric current does not depend on the stream function  $u$ . This is due to the fact that the poloidal current depends only on the toroidal magnetic field component  $B_\phi$ . On the other hand, using the expressions (A.6) and (A.7), the toroidal component of the current is given by:

$$\vec{j}_{tor} = j_\phi \hat{\phi} = -\frac{1}{4\pi r \sin \theta} \Delta_* u \hat{\phi}, \quad (\text{A.12})$$

where the definition was used:

$$\Delta_* u = -\frac{1}{r \sin \theta} \left[ \frac{\partial^2 u}{\partial r^2} - \frac{1}{r^2} \frac{1}{\tan \theta} \frac{\partial u}{\partial \theta} + \frac{\partial^2 u}{\partial \theta^2} \right]. \quad (\text{A.13})$$

We make use of the expression  $\vec{\nabla} u \times \hat{\phi}$  to rewrite Eq. (A.8) as:

$$\vec{B} = \frac{1}{r \sin \theta} (\vec{\nabla} u \times \hat{\phi}) + B_\phi \hat{\phi}, \quad (\text{A.14})$$

which represents the generic form of the magnetic field that can be generated by the electric currents in Eqs. (A.11) and (A.12). In this case, the Lorentz force reads:

$$\begin{aligned} \vec{F} &= \vec{j} \times \vec{B} = (\vec{j}_{pol} + \vec{j}_{tor}) \times (\vec{B}_{pol} + \vec{j}_{tor}) \\ &= \vec{j}_{pol} \times \vec{B}_{pol} + j_\phi \hat{\phi} \times \vec{B}_{pol} + B_\phi \vec{j}_{pol} \times \hat{\phi}, \end{aligned} \quad (\text{A.15})$$

with  $\vec{j}_{pol} \times \vec{B}_{pol} = 0$ , since the equation of motion Eq. (A.1) (and, therefore, the Lorentz force) is axisymmetric. Moreover,  $\vec{j}_{pol}$  and  $\vec{B}_{pol}$  are parallel vectors. As a result, from Eqs. (A.11) and (A.14), one has:

$$r B_\phi \sin \theta = f(u). \quad (\text{A.16})$$

Using the expressions for  $j_\phi$ ,  $j_{\text{pol}}$  and  $B_{\text{pol}}$ , the Eq. (A.15) is expressed as:

$$\vec{F} = -\frac{1}{4\pi r \sin \theta} \left[ \frac{\Delta_* u \vec{\nabla} u}{r \sin \theta} - B_\phi \vec{\nabla} (r B_\phi \sin \theta) \right], \quad (\text{A.17})$$

which, from Eq. (A.3), can be expressed in terms of the function  $M$ :

$$4\pi \rho \frac{dM}{du} = -\frac{\Delta_* u}{r^2 \sin \theta} - \frac{f(u)}{r^2 \sin^2 \theta} \frac{df}{du}, \quad (\text{A.18})$$

where the definitions for  $f(u)$  and the chain rule  $\vec{\nabla} M = \frac{dM}{du} \vec{\nabla} u$ ,  $\vec{\nabla} f = \frac{df}{du} \vec{\nabla} u$  were used. The equation (A.18) is known as Grad-Shafranov equation and represents the equilibrium equation in ideal magnetohydrodynamics (MHD) for a two dimensional fluid.

Using Eq. (A.18) to eliminate  $\Delta_* u$  in Eq. A.12, the total electric current reads:

$$4\pi \vec{j} = -\frac{df}{du} \vec{B}_{\text{pol}} + \frac{1}{r \sin \theta} \left[ 4\pi \rho \frac{dM}{du} r^2 \sin^2 \theta + f(u) \frac{df}{du} \right] \hat{\phi}, \quad (\text{A.19})$$

with  $\vec{B}_{\text{pol}}$  the first term in Eq. (A.14). Finally, with  $f(u)$  as defined in Eq. (A.16) and  $\vec{B} = \vec{B}_{\text{pol}} + \vec{B}_{\text{tor}}$ , we have:

$$\vec{j} = \frac{1}{4\pi} \frac{df}{du} \vec{B} + \rho r \sin \theta \frac{dM}{du} \hat{\phi}. \quad (\text{A.20})$$

The function  $f(u)$  and  $M(u)$  need to be chosen. In the case of purely poloidal magnetic fields, we have  $f(u) = 0$ . We can write:

$$\frac{dM}{du} = g(u), \quad (\text{A.21})$$

where  $g(u)$  is a function to be chosen. Here, we replace the stream function  $u$  by the magnetic vector potential  $A_\phi$ :

$$M = \int_0^{A_\phi} g(u') du'. \quad (\text{A.22})$$

The simplest choice of  $g(u)$  is  $g(u) = k_0 = \text{const.}$





# Appendix B

## A brief review of General Relativity

In this chapter, we present the basic aspects of Einsteins's theory of General Relativity. We want to introduce to the reader the basics tools and concepts that will be used throughout this manuscript. A complete description of the General Relativity Theory can be found in many textbooks, see e.g. [Wald \(2010\)](#).

### B.1 General Relativity

The general theory of relativity includes the geometric theory of gravitation published by Albert Einstein in 1915 and the current description of gravitation in modern physics. General relativity generalizes special relativity and Newton's law of universal gravitation, providing a unified description of gravity, as a geometric property of space and time, or spacetime. In particular, the curvature of spacetime is directly related to the energy and momentum of whatever matter and radiation are present. The relation is specified by the Einstein field equations, a system of partial differential equations.

The most important quantity in General Relativity is the metric tensor. Roughly speaking, the metric tensor is a function that tells how to compute the distance between any two points in a given space. For example, in flat and Euclidean space (i.e. our ordinary space and time), we have that the infinitesimal distance  $ds$  between two points is just given by the Pythagoras theorem:

$$ds^2 = dx^2 + dy^2 + dz^2. \tag{B.1}$$

According to Eq. (B.1), the multiplication factors placed in front of the *spatial* differential displacements  $dx_i$  are equal to 1, with  $i$  running from 1 to 3 and  $x_i$  being the cartesian coordinates  $x_i = (x, y, z)$ . We can rewrite Eq. (B.1) in the following form:

$$ds^2 = g_{ij}dx^i dx^j, \tag{B.2}$$

with  $g_{ij}$  being the metric tensor (or simply the metric). In the case of Eq. (B.2), the Einstein summation (a convention) was used, i.e., repeated indexes are implicitly summed over:

$$ds^2 = g_{11}dx^1 dx^1 + g_{12}dx^1 dx^2 + g_{22}dx^2 dx^2 + \dots \tag{B.3}$$

Nevertheless, due to the symmetry of the flat and Euclidean space, one has  $g_{ij} = \delta_{ij}$ , with  $\delta_{ij}$  being the the Kronecker delta, which is 0 for  $i \neq j$  and 1 for  $i = j$ . As result,  $g_{11} = g_{22} = g_{33} = 1$  and the other combinations are zero, which recovers the relation in Eq. (B.1). The metric tensor can be written in a matrix form so that  $g_{ij} = \text{dig}(1, 1, 1)$ . On the other hand, if we choose to use spherical coordinates to map this flat and Euclidean space  $x_i = (r, \theta, \phi)$ , Eq. (B.1) becomes:

$$ds^2 = dr^2 + r^2 d\theta^2 + r^2 \sin^2 \theta d\phi^2, \quad (\text{B.4})$$

with the metric tensor components given by  $g_{ij} = \text{dig}(1, r^2, r^2 \sin^2 \theta)$ . Note that the terms  $g_{11}$ ,  $g_{22}$  and  $g_{33}$  can depend on the coordinates  $(r, \theta)$ , but they still represents a Cartesian space. According to Eq. (B.1) and (B.4), each choice of coordinates gives a new form for the metric tensor  $g_{ij}$ .

In Euclidean space, the time and spatial coordinates transform in a Galilean form as:

$$x' = x - vt, \quad (\text{B.5})$$

$$t' = t, \quad (\text{B.6})$$

where  $x'$  and  $t'$  are the spatial coordinate and time as measured by an observer moving with constant velocity  $v$  with respect to the coordinate system  $(t, x)$ . Here, we have assumed that the motion of the particle is the  $x$  direction. However, according to the transformations, Albert Einstein (Einstein, 1905) showed that the Maxwell equations are not covariant (they do not have same form) for different observers. This inconsistency with Maxwells equations of electromagnetism led to the birth of Special Relativity, which applies in the special case in which the curvature of spacetime due to gravity is negligible. In addition, the description of the motion of particles occurs in a four-dimensional space-time, where the transformations in Eqs. (B.5) and (B.6) are valid in the limit of small gravitational fields and velocities.

In Special Relativity, Eqs. (B.5) and (B.6) are replaced by the Lorentz transformation:

$$x' = \gamma(x - vt), \quad (\text{B.7})$$

$$t' = \gamma \left( t - \frac{v}{c^2} x \right), \quad (\text{B.8})$$

where  $\gamma$  is the Lorentz factor  $\gamma = (1 - v^2/c^2)^{-1/2}$ . For  $v \ll c$ , Eqs. (B.7) and (B.8) reduce to Eqs. (B.5) and (B.6). Furthermore, as time is on the same foot as the spatial coordinates, in a flat four-dimension space time, the coordinates are represented by a tensor as  $x^\mu = (x^0, x^1, x^2, x^3)$ , where  $\mu$  assume values 0,1,2,3. The zero component refers to time  $t$  and  $x^1, x^2, x^3$  stand for spatial coordinates. In this case, the line element  $ds$  (see Eq. B.2) in rectangular coordinates (Minkowski space-time) is given by:

$$ds^2 = -dt^2 + dx^2 + dy^2 + dz^2, \quad (\text{B.9})$$

and by

$$ds^2 = -dt^2 + dr^2 + r^2 d\theta^2 + r^2 \sin^2 \theta d\phi^2, \quad (\text{B.10})$$

in spherical coordinates. We adopted the units  $c = 1$ . As can be checked, Eqs. (B.9) and (B.10) are invariant under the Lorentz transformation (Eq. (B.7) and (B.8)), i.e,  $ds^2 = ds'^2$ .

## B.2 General Relativity

### B.2.1 Cristoffel symbols

In this section, we will relate the coordinates  $\xi^a$  of a referential where a particle is free falling with the coordinates of an arbitrary referential  $x^\mu$ . Both indices  $a$  and  $\mu$  can assume values 0, 1, 2, 3. In the rest frame of the particle, locally inertial, its equation of motion is given by:

$$\frac{d^2 \xi^a}{d\tau^2} = 0, \quad (\text{B.11})$$

with  $\tau$  being the proper time of the particle. Assuming that  $\xi^a = \xi^a(x^\mu)$ , a infinitesimal change in the coordinate  $x^\mu$  implies a change of  $d\xi^a = \frac{\partial \xi^a}{\partial x^\nu} dx^\nu$  in the coordinate  $\xi^a$ . In this case, one takes the derivative Eq. (B.11) with respect to  $\tau$  to obtain:

$$\frac{d}{d\tau} \left( \frac{d^2 \xi^a}{d\tau^2} \right) = 0, \quad (\text{B.12})$$

$$\left( \frac{\partial \xi^a}{\partial x^\nu} \right) \frac{d^2 x^\nu}{d\tau^2} + \left( \frac{\partial^2 \xi^a}{\partial x^\mu \partial x^\nu} \right) \frac{dx^\mu}{d\tau} \frac{dx^\nu}{d\tau} = 0. \quad (\text{B.13})$$

Multiplying Eq. (B.13) by  $\frac{\partial x^\lambda}{\partial \xi^a}$ , we have:

$$\frac{d^2 x^\lambda}{d\tau^2} + \Gamma_{\mu\nu}^\lambda \frac{dx^\mu}{d\tau} \frac{dx^\nu}{d\tau} = 0, \quad (\text{B.14})$$

where  $\Gamma_{\mu\nu}^\lambda$  is defined as:

$$\Gamma_{\mu\nu}^\lambda = \frac{\partial x^\lambda}{\partial \xi^a} \frac{\partial^2 \xi^a}{\partial x^\mu \partial x^\nu}, \quad (\text{B.15})$$

which are the Christoffel symbols. Equation Eq. (B.14) is known as geodesic and it defines the path of a particle in an arbitrary referential. Note that if  $\Gamma_{\mu\nu}^\lambda = 0$ , the local inertial frame is recovered, with an equation of motion similar to Eq. (B.11). Thereby,  $\Gamma_{\mu\nu}^\lambda$  is interpreted as the force that alters the particle motion. As we will see,  $g_{\mu\nu}$  plays the role of the gravitational potential, while  $\Gamma_{\mu\nu}^\lambda$  represents the gravitational force.

From (B.2), in the locally inertia frame, one has:

$$d\tau^2 = \eta_{\alpha\beta} d\xi^\alpha d\xi^\beta, \quad (\text{B.16})$$

with  $\eta_{\alpha\beta}$  being the metric tensor and  $d\tau$  the proper time. On the other hand, an arbitrary referential with metric tensor  $g_{\mu\nu}$ , the distance between two points is given by:

$$d\tau'^2 = g_{\mu\nu} dx^\mu dx^\nu. \quad (\text{B.17})$$

Through the chain rule and making use of Eqs. (B.16) and (B.17), :

$$g_{\mu\nu} = \frac{\partial \xi^\alpha}{\partial x^\mu} \frac{\partial \xi^\beta}{\partial x^\nu} \eta_{\alpha\beta}, \quad (\text{B.18})$$

which relates the Minkowski metric tensor with the metric tensor in arbitrary referential.

Taking the derivative of (B.18) with respect to  $x^\lambda$ , and using the notation  $g_{\mu\nu,\lambda} = \frac{\partial g_{\mu\nu}}{\partial x^\lambda}$ , we have:

$$g_{\mu\nu,\lambda} = \frac{\partial^2 \xi^\alpha}{\partial x^\lambda \partial x^\mu} \frac{\partial \xi^\beta}{\partial x^\nu} \eta_{\alpha\beta} + \frac{\partial \xi^\alpha}{\partial x^\mu} \frac{\partial^2 \xi^\beta}{\partial x^\lambda \partial x^\nu} \eta_{\alpha\beta}, \quad (\text{B.19})$$

that, with Eq. B.15 and (B.18), is rewritten as:

$$g_{\mu\nu,\lambda} = \Gamma_{\lambda\mu}^\sigma g_{\sigma\nu} + \Gamma_{\lambda\nu}^\sigma g_{\mu\sigma}. \quad (\text{B.20})$$

Adding  $g_{\lambda\nu,\mu}$ , subtracting  $g_{\mu\lambda,\nu}$  in Eq. (B.20) and by using  $g_{\alpha\beta} = g_{\beta\alpha}$  and  $\Gamma_{\mu\lambda}^\sigma = \Gamma_{\lambda\mu}^\sigma$ , one has:

$$g_{\mu\nu,\lambda} + g_{\lambda\nu,\mu} - g_{\mu\lambda,\nu} = 2g_{\sigma\nu}\Gamma_{\mu\lambda}^\sigma. \quad (\text{B.21})$$

Multiplying the last equation by  $g^{\rho\nu}$ , one concludes that:

$$\Gamma_{\mu\lambda}^\rho = \frac{1}{2}g^{\rho\nu} \left( \frac{\partial g_{\mu\nu}}{\partial x^\lambda} + \frac{\partial g_{\lambda\nu}}{\partial x^\mu} - \frac{\partial g_{\mu\lambda}}{\partial x^\nu} \right), \quad (\text{B.22})$$

which shows that the Christoffel symbols are just function of the metric tensor and its derivatives. In this case, for flat space time of any kind, one has  $\Gamma_{\mu\lambda}^\rho = 0$ .

## B.2.2 Einstein Equation

The above equation shows the Christoffel symbols in terms of a generic metric tensor and its derivatives. The same results are obtained assuming that the covariant derivative (see Eq. (B.27) below for its definition) of the metric tensor is zero,  $\nabla_\mu g^{\mu\nu} = 0$ . With Eq. (B.22) and its derivatives, one builds the Riemann tensor (Glendenning, 2012; Weinberg, 1972):

$$R_{\sigma\mu\nu}^\rho = \Gamma_{\sigma\nu,\mu}^\rho - \Gamma_{\sigma\mu,\nu}^\rho + \Gamma_{\sigma\nu}^\alpha \Gamma_{\alpha\mu}^\rho - \Gamma_{\sigma\mu}^\alpha \Gamma_{\alpha\nu}^\rho, \quad (\text{B.23})$$

with the following properties:

$$\begin{aligned} \text{I. } R_{\nu\rho\sigma}^\mu &= -R_{\nu\sigma\rho}^\mu; \\ \text{II. } R_{\nu\rho\sigma}^\alpha + R_{\sigma\nu\rho}^\alpha + R_{\rho\sigma\nu}^\alpha &= 0; \\ \text{III. } R^{\rho\sigma\mu\nu} &= g_{\rho\alpha} R_{\sigma\mu\nu}^\alpha \\ \text{IV. } R_{\mu\nu\rho\sigma} &= -R_{\nu\mu\rho\sigma} = -R_{\mu\nu\sigma\rho}; \\ \text{V. } R_{\mu\nu\rho\sigma} &= R_{\rho\sigma\mu\nu} = R_{\sigma\rho\nu\mu}. \end{aligned} \quad (\text{B.24})$$

From the set of equations in Eq. (B.24), two new objects are defined. First, the Ricci tensor,

$$R_{\mu\nu} = R_{\mu\nu\rho}^\rho, \quad (\text{B.25})$$

and the scalar curvature:

$$R = g^{\mu\nu} R_{\mu\nu}, \quad (\text{B.26})$$

with covariant derivative of vector fields (or tensors)  $A_\mu$ :

$$A_{\mu;\nu} \equiv \frac{dA_\mu}{dx^\nu} - \Gamma_{\mu\nu}^\lambda A_\lambda, \quad (\text{B.27})$$

one has the Bianchi identity:

$$R_{\mu\nu\rho;\sigma}^{\alpha} + R_{\mu\sigma\nu;\rho}^{\alpha} + R_{\mu\rho\sigma;\nu}^{\alpha} = 0, \quad (\text{B.28})$$

which, multiplied by  $g^{\mu\nu}$  and choosing  $\sigma = \alpha$ , gives:

$$g^{\mu\nu} R_{\mu\nu\rho;\alpha}^{\alpha} + g^{\mu\nu} R_{\mu\alpha\nu;\rho}^{\alpha} + g^{\mu\nu} R_{\mu\rho\alpha;\nu}^{\alpha} = 0. \quad (\text{B.29})$$

Making use of the property (III) in Eq. (B.24), one has the following result:

$$2R_{\rho;\alpha}^{\alpha} - R_{;\rho} = 0, \quad (\text{B.30})$$

which, multiplied by  $g^{\mu\rho}$ , can be rewritten as:

$$2R^{\mu\nu}_{;\nu} - g^{\mu\nu} R_{;\nu} = 0, \quad (\text{B.31})$$

i.e.,

$$\left( R^{\mu\nu} - \frac{1}{2} g^{\mu\nu} R \right)_{;\nu} = 0, \quad (\text{B.32})$$

where the Einstein tensor is defined as:

$$G^{\mu\nu} \equiv R^{\mu\nu} - \frac{1}{2} g^{\mu\nu} R, \quad (\text{B.33})$$

which, naturally, satisfies the property:

$$G^{\mu\nu}_{;\nu} = 0, \quad (\text{B.34})$$

which satisfies the condition:

$$\boxed{G^{\mu\nu} = kT^{\mu\nu}}, \quad (\text{B.35})$$

with  $k$  being a constant (to be determined) and  $T^{\mu\nu}$  the energy-momentum tensor of the system. Note that the choice in Eq. (B.35) is possible, since  $T^{\mu\nu}$  is divergence free. Eq. (B.35) is the Einstein field equation.

### B.3 Spherical solutions of Einstein Equations

The Einstein equations can be written as:

$$G_{\mu\nu} \equiv R_{\mu\nu} - \frac{1}{2} g_{\mu\nu} R = kT_{\mu\nu}. \quad (\text{B.36})$$

To illustrate how to calculate the structure of stars, it is convenient to solve Eq. (B.35) for spherically symmetric metric. For this, we use the Schwarzschild metric,

$$ds^2 = e^{2\nu(r)} dt^2 - e^{2\lambda(r)} dr^2 - r^2 d\theta^2 - r^2 \sin^2(\theta) d\phi^2, \quad (\text{B.37})$$

which represents the distance between two points on the spherical surface with coordinates  $(r, \theta, \phi)$ . Still, the radial functions  $e^{2\nu(r)}$  and  $e^{2\lambda(r)}$  need to be found. From Eq. B.37, the components of the

metric tensor are:

$$g_{00} = e^{2\nu(r)}, \quad (\text{B.38})$$

$$g_{11} = -e^{2\lambda(r)}, \quad (\text{B.39})$$

$$g_{22} = -r^2, \quad (\text{B.40})$$

$$g_{33} = -r^2 \sin^2(\theta). \quad (\text{B.41})$$

Therefore, the matrix that represents the covariant metric tensor components is diagonal and symmetric,

$$g_{\mu\nu} = \begin{pmatrix} e^{2\nu(r)} & 0 & 0 & 0 \\ 0 & -e^{2\lambda(r)} & 0 & 0 \\ 0 & 0 & -r^2 & 0 \\ 0 & 0 & 0 & -r^2 \sin^2\theta \end{pmatrix}, \quad (\text{B.42})$$

with the contravariant components of the metric tensor given by:

$$g^{\mu\nu} = \begin{pmatrix} e^{-2\nu(r)} & 0 & 0 & 0 \\ 0 & -e^{-2\lambda(r)} & 0 & 0 \\ 0 & 0 & -\frac{1}{r^2} & 0 \\ 0 & 0 & 0 & -\frac{1}{r^2 \sin^2\theta} \end{pmatrix}, \quad (\text{B.43})$$

where the relation  $g^{\mu\nu} g_{\mu\nu} = I$  emerges.

In order to solve Eq. (B.35), the first step is to find the Christoffel symbols, which, from Eq. B.15 and the components of the metric tensor, are:

$$\begin{aligned} \Gamma_{00}^1 &= \nu' e^{2(\nu-\lambda)}, & \Gamma_{10}^0 &= \nu', \\ \Gamma_{11}^1 &= \lambda', & \Gamma_{22}^1 &= -r e^{-2\lambda}, \\ \Gamma_{33}^1 &= -r \sin^2 \theta e^{-2\lambda}, & \Gamma_{10}^0 &= \nu', \\ \Gamma_{12}^2 &= \Gamma_{13}^3 = \frac{1}{r}, & \Gamma_{23}^3 &= \cot \theta, \\ \Gamma_{33}^2 &= -\sin \theta \cos \theta, \end{aligned} \quad (\text{B.44})$$

and the components of the Ricci tensor are given by:

$$R_{00} = \left( -\nu'' + \lambda' \nu' - \nu'^2 - \frac{2\nu'}{r} \right) e^{2(\nu-\lambda)}, \quad (\text{B.45})$$

$$R_{11} = \nu'' - \lambda' \nu' + \nu'^2 - \frac{2\lambda'}{r}, \quad (\text{B.46})$$

$$R_{22} = (1 + r\nu' - r\lambda') e^{-2\lambda} - 1, \quad (\text{B.47})$$

$$R_{33} = R_{22} \sin^2 \theta. \quad (\text{B.48})$$

The scalar curvature in Eq. (B.26) can be written as:

$$R = g^{00} R_{00} + g^{11} R_{11} + g^{22} R_{22} + g^{33} R_{33}, \quad (\text{B.49})$$

and, therefore, using the results for the Ricci tensor with the metric tensor components as in Eq. (B.43), one gets:

$$R = e^{-2\lambda} \left( -2\nu'' + 2\lambda' \nu' - 2\nu'^2 - \frac{2}{r^2} + \frac{4\lambda'}{r} - \frac{4\nu'}{r} \right) + \frac{2}{r^2}. \quad (\text{B.50})$$

Finally, the Einstein equations can be expressed as:

$$G_0^0 = -\frac{1}{r^2} \frac{d}{dr} \left[ r \left( 1 - e^{-2\lambda} \right) \right], \quad (\text{B.51})$$

$$G_1^1 = e^{-2\lambda} \left( \frac{1}{r^2} + \frac{2\nu'}{r} \right) - \frac{1}{r^2}, \quad (\text{B.52})$$

$$G_2^2 = e^{-2\lambda} \left( \nu'' + \nu'^2 - \lambda'\nu' + \frac{\nu' - \lambda'}{r} \right), \quad (\text{B.53})$$

$$G_3^3 = G_2^2. \quad (\text{B.54})$$

From now on, we are going to consider in Eq. (B.35) the term which contains information about the energy content of the system. Assuming that the stellar interior is described by an energy-momentum tensor of a perfect fluid, we have:

$$T^{\mu\nu} = (p + \epsilon)u^\mu u^\nu - pg^{\mu\nu}, \quad (\text{B.55})$$

with  $u^\mu$  being the four-velocity of the fluid defined as:

$$u^\mu = \frac{dx^\mu}{d\tau}. \quad (\text{B.56})$$

For an observer co-moving with the fluid,  $\vec{u} = 0$ , the time component of  $u^\mu$  is:

$$u^0 = \frac{dt}{d\tau}, \quad (\text{B.57})$$

therefore,

$$u^0 = \frac{1}{\sqrt{g_{00}}} = e^{-\nu}, \quad (\text{B.58})$$

and, finally,

$$u_0 = e^\nu. \quad (\text{B.59})$$

Motivated by the tensor algebra, where scalars are represented by tensors with equal covariant and contravariant indices, we rewrite Eq. (B.55) as:

$$T_\mu{}^\nu = (\epsilon + p)u_\mu u^\nu - p\delta_\mu{}^\nu, \quad (\text{B.60})$$

with

$$T_0^0 = \epsilon, \quad (\text{B.61})$$

the energy density and

$$T_i{}^i = -p, \quad (\text{B.62})$$

the pressure components of the system, where  $i = 1, 2, 3$  are the spatial coordinates. In this case, we find:

$$G_0^0 = -\frac{1}{r^2} \frac{d}{dr} \left[ r \left( 1 - e^{-2\lambda} \right) \right] = k\epsilon, \quad (\text{B.63})$$

which, by integration in  $r$ , gives us:

$$e^{-2\lambda} = 1 - \frac{k}{r} \int_0^r \epsilon(r') r'^2 dr'. \quad (\text{B.64})$$

On the other hand, the stellar mass enclosed in a element  $dr$ , at distance  $r$  from the center of the star is:

$$M(r) = 4\pi \int_0^r \epsilon(r') r'^2 dr', \quad (\text{B.65})$$

so that the total stellar mass is  $M \equiv M(R)$ , with  $R$  being the stellar radius. In this case, Eq. (B.64) becomes:

$$e^{-2\lambda} = 1 + \frac{kM(r)}{4\pi r}, \quad (\text{B.66})$$

with  $k$  being a constant to be determined. In order to do so, we apply the Einstein equations outside the star, i.e, in the region where there is no matter or moment flux, and, therefore,  $T_{\mu\nu} = 0$ . Multiplying Eq. (B.35) by  $g^{\mu\nu}$  and using,

$$g^{\mu\nu} g_{\mu\nu} = 4, \quad (\text{B.67})$$

we find that the escalar curvature is:

$$R = 0, \quad (\text{B.68})$$

the Ricci tensor,

$$R_{\mu\nu} = 0. \quad (\text{B.69})$$

In other words,

$$R_{00} = 0, \quad (\text{B.70})$$

and

$$R_{ii} = 0. \quad (\text{B.71})$$

From  $R_{00}$  (already obtained in Eq. (B.48)), equation Eq. (B.70) becomes:

$$\left( -\nu'' + \lambda'\nu' - \nu'^2 - \frac{2\nu'}{r} \right) e^{-2\lambda} = 0. \quad (\text{B.72})$$

In the same way,  $R_{11}$  gives:

$$\left( \nu'' - \lambda'\nu' + \nu'^2 - \frac{2\lambda'}{r} \right) e^{-2\lambda} = 0, \quad (\text{B.73})$$

which summed with Eq.(B.72) gives the result:

$$\nu'(r) + \lambda'(r) = 0. \quad (\text{B.74})$$

At infinity, the Minkowski metric needs to be recovered. In this case, the metric potentials in Eq. (B.37),  $e^{2\nu(r)}$  and  $e^{2\lambda(r)}$ , go to 1. Thereby, we have that the product of those terms, namely  $e^{2(\nu(r)+\lambda(r))}$ , goes also to 1, which implies:

$$\nu(r) + \lambda(r) = 0. \quad (\text{B.75})$$

With  $R_{22}$  e  $g_{22}$ , from Eq. (B.71) for  $i = 2$ , we have:

$$(1 + 2r\nu') e^\nu = 1, \quad (\text{B.76})$$

that can be rewritten as:

$$\frac{d}{dr} (re^{2\nu}) = 1, \quad (\text{B.77})$$



whose integration turns out to be:

$$e^{2\nu} = 1 - \frac{2GM}{r}, \quad (\text{B.78})$$

where the integration constant is chosen to be  $-2GM$ , with  $G$  being the gravitational constant and  $M$  the gravitational mass of the star. If we compare Eq. (B.78) with Eq. (B.66), knowing that  $\lambda = -\nu$  and having  $M \equiv M(r = R)$ , the constant  $k$  reads:

$$k = -8\pi G. \quad (\text{B.79})$$

Therefore, the final form of Einstein equations is:

$$\boxed{R_{\mu\nu} - \frac{1}{2}Rg_{\mu\nu} = 8\pi GT_{\mu\nu}}. \quad (\text{B.80})$$



## Appendix C

# Einstein equation in the 3+1 formalism

*In this appendix, we will present the formalism that couples Einstein equations to Maxwell equations. In this context, this chapter serves as a guide necessary to understand the physics of highly magnetized compact stars.*

General relativity is ruled by the Einstein equations (EE):

$$R_{\mu\nu} - \frac{1}{2}Rg_{\mu\nu} = 8\pi GT_{\mu\nu}, \quad (\text{C.1})$$

with  $R_{\mu\nu}$  being the Ricci tensor (see Eq. B.25),  $R$  the Ricci scalar and  $T_{\mu\nu}$  the energy-momentum tensor of matter and electromagnetic fields. The constant  $G$  is the Newton's gravitational constant.

Equation (C.1) states an intrinsic relation between the geometry of the spacetime (on the left-hand side) and the mass-energy content (on the right-hand side). Due to the non-linearity and complexity of EE combined to the relativistic-hydrodynamics equations, one cannot find analytic solutions, excepted in special cases, as for example, for spherically symmetric systems. In this section, we address the formalism necessary to obtain the gravitational field equations that were used in the numerical calculation in Chapters 1-6, together with different matter contents to be described by the energy momentum tensor on the right-hand side of Eq. (C.1).

The 3+1 decomposition of spacetime (Misner et al., 1973) is a usual way to obtain the gravitational field equations in General Relativity. The idea behind it is simple, and it consists in the foliation of the 4 dimension spacetime in spacelike hyper-surfaces parameterized by the time coordinate  $t$ :  $\Sigma_t$ . The most important feature of this approach is the separation of the temporal coordinate from the spatial ones. As we will see, this is useful to project four-vectors and also tensors in their time and spatial components.

Before focusing on the energy-momentum tensor,  $T_{\mu\nu}$ , let us introduce a generic observer  $\mathcal{O}$ , co-moving with the fluid, whose timelike 4-vector velocity  $u^\mu$  satisfies:

$$u^\mu u_\mu = -1. \quad (\text{C.2})$$

One can define an operator  $\perp$ , orthogonal to  $u^\mu$ , and, therefore, purely spatial, with components:

$$\perp_\beta^\alpha = \delta_\beta^\alpha + u^\alpha u_\beta, \quad (\text{C.3})$$

with  $\delta_\beta^\alpha$  being the Kronecker delta. Note that,  $\perp_\beta^\alpha u^\beta = (\delta_\beta^\alpha + u^\alpha u_\beta)u^\beta = u^\alpha + u^\alpha(-1) = 0$ . In the so-called 3+1 decomposition, physical quantities are obtained from the projection of the

energy-momentum tensor. For example, the energy density as measured by the observer  $\mathcal{O}$  is:

$$E = T_{\mu\nu} u^\mu u^\nu, \quad (\text{C.4})$$

the momentum density flux is written as:

$$p_\alpha = -T_{\mu\nu} u^\mu \perp_\alpha^\nu, \quad (\text{C.5})$$

while the energy flux (the corresponding Poincaré vector for an electromagnetic field) reads:

$$\phi_\alpha = -T_{\mu\nu} u^\nu \perp_\alpha^\mu, \quad (\text{C.6})$$

and, finally, the components of the stress tensor as measured by  $\mathcal{O}$  are:

$$S_{\alpha\beta} = T_{\mu\nu} \perp_\alpha^\mu \perp_\beta^\nu. \quad (\text{C.7})$$

As the left-hand side of Einstein's equations is symmetric, it implies that  $T_{\mu\nu}$  is also symmetric and, therefore, the momentum density and the energy flux are equal, what reflects the equivalence of mass and energy in general relativity. From Eq. (B.34), we saw that  $\nabla_\mu G^{\mu\nu} = 0$ , which implies that  $T_{\mu\nu}$  is divergence free:

$$\boxed{\nabla_\mu T^{\mu\nu} = 0}. \quad (\text{C.8})$$

The properties presented above can be applied to any every energy-momentum tensor.

## C.1 3+1 decomposition of space time

The basic idea of the decomposition of space and time consists in foliating the spacetime in terms of a set of hypersurfaces  $\Sigma_t$  parametrized by a constant value of the time coordinate  $t$ . In this way, all vectors or tensors on  $\Sigma_t$  have purely spatial components and evolve in time from one hypersurface to the next.

Fig. C.1 shows a hypersurface  $\Sigma_t$ , where one defines a unit timelike four-vector,  $n_\mu$ , normal to  $\Sigma_t$ , which satisfies the normalization condition  $n^\mu n_\mu = -1$ . Note that the gradient of the time coordinate  $t$  is parallel to  $n_\mu$  and, therefore,

$$n_\mu = -N \nabla_\mu t, \quad (\text{C.9})$$

with  $N$  being the lapse function, which measures the rate of change of the time coordinate along the vector  $n_\mu$ . As we will see, the lapse  $N$  will be a building block to obtain the metric in the 3+1 decomposition (see Eq. (C.18)). In the same way as for the projector  $\perp_\beta^\alpha$ , which gives the spatial component of a four-velocity  $u^\mu$ , one can define a *purely spatial metric*  $\gamma_{ij}$  associated to each hypersurface  $\Sigma_t$ :

$$\gamma_{ij} := g_{ij} + n_i n_j, \quad (\text{C.10})$$

with  $i$  and  $j$  being spatial indices running from 1 to 3. Thus, the components of a orthogonal projector onto  $\Sigma_t$  reads:

$$\gamma_j^i = g_j^i + n^i n_j. \quad (\text{C.11})$$

For example, applying the operator from Eq. (C.11) on the normal vector  $n^\mu$ , and using that  $n^\mu n_\mu = -1$ , we find  $\gamma_j^i n^i = (g_{ij} + n_i n_j) n^i = n_j - n_j = 0$ , what demonstrates that the three-dimensional metric tensor  $\gamma_j^i$  is orthogonal to  $n^\mu$ .

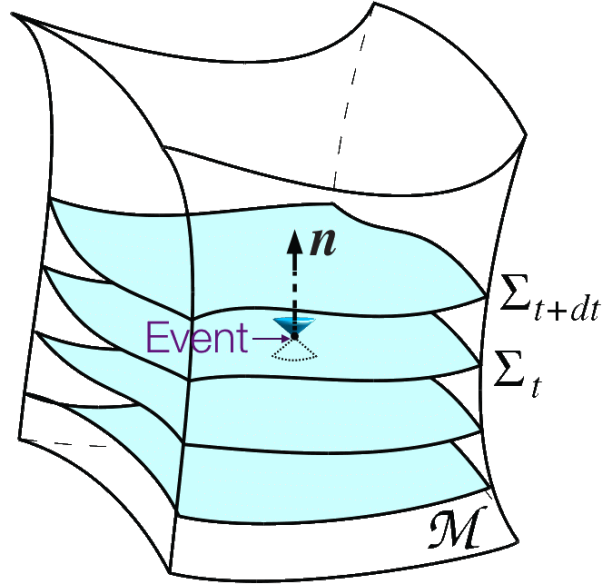


FIGURE C.1: Foliation of the spacetime  $\mathcal{M}$  by a family of hypersurfaces  $\Sigma_t$ . Figure taken from [Gourgoulhon and Bonazzola \(1994\)](#).

The unit normal vector  $n^\mu$  is timelike. In this case, we can consider observers whose four-velocity are  $n^\mu$ . These are called Eulerian observers  $\mathcal{O}_o$ . Likewise, using Eqs. (C.4), (C.5) and (C.6), and having the correspondence  $u^\mu \rightarrow n^\mu$  and  $\perp_\beta^\alpha \rightarrow \gamma_j^i$ , the energy density, the momentum density and the stress tensor as measured by  $\mathcal{O}_o$  are given by:

$$\boxed{E = T_{\mu\nu} n^\mu n^\nu}, \quad (\text{C.12})$$

$$\boxed{p_i = -T_{\mu\nu} n^\mu \gamma_j^\nu}, \quad (\text{C.13})$$

$$\boxed{S_{ij} = T_{\mu\nu} \gamma_i^\mu \gamma_j^\nu}. \quad (\text{C.14})$$

Therefore, the associated 3+1 decomposition of the energy-momentum tensor reads:

$$\boxed{T_{\mu\nu} = E n_\mu n_\nu + p_\mu n_\nu + n_\nu p_\mu + S_{\mu\nu}}. \quad (\text{C.15})$$

In the 3+1 formalism,  $x^0 = t$  and the triplet  $x^i = (x^1, x^2, x^3)$  corresponds to the spatial coordinate system on each hypersurface  $\Sigma_t$ . In this case, a basis vector  $e_\mu$  can be split into a part parallel to  $n^\mu$  and a part tangent to  $\Sigma_t$ , i.e.,

$$e_\mu = N n_\mu + \beta_\mu, \quad (\text{C.16})$$

where the spacelike vector  $\beta_\mu$  is called shift vector, also a building block used to obtain the final form of the metric tensor in the 3+1 formalism. Note that  $n_\mu \beta^\mu = 0$  by construction. It is possible to show that the components of the normal vector  $n_\mu$  read:

$$n_\mu = (-N, 0, 0, 0), \quad n^\mu = \frac{1}{N}(1, -\beta^i). \quad (\text{C.17})$$

Both definitions of lapse function and the shift vector will be crucial to get the final Einstein gravitational fields equations. We make use of the lapse function and shift vector to express the generic

line element in a 3+1 decomposition of space time as:

$$ds^2 = g_{\alpha\beta} dx^\alpha dx^\beta = -N dt^2 + \gamma_{ij} (dx^i + \beta^i dt)(dx^j + \beta^j dt). \quad (\text{C.18})$$

Another important tensor that will be useful to deduce the Einstein equation in a 3+1 decomposition is the extrinsic curvature tensor defined as:

$$K_{ij} := \frac{1}{2N} \mathcal{L}_{\vec{\beta}} \gamma_{ij} = \frac{1}{2N} \left( \beta^k \frac{\partial \gamma_{ij}}{\partial x^k} + \gamma_{kj} \frac{\partial \beta^k}{\partial x^i} + \gamma_{ik} \frac{\partial \beta^k}{\partial x^j} \right), \quad (\text{C.19})$$

where  $\mathcal{L}_{\vec{\beta}}$  is Lie derivative  $\gamma_{ij}$  along the vector field  $\vec{\beta}$ . The extrinsic curvature describes how the hypersurface is embedded in the four-dimensional spacetime. Note that  $K_{ij}$  has purely spatial components, whose trace is just  $K = \gamma^{ij} K_{ij}$ .

## C.2 3+1 decomposition of Einstein equation

In the same way as we did for the energy momentum tensor  $T_{\mu\nu}$ , we will project now the geometric part of Einstein's equations first (A) twice onto  $\Sigma_t$ , then (B) twice along  $n^\mu$  and, finally, (C) once on  $\Sigma_t$  and once along  $n^\mu$ . In the manifold where  $g_{\mu\nu}$  is the metric, we have, as usual:

$$\text{Riemann tensor} : {}^4 R_{\alpha\beta\gamma\sigma}, \quad (\text{C.20})$$

$$\text{Ricci tensor} : {}^4 R_{\mu\nu}, \quad (\text{C.21})$$

$$\text{Scalar curvature} : {}^4 R = {}^4 R^\mu{}_\mu, \quad (\text{C.22})$$

where the number 4 stands for four dimensions. But, in the 3 dimension manifold with metric  $\gamma_{\mu\nu}$  (remember that  $\gamma_{\mu\nu}$  is purely spatial). We keep the  $\mu$  and  $\nu$  as indices to make the comparison more clear), one has:

$$\text{Riemann tensor} : R_{\alpha\beta\gamma\sigma}, \quad (\text{C.23})$$

$$\text{Ricci tensor} : R_{\mu\nu}, \quad (\text{C.24})$$

$$\text{Scalar curvature} : R = R^\mu{}_\mu. \quad (\text{C.25})$$

It is really important to note that  ${}^4 R_{\alpha\beta\gamma\sigma}$  and  $R_{\alpha\beta\gamma\sigma}$  are different, because the former contains temporal derivatives of  $g_{\mu\nu}$ , while the latter does not. With the relationship between  ${}^4 R_{\alpha\beta\gamma\sigma}$  and  $R_{\alpha\beta\gamma\sigma}$  given in the above equations, I will obtain important expressions, namely, the Gauss, the Codazzi, and the Ricci equations. The steps will be the following:

- 1. To obtain the Gauss equation, we will project the Riemann tensor  ${}^4 R_{\alpha\beta\gamma\sigma}$  onto the hypersurface  $\Sigma_t$ ;
- 2. To obtain the Codazzi equation, we will project one index of  ${}^4 R_{\alpha\beta\gamma\sigma}$  into the normal direction  $n^\mu$ ;
- 3. To obtain the Ricci equation, we will project two indices of  ${}^4 R_{\alpha\beta\gamma\sigma}$  into the normal direction  $n^\mu$ .

The first relation between  ${}^4 R_{\alpha\beta\gamma\sigma}$  and  $R_{\alpha\beta\gamma\sigma}$  gives the Gauss equation:

$$R_{\alpha\beta\mu\nu} + K_{\alpha\mu} K_{\beta\nu} - K_{\alpha\nu} K_{\beta\mu} = \gamma_\alpha^\sigma \gamma_\beta^\tau \gamma_\mu^\rho \gamma_\nu^\lambda {}^4 R_{\lambda\rho\sigma\tau}, \quad (\text{C.26})$$

and the Codazzi equation is given by:

$$D_\mu K_{\alpha\nu} - D_\alpha K_{\mu\nu} = \gamma_\alpha^\sigma \gamma_\mu^\tau \gamma_\nu^\rho n^\lambda {}^4R_{\sigma\tau\rho\lambda}, \quad (\text{C.27})$$

where  $D_\mu$  is the projection of the covariante derivative onto  $\Sigma_t$ :  $D_\mu = \gamma_\mu^\sigma \nabla_\sigma$ . The last equation of interest is the Ricci one:

$$\mathcal{L}_{\vec{n}} K_{\alpha\beta} = -n^\mu n^\nu \gamma_\beta^\sigma \gamma_\mu^\tau {}^4R_{\nu\sigma\tau\mu} - \frac{1}{\alpha} D_\beta D_\alpha N - K_{\mu\alpha} K_\beta^\mu. \quad (\text{C.28})$$

### C.2.1 Evolution and constraint equations

We can eliminate the Riemann tensor  ${}^4R_{\alpha\beta\gamma\sigma}$  in Einstein's equations (C.1) by making use of the Gauss, Codazzi and Ricci equations to obtain the momentum and energy constraint equations, and the evolution equation in the 3 + 1 *decomposition* for the metric  $\gamma_{\mu\nu}$  and the extrinsic curvature  $K_{\mu\nu}$ . The Hamiltonian constraint equation, which comes from the Gauss equation (C.26) is:

$$R + K^2 - K_{\mu\beta} K^{\mu\beta} = 16\pi E, \quad (\text{C.29})$$

where E is the total energy density defined as  $E := n^\mu n^\nu T_{\mu\nu}$ . And from the Codazzi equation (C.27), we have the momentum constraint:

$$D_\mu K_\alpha^\mu - D_\alpha K = 8\pi J_\alpha, \quad (\text{C.30})$$

being  $J_\alpha$  the momentum density defined as  $J_\alpha := -\gamma_\alpha^\sigma n^\lambda T_{\sigma\lambda}$ . From the Ricci equation (C.28), we have the evolution equation for the extrinsic curvature components:

$$\begin{aligned} \mathcal{L}_{\vec{n}} K_{\alpha\beta} = & D_\beta D_\alpha N + N(R_{\alpha\beta} - K K_{\alpha\beta} - 2K_\alpha^\sigma K_{\beta\sigma}) + \\ & - 8\pi N(S_{\alpha\beta} - \frac{1}{2}\gamma_{\alpha\beta}(S - \rho)) + \mathcal{L}_{\vec{\beta}} K_{\alpha\beta}, \end{aligned} \quad (\text{C.31})$$

with  $S_{\alpha\beta} = \gamma_\alpha^\tau \gamma_\beta^\sigma T_{\tau\sigma}$  being the projection of the stress tensor onto the hypersurface. Finally, one obtains from the definition of extrinsic curvature  $K_{\alpha\beta}$  in Eq. (C.19):

$$\mathcal{L}_{\vec{t}} \gamma_{\alpha\beta} = -2N K_{\alpha\beta} + \mathcal{L}_{\vec{\beta}} \gamma_{\alpha\beta}, \quad (\text{C.32})$$

which represents the evolution equation for  $\gamma_{\alpha\beta}$ .

As we are working with the 3D hypersurface, the Lie derivative in the evolution equations is reduced to a partial temporal derivative  $\mathcal{L}_{\vec{t}} \rightarrow \partial_t$ . In doing so, our new Hamiltonian constraint, momentum constraint and both evolution equations are, therefore,

$$(A) : R + K^2 - K_{ij} K^{ij} = 16\pi E, \quad (\text{C.33})$$

$$(B) : D_j K^{ij} - D_j (\gamma^{ij} K) = 8\pi p^i, \quad (\text{C.34})$$

and

$$\begin{aligned} (C) : -\mathcal{L}_{\vec{\beta}} K_{ij} = & -D_i D_j N + N(R_{ij} + K K_{ij} - 2K_{ik} K_j^k) \\ & - 8\pi N(S_{ij} - \frac{1}{2}\gamma_{ij}(S - E)), \end{aligned} \quad (\text{C.35})$$

with  $\mathcal{L}_{\vec{\beta}}K_{ij}$  being the Lie derivative of the extrinsic curvature along the vector field  $\vec{\beta}$ . The term  $S$  is simply given by the trace  $S = \gamma^{ij}S_{ij}$ .

### C.3 Stationary, axisymmetric and circular spacetimes

Due to the symmetry of magnetized stars, we make use of a spherical type coordinate system such that  $x^\alpha = (x^0, x^1, x^2, x^3) = (t, r, \theta, \phi)$ , with the coordinate radius  $r \in [0, \infty)$  and the angular polar coordinate  $\theta \in [0, \pi]$ . As usual, the  $\phi$  is the coordinate azimuth angle. In Fig. C.2, we show the spatial coordinates  $(r, \theta, \phi)$  and the associated natural basis vectors  $(\vec{e}_r, \vec{e}_\theta, \vec{e}_\phi)$ .

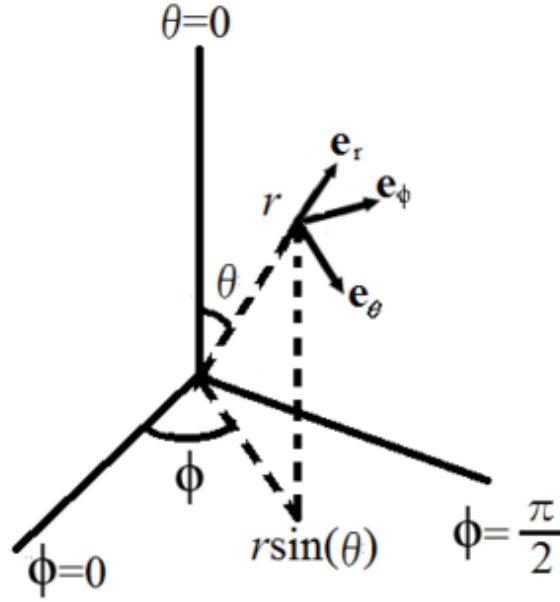


FIGURE C.2: Spherical coordinates as commonly used in physics: radial distance  $r$ , polar angle  $\theta$ , and azimuthal angle  $\phi$ .

In this context, stationary and axisymmetry spacetime is represented by the conditions:

$$\begin{cases} \frac{\partial g_{\alpha\beta}}{\partial t} = 0 \text{ (stationary condition),} \\ \frac{\partial g_{\alpha\beta}}{\partial \phi} = 0 \text{ (axisymmetric condition),} \end{cases}$$

where  $g_{\alpha\beta}$  corresponds to the metric in the spherical polar coordinate system  $(t, r, \theta, \phi)$ . In other words, a spacetime is stationary when the metric potentials, as it appears, for example, in Eq. (C.18), do not depend on time, and axisymmetric means that the metric potentials are invariant under the change of the azimuth angle  $\phi$ . Another way to establish such symmetries is through the Lie derivative of the metric  $g_{\mu\nu}$  along the generator of symmetries  $\vec{\xi}$  (Killing vectors), i.e.  $\mathcal{L}_{\vec{\xi}}g = 0$ , with  $\vec{\xi} = \vec{\partial}_t$  and  $\vec{\xi} = \vec{\partial}_\phi$  being the generator of symmetries in time and in the azimuth direction.

Another important concept which relates the coordinate  $t$  and  $\phi$  is the circular motion of the fluid. Assuming that the system rotates around the  $z$  axis, the angular velocity  $\Omega$  of the fluid is defined as:

$$\Omega := \frac{d\phi}{dt}. \quad (\text{C.36})$$



In what follows, we will be dealing with spacetime that is stationary, axysymmetric and circular, since there is no fluid motion in the meridional surfaces, i.e. no convection, as ensured by Eq. (C.36). We can then label a point in spacetime with the set of coordinates  $(t, \phi)$  and complete it with the coordinates  $(r, \theta)$ , such that the full coordinate system has  $(x^\mu) = (t, r, \theta, \phi)$ . Another important consequence of circular spacetimes is that some metric potentials are identically zero,

$$g_{tr} = g_{t\theta} = g_{\phi r} = g_{\phi\theta} = 0 \quad (\text{no meridional motion}).$$

### C.3.1 Quasi-isotropic and Maximum slice coordinates

In a 2D surface corresponding to the coordinates  $(r, \theta)$ , the line element induced  $g_{\mu\nu}$  can be written as:

$$g_{\alpha\beta} dx^\alpha dx^\beta = A^2(dr^2 + r^2 d\theta^2), \quad (\text{C.37})$$

with  $A$  being a function of  $A(r, \theta)$ . Note that  $g_{rr} = A^2$  and  $g_{\theta\theta} = A^2 r^2$ , i.e.  $g_{\theta\theta} = r^2 g_{rr}$ . In this context, the coordinates  $(x^\mu) = (t, r, \theta, \phi)$  are called quasi-isotropic coordinates (QI).

In order to determine the metric potentials related to the coordinates  $(t, \phi)$ , one defines a scalar function  $N^\phi = N^\phi(r, \theta)$

$$N^\phi(r, \theta) := -\frac{\vec{\xi} \cdot \vec{\chi}}{\vec{\chi} \cdot \vec{\chi}}, \quad (\text{C.38})$$

in terms of the time and azimuth Killing vectors,  $\vec{\xi}$  and  $\vec{\chi}$ , respectively. Since  $g_{t\phi} = \vec{\xi} \cdot \vec{\chi}$  and  $g_{\phi\phi} = \vec{\chi} \cdot \vec{\chi}$ , then  $g_{t\phi} = -N^\phi g_{\phi\phi}$ , with  $g_{\phi\phi}$  chosen to be:

$$g_{\phi\phi} := \lambda^2 r^2 \sin^2 \theta, \quad (\text{C.39})$$

where  $B(r, \theta)$  is a function of the coordinates  $(r, \theta)$ . Note that, for  $A \rightarrow 1$  and  $\lambda \rightarrow 1$ , Eqs. (C.37) and (C.39) reduce to the metric components in flat spacetime as shown in Eq. (B.4). As a consequence, a circular stationary and axysymmetric 4-metric can be cast in the form:

$$ds^2 = -N^2 dt^2 + A^2(dr^2 + r^2 d\theta^2) + \lambda^2 r^2 \sin^2 \theta (d\phi - N^\phi dt)^2, \quad (\text{C.40})$$

with  $N(r, \theta)$ ,  $A(r, \theta)$ ,  $\lambda(r, \theta)$  and  $N^\phi(r, \theta)$  function only of  $(r, \theta)$ . Comparing with the metric in the 3+1 formalism in Eq. (C.18), we have that  $N$  corresponds to the lapse function, and the shift vector has components:

$$\beta^i = (0, 0, -N^\phi), \quad (\text{C.41})$$

where the spatial 3-D metric  $\gamma_{ij}$  is:

$$\gamma^{ij} = A^2(dr^2 + r^2 d\theta^2) + \lambda^2 r^2 \sin^2 \theta d\phi^2, \quad (\text{C.42})$$

and its inverse:

$$\gamma_{ij} = \frac{1}{A^2}(dr^2 + \frac{1}{r^2}d\theta^2) + \frac{1}{\lambda^2 r^2 \sin^2 \theta} d\phi^2. \quad (\text{C.43})$$

As a result, we can evaluate the extrinsic curvature as given in Eq. (C.44):

$$K_{ij} = \frac{1}{2N} \left( -N^\phi \frac{\partial \gamma_{ij}}{\partial \phi} + \gamma_{kj} \frac{\partial (-N^\phi)}{\partial x^i} + \gamma_{ik} \frac{\partial (-N^\phi)}{\partial x^j} \right), \quad (\text{C.44})$$

which, due to the fact that the spacetime is axysymmetric, i.e.,  $\partial\gamma_{ij}/\partial\phi = 0$ , and  $\gamma_{ij}$  diagonal, the non-zero components of  $K_{ij}$  are:

$$K_{r\phi} = -\frac{\lambda^2 r^2 \sin^2 \theta}{2N} \frac{\partial N^\phi}{\partial r}, \quad (\text{C.45})$$

and

$$K_{\theta\phi} = -\frac{\lambda^2 r^2 \sin^2 \theta}{2N} \frac{\partial N^\phi}{\partial \theta}, \quad (\text{C.46})$$

with the properties  $K_{r\phi} = K_{\phi r}$  and  $K_{\theta\phi} = K_{\phi\theta}$ . Note that the diagonal elements of the extrinsic curvature tensor, i.e.,  $K_{rr}$ ,  $K_{\theta\theta}$  and  $K_{\phi\phi}$ , are identically zero. Therefore, the trace  $K = \gamma^{ij} K_{ij}$  becomes  $K = 0$ . In addition, the term  $K_{ij} K^{ij}$ , which appears in the Hamiltonian constraint in Eq. (C.33) reads:

$$\begin{aligned} K_{ij} K^{ij} &= \gamma^{ii} \gamma^{jj} K_{ij} K_{ij} \\ &= 2(\gamma^{rr} \gamma^{\theta\theta} K_{r\theta} K_{r\theta} + \gamma^{\theta\theta} \gamma^{\phi\phi} K_{\theta\phi} K_{\theta\phi}) \\ &= \frac{\lambda^2 r^2 \sin^2 \theta}{2A^2 N^2} \left[ \left( \frac{\partial N^\phi}{\partial r} \right)^2 + \left( \frac{1}{r} \frac{\partial N^\phi}{\partial \theta} \right)^2 \right]. \end{aligned} \quad (\text{C.47})$$

The choice of the coordinates in General Relativity is not only crucial to write the gravitational equations in an advantageous form, but it can also make the problem easier to solve numerically. In our case, due to the symmetry of the problem, a polar-spherical type coordinates is chosen, namely, the Maximal-Slicing-Quasi-Isotropic coordinates (MSQI).

By *isotropic coordinates* we refer to the choice of the spatial coordinate  $(r, \theta, \phi)$ , which makes possible to write the spatial part of the metric  $\gamma_{\mu\nu}$  (see Eq. (C.11)) in terms of 3 independent components by imposing the isothermal gauge  $\gamma_{r\theta} = \gamma_{r\phi} = 0$  and  $\gamma_{\theta\theta} = r^2 \gamma_{rr}$ . For *maximum slice*, we refer to the extrinsic curvature (also defined in Eq. (C.44)), i.e., a condition is imposed on the *extrinsic curvature* so that  $\text{Tr} K_{\mu\nu} = 0$ . This condition represents the extremal of the volume element in 3D defined as  $V = \int_{\Sigma} \sqrt{-\gamma} d^3x$ , i.e.,  $\partial_t V = 0$  if  $K_{\mu}^{\mu} = 0$ . In other words, it is a way to avoid a singularity.

## C.4 Einstein field equations in 3+1 formalism

In this section we deduce the Einstein's equations in the 3+1 formalism. We begin with the trace (with respect to the 3-D metric  $\gamma^{ij}$ ) of the evolution equation Eq. (C.35) to obtain:

$$D_i D^i N = N [R + 4\pi(S - 3E)], \quad (\text{C.48})$$

that, by using the expression for  $R$  in the momentum constrain equation (Eq. C.34), becomes:

$$D_i D^i N = N [4\pi(S + E) + K_{ij} K^{ij}], \quad (\text{C.49})$$

where the 3D Laplacian  $D_i D^i N$  is given by the standard formula:

$$D_i D^i N = \frac{1}{\sqrt{\gamma}} \frac{\partial}{\partial x^i} \left( \sqrt{\gamma} \gamma^{ij} \frac{\partial N}{\partial x^j} \right), \quad (\text{C.50})$$

with  $x^i = (r, \theta, \phi)$  being the spatial coordinates. Since  $N = N(r, \theta)$  (and then  $\partial N / \partial \phi = 0$ ) and  $\gamma^{ij}$  is diagonal, the non-vanishing components of the Laplacian in Eq. (C.50) are:

$$D_r D^r N = \frac{1}{A^2} \left[ \frac{1}{\lambda} \frac{\partial \lambda}{\partial r} \frac{\partial N}{\partial r} + \frac{2}{r} \frac{\partial N}{\partial r} + \frac{\partial^2 N}{\partial r^2} \right], \quad (\text{C.51})$$

and

$$D_\theta D^\theta N = \frac{1}{A^2} \left[ \frac{1}{\lambda r^2} \frac{\partial \lambda}{\partial \theta} \frac{\partial N}{\partial \theta} + \frac{1}{r^2 \tan \theta} \frac{\partial N}{\partial \theta} + \frac{1}{r^2} \frac{\partial^2 N}{\partial \theta^2} \right]. \quad (\text{C.52})$$

Making use of Eqs. (C.51), (C.52) and (C.47), Eq. (C.49) becomes:

$$\begin{aligned} & \frac{\partial^2 N}{\partial r^2} + \frac{1}{r^2} \frac{\partial^2 N}{\partial \theta^2} + \frac{2}{r} \frac{\partial N}{\partial r} + \frac{1}{r^2 \tan \theta} \frac{\partial N}{\partial \theta} = \\ & 4\pi N A^2 (E + S) + \frac{\lambda^2 r^2 \sin^2 \theta}{2A^2 N^2} \left[ \left( \frac{\partial N^\phi}{\partial r} \right)^2 + \left( \frac{1}{r} \frac{\partial N^\phi}{\partial \theta} \right)^2 \right] \\ & - \frac{\partial \ln \lambda}{\partial \theta} \frac{\partial N}{\partial \theta} - \frac{1}{r^2} \frac{\partial \ln \lambda}{\partial \theta} \frac{\partial N}{\partial \theta}, \end{aligned} \quad (\text{C.53})$$

where the relation  $(1/\lambda)\partial\lambda/\partial r = \partial \ln \lambda / \partial r$  was used.

Now, let's focus our attention on the Hamiltonian constrains in Eq. (C.33) to determine the scalar curvature  $R$ , which is related to the Ricci tensor as in Eq. (B.25) with the corresponding exchange  $g^{\mu\nu} \rightarrow \gamma^{ij}$  and  $R_{\mu\nu} \rightarrow R_{ij}$ , i.e.,  $R = \gamma^{ij} R_{ij}$ . The Ricci tensor, in turn, is written in terms of the Riemann tensor as in Eq. (B.25), which depends only on the Christofel symbols as in Eq. (B.23). The Christofel symbols are functions of the metric tensor and its derivatives as in Eq. (B.22). As a result, by using the 3D metric  $\gamma^{ij}$ , we obtain the 3D Christoffel symbols, which are used to calculate both the spatial Riemann tensor and, finally, the 3D Ricci tensor  $R$ . In this case, the Hamiltonian constrain (Eq. (C.33)) reads:

$$\begin{aligned} & \frac{1}{A} \left[ \frac{\partial^2 A}{\partial r^2} + \frac{1}{r} \frac{\partial A}{\partial r} - \frac{1}{A} \left( \frac{\partial A}{\partial r} \right)^2 + \frac{1}{r^2} \frac{\partial^2 A}{\partial \theta^2} - \frac{1}{Ar^2} \left( \frac{\partial A}{\partial \theta} \right)^2 \right] \\ & + \frac{1}{\lambda} \left( \frac{\partial^2 \lambda}{\partial r^2} + \frac{3}{r} \frac{\partial \lambda}{\partial r} + \frac{1}{r^2} \frac{\partial^2 \lambda}{\partial \theta^2} + \frac{2}{r^2 \tan \theta} \frac{\partial \lambda}{\partial \theta} \right) \\ & + \frac{\lambda^2 r^2 \sin^2 \theta}{2A^2 N^2} \left[ \left( \frac{\partial N^\phi}{\partial r} \right)^2 + \left( \frac{1}{r} \frac{\partial N^\phi}{\partial \theta} \right)^2 \right] \\ & = -8\pi A^2 E. \end{aligned} \quad (\text{C.54})$$

The only equation left up to now is the momentum constrain in Eq. (C.34). As already calculated, we have that  $K = 0$ , which simplifies Eq. (C.34). However, in order to evaluate the term  $D_j K_i^j$ , we make use of the standard expression for the divergence of a symmetric tensor:

$$D_j K_i^j = \frac{1}{\sqrt{\gamma}} \frac{\partial}{\partial x^j} (\sqrt{\gamma} K_i^j) - \frac{1}{2} \frac{\partial \gamma_{ik}}{\partial x^i} K^{jk}, \quad (\text{C.55})$$

to obtain

$$D_j K_i^j = \frac{1}{\sqrt{\gamma}} \frac{\partial}{\partial r} (\sqrt{\gamma} K_i^r) + \frac{1}{\sqrt{\gamma}} \frac{\partial}{\partial \theta} (\sqrt{\gamma} K_i^\theta), \quad (\text{C.56})$$

where we have used that the 3D metric is diagonal, the extrinsic curvature tensor has non-vanishing components for non-diagonal terms and the system is axysymmetric. According to these conditions, terms such as  $(\partial\gamma_{r\theta}/\partial r)K^{r\theta}$ ,  $(\partial\gamma_{\theta\theta}/\partial r)K^{\theta\theta}$  and  $\partial/\partial\phi$  are identically zero.

The term  $K_i^r$  is non-zero only for the component  $K_\phi^r$  and  $K_\phi^\theta$ . For example,  $K_r^r = \gamma^{r\alpha}K_{\alpha r}$ , but  $\gamma^{r\alpha}$  is diagonal, what implies that  $\alpha = r$  for non-trivial solutions. As a consequence, we have  $K_{\alpha r} = K_{rr} = 0$  and, therefore,  $K_r^r = 0$ . The same argument is valid for the other zero components. Finally, among all combinations, the only non-zero component of the divergent  $D_j K_i^j$  is such that  $i = \phi$ :

$$D_j K_\phi^j = \frac{1}{\sqrt{\gamma}} \frac{\partial}{\partial r} (\sqrt{\gamma} K_\phi^r) + \frac{1}{\sqrt{\gamma}} \frac{\partial}{\partial \theta} (\sqrt{\gamma} K_\phi^\theta) = 8\pi p_\phi, \quad (\text{C.57})$$

where we used the fact that  $D_j K_\phi^j = 8\pi p_\phi$  as in Eq. C.34. More importantly, see that there is no momentum in  $r$  and  $\theta$  directions. This is a consequence of the axysymmetry adopted throughout this work.

Then, we have that:

$$\begin{aligned} K_\phi^r &= \gamma^{r\alpha} K_{\alpha\phi} = \gamma^{rr} K_{r\phi}, \\ K_\phi^\theta &= \gamma^{\theta\alpha} K_{\alpha\phi} = \gamma^{\theta\theta} K_{\theta\phi}, \end{aligned}$$

which with the help of Eqs. (C.45)-(C.46) and (C.43), allows Eq. (C.57) to be written as:

$$\begin{aligned} &\frac{\sin^2 \theta}{2A^2 \lambda r^2} \frac{\partial}{\partial r} \left( \frac{\lambda^3 r^4}{N} \frac{\partial N^\phi}{\partial r} \right) + \frac{1}{2A^2 \lambda \sin \theta} \frac{\partial}{\partial \theta} \left( \frac{\lambda^3}{N} \sin^3 \theta \frac{\partial N^\phi}{\partial \theta} \right) \\ &= -8\pi p_\phi, \end{aligned}$$

which, multiplying by the factor  $A^2 \lambda / r \sin \theta$ , can be rewritten as:

$$\begin{aligned} &\frac{\sin \theta}{r^3} \frac{\partial}{\partial r} \left( \frac{\lambda^3 r^4}{N} \frac{\partial N^\phi}{\partial r} \right) + \frac{1}{r \sin^2 \theta} \frac{\partial}{\partial \theta} \left( \frac{\lambda^3}{N} \sin^3 \theta \frac{\partial N^\phi}{\partial \theta} \right) \\ &= -16\pi A^2 \lambda \frac{p_\phi}{r \sin \theta}. \end{aligned} \quad (\text{C.58})$$

At last, we consider in Eq. (C.35) the components  $i = j = \phi$  such that the Lie Derivative of the extrinsic curvature (left hand side term) is given by:

$$\mathcal{L}_{\vec{\beta}} K_{\phi\phi} = \left( \beta^k \frac{\partial K_{\phi\phi}}{\partial x^k} + K_{k\phi} \frac{\partial \beta^k}{\partial \phi} + K_\phi \frac{\partial \beta^k}{\partial \phi} \right) = 0,$$

where we have replaced  $\gamma_{ij}$  by  $K_{ij}$  in Eq. (C.44) to obtain  $\mathcal{L}_{\vec{\beta}} K_{ij}$  and the fact that  $K_{\phi\phi} = 0$  and the shift vector  $\beta^k$  is a function only of  $(r, \theta)$ . In this case, Eq. (C.35) becomes:

$$\begin{aligned} D_\phi D_\phi N &= N(R_{\phi\phi} - 2K_{\phi k} K_\phi^k) \\ &\quad - 8\pi N(S_{\phi\phi} - \frac{1}{2}\gamma_{\phi\phi}(S - E)) \\ &= N(R_{\phi\phi} - 2K_{\phi k} K_\phi^k) \\ &\quad + 4\pi N \lambda^2 r^2 \sin^2 \theta (S_r^r + S_\theta^\theta - S_\phi^\phi - E), \end{aligned} \quad (\text{C.59})$$

where we have made use of the expressions  $S = S_r^r + S_\theta^\theta + S_\phi^\phi$  and  $\gamma_{\phi\phi} = \lambda^2 r^2 \sin^2 \theta$ . We need now to determine  $R_{\phi\phi}$ ,  $K_{\phi k} K_\phi^k$  and  $D_\phi D_\phi N$ . For  $D_\phi D_\phi N$ , we can make use of the fact that the covariant derivative of a scalar field coincides with the partial derivative of this scalar, i.e.,  $D_i N = \partial_i N$ . In

this case, by using the definition of the covariant derivative of a vector field, we find:

$$\begin{aligned}
D_\phi(D_\phi N) &= \partial_\phi(\overbrace{\partial_\phi N}^0) - \Gamma_{\phi\phi}^i \partial_i N \\
&= -\Gamma_{\phi\phi}^r \partial_r N - \Gamma_{\phi\phi}^\theta \partial_\theta N \\
&= \frac{\lambda^2 r^2 \sin^2 \theta}{A^2} \left[ \frac{\partial N}{\partial r} \left( \frac{1}{\lambda} \frac{\partial \lambda}{\partial r} + \frac{1}{r} \right) + \frac{\partial N}{\partial \theta} \frac{1}{r^2} \left( \frac{1}{\lambda} \frac{\partial \lambda}{\partial \theta} + \frac{1}{\tan \theta} \right) \right], \tag{C.60}
\end{aligned}$$

and

$$\begin{aligned}
K_{\phi k} K_\phi^k &= \gamma^{rr} (K_{r\phi})^2 + \gamma^{\theta\theta} (K_{\theta\phi})^2 \\
&= \frac{\lambda^2 r^4 \sin^2 \theta}{4A^2 N^2} \left[ \left( \frac{\partial N^\phi}{\partial r} \right)^2 + \left( \frac{1}{r} \frac{\partial N^\phi}{\partial \theta} \right)^2 \right], \tag{C.61}
\end{aligned}$$

and from Eqs. (B.25), (B.23), (B.22), the Ricci tensor  $R_{\phi\phi}$  becomes:

$$R_{\phi\phi} = \frac{-\lambda r^2 \sin^2 \theta}{A^2} \left( \frac{\partial^2 \lambda}{\partial r^2} + \frac{3}{r} \frac{\partial \lambda}{\partial r} + \frac{1}{r^2} \frac{\partial^2 \lambda}{\partial \theta^2} + \frac{2}{r^2 \tan \theta} \frac{\partial \lambda}{\partial \theta} \right) \tag{C.62}$$

Finally, with Eqs. (C.60), (C.61) and (C.62), Eq. (C.59) can be cast in the form:

$$\begin{aligned}
&\frac{1}{N} \left[ \frac{\partial N}{\partial r} \left( \frac{1}{\lambda} \frac{\partial \lambda}{\partial r} + \frac{1}{r} \right) + \frac{\partial N}{\partial \theta} \frac{1}{r^2} \left( \frac{1}{\lambda} \frac{\partial \lambda}{\partial \theta} + \frac{1}{\tan \theta} \right) \right] = \\
&- \frac{1}{\lambda} \left( \frac{\partial^2 \lambda}{\partial r^2} + \frac{3}{r} \frac{\partial \lambda}{\partial r} + \frac{1}{r^2} \frac{\partial^2 \lambda}{\partial \theta^2} + \frac{2}{r^2 \tan \theta} \frac{\partial \lambda}{\partial \theta} \right) \\
&- \frac{\lambda^2 r^2 \sin^2 \theta}{2N^2} \left[ \left( \frac{\partial N^\phi}{\partial r} \right)^2 + \left( \frac{1}{r} \frac{\partial N^\phi}{\partial \theta} \right)^2 \right] \\
&+ 4\pi A^2 (S_r^r + S_\theta^\theta - S_\phi^\phi - E), \tag{C.63}
\end{aligned}$$

which, using the short notation defined as:

$$\partial f \partial g := \frac{\partial f}{\partial r} \frac{\partial g}{\partial r} + \frac{1}{r^2} \frac{\partial f}{\partial \theta} \frac{\partial g}{\partial \theta}, \tag{C.64}$$

we get:

$$\begin{aligned}
&\frac{1}{N\lambda} \partial \lambda \partial N + \frac{1}{Nr} \left( \frac{\partial N}{\partial r} + \frac{1}{r \tan \theta} \frac{\partial N}{\partial \theta} \right) \\
&+ \frac{1}{\lambda} \left( \frac{\partial^2 \lambda}{\partial r^2} + \frac{3}{r} \frac{\partial \lambda}{\partial r} + \frac{1}{r^2} \frac{\partial^2 \lambda}{\partial \theta^2} + \frac{2}{r^2 \tan \theta} \frac{\partial \lambda}{\partial \theta} \right) \\
&+ \frac{\lambda^2 r^2 \sin^2 \theta}{2N^2} \partial N^\phi \partial N^\phi \\
&= 4\pi A^2 (S_r^r + S_\theta^\theta - S_\phi^\phi - E), \tag{C.65}
\end{aligned}$$

Note that Eqs.(C.53), (C.54), (C.58) and (C.65) are equations for the four (unknowns) metric potentials  $N, \lambda, A$  and  $N^\phi$  as already shown in Eq. (C.40). To obtain the final gravitational equations,

we first multiply Eq. (C.53) by  $\lambda$  and Eq. (C.65) by  $N\lambda$ . Then we add both to get:

$$\begin{aligned} & \left[ \frac{\partial^2}{\partial r^2} + \frac{3}{r} \frac{\partial}{\partial r} + \frac{1}{r^2} \frac{\partial^2}{\partial \theta^2} + \frac{2}{r^2 \tan \theta} \frac{\partial}{\partial \theta} \right] (N\lambda) \\ & = 8\pi A^2 N\lambda (S_r^r + S_\theta^\theta). \end{aligned} \quad (\text{C.66})$$

Next, we divide Eq. (C.53) by  $N$ , we add it to Eq. (C.54) and, from the result, we subtract Eq. (C.65) to yield:

$$\begin{aligned} & \frac{1}{N} \frac{\partial^2 N}{\partial r^2} + \frac{1}{rN} \frac{\partial N}{\partial r} + \frac{1}{r^2 N} \frac{\partial^2 N}{\partial \theta^2} + \frac{1}{A} \frac{\partial^2 A}{\partial r^2} + \frac{1}{rA} \frac{\partial A}{\partial r} + \frac{1}{r^2 A} \frac{\partial^2 A}{\partial \theta^2} \\ & = 8\pi A^2 S_\phi^\phi + \frac{1}{A^2} \partial A \partial A + \frac{3\lambda^2 r^2 \sin^2 \theta}{24N^2} \partial N^\phi \partial N^\phi. \end{aligned} \quad (\text{C.67})$$

Finally, the final system of equations is achieved by rearranging Eq. (C.66) to obtain:

$$\Delta_2[(N\lambda - 1)r \sin \theta] = 8\pi N A^2 \lambda r \sin \theta (S_r^r + S_\theta^\theta). \quad (\text{C.68})$$

Rearranging Eq. (C.67) we get

$$\Delta_2[\ln A + \nu] = 8\pi A^2 S_\phi^\phi + \frac{3\lambda^2 r^2 \sin^2 \theta}{4N^2} \partial N^\phi \partial N^\phi - \partial \nu \partial \nu, \quad (\text{C.69})$$

and, in closing, reorganizing Eq. (C.53) and Eq. (C.58), we obtain:

$$\Delta_3 \nu = 4\pi A^2 (E + S) + \frac{\lambda^2 r^2 \sin^2 \theta}{2N^2} \partial N^\phi \partial N^\phi - \partial \nu \partial (\nu + \ln \lambda), \quad (\text{C.70})$$

and

$$\left[ \Delta_3 - \frac{1}{r^2 \sin^2 \theta} \right] (N^\phi r \sin \theta) = -16\pi \frac{N A^2}{\lambda^2} \frac{p_\phi}{r \sin \theta} + r \sin \theta \partial N^\phi \partial (\nu - 3 \ln \lambda), \quad (\text{C.71})$$

where the short notation was introduced:

$$\Delta_2 = \frac{\partial^2}{\partial r^2} + \frac{1}{r} \frac{\partial}{\partial r} + \frac{1}{r^2} \frac{\partial^2}{\partial \theta^2} \quad (\text{C.72})$$

$$\Delta_3 = \frac{\partial^2}{\partial r^2} + \frac{2}{r} \frac{\partial}{\partial r} + \frac{1}{r^2} \frac{\partial^2}{\partial \theta^2} + \frac{1}{r^2 \tan \theta} \frac{\partial}{\partial \theta} \quad (\text{C.73})$$

$$\nu = \ln N. \quad (\text{C.74})$$

In addition, in the final gravitational field equation system, Eqs. (C.68)-(C.71), terms like  $\partial N^\phi \partial N^\phi$  defined in Eq. (C.64) were used. Finally, the equation of motion for the matter,  $\nabla_\mu T^{\mu\nu} = 0$ , in the MSQI coordinates is given by:

$$\frac{N}{\sqrt{\gamma}} \frac{\partial}{\partial x^j} (\sqrt{\gamma} S_i^i) - \frac{N}{2} \frac{\partial \gamma_{jk}}{\partial x^i} S^{jk} + S^{jk} \frac{\partial N}{\partial x^j} + E \frac{\partial N}{\partial x^i} + J_\phi \frac{\partial N^\phi}{\partial x^i} = 0, \quad (\text{C.75})$$

where  $x^i$  stands for  $r$  and  $\theta$ . In the next pages this equation of motion is applied to a perfect fluid with and without a magnetic field.

## C.5 Application to astrophysical cases

### C.5.1 Perfect fluid without magnetic field

The first and simplest case we can treat is the perfect fluid without magnetic field. In this case, we have the energy-momentum tensor:

$$T^{\mu\nu} = (e + p) u^\mu u^\nu + p g^{\mu\nu}, \quad (\text{C.76})$$

with  $u^\mu = (u^t, 0, 0, u^\phi)$  being the fluid four-velocity for the fluid comoving observer  $\mathcal{O}_1$ . In our coordinate, the Eulerian observer  $\mathcal{O}_0$  (the observer with four-velocity  $n_\mu$ ) is related to the  $\mathcal{O}_1$  observer by the Lorentz factor,

$$\Gamma := -n_\mu u^\mu = N u^t. \quad (\text{C.77})$$

Then, fluid velocity  $U$  measured by  $\mathcal{O}_0$  is:

$$U = \frac{A^2 \lambda r \sin \theta}{N} (\Omega - N^\phi), \quad (\text{C.78})$$

and with the normalization of the 4-velocity  $u_\mu u^\mu = -1$  we get  $\Gamma = (1 - U^2)^{-\frac{1}{2}}$ . In this scenario, the energy density, momentum density and stress tensor of a perfect fluid (PF) as described by Eq. (C.76) are obtained from Eqs. (C.12)-(C.14):

$$E^{PF} = \Gamma^2 (e + p) - p, \quad (\text{C.79})$$

$$J_\phi^{PF} = (E + p) A^2 \lambda r \sin \theta U, \quad (\text{C.80})$$

$$S_r^{PF} = p = S_\theta^\theta, \quad S_\phi^{PF} = p + (E + p) U^2. \quad (\text{C.81})$$

Then, the equation of motion (C.75) becomes:

$$\frac{1}{e + p} \left( \frac{\partial p}{\partial x^i} \right) + \frac{\partial \nu}{\partial x^i} - \frac{\partial}{\partial x^i} \ln \Gamma = -F \frac{\partial \Omega}{\partial x^i}, \quad (\text{C.82})$$

with  $F = u_\phi u^t = \frac{A^2 \lambda}{N} \Gamma^2 U r \sin \theta$ . Defining the heat function as

$$H(n) := \int_0^n \frac{1}{e(n') + (pn')} \frac{dp}{dn} (n') dn', \quad (\text{C.83})$$

which can be written as  $H(n) = \ln f(n)$ , being  $f(n) := \frac{e+p}{n}$  the relativistic enthalpy per baryon. As a result, the equation of motion is:

$$\frac{\partial}{\partial x^i} (H + \nu - \ln \Gamma) = -F \frac{\partial \Omega}{\partial x^i}, \quad (\text{C.84})$$

and, as usual,  $x^i$  are de radial and angular coordinates  $r$  and  $\theta$ . Integrating the above equation for the case of uniform rotation, i.e.,  $\Omega = cte$  we have:

$$H(r, \theta) + \nu(r, \theta) - \ln \Gamma(r, \theta) = C. \quad (\text{C.85})$$

In Chapter 2, it is shown that the constant  $C$  can be calculated at every point in the star. We will treat now the equation of motion taking into account a perfect fluid endowed with a magnetic field.

### C.5.2 Perfect fluid with magnetic field

Carter (1973), showed that the most general electric current for stationary, axisymmetry spacetime is given by:

$$j^\mu = (j^t, 0, 0, j^\phi). \quad (\text{C.86})$$

There it is also shown that the electromagnetic field tensor  $F_{\alpha\beta}$  must come from the potential  $A_\alpha$ , which has the property:  $A_\alpha = A_t dt + A_\phi d\phi$ . In this case, the electric field measured by the observer  $\mathcal{O}_0$  (Lichnerowicz et al., 1967) is:

$$E_\alpha = F_{\alpha\beta} n^\beta = \left( 0, \frac{1}{N} \left[ \frac{\partial A_t}{\partial r} + N^\phi \frac{\partial A_\phi}{\partial r} \right], \frac{1}{N} \left[ \frac{\partial A_t}{\partial \theta} + N^\phi \frac{\partial A_\phi}{\partial \theta} \right], 0 \right), \quad (\text{C.87})$$

and the magnetic field given by:

$$B_\alpha = -\frac{1}{2} \epsilon_{\alpha\beta\gamma\sigma} F^{\gamma\sigma} n^\beta = \left( 0, \frac{1}{A^2 \lambda r^2 \sin \theta} \frac{\partial A_\phi}{\partial \theta}, -\frac{1}{A^2 \lambda \sin \theta} \frac{\partial A_\phi}{\partial r}, 0 \right), \quad (\text{C.88})$$

where  $\epsilon_{\alpha\beta\gamma\sigma}$  is the Levi - Civita tensor related to the metric  $g_{\mu\nu}$ . Assuming that matter inside the star has infinite conductivity, the electric field measured by the coming observer  $\mathcal{O}_1$  must be zero, i.e.  $E'_\alpha = F_{\alpha\beta} n^\beta = 0$ . This condition leads to the following relation of the 4-vector potential inside the star:

$$\frac{\partial A_t}{\partial x^i} = -\Omega \frac{\partial A_\phi}{\partial x^i}, \quad (\text{C.89})$$

which for the case of rigid rotation,  $\Omega = \text{const}$ , becomes (up to some additive constant):

$$A_t = -\Omega A_\phi. \quad (\text{C.90})$$

### C.5.3 Maxwell equations

$F_{\mu\nu}$  can be derived from the potential  $F_{\mu\nu} = A_{\nu,\mu} - A_{\mu,\nu}$ , so that the Maxwell equation

$$F_{\alpha\beta;\gamma} + F_{\beta\gamma;\alpha} + F_{\gamma\alpha;\beta} = 0, \quad (\text{C.91})$$

is automatically satisfied. The remaining Maxwell equations,

$$F_{;\beta}^{\alpha\beta} = 4\pi j^\alpha, \quad (\text{C.92})$$

can be expressed in terms of the two non- vanishing components of the magnetic vector potential  $A_\mu$ . For example, the Maxwell-Gauss equation for  $A_t$  reads (Lichnerowicz et al., 1967):

$$\begin{aligned} \Delta_3 A_t = & -\mu_0 A^2 (g_{tt} j^t + g_{t\phi} j^\phi) \\ & - \frac{\lambda^2}{N^2} N^\phi r^2 \sin^2 \theta \partial A_t \partial N^\phi \\ & - \left( 1 + \frac{\lambda^2}{N^2} r^2 \sin^2 \theta (N^\phi)^2 \right) \partial A_\phi \partial N^\phi \\ & - (\partial A_t + 2N^\phi \partial A_\phi) \partial (\ln \lambda - \nu) \\ & - 2 \frac{N^\phi}{r} \left( \frac{\partial A_\phi}{\partial r} + \frac{1}{r \tan \theta} \frac{\partial A_\phi}{\partial r} \right), \end{aligned} \quad (\text{C.93})$$



and from the Maxwell-Ampere equation, we have an equation for  $A_\phi$ :

$$\begin{aligned} \left[ \Delta_3 - \frac{1}{r^2 \sin^2 \theta} \right] \left( \frac{A_\phi}{r \sin \theta} \right) &= -\mu_0 A^2 \lambda^2 (j^\phi - N^\phi j^t) r \sin \theta \\ &\quad - \frac{\lambda^2}{N^2} r \sin \theta \partial N^\phi (\partial A_t + N^\phi \partial A_\phi) \\ &\quad + \frac{1}{r} \partial A_\phi \partial (\ln \lambda - \nu). \end{aligned} \quad (\text{C.94})$$

In this approach, the equation of motion can be deduced from (C.85) by adding the Lorentz force term  $f_\alpha = F_{\alpha\beta} j^\beta$ :

$$\frac{\partial}{\partial x^i} (H + \nu - \ln \Gamma) - \frac{1}{e+p} (j^\phi - \Omega j^t) \frac{\partial A_\phi}{\partial x^i} = 0. \quad (\text{C.95})$$

The integrability condition says the last term can be written in terms of a function  $M(r, \theta)$ :

$$-\frac{1}{e+p} (j^\phi - \Omega j^t) \frac{\partial A_\phi}{\partial x^i} = \frac{\partial M}{\partial x^i}. \quad (\text{C.96})$$

As already discussed in Chapter 2, there is a current function  $f : \mathbb{R} \rightarrow \mathbb{R}$  such that

$$j^\phi - \Omega j^t = (e+p) f(A_\phi), \quad (\text{C.97})$$

with  $A_\phi$  being the magnetic vector potential and  $f(x)$  an arbitrary function  $f(A_\phi)$  that needs to be chosen (Bocquet et al., 1995). In our case, we construct stellar models for constant values of  $f(A_\phi) = f_0$ . As shown by Bocquet et al. (1995), the current function can have a more complex structure, however this does not affect significantly the global properties of stars.

As a result, integrating the equation of motion on gets:

$$H(r, \theta) + \nu(r, \theta) - \ln \Gamma(r, \theta) + M(r, \theta) = \text{const}, \quad (\text{C.98})$$

where

$$M(r, \theta) = M(A_\phi(r, \theta)) := \int_0^{A_\phi(r, \theta)} f(x) dx \quad (\text{C.99})$$

To make clear why these current function  $f(x)$  and the magnetic potential function  $M(r, \theta)$  appear in the problem, in Appendix A we showed in Newtonian physics that the electric current in magnetized stars is also related to a current function (see Eq. (A.22)). In this case, one has the correspondence  $u \rightarrow A_\phi$  and  $k_0 \rightarrow f(x)$ .

The stress-energy tensor of the magnetic field is calculated using the standard formula:

$$T_{\alpha\beta}^{EM} = \frac{1}{4\pi} \left( F_{\alpha\mu} F_{\beta}^{\mu} - \frac{1}{4} F_{\mu\nu} F^{\mu\nu} g_{\alpha\beta} \right), \quad (\text{C.100})$$

from which one can obtain the sources of the gravitational fields. Replacing  $T_{\mu\nu}$  by  $T_{\alpha\beta}^{EM}$  in Eqs. (C.12)-(C.14), the electromagnetic contribution (EM) contribution to the total energy of the system is:

$$E^{EM} = \frac{1}{2\mu_0} B^i B_i, \quad (\text{C.101})$$

while the EM contribution to the momentum density can be written as:

$$J_{\phi}^{EM} = \frac{1}{\mu_0} A^2 (B^r E^{\theta} - E^r B^{\theta}), \quad (\text{C.102})$$

and the stress 3-tensor components are given by:

$$S_r^{EMr} = \frac{1}{2\mu_0} (E^{\theta} E_{\theta} - E^r E_r + B^{\theta} B_{\theta} - B^r B_r) \quad (\text{C.103})$$

$$S_{\theta}^{EM\theta} = \frac{1}{2\mu_0} (E^r E_r - E^{\theta} E_{\theta} + B^r B_r - B^{\theta} B_{\theta}) \quad (\text{C.104})$$

$$S_{\phi}^{EM\phi} = \frac{1}{2\mu_0} (E^i E_i + B^i B_i), \quad (\text{C.105})$$

where the electric and magnetic field components are given in Eq. (C.87) and Eq. (C.88). Moreover, the total energy of the system is  $E = E^{PF} + E^{EM}$ , the total momentum density flux is  $J_{\phi} = J_{\phi}^{PF} + J_{\phi}^{EM}$  and the total stress tensor  $S = S^{PF} + S^{EM}$ .

# Bibliography

- Deborah N Aguilera, José A Pons, and Juan A Miralles. 2d cooling of magnetized neutron stars. *Astronomy & Astrophysics*, 486(1):255–271, 2008.
- Shizuka Akiyama, J Craig Wheeler, David L Meier, and Itamar Lichtenstadt. The magnetorotational instability in core-collapse supernova explosions. *The Astrophysical Journal*, 584(2):954, 2003.
- A. G. Alaverdyan, G. B. Alaverdyan, and A. O. Chiladze. Deconfinement phase transition in neutron stars and delta-meson field in RMF theory. *Int. J. Mod. Phys.*, D19:1557–1561, 2010.
- Mark Alford, David Blaschke, Alessandro Drago, T Klähn, Giuseppe Pagliara, and Juergen Schaffner-Bielich. Astrophysics: Quark matter in compact stars? *Nature*, 445(7125):E7–E8, 2007.
- Leandro Gabriel Althaus, Jorge Alejandro Panei, MM Miller Bertolami, Enrique García-Berro, Alejandro Hugo Córscico, Alejandra Daniela Romero, Souza Oliveira Kepler, and RD Rohrmann. New evolutionary sequences for hot h-deficient white dwarfs on the basis of a full account of progenitor evolution. *The Astrophysical Journal*, 704(2):1605, 2009.
- D. E. Alvarez-Castillo and D. Blaschke. Mixed phase effects on high-mass twin stars. *Phys. Part. Nucl.*, 46(5):846–848, 2015.
- SPS Anand. On Chandrasekhar’s limiting mass for rotating white dwarf stars. *Proceedings of the National Academy of Sciences of the United States of America*, 54(1):23, 1965.
- JRP Angel. Magnetic white dwarfs. *Annual Review of Astronomy and Astrophysics*, 16:487–519, 1978.
- Marcus Ansorg, Dorota Gondek-Rosińska, and Loïc Villain. On the solution space of differentially rotating neutron stars in general relativity. *Monthly Notices of the Royal Astronomical Society*, 396(4):2359–2366, 2009.
- John Antoniadis. On the formation of eccentric millisecond pulsars with helium white-dwarf companions. *The Astrophysical Journal Letters*, 797(2):L24, 2014.
- John Antoniadis, Paulo CC Freire, Norbert Wex, Thomas M Tauris, Ryan S Lynch, Marten H van Kerkwijk, Michael Kramer, Cees Bassa, Vik S Dhillon, Thomas Driebe, et al. A massive pulsar in a compact relativistic binary. *Science*, 340(6131):1233232, 2013.
- GG Arutyunyan, DM Sedrakyan, and ÉV Chubaryan. Rotating superdense configurations in general relativity. *Soviet Astronomy*, 15:390, 1971.
- Narine S. Ayvazyan, Giuseppe Colucci, Dirk H. Rischke, and Armen Sedrakian. Rotating hybrid compact stars. *Astron. Astrophys.*, 559:A118, 2013.
- Walter Baade and Fritz Zwicky. Remarks on super-novae and cosmic rays. *Physical Review*, 46(1):76, 1934.

- Marcello Baldo. Quark matter in neutron stars. In *Perspectives in Hadronic Physics*, pages 189–196. Springer, 2004.
- Marcello Baldo, M Buballa, GF Burgio, F Neumann, M Oertel, and H-J Schulze. Neutron stars and the transition to color superconducting quark matter. *Physics Letters B*, 562(3):153–160, 2003.
- Thomas W Baumgarte, Stuart L Shapiro, and Masaru Shibata. On the maximum mass of differentially rotating neutron stars. *The Astrophysical Journal Letters*, 528(1):L29, 1999.
- Prasanta Bera and Dipankar Bhattacharya. Mass-radius relation of strongly magnetized white dwarfs: nearly independent of Landau quantization. *Mon. Not. Roy. Astron. Soc.*, 445(4):3951–3958, 2014.
- Abhijit Bhattacharyya, Igor N. Mishustin, and Walter Greiner. Deconfinement Phase Transition in Compact Stars : Maxwell vs. Gibbs Construction of the Mixed Phase. *J. Phys.*, G37:025201, 2010.
- Roger D Blandford and Roger W Romani. On the interpretation of pulsar braking indices. *Monthly Notices of the Royal Astronomical Society*, 234(1):57P–60P, 1988.
- M. Bocquet, S. Bonazzola, E. Gourgoulhon, and J. Novak. Rotating neutron star models with magnetic field. *Astron. Astrophys.*, 301:757, 1995.
- I. Bombaci, D. Logoteta, P. K. Panda, C. Providencia, and I. Vidana. Quark matter nucleation in hot hadronic matter. *Phys. Lett.*, B680:448–452, 2009.
- I. Bombaci, G. Lugones, and I. Vidana. Effects of color superconductivity on the nucleation of quark matter in neutron stars. *Astron. Astrophys.*, 462:1017–1022, 2007.
- S. Bonazzola and E. Gourgoulhon. Gravitational waves from pulsars: Emission by the magnetic field induced distortion. *Astron. Astrophys.*, 312:675, 1996.
- S Bonazzola, E Gourgoulhon, M Salgado, and JA Marck. Axisymmetric rotating relativistic bodies: a new numerical approach for 'exact' solutions. *Astronomy and Astrophysics*, 278:421–443, 1993.
- Silvano Bonazzola. The virial theorem in general relativity. *The Astrophysical Journal*, 182:335–340, 1973.
- Silvano Bonazzola and Eric Gourgoulhon. A virial identity applied to relativistic stellar models. *Classical and Quantum Gravity*, 11(7):1775, 1994.
- Silvano Bonazzola, Eric Gourgoulhon, and Jean-Alain Marck. Numerical approach for high precision 3d relativistic star models. *Physical Review D*, 58(10):104020, 1998.
- Kuantay Boshkayev, Jorge A Rueda, Remo Ruffini, and Ivan Siutsou. On general relativistic uniformly rotating white dwarfs. *The Astrophysical Journal*, 762(2):117, 2013.
- Jonathan Braithwaite. The stability of toroidal fields in stars. *Astronomy & Astrophysics*, 453(2):687–698, 2006.
- Alessandro Brillante and Igor N. Mishustin. Radial oscillations of neutral and charged hybrid stars. *Europhys. Lett.*, 105:39001, 2014.
- N Bucciantini and L Del Zanna. General relativistic magnetohydrodynamics in axisymmetric dynamical spacetimes: the x-echo code. *Astronomy & Astrophysics*, 528:A101, 2011.
- Adam Burrows and James M Lattimer. The birth of neutron stars. *The Astrophysical Journal*, 307:178–196, 1986a.

- Adam Burrows and James M. Lattimer. The birth of neutron stars. *Astrophys. J.*, 307:178–196, 1986b.
- Christian Y Cardall, Madappa Prakash, and James M Lattimer. Effects of strong magnetic fields on neutron star structure. *The Astrophysical Journal*, 554(1):322, 2001.
- Brandon Carter. Black hole equilibrium states. *Black holes*, pages 57–214, 1973.
- Pablo Cerdá-Durán, José A Font, Luis Antón, and Ewald Müller. A new general relativistic magnetohydrodynamics code for dynamical spacetimes. *Astronomy & Astrophysics*, 492(3):937–953, 2008.
- James Chadwick. Possible existence of a neutron. *Nature*, 129(3252):312, 1932.
- Somenath Chakrabarty. Quark Matter in Strong Magnetic Field. *Phys. Rev.*, D54:1306–1316, 1996.
- Nicolas Chamel, AF Fantina, and PJ Davis. Stability of super-chandrasekhar magnetic white dwarfs. *Physical Review D*, 88(8):081301, 2013.
- Nicolas Chamel and Pawel Haensel. " physics of neutron star crusts. *Living Rev. Relativity*, 11(10), 2008.
- S. Chandrasekhar. *An Introduction to the Study of Stellar Structure*. Chicago : Univ. Chicago Press, 1939.
- Subrahmanyan Chandrasekhar. The maximum mass of ideal white dwarfs. *The Astrophysical Journal*, 74:81, 1931.
- Debarati Chatterjee, Thomas Elghozi, Jerome Novak, and Micaela Oertel. Consistent neutron star models with magnetic field dependent equations of state. *Mon. Not. Roy. Astron. Soc.*, 447:3785, 2015.
- Debarati Chatterjee and Isaac Vidaa. Do hyperons exist in the interior of neutron stars? *Eur. Phys. J.*, A52(2):29, 2016.
- KS Cheng, YF Yuan, and JL Zhang. Phase transitions in rotating neutron stars: Effects of stellar crusts. *The Astrophysical Journal*, 564(2):909, 2002.
- E. Chubarian, H. Grigorian, Gevorg S. Poghosyan, and D. Blaschke. Deconfinement phase transition in rotating nonspherical compact stars. *Astron. Astrophys.*, 357:968–976, 2000.
- R Ciolfi, V Ferrari, L Gualtieri, and JA Pons. Relativistic models of magnetars: the twisted torus magnetic field configuration. *Monthly Notices of the Royal Astronomical Society*, 397(2):913–924, 2009.
- Riccardo Ciolfi and Luciano Rezzolla. Twisted-torus configurations with large toroidal magnetic fields in relativistic stars. *Monthly Notices of the Royal Astronomical Society: Letters*, 435(1):L43–L47, 2013.
- J. G. Coelho, R. M. Marinho, M. Malheiro, R. Negreiros, D. L. Cáceres, J. A. Rueda, and R. Ruffini. Dynamical Instability of White Dwarfs and Breaking of Spherical Symmetry Under the Presence of Extreme Magnetic Fields. *apj*, 794:86, October 2014a.
- J.G. Coelho, R.M. Marinho, M. Malheiro, R. Negreiros, J.A. Rueda, et al. Dynamical instability of white dwarfs and breaking of spherical symmetry under the presence of extreme magnetic fields. *Astrophys.J.*, 794(1):86, 2014b.

- Gregory B Cook, Stuart L Shapiro, and Saul A Teukolsky. Spin-up of a rapidly rotating star by angular momentum loss-effects of general relativity. *The Astrophysical Journal*, 398:203–223, 1992.
- Gregory B Cook, Stuart L Shapiro, and Saul A Teukolsky. Rapidly rotating neutron stars in general relativity: Realistic equations of state. *The Astrophysical Journal*, 424:823–845, 1994.
- Karsten Danzmann, LISA Study Team, et al. Lisa: laser interferometer space antenna for gravitational wave measurements. *Classical and Quantum Gravity*, 13(11A):A247, 1996.
- Upasana Das and Banibrata Mukhopadhyay. Strongly magnetized cold electron degenerate gas: Mass-radius relation of the magnetized white dwarf. *Phys. Rev.*, D86:042001, 2012.
- Upasana Das and Banibrata Mukhopadhyay. New mass limit for white dwarfs: super-Chandrasekhar type Ia supernova as a new standard candle. *Phys.Rev.Lett.*, 110(7):071102, 2013.
- S. M. de Carvalho, R. Negreiros, M. Orsaria, G. A. Contrera, F. Weber, and W. Spinella. Thermal evolution of hybrid stars within the framework of a nonlocal NambuJona-Lasinio model. *Phys. Rev.*, C92(3):035810, 2015.
- PB Demorest, Tim Pennucci, SM Ransom, MSE Roberts, and JWT Hessels. A two-solar-mass neutron star measured using Shapiro delay. *Nature*, 467(7319):1081–1083, 2010.
- V. Dexheimer, B. Franzon, R. O. Gomes, R. L. S. Farias, S. S. Avancini, and S. Schramm. The Magnetic Field Profile in Strongly Magnetized Neutron Stars. 2016.
- V Dexheimer, DP Menezes, and M Strickland. The influence of strong magnetic fields on proto-quark stars. *Journal of Physics G: Nuclear and Particle Physics*, 41(1):015203, 2013a.
- V. Dexheimer, R. Negreiros, and S. Schramm. Hybrid Stars in a Strong Magnetic Field. *Eur.Phys.J.*, A48:189, 2012a.
- V. Dexheimer, R. Negreiros, and S. Schramm. Role of strangeness in hybrid stars and possible observables. *Phys.Rev.*, C91(5):055808, 2015.
- V. Dexheimer, R. Negreiros, S. Schramm, and M. Hempel. Deconfinement to Quark Matter in Neutron Stars - The Influence of Strong Magnetic Fields. *AIP Conf.Proc.*, 1520:264–269, 2013b.
- V. Dexheimer and S. Schramm. Proto-Neutron and Neutron Stars in a Chiral SU(3) Model. *Astrophys.J.*, 683:943–948, 2008.
- V.A. Dexheimer and S. Schramm. A Novel Approach to Model Hybrid Stars. *Phys.Rev.*, C81:045201, 2010.
- Veronica Dexheimer, Stefan Schramm, and Jirina Stone. Modeling Hybrid Stars. *PoS, NICXII*:101, 2012b.
- Paul AM Dirac. On the theory of quantum mechanics. In *Proceedings of the Royal Society of London A: Mathematical, Physical and Engineering Sciences*, volume 112, pages 661–677. The Royal Society, 1926.
- MV Diwan and CK Jung. Next generation nucleon decay and neutrino detector. nnn99. aip conference proceedings, no. 533 [apcpcs]. Technical report, American Institute of Physics, Melville, NY (US), 2000.
- Robert C. Duncan and Christopher Thompson. Formation of very strongly magnetized neutron stars - implications for gamma-ray bursts. *Astrophys. J.*, 392:L9, 1992.

- Albert Einstein. On the electrodynamics of moving bodies. 1905.
- Albert Einstein. Approximative integration of the field equations of gravitation. *Sitzungsber. Preuss. Akad. Wiss. Berlin (Math. Phys.)*, 688:1916, 1916.
- R. Gonzalez Felipe, A. Perez Martinez, H. Perez Rojas, and M. Orsaria. Magnetized strange quark matter and magnetized strange quark stars. *Phys. Rev.*, C77:015807, 2008.
- Enrico Fermi. Sulla quantizzazione del gas perfetto monoatomico. *Rend. Lincei*, 3:145–149, 1926.
- Attilio Ferrari and Remo Ruffini. Theoretical implications of the second time derivative of the period of the pulsar np 0532. *The Astrophysical Journal*, 158:L71, 1969.
- Efrain J Ferrer, Vivian de La Incera, Jason P Keith, Israel Portillo, and Paul L Springsteen. Equation of state of a dense and magnetized fermion system. *Physical Review C*, 82(6):065802, 2010.
- EJ Ferrer, V de la Incera, D Manreza Paret, A Pérez Martínez, and A Sanchez. Insignificance of the anomalous magnetic moment of charged fermions for the equation of state of a magnetized and dense medium. *Physical Review D*, 91(8):085041, 2015.
- T Fischer, SC Whitehouse, Anthony Mezzacappa, F-K Thielemann, and M Liebendörfer. Proton-neutron star evolution and the neutrino-driven wind in general relativistic neutrino radiation hydrodynamics simulations. *Astronomy & Astrophysics*, 517:A80, 2010.
- Ralph H Fowler. On dense matter. *Monthly Notices of the Royal Astronomical Society*, 87:114–122, 1926.
- B. Franzon, V. Dexheimer, and S. Schramm. A self-consistent study of magnetic field effects on hybrid stars. 2015.
- B. Franzon, V. Dexheimer, and S. Schramm. Internal composition of proto-neutron stars under strong magnetic fields. *Phys. Rev.*, D94(4):044018, 2016a.
- B Franzon, V Dexheimer, and S Schramm. A self-consistent study of magnetic field effects on hybrid stars. *Monthly Notices of the Royal Astronomical Society*, 456(3):2937–2945, 2016b.
- B. Franzon, D. A. Fogaca, F. S. Navarra, and J. E. Horvath. Self-bound Interacting QCD Matter in Compact Stars. *Phys. Rev.*, D86:065031, 2012.
- B. Franzon, R. O. Gomes, and S. Schramm. Effects of the quark-hadron phase transition on highly magnetized neutron stars. *Mon. Not. Roy. Astron. Soc.*, 463:571–579, 2016c.
- B. Franzon, R. Negreiros, and S. Schramm. Crust effects and the cooling relaxation time in highly magnetized neutron stars. 2016d.
- B. Franzon and S. Schramm. Global properties of the white dwarf pulsar AR Scorpii. 2016.
- Bruno Franzon, V. Dexheimer, and S. Schramm. Effects of strong magnetic fields on hybrid stars. *PoS*, MPCS2015:018, 2016e.
- Bruno Franzon and Stefan Schramm. Effects of strong magnetic fields and rotation on white dwarf structure. *Phys. Rev.*, D92(8):083006, 2015.
- Joachim Friebe and Luciano Rezzolla. Equilibrium models of relativistic stars with a toroidal magnetic field. *Monthly Notices of the Royal Astronomical Society*, 427(4):3406–3426, 2012a.
- Joachim Friebe and Luciano Rezzolla. Equilibrium models of relativistic stars with a toroidal magnetic field. *Mon. Not. Roy. Astron. Soc.*, 427:3406–3426, 2012b.

- John L Friedman and James R Ipser. Rapidly rotating relativistic stars. *Philosophical Transactions of the Royal Society of London A: Mathematical, Physical and Engineering Sciences*, 340(1658): 391–422, 1992.
- Kenji Fukushima. Chiral effective model with the polyakov loop. *Physics Letters B*, 591(3):277–284, 2004.
- I Fushiki, EH Gudmundsson, and CJ Pethick. Surface structure of neutron stars with high magnetic fields. *The Astrophysical Journal*, 342:958–975, 1989.
- ZF Gao, XD Li, N Wang, JP Yuan, QH Peng, and YJ Du. Constraining the braking indices of magnetars. *arXiv preprint arXiv:1505.07013*, 2015.
- Andre F. Garcia and Marcus Benghi Pinto. Surface tension of magnetized quark matter. *Phys. Rev.*, C88(2):025207, 2013.
- VS Geroyannis and AA Hadjopoulos. Models of white dwarfs under rapid uniform or differential rotation-numerical results. *The Astrophysical Journal Supplement Series*, 70:661–677, 1989.
- Kostas Glampedakis, Nils Andersson, and Samuel K Lander. Hydromagnetic equilibrium in non-barotropic multifluid neutron stars. *Monthly Notices of the Royal Astronomical Society*, 420(2): 1263–1272, 2012.
- NK Glendenning. Hyperons in neutron stars. *Zeitschrift für Physik A Atomic Nuclei*, 326(1):57–64, 1987.
- Norman K Glendenning. *Compact stars: Nuclear physics, particle physics and general relativity*. Springer Science & Business Media, 2012.
- Norman K Glendenning, S Pei, and F Weber. Signal of quark deconfinement in the timing structure of pulsar spin-down. *Physical Review Letters*, 79(9):1603, 1997.
- Norman K Glendenning and Jürgen Schaffner-Bielich. First order kaon condensate. *Physical Review C*, 60(2):025803, 1999.
- T Gold. Rotating neutron stars as the origin of the pulsating radio sources. *Neutron stars, black holes, and binary X-ray sources*, 48:354, 1975.
- Peter Goldreich and Andreas Reisenegger. Magnetic field decay in isolated neutron stars. *The Astrophysical Journal*, 395:250–258, 1992.
- R. O. Gomes, V. Dexheimer, S. Schramm, and C. A. Z. Vasconcellos. Many-body forces, isospin asymmetry and dense hyperonic matter. In *Compact Stars in the QCD Phase Diagram IV Prerow, Germany, September 26-30, 2014*, 2015a.
- Rosana de Oliveira Gomes, V Dexheimer, Stefan Schramm, and Cesar Augusto Zen Vasconcellos. Many-body forces in the equation of state of hyperonic matter. *The Astrophysical Journal*, 808(1):8, 2015b.
- Ericourgoulhon. *3+1 formalism in general relativity: bases of numerical relativity*, volume 846. Springer Science & Business Media, 2012.
- Ericourgoulhon and Silvano Bonazzola. A formulation of the virial theorem in general relativity. *Classical and Quantum Gravity*, 11(2):443, 1994.
- J-O. Goussard, P. Haensel, and J. L. Zdunik. Rapid uniform rotation of protoneutron stars. *Astron. Astrophys.*, 321:822–834, 1997.



- J. O. Goussard, P. Haensel, and J. L. Zdunik. Rapid differential rotation of protoneutron stars and constraints on radio pulsars periods. *Astron. Astrophys.*, 330:1005–1016, 1998.
- EINAR H Gudmundsson and JR Buchler. On the consequence of neutrino trapping in gravitational collapse. *The Astrophysical Journal*, 238:717–721, 1980.
- P Haensel, JL Zdunik, M Bejger, and JM Lattimer. Keplerian frequency of uniformly rotating neutron stars and strange stars. *Astronomy & Astrophysics*, 502(2):605–610, 2009.
- O. Hamil, J.R. Stone, M. Urbanec, and G. Urbancov. Braking index of isolated pulsars. *Phys. Rev.*, D91(6):063007, 2015.
- James B Hartle. Slowly rotating relativistic stars. i. equations of structure. *The Astrophysical Journal*, 150:1005, 1967.
- Henning Heiselberg and Morten Hjorth-Jensen. Phase transitions in rotating neutron stars. *Physical Review Letters*, 80(25):5485, 1998.
- M. Hempel, G. Pagliara, and J. Schaffner-Bielich. Conditions for Phase Equilibrium in Supernovae, Proto-Neutron and Neutron Stars. *Phys. Rev.*, D80:125014, 2009.
- Jason WT Hessels, Scott M Ransom, Ingrid H Stairs, Paulo CC Freire, Victoria M Kaspi, and Fernando Camilo. A radio pulsar spinning at 716 hz. *Science*, 311(5769):1901–1904, 2006.
- Antony Hewish, S Jocelyn Bell, JDH Pilkington, PF Scott, and RA Collins. Observation of a rapidly pulsating radio source. *Nature*, 217(5130):709–713, 1968.
- M. Hicken, P. M. Garnavich, J. L. Prieto, S. Blondin, D. L. DePoy, R. P. Kirshner, and J. Parrent. The Luminous and Carbon-Rich Supernova 2006gz: A Double Degenerate Merger? *Astrophys. J.*, 669:L17–L20, 2007.
- D. Andrew Howell et al. The type Ia supernova SNLS-03D3bb from a super-Chandrasekhar-mass white dwarf star. *Nature*, 443:308, 2006.
- RA James. The structure and stability of rotating gas masses. *The Astrophysical Journal*, 140:552, 1964.
- David B Kaplan and Sanjay Reddy. Novel phases and transitions in color flavor locked matter. *Physical Review D*, 65(5):054042, 2002.
- Victoria M Kaspi. Grand unification of neutron stars. *Proceedings of the National Academy of Sciences*, 107(16):7147–7152, 2010.
- W. Keil and H. Th. Janka. Hadronic phase transitions at supranuclear densities and the delayed collapse of newly formed neutron stars. *Astron. Astrophys.*, 296:145, 1995.
- James C. Kemp, John B. Swedlund, J. D. Landstreet, and J. R. P. Angel. Discovery of Circularly Polarized Light from a White Dwarf. *Astrophys. J.*, 161:L77–L79, 1970.
- Kenta Kiuchi and Kei Kotake. Equilibrium configurations of strongly magnetized neutron stars with realistic equations of state. *Monthly Notices of the Royal Astronomical Society*, 385(3):1327–1347, 2008.
- Kenta Kiuchi, Kei Kotake, and Shijun Yoshida. Equilibrium configurations of relativistic stars with purely toroidal magnetic fields: Effects of realistic equations of state. *The Astrophysical Journal*, 698(1):541, 2009.

- Hidemi Komatsu, Yoshiharu Eriguchi, and Izumi Hachisu. Rapidly rotating general relativistic stars—i. numerical method and its application to uniformly rotating polytropes. *Monthly Notices of the Royal Astronomical Society*, 237(2):355–379, 1989.
- Sushan Konar. The magnetic fields of millisecond pulsars in globular clusters. *Monthly Notices of the Royal Astronomical Society*, 409(1):259–268, 2010.
- Chryssa Kouveliotou, S Dieters, T Strohmayer, J Van Paradijs, GJ Fishman, CA Meegan, K Hurley, J Kommers, I Smith, D Frail, et al. An x-ray pulsar with a superstrong magnetic field in the soft  $\gamma$ -ray repeater sgr1806- 20. *Nature*, 393(6682):235–237, 1998.
- S Krishan and RS Kushwaha. On the limiting mass of a rotating white dwarf. *Publications of the Astronomical Society of Japan*, 15:253, 1963.
- Woltjer L. *The Astrophysical Journal*, 140:1309, 1964.
- Dong Lai and Stuart L Shapiro. Cold equation of state in a strong magnetic field-effects of inverse beta-decay. *The Astrophysical Journal*, 383:745–751, 1991.
- LD Landau and EM Lifshitz. Electrodynamics of continuous media addison-wesley. *Reading, MA*, 1960.
- Lev Davidovich Landau. On the theory of stars. *Phys. Z. Sowjetunion*, 1(285):152, 1932.
- Samuel K Lander and DI Jones. Are there any stable magnetic fields in barotropic stars? *Monthly Notices of the Royal Astronomical Society*, 424(1):482–494, 2012.
- James M Lattimer. The nuclear equation of state and neutron star masses. *arXiv preprint arXiv:1305.3510*, 2013.
- JM Lattimer and M Prakash. Neutron star structure and the equation of state. *The Astrophysical Journal*, 550(1):426, 2001.
- C. H. Lenzi and G. Lugones. Hybrid stars in the light of the massive pulsar PSR J1614-2230. *Astrophys. J.*, 759:57, 2012.
- André Lichnerowicz, Southwest Center for Advanced Studies, and The Mathematical Physics Monograph Series. *Relativistic hydrodynamics and magnetohydrodynamics*, volume 35. WA Benjamin New York, 1967.
- Ronaldo V Lobato, Manuel Malheiro, and Jaziel G Coelho. Magnetars and white dwarf pulsars. *International Journal of Modern Physics D*, 25(09):1641025, 2016.
- G. Lugones, A. G. Grunfeld, and M. Al Ajmi. Surface tension and curvature energy of quark matter in the Nambu-Jona-Lasinio model. *Phys. Rev.*, C88(4):045803, 2013.
- G Lugones and JE Horvath. High-density qcd pairing in compact star structure. *Astronomy & Astrophysics*, 403(1):173–178, 2003.
- M. Malheiro and J. G. Coelho. MAGNETIC FIELDS OF SGRs/AXPs AS ROTATION-POWERED MASSIVE WHITE DWARF PULSARS. In *Proceedings, 13th Marcel Grossmann Meeting on Recent Developments in Theoretical and Experimental General Relativity, Astrophysics, and Relativistic Field Theories (MG13)*, pages 2462–2464, 2015.
- Ritam Mallick and P. K. Sahu. Phase transitions in neutron star and magnetars and their connection with high energetic bursts in astrophysics. *Nucl. Phys.*, A921:96–113, 2014.

- Ritam Mallick and Stefan Schramm. Deformation of a magnetized neutron star. *Physical Review C*, 89(4):045805, 2014.
- Richard N Manchester and Joseph H Taylor. Pulsars. 1977.
- RN Manchester, JM Durdin, and LM Newton. A second measurement of a pulsar braking index. 1985.
- TR Marsh, BT Gänsicke, S Hümmelich, F-J Hamsch, K Bernhard, C Lloyd, E Breedt, Elizabeth R Stanway, DT Steeghs, SG Parsons, et al. A radio-pulsing white dwarf binary star. *Nature*, 537(7620):374–377, 2016.
- Alpha Mastrano, Arthur George Suvorov, and Andrew Melatos. Neutron star deformation due to poloidal-toroidal magnetic fields of arbitrary multipole order: a new analytic approach. *Mon. Not. Roy. Astron. Soc.*, 447:3475, 2015.
- A Melatos. Bumpy spin-down of anomalous x-ray pulsars: The link with magnetars. *The Astrophysical Journal Letters*, 519(1):L77, 1999.
- Débora P Menezes and Marcelo D Alloy. Maxwell equation violation by density dependent magnetic fields in neutron stars. *arXiv preprint arXiv:1607.07687*, 2016.
- S. Mereghetti, A. Tiengo, P. Esposito, N. La Palombara, G. L. Israel, and L. Stella. An ultra-massive fast-spinning white dwarf in a peculiar binary system. *Science*, 325:1222, 2009.
- Charles W Misner, Kip S Thorne, and John Archibald Wheeler. *Gravitation*. Macmillan, 1973.
- Rainer Moll, Cody Raskin, Daniel Kasen, and Stan Woosley. Type Ia Supernovae from Merging White Dwarfs. I. Prompt Detonations. *Astrophys. J.*, 785:105, 2014.
- JJ Monaghan. The structure of rapidly rotating white dwarfs. *Monthly Notices of the Royal Astronomical Society*, 132(2):305–316, 1966.
- Ian A Morrison, Thomas W Baumgarte, and Stuart L Shapiro. Effect of differential rotation on the maximum mass of neutron stars: realistic nuclear equations of state. *The Astrophysical Journal*, 610(2):941, 2004.
- Philipp Mösta, Christian D Ott, David Radice, Luke F Roberts, Erik Schnetter, and Roland Haas. A large-scale dynamo and magnetoturbulence in rapidly rotating core-collapse supernovae. *Nature*, 528(7582):376–379, 2015.
- Rodrigo Negreiros, VA Dexheimer, and S Schramm. Modeling hybrid stars with an  $su(3)$  nonlinear  $\sigma$  model. *Physical Review C*, 82(3):035803, 2010.
- Jorge L Noronha and Igor A Shovkoy. Color-flavor locked superconductor in a magnetic field. *Physical Review D*, 76(10):105030, 2007.
- Tetsuo Nozawa, Nikolaos Stergioulas, Eric Gourgoulhon, and Yoshiharu Eriguchi. Construction of highly accurate models of rotating neutron stars—comparison of three different numerical schemes. *Astronomy and Astrophysics Supplement Series*, 132(3):431–454, 1998.
- Martin Obergaugling, Pablo Cerdá-Durán, Ewald Müller, and MA Aloy. Semi-global simulations of the magneto-rotational instability in core collapse supernovae. *Astronomy & Astrophysics*, 498(1):241–271, 2009.
- SA Olausen and VM Kaspi. The mcgill magnetar catalogan online version of the catalog is located at <http://www.physics.mcgill.ca/~pulsar/magnetar/main.html>. *The Astrophysical Journal Supplement Series*, 212(1):6, 2014.

- J Robert Oppenheimer and George M Volkoff. On massive neutron cores. *Physical Review*, 55(4): 374, 1939.
- JP Ostriker and JE Gunn. On the nature of pulsars. i. theory. *The Astrophysical Journal*, 157:1395, 1969.
- Edson Otoniel, Bruno Franzon, Manuel Malheiro, Stefan Schramm, and Fridolin Weber. Axisymmetric magnetic fields, electron capture and pycnonuclear reactions in magnetized white dwarfs. *arXiv preprint arXiv:1609.05994*, 2016.
- F Pacini. Energy emission from a neutron star. *Nature*, 216:567–568, 1967.
- F Pacini. Rotating neutron stars, pulsars and supernova remnants. *Nature*, 219:145–146, 1968.
- Bohdan Paczynski. Gb 790305 as a very strongly magnetized neutron star. *Acta Astronomica*, 42: 145–153, 1992.
- P. Papazoglou, D. Zschesche, S. Schramm, J. Schaffner-Bielich, Horst Stoecker, et al. Nuclei in a chiral SU(3) model. *Phys.Rev.*, C59:411–427, 1999.
- L Paulucci, Efrain J Ferrer, Vivian de La Incera, and JE Horvath. Equation of state for the magnetic-color-flavor-locked phase and its implications for compact star models. *Physical Review D*, 83(4): 043009, 2011.
- Aurora Perez Martinez, H. Perez Rojas, H. J. Mosquera Cuesta, M. Boligan, and M. G. Orsaria. Quark stars and quantum-magnetically induced collapse. *Int. J. Mod. Phys.*, D14:1959, 2005.
- CJ Pethick. Cooling of neutron stars. *Reviews of modern physics*, 64(4):1133, 1992.
- ES Phinney, Peter Bender, Saps Buchman, Robert Byer, Neil Cornish, Peter Fritschel, William Folkner, Stephen Merkowitz, Karsten Danzmann, Luciano DiFiore, et al. The big bang observer. *NASA Mission Concept Study*, 2003.
- A. G. Pili, N. Bucciantini, and L. Del Zanna. Axisymmetric equilibrium models for magnetized neutron stars in General Relativity under the Conformally Flat Condition. *Mon. Not. Roy. Astron. Soc.*, 439(4):3541–3563, 2014a.
- AG Pili, N Bucciantini, and L Del Zanna. Axisymmetric equilibrium models for magnetized neutron stars in general relativity under the conformally flat condition. *Monthly Notices of the Royal Astronomical Society*, 439(4):3541–3563, 2014b.
- JA Pons, S Reddy, M Prakash, JM Lattimer, and JA Miralles. Evolution of proto-neutron stars. *The Astrophysical Journal*, 513(2):780, 1999.
- Jose A. Pons, Juan A. Miralles, M. Prakash, and James M. Lattimer. Evolution of protoneutron stars with kaon condensates. *Astrophys. J.*, 553:382–393, 2001a.
- Jose A Pons, Andrew W Steiner, Madappa Prakash, and James M Lattimer. Evolution of proto-neutron stars with quarks. *Physical Review Letters*, 86(23):5223, 2001b.
- M Prakash, JR Cooke, and JM Lattimer. Quark-hadron phase transition in protoneutron stars. *Physical Review D*, 52(2):661, 1995.
- Madappa Prakash, Ignazio Bombaci, Manju Prakash, Paul J Ellis, James M Lattimer, and Roland Knorren. Composition and structure of protoneutron stars. *Physics Reports*, 280(1):1–77, 1997.

- Madappa Prakash, James M Lattimer, Jose A Pons, Andrew W Steiner, and Sanjay Reddy. Evolution of a neutron star from its birth to old age. In *Physics of neutron star interiors*, pages 364–423. Springer, 2001.
- Madappa Prakash, Manju Prakash, James M Lattimer, and CJ Pethick. Rapid cooling of neutron stars by hyperons and delta isobars. *The Astrophysical Journal*, 390:L77–L80, 1992.
- Angela Putney. Three new magnetic white dwarf stars. *The Astrophysical Journal Letters*, 451(2):L67, 1995.
- A Rabhi, H Pais, PK Panda, and C Providencia. Quark–hadron phase transition in a neutron star under strong magnetic fields. *Journal of Physics G: Nuclear and Particle Physics*, 36(11):115204, 2009.
- A Rabhi, C Providência, and J Da Providencia. Stellar matter with a strong magnetic field within density-dependent relativistic models. *Journal of Physics G: Nuclear and Particle Physics*, 35(12):125201, 2008.
- Sanjay Reddy, J Pons, M Prakash, and JM Lattimer. Neutrinos from protoneutron stars. *arXiv preprint astro-ph/9802310*, 1998a.
- Sanjay Reddy, Madappa Prakash, and James M Lattimer. Neutrino interactions in hot and dense matter. *Phys. Rev.*, D58:013009, 1998b.
- D. Reimers, S. Jordan, D. Koester, N. Bade, T. Kohler, and L. Wisotzki. Discovery of four white dwarfs with strong magnetic fields by the Hamburg / ESO survey. *Astron. Astrophys.*, 311:572–578, 1996.
- Tomasz Rembiasz, Jérôme Guilet, Martin Obergaulinger, Pablo Cerdá-Durán, MA Aloy, and Ewald Müller. On the maximum magnetic field amplification by the magnetorotational instability in core-collapse supernovae. *Monthly Notices of the Royal Astronomical Society*, page stw1201, 2016.
- Clifford E Rhoades Jr and Remo Ruffini. Maximum mass of a neutron star. *Physical Review Letters*, 32(6):324, 1974.
- Adam G Riess, Alexei V Filippenko, Peter Challis, Alejandro Clocchiatti, Alan Diercks, Peter M Garnavich, Ron L Gilliland, Craig J Hogan, Saurabh Jha, Robert P Kirshner, et al. Observational evidence from supernovae for an accelerating universe and a cosmological constant. *The Astronomical Journal*, 116(3):1009, 1998.
- IW Roxburgh and BR Durney. Structure, oscillations and stability of rotating white dwarfs. *Zeitschrift fur Astrophysik*, 64:504, 1966.
- M Salgado, S Bonazzola, E Gourgoulhon, and P Haensel. High precision rotating neutron star models 1: Analysis of neutron star properties. *Astronomy and Astrophysics*, 291:155–170, 1994.
- Hidetomo Sawai and Shoichi Yamada. The evolution and impacts of magnetorotational instability in magnetized core-collapse supernovae. *The Astrophysical Journal*, 817(2):153, 2016.
- Hidetomo Sawai, Shoichi Yamada, and Hideyuki Suzuki. Global simulations of magnetorotational instability in the collapsed core of a massive star. *The Astrophysical Journal Letters*, 770(2):L19, 2013.
- R. A. Scalzo et al. Nearby Supernova Factory Observations of SN 2007if: First Total Mass Measurement of a Super-Chandrasekhar-Mass Progenitor. *Astrophys. J.*, 713:1073–1094, 2010.

- Gary D. Schmidt and Paul S. Smith. A Search for magnetic fields among DA white dwarfs. *Astrophys. J.*, 448:305, 1995.
- Naoki Seto, Seiji Kawamura, and Takashi Nakamura. Possibility of direct measurement of the acceleration of the universe using 0.1 hz band laser interferometer gravitational wave antenna in space. *Physical Review Letters*, 87(22):221103, 2001.
- Stuart L Shapiro and Saul A Teukolsky. *Black holes, white dwarfs and neutron stars: the physics of compact objects*. 2008.
- Monika Sinha, Xu-Guang Huang, and Armen Sedrakian. Strange quark matter in strong magnetic fields within a confining model. *Physical Review D*, 88(2):025008, 2013.
- Larry Smarr and James W York Jr. Kinematical conditions in the construction of spacetime. *Physical Review D*, 17(10):2529, 1978.
- NK Spyrou and N Stergioulas. Spin-down of relativistic stars with phase transitions and psr j0537-6910. *Astronomy & Astrophysics*, 395(1):151–160, 2002.
- David H Staelin and Edward C Reifstein. Pulsating radio sources near the crab nebula. *Science*, 162(3861):1481–1483, 1968.
- Josef Stein and J. Craig Wheeler. The convective urca process with implicit two-dimensional hydrodynamics. *Astrophys. J.*, 643:1190–1197, 2006.
- Nikolaos Stergioulas and John L Friedman. Comparing models of rapidly rotating relativistic stars constructed by two numerical methods. *arXiv preprint astro-ph/9411032*, 1994.
- Michael Strickland, Veronica Dexheimer, and Debora P Menezes. Bulk properties of a fermi gas in a magnetic field. *Physical Review D*, 86(12):125032, 2012.
- In-Saeng Suh and GJ Mathews. Mass-radius relation for magnetic white dwarfs. *The Astrophysical Journal*, 530(2):949, 2000.
- In-Saeng Suh, G.J. Mathews, and F. Weber. Comment on 'Can there be a quark matter core in a magnetar?'. *Phys.Rev.D*, 2001.
- F Douglas Swesty. Thermodynamically consistent interpolation for equation of state tables. *Journal of Computational Physics*, 127(1):118–127, 1996.
- Ngo Hai Tan, Doan Thi Loan, Dao T. Khoa, and Jerome Margueron. Mean-field study of hot  $\beta$ -stable protoneutron star matter: Impact of the symmetry energy and nucleon effective mass. *Phys. Rev.*, C93(3):035806, 2016.
- Toshitaka Tatsumi. Ferromagnetism of quark liquid. *Physics Letters B*, 489(3):280–286, 2000.
- S Taubenberger, S Benetti, M Childress, R Pakmor, S Hachinger, PA Mazzali, V Stanishev, Nancy Elias-Rosa, I Agnoletto, F Bufano, et al. High luminosity, slow ejecta and persistent carbon lines: Sn 2009dc challenges thermonuclear explosion scenarios. *Monthly Notices of the Royal Astronomical Society*, 412(4):2735–2762, 2011.
- Yukikatsu Terada, Takayuki Hayashi, Manabu Ishida, Koji Mukai, Tadayasu Dotani, Shunsaku Okada, Ryoko Nakamura, Sachindra Naik, Aya Bamba, and Kazuo Makishima. Suzaku Discovery of Non-thermal X-ray Emission from the Rotating Magnetized White Dwarf, AE Aquarii. *Publ. Astron. Soc. Jap.*, 60:387, 2008.

- Christopher Thompson and Robert C. Duncan. Neutron star dynamos and the origins of pulsar magnetism. *Astrophys. J.*, 408:194, 1993.
- Christopher Thompson and Robert C. Duncan. The Soft gamma repeaters as very strongly magnetized neutron stars. 2. Quiescent neutrino, x-ray, and Alfvén wave emission. *Astrophys. J.*, 473:322, 1996.
- Richard C Tolman. Static solutions of Einstein's field equations for spheres of fluid. *Physical Review*, 55(4):364, 1939.
- MH Van Kerkwijk, RP Breton, and SR Kulkarni. Evidence for a massive neutron star from a radial-velocity study of the companion to the black-widow pulsar PSR B1957+20. *The Astrophysical Journal*, 728(2):95, 2011.
- Isaac Vidaña. Hyperons and neutron stars. *Nuclear Physics A*, 914:367–376, 2013.
- Jacco Vink and Lucien Kuiper. Supernova remnant energetics and magnetars: no evidence in favour of millisecond proto-neutron stars. *Monthly Notices of the Royal Astronomical Society: Letters*, 370(1):L14–L18, 2006.
- Andrey D Vlasov, Brian D Metzger, and Todd A Thompson. Neutrino-heated winds from rotating protomagnetars. *Monthly Notices of the Royal Astronomical Society*, 444(4):3537–3558, 2014.
- Robert M Wald. *General relativity*. University of Chicago press, 2010.
- F Weber. Quark matter in neutron stars. *Journal of Physics G: Nuclear and Particle Physics*, 25(9):R195, 1999a.
- F Weber, NK Glendenning, and MK Weigel. Structure and stability of rotating relativistic neutron stars. *The Astrophysical Journal*, 373:579–591, 1991.
- Fridolin Weber. *Pulsars as astrophysical laboratories for nuclear and particle physics*. CRC Press, 1999b.
- Fridolin Weber, Norman K Glendenning, and Shouyong Pei. Signal for the quark-hadron phase transition in rotating hybrid stars. *arXiv preprint astro-ph/9705202*, 1997.
- Steven Weinberg. *Gravitation and cosmology: principles and applications of the general theory of relativity*, volume 1. Wiley New York, 1972.
- Steven Weinberg. Why do quarks behave like bare Dirac particles? *Phys.Rev.Lett.*, 65:1181–1183, 1990.
- M. Yamanaka et al. Early phase observations of extremely luminous Type Ia Supernova 2009dc. *Astrophys. J.*, 707:L118–L122, 2009.
- N. Yasutake, G. F. Burgio, and H. J. Schulze. Hadron-Quark Phase Transitions in Hyperon Stars. *Phys. Atom. Nucl.*, 74:1502–1507, 2011.
- Nobutoshi Yasutake and Kouji Kashiwa. Lepton effects on the proto-neutron stars with the hadron-quark mixed phase in the Nambu-Jona-Lasinio model. *Phys. Rev.*, D79:043012, 2009.
- Shijun Yoshida, Shinichirou Yoshida, and Yoshiharu Eriguchi. Twisted-torus equilibrium structures of magnetic fields in magnetized stars. *The Astrophysical Journal*, 651(1):462, 2006.
- JL Zdenek, M Bejger, P Haensel, and E Gourgoulhon. Phase transitions in rotating neutron star cores: back bending, stability, corequakes, and pulsar timing. *Astronomy & Astrophysics*, 450(2):747–758, 2006.

JL Zdunik, M Bejger, P Haensel, and E Gourgoulhon. Strong first-order phase transition in a rotating neutron star core and the associated energy release. *Astronomy & Astrophysics*, 479(2):515–522, 2008.

Julian L Zdunik, P Haensel, E Gourgoulhon, and M Bejger. Hyperon softening of the eos of dense matter and the spin evolution of isolated neutron stars. *Astronomy & Astrophysics*, 416(3): 1013–1022, 2004.



# Acknowledgements

I would like to thank firstly my adviser Stefan Schramm for the constant support. I have enjoyed his fruitful comments, constant encouragement and interest in my work. I am also grateful to Veronica Dexheimer with whom I collaborated during my PhD studies. Our numerous scientific discussions have been of great value to me. I especially thank to the friends that I made in Germany. Their love, unconditional support and understanding were very important to me. I cannot imagine how I could have succeeded without them. I would like also to thank my family for all their support throughout my life that made it possible for me to pursue my Ph.D. degree. Finally, I acknowledge the support from CNPq/Brazil, DAAD and HGS-HIRe for FAIR.

*To my grandmother, my mother and my sister.*



# Academic CV

## Personal Data

Sex: M  
Birth date: 08/19/1987  
Birth place: Tupi Paulista - SP  
Nationality: Brazilian  
Single

## Current Academic Position

PhD student at Frankfurt Institute for Advanced Studies (FIAS), Frankfurt-Germany.  
Period April 2013 - March 2017

## Skills

- Programming Skills: Fortran, C++, Mathematica
- Environment: Windows, Linux, Mac OSX
- Languages: Portuguese (native), English (fluent), German (fluent)

## Education

2005–2009 - Bachelor's Degree, Physics Institute, University of São Paulo, São Paulo, Brazil,

2007–2008 - Undergraduate research in Paleomagnetism, Astronomy and Geophysics Institute, University of São Paulo, São Paulo, Brazil.

2008–2009 - Undergraduate research in Particle and Nuclear Physics Physics Institute, University of São Paulo, São Paulo, Brazil..

## Masters Thesis

**Title:** *On the effect of the gluon condensates in the structure of quark stars.*

**Supervisor:** Prof. Dr. Fernando Silveira Navarra.

**Institution:** University of São Paulo, 2012

## Professional associations

DAAD Alumni

Participant of NewCompStar

Member of Helmholtz Graduate School for Hadron and Ion Research, HGS-HIRe for FAIR.

## Professional Training

- Leadership and Career Development course (1 week), HGS-HIRe, 2016, Buchenau, Germany.
- Research visit at Kent State University, USA. February-March 2016.
- Ion beams for materials science and nanotechnology course (1 week), GSI, HGS-HIRe, 2015, Darmstadt, Germany.
- Leading Teams in a Research Environment (1 week), HGS-HIRe, 2015, Buchenau, Germany.
- Hot/Dense Matter and Nuclear Astrophysics (1 week), HGS-HIRe, 2014, Herborn, Germany.
- Making an Impact as an Effective Researcher (1 week), HGS-HIRe, 2014, Buchenau, Germany.
- German Language Course - DAAD Fellowship, Goethe Institute Dresden, 2012-2013 (6 months), Germany.

## Research Interests

- Nuclear Physics: Equation of state, Phase transitions, Quark matter.
- Astrophysics: General relativity, Gravitational Radiation, Binary neutron star systems, Supernova explosions, Neutron stars, Hyperonic matter, Proto-neutron stars, Star rotation, Quark stars, Stellar Magnetic Fields. White dwarfs.

## List of Publications

### E-prints

- submitted to *Physical Review Letter*: The magnetic field profile in strongly magnetized neutron stars, *arXiv:1612.05795*. Authors: Dexheimer, V.; Franzon, B.; Gomes, R.; R. L. S. Farias; S. S. Avancini; S. Schramm
- submitted to *MNRAS*: Crust effects and the cooling relaxation time in highly magnetized neutron stars, *arXiv:1612.04670*. Authors: Franzon, B.; Negreiros, R.; and Schramm, S.
- submitted to *MNRAS*: Global properties of the white dwarf pulsar AR Scorpii, *arXiv:1609.00493*. Authors: Franzon, B.; and Schramm, S.
- submitted to *Physical Review D*: Axisymmetric Magnetic Fields, Electron Capture and Pycnonuclear Reactions in Magnetized White Dwarfs, *arXiv:1609.05994*. Authors: Edson Otoniel, Franzon, B., Manuel Malheiro, Stefan Schramm, Fridolin Weber.
- Magnetized Neutron Star, 2015, *arXiv:1504.02337*. Authors: Franzon, B.; Schramm, S.

### Refereed Journal Articles

- Franzon, B., V. Dexheimer and S. Schramm. Rotating proto-neutron stars under strong magnetic fields, *Phys.Rev. D94* (2016) no.4, 044018.
- Franzon, B.; Gomes, Rosana; Schramm, Stefan. Effects of quark-hadron phase transition on highly magnetized neutron stars, *MNRAS* 463 (2016) 571-579.
- Franzon, B.; Dexheimer, V.; S. Schramm. A self-consistent study of magnetic field effects on hybrid stars, *MNRAS* 456 (2015) no.3, 2937-2945.
- Franzon, B.; Schramm, S. Effects of strong magnetic fields and rotation on white dwarf structure, *Phys.Rev. D92* (2015) 8, 083006.
- Franzon, B.; Fogaca, D. A.; Navarra, F. S.; Horvath, J. E. Self-bound interacting QCD matter in compact stars. *Physical Review. D*, v. 86, p. 065031, 2012.

### Refereed Proceedings

- Franzon, B.; Schramm, S. A self-consistent study of magnetic field effects on hybrid stars, *PoS(MPCS2015)018*.
- Franzon, B.; D.A. Fogaca; Fernando S. Navarra. Gluons in neutron stars. *International Journal of Modern Physics E*, v. 20, p. 183-187, 2011.
- Fogaca, D. A.; Navarra, F. S.; Franzon, B.; Horvath, J. E. . A mean field theory for the cold quark gluon plasma applied to stellar structure, *XII HADRON PHYSICS, 2013, Bento Goncalves*, p. 379.
- Franzon, B.; Fogaca, D. A.; Navarra, F. S.; Horvath, J. E. Cold quark matter in compact stars, *XII HADRON PHYSICS, 2013, Bento Goncalves*, p. 382.
- Franzon, B.; Fernando S. Navarra; D.A. Fogaca. Stellar structure from QCD. In: 5th International Workshop on Astronomy and Relativistic Astrophysics *IWARA*, Joao Pessoa, 2011, Joao Pessoa. *Stellar structure from QCD*, v. 18, p. 91-95.
- D.A. Fogaca; Fernando S. Navarra; Franzon, B.. A mean field theory for the cold quark gluon plasma applied to stellar structure. In: 5th International Workshop on Astronomy and Relativistic Astrophysics *IWARA*, Joao Pessoa., 2011, Joao Pessoa. *A mean field theory for the cold quark gluon plasma applied to stellar structure*, 2011, v. 18, p. 81-85.
- D.A. Fogaca; Franzon, B.; Fernando S. Navarra . Gluons in the stars. In: 1st Caribbean Symposium, *STARS 2011*, 2011, Havana. *Gluons in the stars.*, 2011. v. 20, p. 183.
- Franzon, B.; Fernando S. Navarra . Inelasticity and the growth of hadronic cross sections at high energies. In: *XI Hadrons Physics*, 2010, Maresias, SP. *AIP Conference Proceedings*, 2010. v. 129, p. 286-289.

### Works in progress

- Many-body forces in magnetic neutron stars (writing process). Authors: Gomes, R.; Franzon, B. and Schramm, S.

- Neutron star inner crust: effects of rotation and magnetic fields (writing process). Authors: Franzon, B.; Paes, H.; Providencia, C.; Schramm, S.

## Professional Experience

2013 - Interview (in Portuguese) given for Deutsche Welle, Link: <http://www.dw.com/pt-br/os-temas-apresentados-no-futurando-66/a-17239994>, Start: 9':35", Bonn, Germany.

2012 - Event Organiser, Compact Stars in the QCD Phase Diagram III, Guaruja.

2012 - Lecturer, Course of Engineering Physics Laboratory III, Physics Institute, University of Sao Paulo, Brazil.

2011 - Teaching Assistant, Course of Physics IV, Physics Institute, University of Sao Paulo, Brazil.

2011 - Teaching Assistant, Course of Electricity and Magnetism, Physics Institute, University of Sao Paulo, Brazil.

2011 - Reviewer of books of Physics for High School, Publisher Santa Maria, Sao Paulo, Brazil.

2010 - Teaching Assistant, Course of Electricity and Magnetism, Physics Institute, University of Sao Paulo, Brazil.

2009 - Teaching Assistant, Course of Introduction to Physics, Physics Institute, University of Sao Paulo, Brazil.

## Seminars presented

2016 - Effects of strong magnetic fields in neutron stars and white dwarfs. Nuclear Physics, Compact Stars, and Compact Star Mergers, Kyoto-Japan, October.

2016 - White Dwarfs under strong magnetic fields. Compact Stars in the QCD phase diagram V, L'aquila, Italy, May.

2016 - Magnetized White Dwarfs. Kent State University, Kent, USA, March.

2016 - Magnetized Compact Objects. Frankfurt Institute for Advanced Studies, Frankfurt-Germany, January.

2015 - A self-consistent study of magnetic field effects on hybrid stars. The Modern Physics of Compact Stars and Relativistic Gravity, Yerevan, Armenia, September.

2014 - Magnetized Neutron Stars. Compact Stars in the QCD Phase Diagram IV, Prerow, Germany.

2011 - Stellar structure from QCD. V International Workshop on Astronomy and Relativistic Astrophysics, João Pessoa, Brazil.

2009 - Effects of quarks and gluons on neutron stars hadronic physics, Rio de Janeiro, Brazil.

2009 - Proton - proton interaction at high energies. Hadronic Physics Meeting, Penedo, Rio de Janeiro.

2009 - Proton - proton interaction at high energies. V Undergraduate Research Internship, São Paulo, Brazil.

2007 - Comparative and paleomagnetic data analysis of magmatic occurrences of the northeastern Brazil. IV Astronomy and Geophysics Institute (IAG-USP), São Paulo-Brazil.

## Events and Workshops/Conferences

2017 - Annual NewCompStar Conference, Warsaw-Poland.

2016 - Compact stars and gravitational waves, Kyoto-Japan, October 31 - November 4.

2016 - NewCompStar Summer School, Neutron stars: gravitational physics and observations, Coimbra-Portugal, September.

2016 - Origin, evolution and observable effects of the magnetic field in neutron stars, Alicante-Spain.

2015 - Dense Matter in Compact Stars: Experimental and Observational Signatures, Bucharest-Romania.

2015 - Annual NewCompStar Conference, Budapest-Hungary.

2014 - The Structure and Signals of Neutron Stars from Birth to Death, Florence-Italy.

2014 - Origin and Evolution of Neutron Star B-fields, Bonn-Germany.

2014 - HGS-HIRe Graduate Days, Grundau-Germany.

2013 - The Helmholtz Graduate School for Hadron and Ion Research, Worms-Germany, Graduate Days.

2012 - Hadron Physics XII, Bento Goncalves-Brazil. Cold Quark Matter in Compact Stars.

2012 - XV Summer School Jorge Andre Swieca of Theoretical Nuclear Physics, Campos do Jordao-Brazil. Poster presented: On the behavior of the cross section  $p - A$  at high energies.

2011 - Hadron Physics XI, Maresias, Brazil. Poster presented: Inelasticity and the growth of hadronic cross section at high energies.

